Corrosion of high surface area carbon supports used in proton-exchange membrane fuel cell electrodes

Luis Filipe Rodrigues Castanheira

UNIVERSITÉ DE GRENOBLE

THÈSE

Pour obtenir le grade de

DOCTEUR DE L'UNIVERSITÉ DE GRENOBLE

Spécialité : **Matériaux, Mécanique, Génie Civil, Electrochimie**

Arrêté ministériel : 7 août 2006

Présentée par

Luis Filipe RODRIGUES CASTANHEIRA

Thèse dirigée par **Frédéric MAILLARD** et par **Laetitia DUBAU**

préparée au sein du **Laboratoire d'Electrochimie et de Physico-chimie des Matériaux et des Interfaces - LEPMI**
dans **l'École Doctorale Ingénierie – Matériaux, Mécanique, Energétique Environnement Procédés Production**

Corrosion of high surface area carbon supports used in proton-exchange membrane fuel cell electrodes

Thèse soutenue publiquement le **14 Novembre 2014**,
devant le jury composé de :

Dr. Michel MERMOUX
Directeur de recherche, CNRS, Grenoble (France), Président

Pr. Plamen ATANASSOV
Professeur, The University of New Mexico, Albuquerque (Etats-Unis), Rapporteur

Dr. Lorenz GUBLER
Chef d'équipe au Paul Scherrer Institute, Villigen (Suisse), Rapporteur

Dr. Gael MARANZANA
Professeur, Université de Lorraine, Nancy (France), Examinateur

Dr. Pierre-André JACQUES
Ingénieur CEA, CEA-Liten, Grenoble (France), Invité

Dr. Frédéric MAILLARD
Chargé de recherche, CNRS, Grenoble (France), Directeur de thèse

Dr. Laetitia DUBAU
Chargée de recherche, CNRS, Grenoble (France), Co-Directrice de thèse

A procura do conhecimento encontra uma vaga noção de tudo, e um conhecimento de nada.

Charles Dickens

Acknowledgments

It's been already 4 years since I left my country in the search of new experiences, new places, new persons and everything that comes with living abroad. This thesis became part of it and now it's time to recognize the ones who were next to me during this period.

Frederic Maillard and Laetitia Dubau were my two supervisors. They attracted me to a new scientific field along with their passion. The mutual confidence while experimenting side to side and the on-going discussions in the lab will always be present in my memory. I own both of them a lot!!

Even if not administratively linked to my work, Marian Chatenet and Julien Durst were part of the H2E project which funded this thesis. Along with Frederic and Laetitia, we were the "Durability team" and we all worked for the same purpose. Such state of mind at work is scarce and I only hope to find it once again.

During my stay I have explored the LEPMI resources to perform my work. In that Alexandre Crisci, Michel Mermoux and Gregory Berthomé were a grateful help concerning Raman spectroscopy and X-ray photoelectron spectroscopy measurements.

A laboratory is nothing without its students, technicians and board team. From office and lab partners I have to mention Marc, Pyo, Anicet, Gwenn, Marie, Jaro, Guillaume, Manue, Phillipe, Bruno, Flavio, Thiago, Manu and all the students that have passed and contributed to our daily madness. The technicians, who fixed my electrochemical cells and have made my nicest setups, thank you. To Claire and Yasmine, the finest accountants of Grenoble INP...merci pour les pauses midi!! A final word of appreciation to the director of the LEPMI, Ricardo Nogueira.

Grenoble is the city where most of the people you meet have an "expiring date". Lots of them are already gone as Marcio, Ricardo, Joao, Daniel and others. Some are still here as Leonardo, Danielle, Julien, Adeline and now thanks to the world cup a huge Portuguese group (too many to cite each one of you) has been made. With all of them I have spent great times and I thank you all a lot.

I would also like to appreciate Claire, a special encounter from my stay in Grenoble.

To the end I leave my closest friends of Portugal and my beloved family. You mainly give me two things around a year: *Saudade* while I'm gone and *Felicidade* when I'm back. As someone says in our country and I agree: *Não ha nada como casa!* (There's nothing like home!)

Obrigado a todos!!!!!

Table of Contents

List of Figures

List of Tables

List of symbols and abbreviations

$\bar{d}_N$:	Mean particle size (nm)
$\bar{d}_S$:	Surface averaged particle size (nm)
E:	Potential (V)
$E^0_{M^+/M}$:	Standard equilibrium potential of the M^+/M redox couple (V)
E_{ox}:	Potential of oxide formation of an electrode (V)
E_l:	Excitation laser energy (eV)
E_{AST}:	Potential of Accelerated Stress Test (V)
H_{upd}:	Hydrogen under potential deposition
I:	Current (A)
I/C:	Ionomer to carbon weight ratio
j:	Current density (A cm^{-2})
T:	Temperature (K)
t:	Time (h)
v:	Linear potential scan rate (V s^{-1})
L_a:	Average in-plane crystallite size (nm)
L_c:	Average size of the graphitic domains perpendicularly to the graphene layers
d_{002}:	Average inter-planar space within graphene layers
S_{BET}:	Brunauer-Emmet-Teller surface area
i:	Mass-specific current density
k:	Temperature and potential rate parameter
n:	Potential-dependent parameter
I_D/I_G:	Ratio between D1-band and G-band
$\bar{\upsilon}$:	Vibrational frequency
λ:	Laser wave-lenght

APUs:	Auxiliary Power Units
AFC:	Alkaline Fuel Cell
ASTs:	Accelerated Stress Tests
BET:	Brunauer-Emmet-Teller
BoL:	Beginning-of-Life
BSE:	Backscattered Electron
CHP:	Combined Heat and Power systems
COR:	Carbon Oxidation Reaction
COsurf:	Carbon Oxide surface species
CCM:	Catalyst Coated Membrane
CCB:	Catalyst Coated Backing
CL:	Catalytic Layer
CV:	Cyclic Voltammogram
DMFC:	Direct Methanol Fuel Cell
DEMS:	Differential Electrochemical Mass Spectrometry
DoE:	American Department of Energy
EoL:	End-of-Life
EU:	European Union

ECSA:	Electrochemical Surface Area
EIS:	Electrochemical Impedance Spectroscopy
EW:	Equivalent Weight
FCEVs:	Fuel Cell Electric Vehicles
FCCJ:	Fuel Cell Commercialization Conference of Japan
FEG:	Field Emission Gun
GDL:	Gas Diffusion Layer
HOPG:	Highly Oriented Pyrolytic Graphite
HOR:	Hydrogen Oxidation Reaction
HSAC:	High Surface Area Carbon
H2E:	Horizon Hydrogen Energy
IR:	Infra-Red
IL-TEM:	Identical-Location Transmission Electron Microscopy
MCFC:	Molten Carbonate Fuel Cell
MEA:	Membrane Electrode Assembly
MSE:	Mercury Sulphate Electrode
NHE:	Normal Hydrogen Electrode
OCP:	Open Circuit Potential
ORR:	Oxygen Reduction Reaction
PEM:	Proton Electrolyte Membrane
PEMFC:	Proton Exchange Membrane Fuel Cell
PAFC:	Phosphoric Acid Fuel Cell
PFSA:	Perfluorosulfonic Acid
PSD:	Particle Size Distribution
PTFE:	Polytetrafluoroethylene
RG :	Reinforced Graphite
RDE:	Rotating Disk Electrode
RH:	Relative Humidity
RHE:	Reversible Hydrogen Electrode
SOFC:	Solid Oxide Fuel Cell
SHE:	Standard Hydrogen Electrode
SEM:	Scanning Electron Microscopy
SE:	secondary Electrons
T.K.K. :	Tanaka Kikinzoku Kogyo
TEM:	Transmission Electron Microscopy
UN:	United Nations
UHV:	Ultra-High Vacuum

Chapter I.

Introduction

1.1 Fuel cell technologies and industrial overview

1.1.1 Energy issues of today's society

Since the beginning of the industrial revolution, several benefits raised for the modern society: (*i*) mass production of goods (*ii*) improvement of the knowledge in science, engineering, and technology (*iii*) increase of employment opportunities (*iv*) construction of a worldwide network of transportation and communications. These benefits led to an outstanding growth of the World population to 7 billion people and, according to the Department of Economic and Social Affairs – Population Division from the United Nations (UN) [1], the mark of 10 billion people will be reached in 2060 (Figure I - 1. a)). These numbers imply a huge demand in terms of energy: industries have to keep their production lines working, transportation and communication networks must be constantly operational and the population has a need in terms of housing electricity and heating.

Essentially non-renewable resources, such as coal, petroleum and uranium (nuclear energy), are mainly used to meet the energy demand. The extraction of these natural resources and their transformation into useful energy (combustion engines, electricity and nuclear plants) result in emissions of carbon dioxide gas (CO_2) [2]. Such emissions contribute to the human-induced global warming that is the continuous rise in the temperature of the Earth. Figure I - 1. b) shows the world CO_2 emissions by sector in 2011 as reported by the International Energy Agency [3]. The generation of electricity and heat combined with transport represent almost two-thirds of the global emissions in 2011. This fact, combined with the UN projections of the increase of the World population, forces the governments to decrease CO_2 emissions with the establishment of economical/ecological treaties (Kyoto protocol, Climate change roadmaps) and drives intensive search for low-carbon or carbon-neutral energy. In particular, the use of renewable-energy sources (wind, solar, geothermal, ocean energy) is promoted and growing rapidly. However, the energy supply from these sources is intermittent, and does not satisfy the energy demand. Solving intermittency is possible by storing excess-energy in batteries, compressed air, or chemical bonds. In the latter example, for example, hydrogen (H_2) and oxygen (O_2) can be produced *via* water (H_2O) electrolysis, stored in adequate tanks and then recombined efficiently in a fuel cell to produce electricity when needed. Moreover, this cycle uses and generates only water (non-polluting technology) and offers the possibility to be incorporated in the previously referred sectors that more contribute for the CO_2 emissions: electricity/heat production and transports.

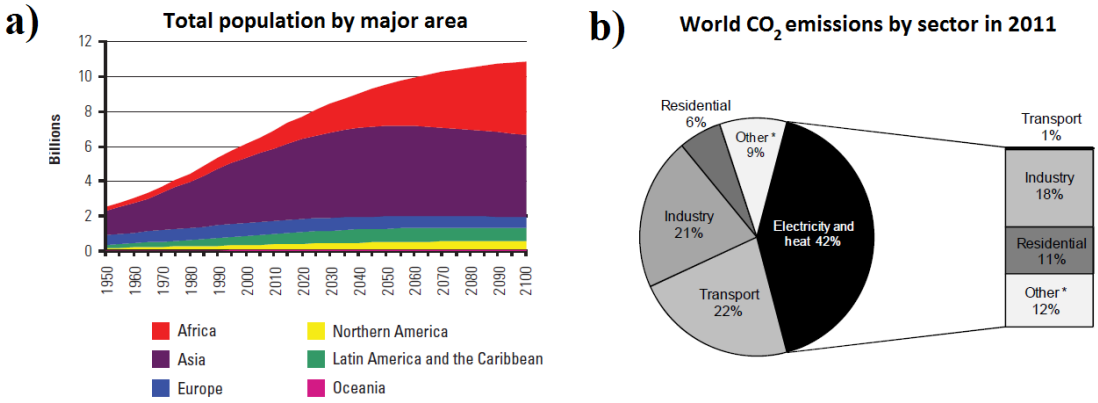

Figure I - 1. a) Evolution of the world population (projections of United Nations) b) world CO_2 emissions by sector (Other* includes: commercial/public services, agriculture/forestry, fishing, energy industries other than electricity and heat generation, and other emissions not specified elsewhere). Reprinted from Ref. [1] and [2].

1.1.2 Fuel cell technology: operating principle, applications and types of fuel cells

The fuel cell concept was developed in the early 19th century when Christian Friedrich Schönbein from University of Basel (Switzerland) and Mr. William Grove first detected a voltage from an electrochemical reaction between hydrogen and oxygen, in the presence of platinum (Pt) electrodes. Over the years, and especially with the "space race" between the United States and Russia during the 1950s and 1960s, the National Aeronautics and Space Administration (NASA) collaborated with several industrial partners to develop fuel cells for their manned space missions [4]. The fuel cells used for the Gemini space program had to provide electricity for the electrical equipment's and produce water for the astronaut's crew.

Fuel cells combine a fuel with oxygen to produce electricity, heat and water. There are several types of fuel cells but their standard components are the same (Figure I - 2). Two electrodes, an anode and a cathode, are used to electrochemically oxidize the fuel and reduce oxygen, respectively. The electrodes are separated by a solid or liquid electrolyte (depending on the type of fuel cell), which provides the ionic conduction from the anode to the cathode, while an external circuit (bipolar plates) collects the electrons and conducts them to an application (for direct use of electrical energy) or to a set of batteries (to store electrical energy).

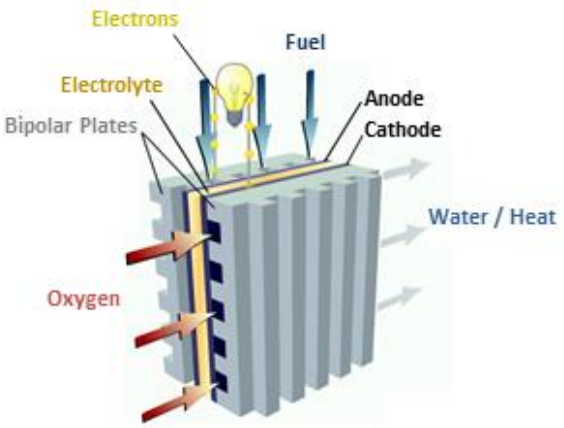

Figure I - 2. Schematics of a fuel cell with its standard components.

Presently, fuel cells are used in three main areas:

- Portable power generation: this concerns all the products that may be moved as auxiliary power units (APUs), cell phones, laptops, educational toys and recharging devices for small electronic products;
- Stationary power generation: the biggest fuel cell systems provide a continuous source of energy to industrial facilities, telecommunication towers and even domestic energy as combined heat and power systems (micro-CHP);
- Power for transportation: provide propulsive power to a vehicle, directly or indirectly (range extender). Three types of vehicles are envisaged: light-duty vehicles or fuel cell electric vehicles (FCEVs), city buses and material handling vehicles (forklift trucks).

Depending on the type of application, the desired electrical power and the constraints present for the implementation of the fuel cell (temperature limits, type of fuel available), different types of fuel cells may be used, each one with its own specificities and limits. The main characteristics that differ between each type of fuel cell are the nature of the electrolyte: either a solid electrolyte (polymeric membrane or ceramic) or a liquid electrolyte. The different types of fuel cell are presented in Table I - 1. PEMFCs, running on pure hydrogen, appear the most promising candidate for automotive and portable applications because of their low working temperature, high specific energy density and low refuelling time.

Table I - 1. Different types of fuel cells.

	PEMFC	HT PEMFC	DMFC	MCFC	PAFC	SOFC	AFC
Electrolyte	Polymer membrane	Mineral acid-based	Polymer membrane	Immobilised liquid molten carbonate	Immobilised liquid phosphoric acid	Ceramic	Potassium hydroxide
Operating temperatures	323-353 K	393 – 473 K	333 – 403 K	923 K	423 – 493 K	1273 K	343 – 373 K
Electrical efficiency	40-60%	60%	40%	45-60%	35-40%	50-65%	45-60%
Typical electrical power	< 250 kW	< 100 kW	< 1 kW	> 200 kW	> 50 kW	< 200 kW	> 20 kW
Applications	Vehicles, small stationary	Small stationary	Portable	Stationary	Stationary	Stationary	Submarines, spacecraft

1.1.3 Fuel cell industrialization and market

According to the Industrial Review of FuelCellToday [5-7] (part of Johnson Matthey group) and the Fuel cell Technologies Market Report of the American Department of Energy (DoE) [8], PEMFCs started to be commercially available since mid-2000s and are now established in certain markets. They are sold with warranties and service contracts, and meet the codes and standards of the markets in which they are implemented. Figure I - 3 shows how the shipments of fuel cells have evolved for the last five years, in terms of application, region of the world and type of fuel cell. In general, the trends for the fuel cell industry are promising due to the continuous growth of the shipments throughout the years. The values for 2013 are a forecast from the authors, while values for the previous periods correspond to the respective result of the year.

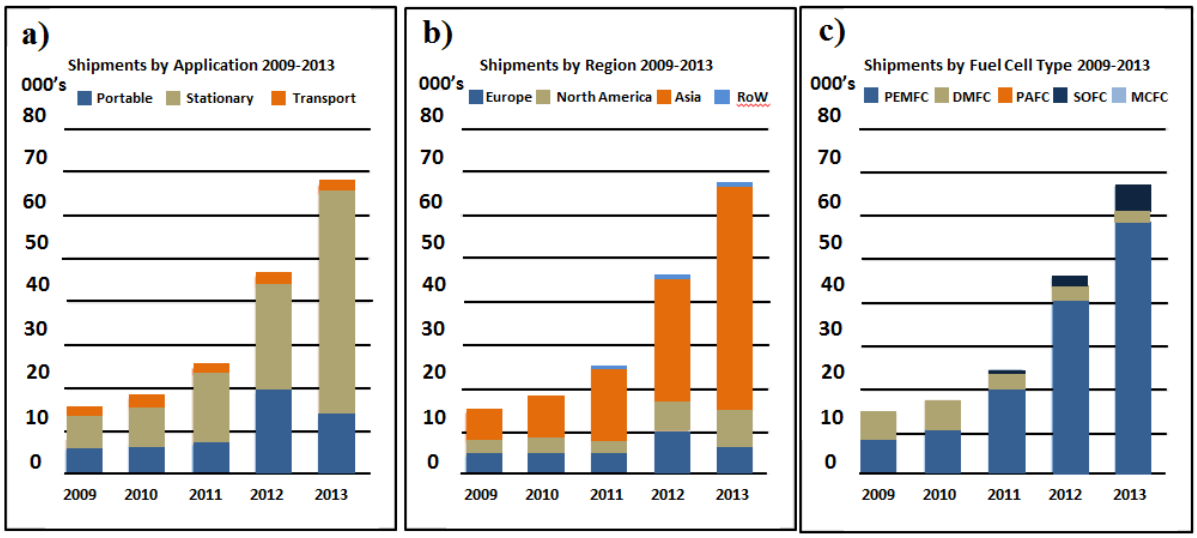

Figure I - 3. FuelCellToday data from 2009-2013 for a) shipments by application b) shipments by region and c) shipments by fuel cell type. Reprinted from [7].

Fuel cells found their "pillar" with stationary applications, with a serious impulse of the market from 2011. Between 2011 and 2012 the stationary shipments have doubled, with approximately 23,000 shipments. This trend is a result of the Japanese Ene-Farm project (a large-scale residential CHP program) [9] supported by government subsidies. In 2012, 20,000 systems were deployed, 80% of which are PEMFCs and 20% SOFCs. The United States of America (USA) and South Korea settled as well politics to implement reliable back-up energy (mobile phone towers) and prime power for industrial complexes. Such strategy has positioned Asia and North America as the main propellers for the fuel cell technology worldwide (Figure I - 3 b)).

Portable applications are related to consumer electronics and a particular interest for military applications is developing, but challenges associated with miniaturization of fuel cells have still to be overcome. In 2012, devices based on PEMFCs as portable electronic chargers were launched on the market, as myFC PowerTrekk [10] and Horizon MiniPak [11]. However, production drawbacks delayed the availability of some of these systems and in parallel the adoption of such solutions were not as promising as expected by the final consumer. The transport sector share for fuel cells shipments is quite homogeneous through-out the years. The main markets for transport related fuel cells are material-handling vehicles (forklifts) and fuel cell electric vehicles, where the first positions itself as the leading market for transport applications. The success of material-handling vehicles is behind the pioneer investments, made in the USA, by international companies (Coca-Cola, Walmart, BMW, Sysco, FedEx) to replace in their warehouses the usual battery-powered forklifts by fuel cell-powered forklifts.

The elimination of battery changing facilities combined with the nearly continuous operation of the fuel cell forklifts, justify the additional investment for fuel cells and hydrogen refuelling infrastructure. More than 3,000 fuel cell forklifts were deployed in the United States of America (USA) and Canada, and the 56 % bigger European market for forklifts represents an opportunity to spread the fuel cell technology. The conversion of only 10% of the world fleet of forklifts would already represent a potential market of 7 billions € for fuel cells. In November 2011, a joint venture was created between PlugPower (market leader in the USA) and Air Liquide through the project HyPulsion [12] to introduce fuel cell-powered forklifts in Europe. Two years later, 20 forklifts and a hydrogen station were installed at the Ikea's logistics platform near Lyon.

Until now, the use of PEMFCs in electric vehicles (FCEVs) remains limited to pilot projects of demonstration, where small fleets of buses or cars are available to show their viability, potentiality and gain the attention from the costumers. To achieve a point of mass production and general availability of FCEVs, some challenging issues have to be overcome. A primary role should be played by the governments, which have to provide supporting politics to develop the hydrogen energy. In the "Horizon 2020" project from the European Union (EU), the already existing public-private partnerships of previous projects will share a budget of 1.4 billion € between 2014 and 2020 focusing the projects on sustainable transport and energy security. The promotion of low-to-zero-emission vehicles is addressed in the project. At the national level, European countries are as well promoting the deployment of hydrogen vehicles and infrastructures: (*i*) in 2012, United Kingdom (UK) started the UKH_2Mobility to evaluate the consumer demand for fuel cell electric vehicles (FCEVs), to plan the deployment of the refuelling infrastructure and quantify the benefits of FCEVs in the UK (the first results may be consulted at http://www.ukh2mobility.co.uk/wp-content/uploads/2013/08/UKH2-Mobility-Phase-1-Results-April-2013.pdf, see Ref. [13]), (*ii*) Germany wants to have 50 hydrogen refuelling stations by 2015, (*iii*) Sweden, Denmark and Finland are as well investing in deploying a hydrogen fuelling infrastructure. The main automotive constructors are responsible for developing attractive FCEVs and present them as competitive as the present combustion vehicles. Most of the major constructors have fuel cell R&D programs, where they develop prototypes of FCEVs like Mercedes Benz F-Cell, Hyundai Tucson Fuel Cell and Honda FCX Clarity. Some constructors are more advanced than others on their respective fuel cell program, but all have plans to launch vehicles between 2015 and 2020. In 2012, several partnerships between automotive constructors have been created to advance the

commercialization of FCEVs: BMW with Toyota, Renault-Nissan with Daimler and Ford, General Motors with Ford, Volkswagen with Ballard Power Systems. All the research and development (R&D) programs of the major constructors use low temperature fuel cells, more precisely polymer electrolyte fuel cells (PEMFCs), and all have developed proprietary designs of the fuel cell system for their vehicles. The partnerships between the major constructors is of crucial importance since it will benefit from the exchange of information, creating automated production processes and quality controls which will lead to standards in the FCEVs production. In this way, the large scale production and commercialization of FCEVs will soon come to light.

In summary, it is remarkable to note that the fuel cell technology has achieved major progresses during the last 4 years. Its promising role in providing clean energy has already been proven by the Ene-farm program in Japan. The versatility of fuel cells is notorious within the transportation sector, with the imposition of fuel cells applied to material-handling vehicles, which may boost the development of the fuel cell technology. Thanks to the new governmental projects, the construction of the hydrogen infrastructure and the partnerships between automotive constructors, the commercialization of FCEVs is expected to start soon.

1.2 PEMFC – Proton Exchange Membrane Fuel Cell

1.2.1 Single cell: electrochemical reactions and membrane electrode assembly (MEA)

This thesis will focus on the proton exchange membrane fuel cell (PEMFC). In a PEMFC, pure hydrogen is oxidized at the anode (hydrogen oxidation reaction, HOR see Eq. I – 1) and oxygen is reduced at the cathode (oxygen reduction reaction, ORR see Eq. I – 2). The HOR produces protons and electrons, which both flow to the cathode to participate in the ORR (the protons through the proton-exchange membrane, and the electrons *via* an external circuit). The global PEMFC reaction of hydrogen with oxygen is Eq. I – 3.

$$HOR: H_2 \rightarrow 2H^+ + 2e^- \qquad E^{\circ}_{H^+/H_2} = 0\ V\ vs.NHE\ (T = 298\ K) \qquad \text{(Eq. I – 1)}$$

$$ORR: O_2 + 4H^+ + 4e^- \rightarrow 2H_2O \qquad E^{\circ}_{O_2/H_2O} = 1.23\ V\ vs.NHE\ (T = 298\ K) \qquad \text{(Eq. I – 2)}$$

$$Global\ reaction: H_2 + \frac{1}{2}O_2 \rightarrow H_2O + heat \qquad \Delta E = 1.23\ V\ (T = 298\ K) \qquad \text{(Eq. I – 3)}$$

The electrical performance of a PEMFC primarily depends of the kinetics of the electrochemical reactions previously referred. The HOR is a simple and direct reaction, which features fast oxidation kinetics [14]. The ORR may occur *via* two pathways: (*i*) a direct reduction to water or (*ii*) a series pathway, where hydrogen peroxide (H_2O_2) is formed as reaction intermediate before its reduction to water [15]. Due to the complexity of the reaction, the ORR features sluggish kinetics, which cause a dramatic loss of operating voltage [16, 17]. The heart of a PEMFC is the MEA. It is a multi-layered component with a proton-conducting polymer electrolyte membrane (PEM), two catalytic layers (CLs) where the fuel cell reactions described in Eq. I – 1 and Eq. I – 2 are taking place, and two gas-diffusion layers (GDLs) providing access of the fuel and of the oxidant to the CLs, the electronic/heat conduction and the management of water. In what follows, the materials employed and the desired properties for each component of the MEA will be briefly described.

1.2.2 Proton Exchange Membrane (PEM)

Perfluorosulfonic acid (PFSA) membranes, distributed by Du Pont de Nemours (USA) with the trade-name of Nafion®, are commonly used in PEMFCs but other membrane are commercially-available as Gore-Select® (Gore™), Aciplex® and Flemion® (Asahi™). Structurally, Nafion® consists of a continuous fluoropolymer backbone of $–(CF_2)_n–$ groups, which provide mechanical stability, upon which hydrophilic segments containing sulfonic acid groups $– SO_3H –$ are attached, enabling proton conduction. The chemical structure of the PFSA membrane is shown in Figure I - 4. More details can be found in Refs. [18-20].

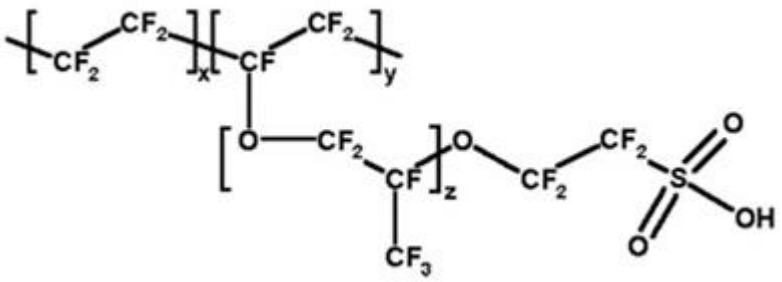

Figure I - 4. Chemical structure of PFSA ionomer.

The PEM: (*i*) ensures a physical separation between the electrodes, preventing the direct recombination of the fuel and of the oxidant, (*ii*) has high ionic conductivity at low relative humidity, (*iii*) features high stability under reducing (anode) and oxidizing (cathode) environments and (*iv*) is mechanically and electrically robust [20]. Nafion® membranes are

classified by their equivalent weight (EW), the weight of polymer in molecular mass per mole of sulfonic acid group, and thickness (in thousands of an inch). The EW strongly affects the mechanical and transport properties: for instance a decrease of the EW improves the mechanical properties but negatively affects the proton conductivity [21]. The structural organization of Nafion® depends on its hydration state. Indeed, the strong hydrophilic nature of the SO_3H groups causes a Nafion® membrane to swell considerably when exposed to humid environment [22, 23]. The water content of the membrane is expressed as λ (the number of water molecules present in the membrane for each sulfonic acid group), and it is known that its conductivity increases when hydrated, but how does the hydrophobic and hydrophilic phases arrange themselves is still open to discussion. Two mechanisms are accepted for the proton conduction: (*i*) Grotthuss hopping, present at high membrane water contents with a stepwise proton transport from one sulfonic acid group to the other, and (*ii*) vehicular transport with the passage of hydronium ions through the water-filled domains of the membrane [19, 24, 25].

1.2.3 Catalytic layers (CLs)

Metallic Pt (Pt/HSAC) or Pt alloy (Pt-M/HSAC, where M is a 3d transition metal) nanoparticles supported onto a high-surface area carbon support and impregnated with Nafion® ionomer are the standard materials of PEMFC CLs [16, 26]. The CLs should present specific characteristics: (*i*) highly porous network for the diffusion of gases and the removal of water, (*ii*) high ionic conductivity to provide proton transport to/from the polymer electrolyte and (*iii*) high electronic conductivity to provide the electron transfer from the anode to the cathode. These characteristics reflect the "three-phase boundary" condition, *i.e.* only the regions of the CL where the electrocatalyst is in contact with the gas pores (connected with the gas diffusion layer) and the ionomer phase (connected with the membrane) can operate efficiently. If one of these interactions fails, the conditions of efficient electrochemical reactions in the PEMFC are not met. Figure I - 5 presents a SEM cross-section of an MEA, highlighting the structure of a PEMFC catalytic layer. In what follows, the constituting elements of the catalytic layers will be described, with a special emphasis for the high-surface area carbon support which is the main research focus of this thesis.

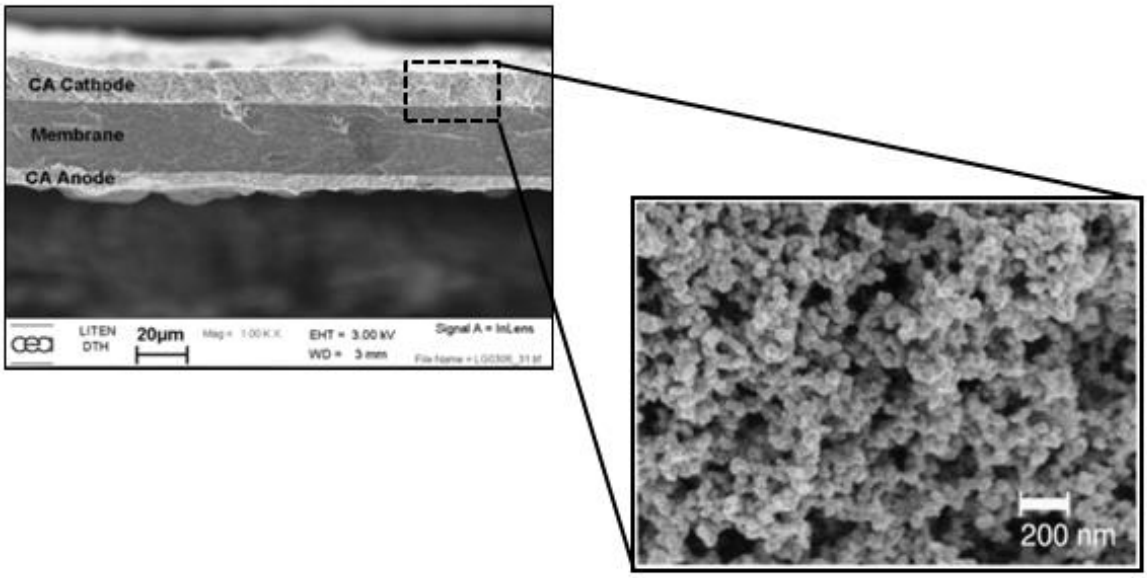

Figure I - 5. Scanning electron microscopy images of a MEA at different scales. Reprinted from [27] and [28].

a. Pt-based nanoparticles

Despite the intensive efforts in research and development made during the last 20 years, Pt or Pt-based alloy nanoparticles of *ca*. 3–5 nm in size, which are dispersed onto a high surface area carbon support (Figure I - 6) remain the electrocatalyst of choice. This is due to their low overpotential for the HOR and the ORR reactions as well as their remarkable stability in the harsh operating conditions of a PEMFC.

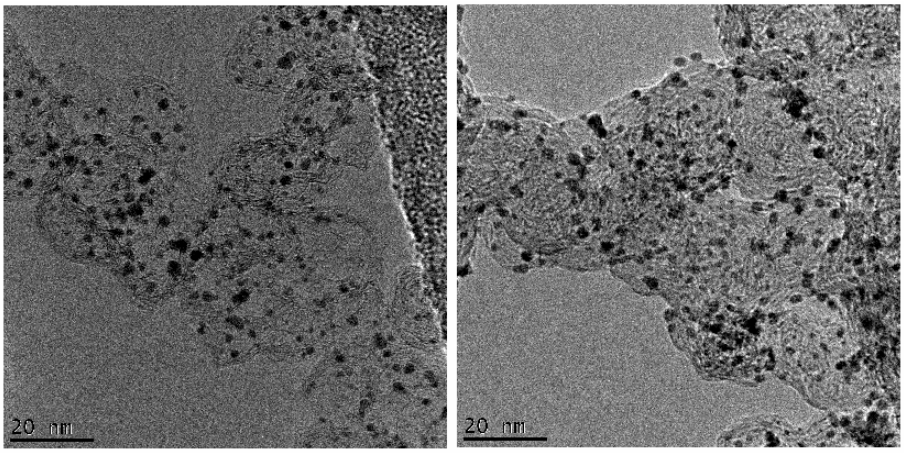

Figure I - 6. TEM images of Pt or Pt-M nanoparticles supported on a high-surface area carbon.

Commercial PEMFCs electrodes have Pt loadings of 0.05 – 0.2 mg cm^{-2} at the anode while at the cathode loadings around 0.4 – 0.5 mg cm^{-2} are needed to maintain fuel cell performance [17, 26, 29, 30]. The higher Pt loading at the cathode intends to compensate the

sluggish ORR kinetics (the cathode ORR is nearly six times slower than the HOR at the anode) [16, 26]. Most of the effort in the electrocatalysis of PEMFC focus on improving the ORR mass activity (in A per gram of Pt) [31-38]. This objective is best achieved with homogeneous Pt-M/C nanoalloys [16, 35, 38-40] or core-shell nanoparticles composed of a Pt-enriched shell and a metallic or alloyed core [32, 33, 39, 41-43] (see Figure I - 7 a and Figure I - 7 b). The observed improvement of the ORR activity is believed to be due to a combination of electronic (ligand) and geometric (strain) effects [44]. The strain effect arises from the compressed arrangement of surface atoms, which results into a downshift of its average energy with respect to the Fermi level. The ligand effect is due to the change in the electronic structure of the active sites by the neighbouring M atoms [45, 46]. Both effects weaken the chemisorption energies of the ORR intermediates (OH, OOH and O), and increase the global ORR rate. Similarly, in core-shell electrocatalysts [40, 47, 48] (Figure I - 7 b)) or even hollow-particles [49, 50] (Figure I - 7 c)), the structural and electronic properties of Pt are modified, which accelerates the rate of the ORR.

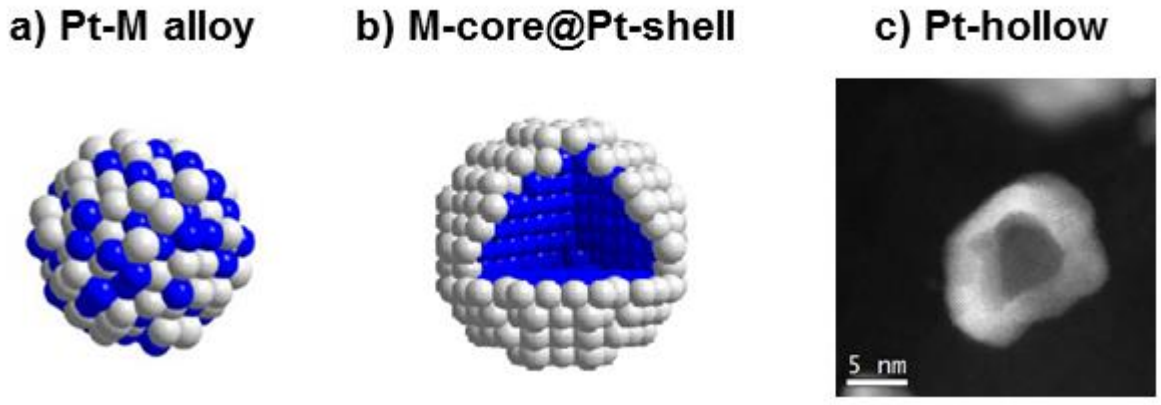

Figure I - 7. a) Pt-M alloy nanoparticle b) M-Core@Pt-shell nanoparticle and c) Pt-hollow nanoparticle. a) and b) reprinted from [40] and c) from [51].

b. High-surface area carbon support (HSAC)

Carbon materials are commonly used to support the Pt-based nanoparticles because they possess a wide range of suitable properties such as: (*i*) their high specific surface area (ranging from 100 to several 1000 of m^2 g^{-1}), (*ii*) their adequate porosity, which ensures efficient mass transport of reactants and products to and from the CLs, (*iii*) their chemical inertness resistance to acidic or basic media, (*iv*) their compatibility with proton conducting polymers, (*v*) their good electrical conductivity and (*vi*) their low cost [52]. From the different types of carbon supports available [53-56], carbon soots or blacks are the most widely used.

They are produced by pyrolysis or incomplete combustion of gaseous or liquid hydrocarbons under controlled conditions. Depending on the type of stock material, and the production method they are classified into furnace, channel, thermal and lamp blacks. Details of their preparation methods can be found in references [53, 55, 56].

Carbon blacks consist of graphene clusters arranged in near-spherical particles (10 – 100 nm) that are fused together by van-der-Waals interactions to form aggregates (100 – 800 nm), that pack into loosely bond agglomerates (> 1 μm). Figure I - 8 a) shows the microstructural model of carbon blacks. The limits of an aggregate are highlighted by the red-dotted line.

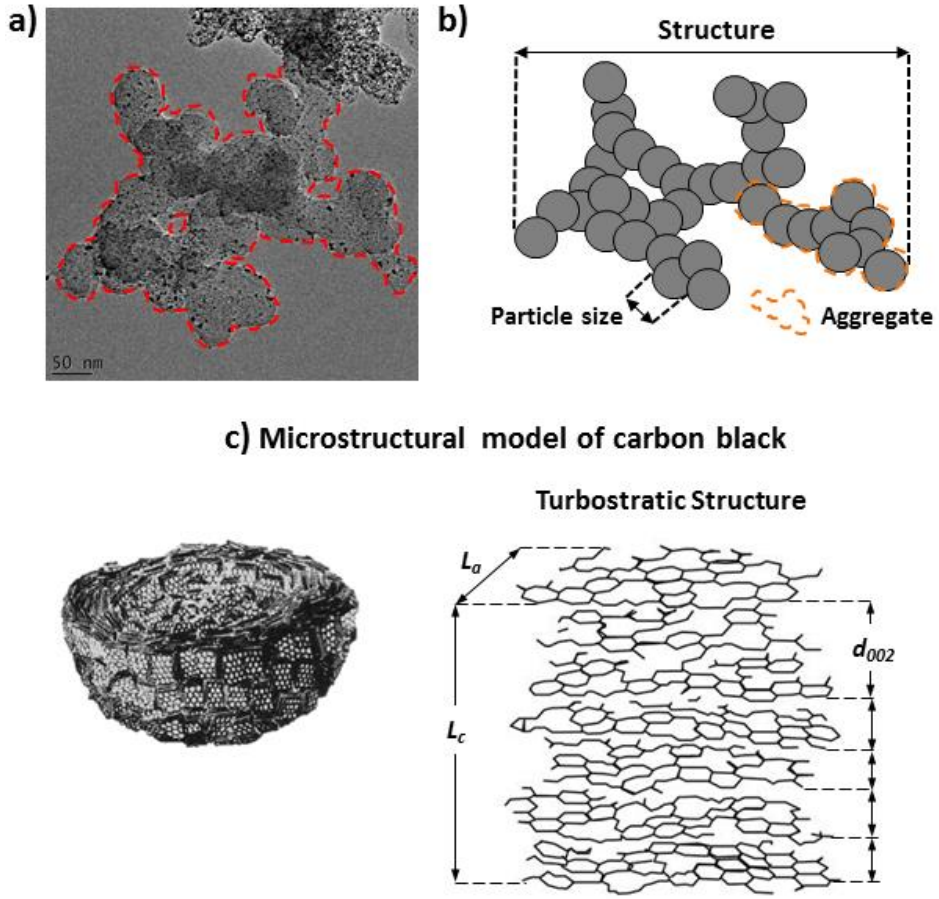

Figure I - 8. a) TEM image of a Pt/HSAC electrocatalyst. The red-dotted line serves as a guide to the eye to indicate the structure of an aggregate b) schematics of a carbon black agglomerate and c) microstructural model and structural parameters of primary carbon particles (basic structural units).

Two morphological properties are used to classify carbon blacks (Figure I - 8 b)): (*i*) their primary carbon particle size, that is the average dimension of the nodular portion of an aggregate, (*ii*) their aggregate size and structure, *i.e.* the size of the aggregates (for blacks of

the same particle size), the number of particles per aggregate (for blacks of different particle size) and the aspect ratio. The basic structural unit of carbon blacks is the carbon primary particle, the size of which depends on the production method [55]. Contrary to graphite where a perfect hexagonal structure exists, in carbon blacks, the stacking of the planes remains but the layers are disoriented with respect to one another resulting in a so-called turbostratic structure [53, 56]. Thanks to microscopy techniques [56-58], it could be evidenced that carbon black are organized according to a "concentric crystallite" structural model in which the outer-shell of the carbon nanoparticles is well organized and covers a less well organized inner-core, as depicted in Figure I - 8 c). The central region is believed to be made up of "disordered carbon domains" that is small, imperfect crystallites, with poor inter-layer ordering and possibly fully amorphous carbon. In the outer shell, the crystallites are larger and the arrangement perpendicular to the plane is also more parallel, in other words the carbon domains are more ordered (see Figure I - 8 c). This particular nanostructure results in the formation of hollow shell types of particles upon thermal, liquid phase [56], or electrochemical oxidation [59, 60].

The carbon blacks differ by: (*i*) the average in-plane crystallite size (L_a), (*ii*) the average size of the graphitic domains in the direction perpendicular to the graphene layers (L_c) and (*iii*) the average inter-planar space within the graphene domains (d_{002}) [53, 61]. These properties are dependent on the production parameters (stock material, temperature and duration of the combustion). Amorphous carbons are characterized by smaller graphitic crystallites ($\downarrow L_a$) without organization ($\downarrow L_c$) while graphitic carbons have larger crystallites ($\uparrow L_a$) and are more structured materials ($\uparrow L_c$) [62]. Such differences are visible in Figure I - 9, where TEM images of carbon blacks with distinct degree of graphitization are displayed. The high-surface area carbons (Figure I - 9 a)) present a uniform dispersion of smaller crystallites and amorphous domains while for graphitized carbon supports (Figure I - 9 b)), it is possible to identify a dense organization of the graphitic crystallites at the outer-surface of the carbon black particle.

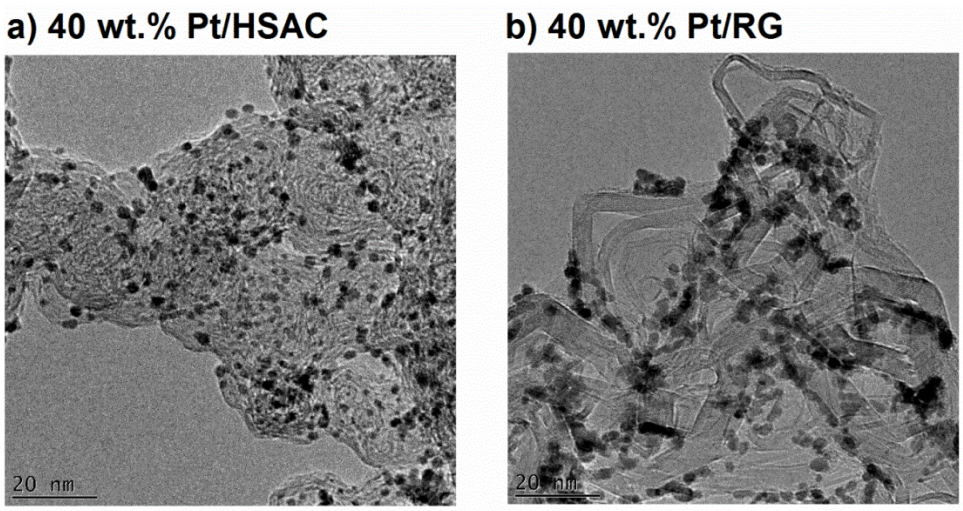

Figure I - 9. TEM images of Pt nanoparticles supported onto a) high-surface area carbon support and b) reinforced graphite carbon support.

Acetylene Black, Vulcan XC-72, Black Pearls BP 2000 and Ketjen Black DJ-600 are commercially available for PEMFC fuel cell applications. In Table I - 2, some morphological and structural properties of these carbon blacks are summarized. They have a porous structure composed of: (*i*) micropores (size up to 2 nm), (*ii*) mesopores (2 < size < 50 nm) and (*iii*) macropores (size > 50 nm) [52]. Except for Acetylene Blacks, Vulcan XC-72 features the lowest value of Brunauer Emmet and Teller (BET) surface area. This is related to the inferior amount of mesopores in Vulcan XC-72 in comparison to Ketjen-black or Black Pearls and in a smaller extent, to the micropore volume. Most of the carbon blacks suitable for PEMFC applications are mesoporous, which indicates that the appropriate porosity to satisfy catalyst nanoparticle dispersion, ionomer impregnation and reactants/products flow is meso- and macroporosity.

Table I - 2. Morphological and structural properties of commercial available carbon blacks for PEMFCs [55].

	Property	Acetylene Black	Vulcan XC-72	Ketjen-black DJ-600	Black Pearls 2000
Morphological properties	**Primary particle diameter (nm)**	42	20 - 30	35 - 40	10 – 15
	BET surface area (m^2 g^{-1})	64	252	1300	1500
	Total pore volume (cm^3 g^{-1})	0.20	0.63	2.68	2.56
	Area of mesopores (m^2 g^{-1})	64	177	1230	1020
	Micropore volume (cm^3 g^{-1})	0.00	0.037	0.029	0.208
	Average pore diameter	14.4	15.9	9.45	20.6
Structural properties	**L_a (nm)**	3.0	1.6	2.1	1.4
	L_c (nm)	4.1	2.0	1.4	1.1
	d_{002} (nm)	0.348	0.363	0.356	0.374

The distribution of the ionomer in the porosity is a very important parameter to the PEMFC performance [63, 64]. Using electrodes which present the same ionomer content but carbon supports with different surface areas, Liu *et al*. [65] reported that the thickness of the ionomer layer responsible for the proton conduction was smaller for the supports with superior values of surface area, resulting in the increase of the resistivity of the electrode. Such result was ascribed to the impregnation of the micropores, which absorb an important amount of ionomer. Contrary to these results, Uchida *et al.* [66, 67] suggested that metal nanoparticles residing in carbon pores below 40 nm diameter, have no access to ionomer and thus do not contribute to the PEMFC performance. In an attempt to isolate the effect of the porous structure of carbon materials, Kaiser *et al.* [68] kept the both metal dispersion and the Nafion® content in cathodic MEAs prepared for different carbon supports. The compared supports were from the Sibunit family, with various degrees of activation and BET surface areas ranging from 22 to 415 m^2 g^{-1}, and conventional 20 wt. % Pt catalyst supported on Vulcan XC-72. Fuel cell tests revealed improved mass transport properties in the cathode

layers, intrinsically dependent on the specific surface area and on the texture of the support. Both the mass transport losses and the Nafion® loading per m² of carbon decrease with increasing S_{BET}. The mesoporosity present in the Sibunit family and inexistent for the Vulcan XC-72 plays a significant role for fuel cell performance.

c. Ionomer

In order to maximize gas and proton transport throughout the CLs, ionomer is added to the electrocatalyst ink (usually the same as the one present in the PEM). This ionomer covers a certain fraction of the carbon primary particles and agglomerates and the Pt-based nanoparticles therefore resulting in an increase of the number of effective catalytic sites ("three-phase boundary" condition, see Figure I - 10 a) and b). The ratio of the mass of ionomer over the mass of the carbon support is defined by the *I*/*C* ratio. High values of the *I*/*C* ratio affect the mass transport of gases and water, while lower values result in regions of the electrode without any thin-film of ionomer [69, 70]. Gasteiger *et al*. [71] defined a *I*/*C* ratio between 0.5 and 1 as an optimal value, but this ratio depends on the type of carbon support used to support the Pt-based nanoparticles. Indeed, some intrinsic properties of the carbon support, as the specific surface area and the micro, meso and macroporous volumes interfere in the way the ionomer is dispersed over the Pt-based/C surface [72], creating heterogeneous zones that are rich/poor in ionomer resulting in the blocking of active-sites for the electrochemical reactions [64, 73]. The location of the Nafion® ionomer on the Pt-based/C electrocatalyst remains a heated debate. Uchida *et al.* [66, 67] first proposed that Nafion® only penetrates pores with sizes > 40 nm (macropores). However, according to Xie *et al*. [74], ionomer molecules do penetrate mesopores in carbon materials. Using mercury porosimetry, the authors reported a continuous decrease of the volume of pores with size below *ca*. 17 nm in diameter within agglomerates of Vulcan XC-72 with the increase of Nafion® content. The discrepancy between these two studies may arise from different dielectric constant ε of the solvent used for the ink preparation. Indeed, as suggested by Uchida *et al.*, [66, 75] perfluorosulfonate molecules form a solution at $\varepsilon > 10$, precipitate at $\varepsilon < 3$ and reversed micelles at $3 < \varepsilon < 10$.

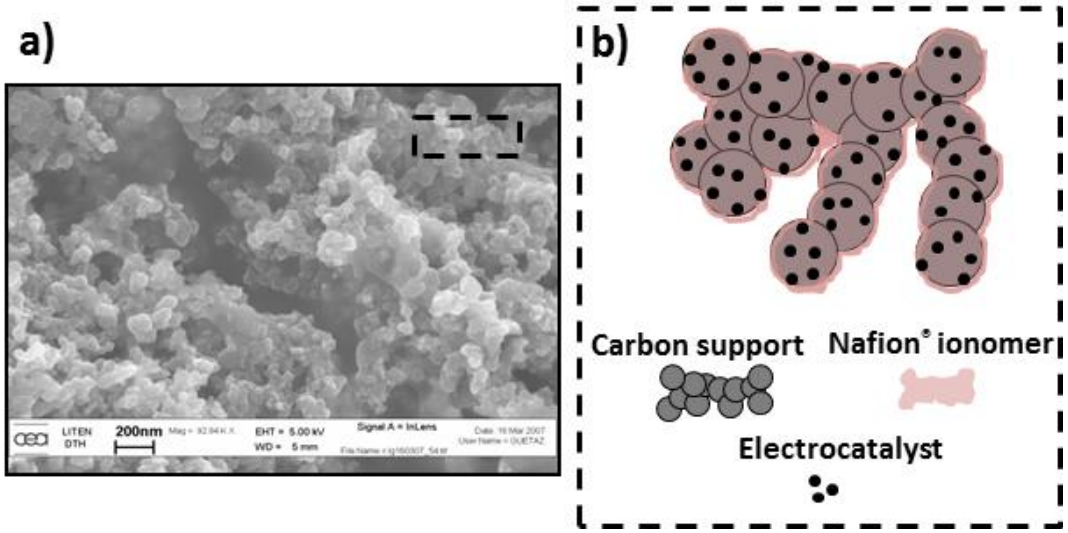

Figure I - 10. a) SEM image of electrocatalyst with Nafion® ionomer and b) schematic representation. SEM image reprinted from [27].

1.2.4 Gas diffusion layers (GDLs)

The gas diffusion layers are the outermost components of the MEA. GDLs consist of two layers bonded together, a macro-porous layer and a micro-porous layer. Structurally the GDLs are made of electrically conductive materials, as woven carbon cloth or non-woven carbon fibres, coated with a thin micro-porous layer made of carbon particles mixed with polytetrafluoroethylene (PTFE) [76, 77]. The main functions of the GDLs are: (*i*) providing electrical contact between the catalyst layer and the current collectors of the PEMFC, (*ii*) offering mechanical stability for the MEA after stack compression, (*iii*) supplying homogeneous fluxes of hydrogen/air to the electrodes and (*iv*) removing efficiently the water produced from the electrochemical reactions. To achieve these functions, both the materials and the structure of the GDLs are important parameters. The microporous layer plays a dual-role: it enhances the electronic contact between the CLs and the macroporous layer (due to the increased contact surface of the carbon particles) and improves the removal of water from the CLs. The removal of water from the CLs and the GDLs is necessary to avoid flooding of the electrodes and the associated loss of electrical performance. To do so, the GDLs are impregnated with PTFE. In addition, the presence of two distinct structural layers creates a gradient of porosity which stimulates the removal of water. For a deeper understanding of issues associated with the GDLs, their structural characteristics and their characterization methods for the GDLs, the following references are indicated [77, 78].

1.3 From single cell to stack and fuel cell system

The potential of a single cell is around 0.75 V at j = 1.0 A cm^{-2} [26], which is too low for automotive applications or stationary generators for domestic use. To power efficiently these applications, a fuel cell stack composed of individual single cells connected in-series is designed (Figure I - 11 b)). In a PEMFC stack, the MEAs are fitted in-between two bipolar plates (also known as flow-field plates) which perform the gas distribution, the heat management and serve as current collectors. The bipolar-plates have imprinted in their surfaces flow-field channels (for both gases and coolant fluids). They are made either of metallic materials such as stainless steels, titanium, aluminium and other alloys or graphite-based composites [79-81]. Research in bipolar-plates is focused on developing more conductive and resistant materials and improving the designs of the flow-fields circuits [82].

To operate correctly, a PEMFC stack needs (Figure I - 11 b)) a whole set of components: (*i*) auxiliary commands and control systems, (*ii*) power electronics, (*iii*) air compressor, (*iv*) humidifier, (*v*) battery and (*vi*) gas distribution system. The complexity of fuel cell development is not only focused on the heart of the fuel cell (the MEA) but aside, stack design and configuration are pivotal aspects to convert technological capabilities into commercially viable products.

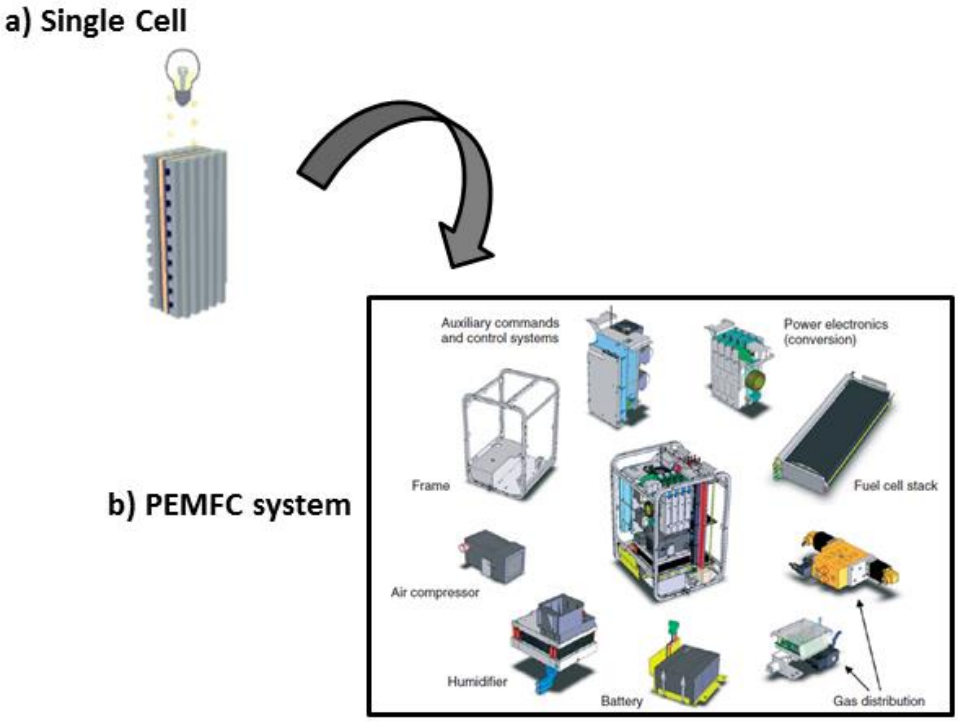

Figure I - 11. From a single cell to a complete PEMFC system: a) single cell (MEA) b) stack and c) exploded view. Reprinted from Ref. [83].

1.4 Degradation mechanisms of MEAs during PEMFC operation

The harsh operating conditions of PEMFC, and especially those encountered at the cathode (oxygen-saturated environment, high electrochemical potential, water splitting *via* surface metal oxide formation) render stability of the catalytic materials the major source of PEMFC performance loss and constitute a major research challenge. Despite the fact that the degradation of the PEM, of the CL and of the GDL are correlated [83, 84], the next section will present succinctly the major degradation mechanism of each individual component.

1.4.1 PEM and ionomer degradation during PEMFC operation

The PEM is responsible for the physical separation and the proton conduction between the anode and the cathode of the fuel cell. The ionomer, of the same nature as the PEM, is used to maximize the number of catalytic sites satisfying the "three-phase boundary" condition. Under PEMFC operation, both elements are subjected to gradients of temperature, humidity and chemical environment, which after long-time operation induce changes in the conformation of the PFSA polymer and its performance. The failure and degradation mechanisms of PEMs are classified into three categories: (*i*) mechanical, (*ii*) thermal and (*iii*) chemical degradation [84, 85]. The mechanical properties of the membrane vary with the hydration state and the PEMFC operating temperature [86, 87], depending on the final application, the fuel cell environmental operation and the start/stop events, those variables change. Temperature and humidity cycling during PEMFC operation induces expansion (swelling) and contraction (drying) of the PEM, producing on the long-term local stress areas. Eventually physical defects appear with the formation of cracks, tears, punctures and pinholes [83, 88, 89]. The major drawback of these defects is the possibility of fuel crossover into the other electrode, generating hot spots and radical species (in case of O_2 crossover to the anode and enhanced H_2O_2 formation) [90]. The thermal degradation is mostly due to dehydration of the membrane owing to the high operation temperature and the humidity management of the system. As already stated, a poor hydration state of the PEM affects the proton conductivity, increasing the resistivity of the electrodes and leading to the loss of performance of the PEMFC. Finally, the chemical degradation of the membrane is believed to proceed primarily by radical attack of the linear polymer backbone or the sulfonic acid groups. These radical species - peroxides ($HO^{\cdot}$) and hydroperoxides ($HOO^{\cdot}$) - are generated by the two-electron pathway of the ORR [91-93].

1.4.2 Pt nanoparticles degradation during PEMFC operation

The sintering of Pt-based nanoparticles observed during long-term PEMFC operation, and the associated loss of electrochemically active surface area (ECSA), is highly detrimental for the fuel cell performance. The major degradation mechanisms of Pt/C nanoparticles are well-established: (*i*) Pt nanoparticle agglomeration and concomitant coalescence or Pt nanoparticle detachment from the carbon support, [94-96] (*ii*) electrochemical Ostwald ripening *i.e.* the preferential dissolution of the smallest Pt crystallites, yielding the formation of Pt^{z+} ions and their redeposition onto larger particles, following the Gibbs–Thomson effect [84, 94, 97] and (*iii*) the chemical reduction of Pt^{z+} in the PEM *via* H_2 crossing-over from the anode to the cathode [84, 94, 97].

The agglomeration of Pt nanoparticles is caused by the migration of individual nanocrystallites on the carbon support. The extent to which Pt migration and coalescence contribute to the ECSA loss depends, among others, on the mass fraction of Pt, and the specific surface and the pore size distribution of the carbon support. At constant carbon specific surface area, the electrocatalysts with high mass fraction (*i.e.* high particle density) are more sensible to particle agglomeration [98] (Figure I - 12 a)). The degradation of the high-surface area carbon support contributes significantly to the agglomeration/coalescence or the detachment of Pt nanoparticles (Figure I - 12 c)) and will be addressed further in the text.

The dissolution of the Pt nanocrystallites depends on many different parameters such as their size, the temperature, the pH, the nature of the anions contained in the electrolyte, the gaseous atmosphere, the potential range and the potential sweep rate used in model or real PEMFC operating conditions [84, 97, 99, 100]. It may occur by a single electrochemical step (Eq. I – 4):

$$Pt \rightarrow Pt^{2+} + 2e^- \qquad \text{(Eq. I – 4)}$$

or by the electrochemical formation of Pt surface oxide (Eq. I – 5) followed by a chemical dissolution of the oxide [101] (Eq. I – 6):

$$Pt + H_2O \rightarrow PtO + 2H^+ + 2e^- \qquad \text{(Eq. I – 5)}$$

$$PtO + 2H^+ \rightarrow Pt^{2+} + H_2O \qquad \text{(Eq. I – 6)}$$

or the electrochemical reduction of the oxide (Eq. I – 7):

$$PtO_2 + 4H^+ + 2e^- \rightarrow Pt^{2+} + 2H_2O \qquad \text{(Eq. I – 7)}$$

The nature of the oxide layer at a given electrode potential is highly debated. It is suspected that, at high electrode potential (E > 1.0 - 1.1 V *vs.* RHE [102]), the formation of a "sub-surface oxide" proceeds *via* the "place-exchange" process. This phenomenon, first introduced by Conway *et al.* [103], is due to the strong dipole moment between Pt and O atoms. The latter results in Pt and adsorbed O atoms swapping their place, and results in O atoms entering the Pt lattice, and Pt atoms becoming Pt adatoms with no or small lateral coordination. During the electrochemical reduction of PtO, the dissolution of Pt atoms is exacerbated [104-106]. Once the Pt^{z+} ions (z = 2 or 4) are dissolved in the electrode, they may redeposit electrochemically onto larger Pt nanocrystallites (Ostwald ripening, see Figure I - 12 b)), and/or diffuse and be chemically reduced throughout the ionomer phase or in the PEM, forming the so-called "Pt band in the PEM" (Figure I - 12 d)) [107, 108].

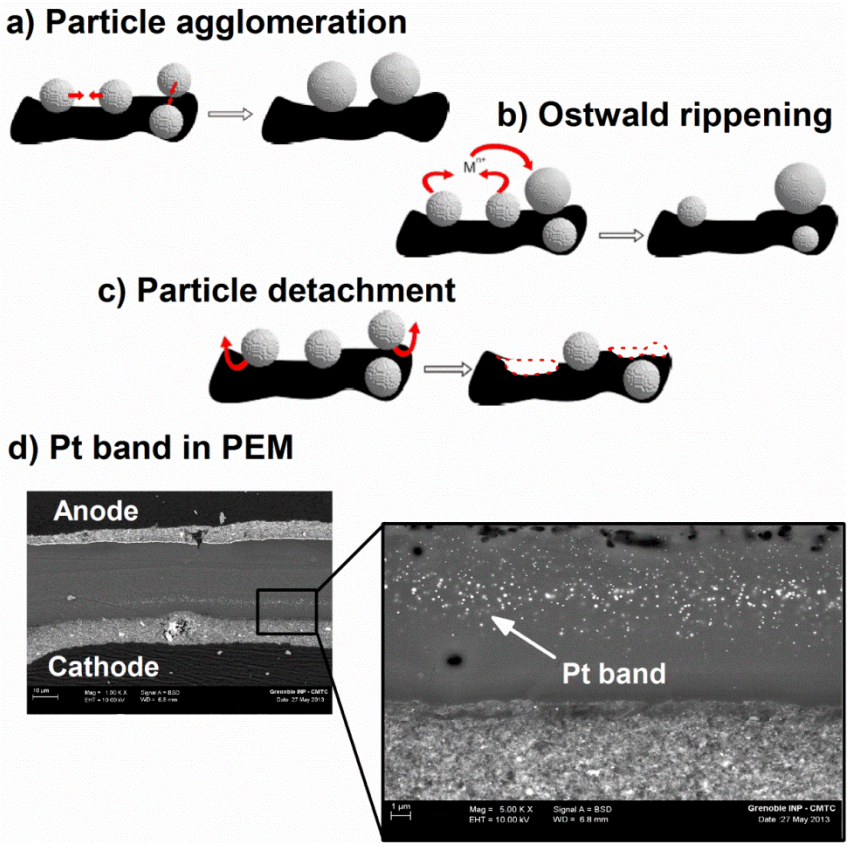

Figure I - 12. Pt nanoparticles degradation mechanisms: a) particle agglomeration b) electrochemical Ostwald ripening c) Pt nanoparticle detachment and d) evidence of the formation of a Pt-band in the PEM. a), b) and c) are reprinted from Ref. [109].

1.4.3 Carbon support degradation during PEMFC operation

The first studies dealing with the degradation of carbon supports in fuel cells electrodes date from the decades of 70s - 80s, and were made by Binder [110], Kinoshita and Bett [111-114]. At that time, research was focused on PAFCs which work at temperatures of $423 < T < 493$ K. Since PEMFC operate at lower temperatures ($T < 373$ K), carbon corrosion was believed to be a negligible phenomenon in PEMFCs, which was proven incorrect [115, 116]. Driven by the durability targets for automotive PEMFCs, the understanding of the degradation mechanisms of carbon supports has become a major research topic and is the focus of this thesis.

The thermodynamical potential of carbon oxidation to carbon dioxide is $E^{\circ}_{C/CO_2} = 0.207$ V *vs* the normal hydrogen electrode (NHE). The electrochemical carbon oxidation reaction (COR) is believed to proceed *via* a dual pathway mechanism, which was first described by Kinoshita *et al*. [53]. In the direct pathway, carbon is directly oxidized into carbon dioxide (CO_2) and carbon monoxide (CO), the latter being produced to a lesser extent at $E > 0.9$ V *vs* RHE [117]:

$$C + 2\,H_2O \rightarrow CO_2 + 4\,H^+ + 4\,e^- \qquad E^{\circ}_{C/CO_2} = 0.207\,V\ vs.NHE\ (T = 298\,K) \quad \text{(Eq. I - 8)}$$

$$C + H_2O \rightarrow CO + 2\,H^+ + 2\,e^- \qquad E^{\circ}_{C/CO} = 0.518\,V\ vs.NHE\ (T = 298\,K) \quad \text{(Eq. I - 9)}$$

In the indirect pathway, the COR is believed to occur *via* oxidation of the carbon lattice (Eq. I – 10) yielding the formation of carbon defects designed as $C^+_{(s)}$. These defects are highly reactive and allow the formation of carbon surface oxides (CO_{surf}) (Eq. I – 11), which are then ultimately oxidized into CO_2 (Eq. I – 12):

$$C \rightarrow C^+_{(s)} + e^- \quad \text{(Eq. I – 10)}$$

$$C^+_{(s)} + H_2O \rightarrow CO_{surf} + 2H^+ + e^- \quad \text{(Eq. I – 11)}$$

$$CO_{surf} + H_2O \rightarrow CO_2 + 2H^+ + 2e^- \quad \text{(Eq. I – 12)}$$

The electrochemical corrosion currents of carbon supports measured under potentiostatic control follow an empirical relation current-time relation [111]:

$$i = kt^{-n} \quad \text{(Eq. I – 13)}$$

where *i* is the mass-specific current density, *k* is a temperature and potential rate parameter, *t* the time elapsed and *n* a potential-dependent parameter (*n* = 0.42 at 1.0 V, *n* = 0.62 at 0.9 V, *n* = 0.7 at 0.8 V and *n* = 0.76 at 0.7 V). The asymptotically decrease of the COR currents suggest passivation of the surface [118].

The COR kinetics is strongly affected by the potential, the temperature, the morphology, the structure and the surface properties of the carbon materials [62, 119-122]. The Pt or Pt-based nanoparticles deposited onto the carbon support also catalyse the rate of the COR, as first documented by Willsau *et al*. [117] using differential electrochemical mass spectroscopy (DEMS), and later on explored in other works [116, 118, 123-126]. It is suggested that, for $E > 0.3$ V *vs* RHE, CO_{surf} species are formed (Eq. I – 11) and the ones present in the vicinity of the Pt nanoparticles may spillover back from the carbon support to Pt nanoparticles, where they are converted to adsorbed CO (Eq. I – 14) [126]. With an increase of the electrode potential, the adsorbed CO molecules are then electrooxidized into CO_2 at $E \approx 0.8$ V *vs* RHE (Eq. I – 15).

$$CO_{surf} + Pt \rightarrow Pt - CO_{ads} \quad \text{(Eq. I – 14)}$$

$$Pt - CO_{ads} + H_2O \rightarrow CO_2 + 2H^+ + 2e^- \quad \text{(Eq. I – 15)}$$

The catalysis of the COR by Pt nanoparticles strongly depends on the electrode potential, as shown by accelerated stress tests [118, 125]. At elevated electrode potentials ($E >$ 1.0 V *vs* RHE), the Pt surface is passivated by surface oxides, and no catalysis of the COR by Pt is found. However, if the lower potential limit is inferior to 0.7 V *vs* RHE, the complete reduction of the Pt oxides exposes the surface of the Pt nanoparticles and strongly accelerates the COR rate. Enhanced COR kinetics are found during voltage cycling, the reason for that being the repeated reduction and oxidation of Pt nanoparticles and/or carbon surface groups during voltage cycles [125, 127]. As for the carbon support, some CO_{surf} groups formed at high electrode potential may be electrochemically reduced or dehydrogenated onto Pt (Eq. I – 14), which facilitates their oxidation during the anodic scan (Eq. I – 15).

The structural parameters (L_a, L_c and d_{002}), the specific surface area, the pore volume and the surface chemistry of carbon blacks exert strong influence on the COR kinetics. One of the first studies bridging structure of the carbon support and COR kinetics was performed by Antonucci *et. al* [128]. The authors observed that carbons which were submitted to heat-treatments (resulting in graphitization of the carbon structure), presented smaller inter-planar distances (d_{002}) than the pristine carbon support and were less prone to corrosion. Later, Cherstiouk *et al.* [62] studied the corrosion tolerance of different carbon supports, amorphous (carbon blacks) and graphitic carbons (nanofilaments), in sulphuric acid (H_2SO_4) at T = 353 K at 1.2 V *vs* RHE. The larger COR currents were found for small and disordered graphitic crystallites ($\downarrow L_a$, $\downarrow L_c$) with high inter-planar distances ($\uparrow d_{002}$). Recently, Artyushkova *et al*. [121] pointed out that such parameters are not enough to predict the resistance to corrosion of high surface area carbon supports. The authors suggested an interesting relationship between structural and chemical parameters, hydrophilicity/phobicity, electrochemical activity for the ORR and resistance to electrochemical corrosion. The carbon samples with high graphitic content, small BET surface area, low amount of carbon surface oxides, and large amount of elongated and large-sized pores were found to be more electrochemically active for the ORR and less reactive towards the COR [121].

The surface chemistry of carbon is extremely rich and different species as phenols, anhydride, carbonyls, ethers, quinones, lactones and carboxylic acids have been identified by acid-base titration, infrared (IR) and X-ray photoelectron spectroscopy (XPS) [129-132]. The amount of CO_{surf} present in a carbon support depends on its structure and production method [121, 133]. Only quinone-hydroquinone (Q/HQ) groups are electrochemically active, and this manifests by a peak in the potential interval 0.5 V < E < 0.8 V *vs* RHE:

$$C = O_{(s)} + H^+ + e^- \leftrightarrow C - OH_{(s)} \qquad \text{(Eq. I – 16)}$$

It is not completely clear if a specific group of CO_{surf} catalyses the COR rate or if, under specific degradation conditions, there is a predominant CO_{surf} group. Giordano *et al.* [133] submitted different carbon blacks materials to potentiostatic polarization (E = 1.0 V *vs* RHE in 85% H_3PO_4 at T = 443 K for t = 100 min). The authors reported that the amount of carbonyl and carboxylic groups increased after polarisation and that the specific COR rate depends on the surface concentration of CO_{surf} groups and not on their chemical nature. The electrochemical oxidation of Vulcan-XC72 (E = 1.2V *vs* RHE for 120 hours in 1 M H_2SO_4 at

room temperature or T = 338 K) by Kanganiesmi *et al*. [115] revealed an increase in the amount of carboxylic species, in comparison to the fresh state of the electrode. On a model highly-oriented pyrolytic graphite (HOPG) surface, Ogumi *et al.* [134, 135] demonstrated a similar increase of the content of alcohol and carbonyl groups during electrochemical oxidation. Even if a direct comparison between carbon blacks and HOPG is not possible (due to the structural differences that both materials present), HOPG remains a material of choice to investigate the initial steps of the COR such as the formation of atomic-scale defects (Eq. I – 10) in the graphitic crystallites and their further oxidation.

The COR is promoted by the harsh operating conditions of a PEMFC cathode: (*i*) acidic environment (pH < 1), (*ii*) presence of water, (*iii*) oxidizing atmosphere (presence of O_2), (*iv*) elevated temperatures (333 – 353 K), (*v*) high electrochemical potentials (0.60 – 1.50 V *vs* RHE) and (*vi*) presence of Pt-based nanoparticles. Due to the electrochemical activation of the COR, the carbon corrosion kinetics is known to be faster at open circuit voltage than in stationary operation [115]. Moreover, this electrode can experience excursions to high potential ≥ 1.5 V *vs*. RHE during start/stop or fuel starvation events [28, 83, 136, 137]. In these conditions, the COR becomes so fast that it may cause the collapse of the porous structure of the MEA within a few hundred seconds. The rationale for that is the simultaneous presence of hydrogen/air and air/air fronts in the anode [136] because air is used to flush hydrogen from the anode during a PEMFC stop. Also, transient conditions, such as localized fuel starvation may occur when water droplets flood temporarily block the channels of the bipolar plates. These events cause significant potential differences between the anode and the cathode, leading the fuel cell to a transient "reverse-current" situation, as first shown by Reiser *et al.* [136] and results in severe carbon corrosion [28, 137]. Figure I - 13 show the potential distribution in the MEA during a PEMFC start-up. It can be noted that one portion of the MEA is in normal operating conditions (region A, H_2 at the anode and air at the cathode), and the other has air at both electrodes. Since the in-plane H^+ transport isn't fast to provide protons to the region B, the hydrogen/air front acts as a power source that drives a current through the air/air segment, resulting in a high potential difference ($\Delta E \approx 1.4$ V). This drives fast COR and oxygen evolution reaction (OER) currents, and results in fast corrosion of the cathode in the region B. To avoid the detrimental effects of such fuel-air boundaries, mitigation strategies as interrupted hydrogen supply to the anode of the MEAs or filling of the anode compartment with inert gases during shut-down periods are implemented.

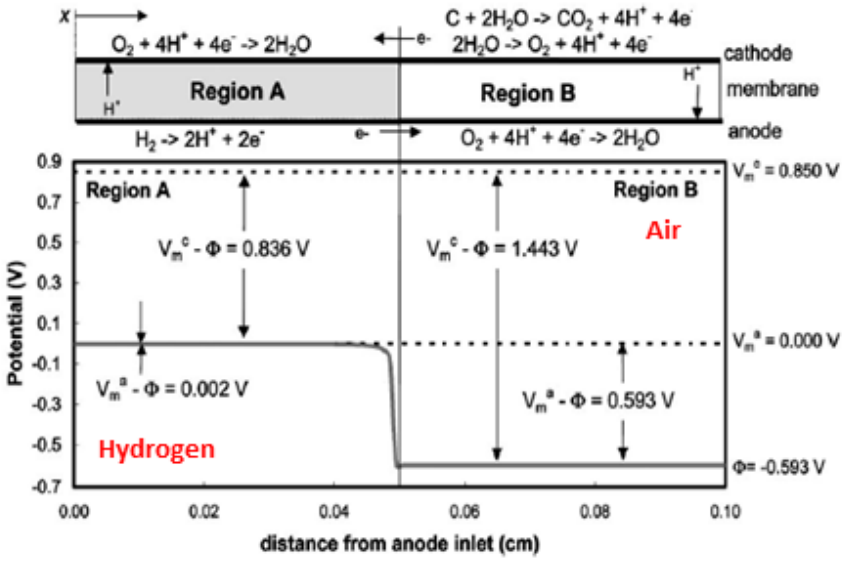

Figure I - 13. Potential distribution in the MEA during the reverse-current situation. Reprinted from [136].

The changes of the cathode structure due to "reverse-current" phenomenon are highlighted in Figure I - 14. At the macro-scale, a severe decrease of the cathode thickness is measured along with a significant change of its porous structure. Both cause increased mass-transport losses and electronic resistance at the electrode [60, 108, 138-141]. At the nano-scale, the Pt-based nanoparticles agglomerate/coalesce/detach, which results into lower catalyst utilization and decrease of the ECSA [94, 108]. On the chemical viewpoint, it should be noted that the formation of CO_{surf} groups turn the carbon surface into very hydrophilic and renders the water management more difficult [115, 142, 143].

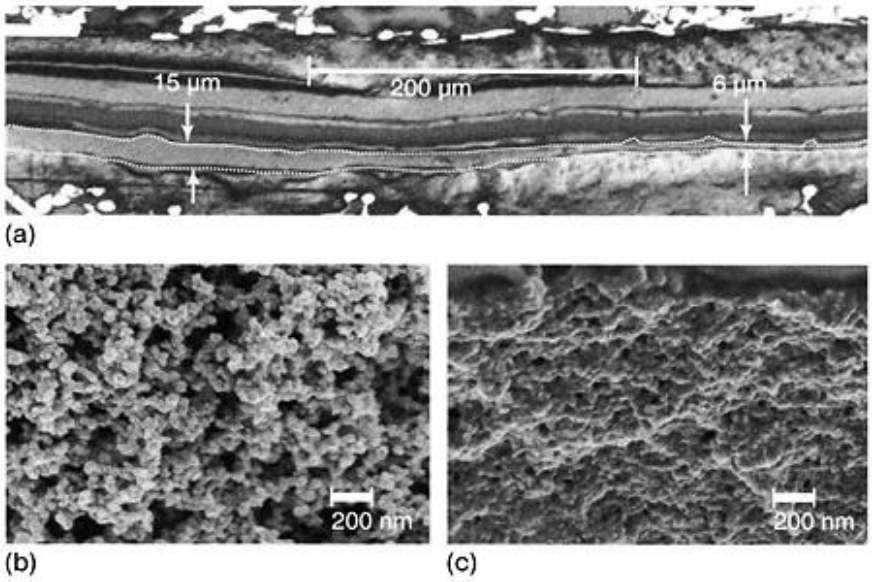

Figure I - 14. a) Cross-section of an aged MEA showing regions which were fuel-starved (right-side) and non-starved (left-side). The cathode is located at the bottom and the thickness values are presented. b) SEM micrograph of carbon structure in non-starved region and c) SEM micrograph of carbon structure in starved region. Reprinted from [28].

References

[1] U.N.-D.o.E.a.S.A.-P. Division, World population 2012, United Nations, USA, 2012.
[2] M.M. Jos G.J. Olivier, Trends in global CO2 emissions: 2013 report, Joint Research Centre & PBL Netherlands Environmental Assessment Agency, 2013.
[3] International Energy Agency, CO2 emissions from fuel combustion, International Energy Agency, France, 2013.
[4] G. Sandstede, E.J. Cairns, V.S. Bagotsky, K. Wiesener, History of low temperature fuel cells, in: A.L. Wolf Vielstich, Hubert A. Gasteiger (Ed.) Handbook of Fuel Cells - Fundamentals, Technology and Applications, John Wiley & Sons2003, pp. 145 - 218.
[5] D. Carter, J. Wing, The fuel cell industry review, (2011) Accessible at: http://www.fuelcelltoday.com/analysis/industry-review/2011/the-industry-review-2011.
[6] D. Carter, J. Wing, The fuel cell industry review, (2012) Accessible at: http://www.fuelcelltoday.com/analysis/industry-review/2012/the-industry-review-2012.
[7] D. Carter, J. Wing, The fuel cell industry review, (2013) Accessible at: http://fuelcelltoday.com/analysis/industry-review/2013/the-industry-review-2013.
[8] Breakthrough Technologies Institute, 2012 Fuell cell technologies market report, U.S. Department of Energy, 2013.
[9] D. Carter, J. Wing, Latest developments in the Ene-Farm scheme, (2013) Accessible at: http://www.fuelcelltoday.com/analysis/analyst-views/2013/2013-2002-2027-latest-developments-in-the-ene-farm-scheme.
[10] myFC, myFC POWERTREKK, 2014 (2014) Accessible at: http://powertrekk.com/collections/products.
[11] H.F. Cell, MiniPak, (2014) Accessible at: http://www.horizonfuelcell.com/#!minipak/c156u.
[12] A. Liquide, Hypulsion Project, (2014) Accessible at: http://www.airliquideadvancedbusiness.com/fr/qui-sommes-nous/hypulsion-1.html.
[13] UKH2Mobility, UKH2Mobility - phase 1 results - april 2013, (2013) Accessible at: http://www.ukh2mobility.co.uk/wp-content/uploads/2013/2008/UKH2012-Mobility-Phase-2011-Results-April-2013.pdf.
[14] K.C. Neyerlin, W. Gu, J. Jorne, H.A. Gasteiger, Determination of catalyst unique parameters for the oxygen reduction reaction in a PEMFC, J. Electrochem. Soc., 153 (2006) A1955-A1963.
[15] H.S. Wroblowa, P. Yen Chi, G. Razumney, Electroreduction of oxygen: A new mechanistic criterion, J. Electroanal. Chem. Interfacial Electrochem., 69 (1976) 195-201.
[16] H.A. Gasteiger, N.M. Marković, Just a dream—or future reality?, Science, 324 (2009) 48-49.
[17] F.T. Wagner, B. Lakshmanan, M.F. Mathias, Electrochemistry and the future of the automobile, J. Phys. Chem. Lett., 1 (2010) 2204-2219.
[18] K.A. Mauritz, R.B. Moore, State of Understanding of Nafion, Chem. Rev., 104 (2004) 4535-4586.
[19] D. Gierke T, Y. Hsu W, The Cluster Network Model of Ion Clustering in Perfluorosulfonated Membranes, Perfluorinated Ionomer Membranes, AMERICAN CHEMICAL SOCIETY1982, pp. 283-307.
[20] A.K. Sahu, S. Pitchumani, P. Sridhar, A.K. Shukla, Nafion and modified-Nafion membranes for polymer electrolyte fuel cells: An overview, Bulletin of Materials Science, 32 (2009) 285-294.
[21] V.S. Bagotsky, Fuel cells - problems and solutions, John Wiley & Sons, New Jersey, 2012.
[22] T.A. Zawodzinski, C. Derouin, S. Radzinski, R.J. Sherman, V.T. Smith, T.E. Springer, S. Gottesfeld, Water-uptake by and transport through Nafion® 117 membranes, J. Electrochem. Soc., 140 (1993) 1041-1047.
[23] T.A. Zawodzinski, T.E. Springer, J. Davey, R. Jestel, C. Lopez, J. Valerio, S. Gottesfeld, A comparative-study of water-uptake by and transport through ionomeric fuel-cell membranes, J. Electrochem. Soc., 140 (1993) 1981-1985.
[24] K. Schmidt-Rohr, Q. Chen, Parallel cylindrical water nanochannels in Nafion fuel-cell membranes, Nat. Mater., 7 (2008) 75-83.
[25] Perfluorinated Ionomer Membranes, AMERICAN CHEMICAL SOCIETY1982.
[26] H.A. Gasteiger, S.S. Kocha, B. Sompalli, F.T. Wagner, Activity benchmarks and requirements for Pt, Pt-alloy, and non-Pt oxygen reduction catalysts for PEMFCs, Appl. Catal. B, 56 (2005) 9-35.

[27] B. Vion-Dury, Mécanismes de vieillissement des électrocatalyseurs de pile à combustible de type PEMFC, IMEP2, University of Grenoble, Grenoble, 2011.
[28] R.N. Carter, W. Gu, B. Brady, P.T. Yu, K. Subramanian, H.A. Gasteiger, Electrode degradation mechanisms studies by current distribution measurements, in: W. Vielstich, A. Lamn, H.A. Gasteiger (Eds.) Handbook of Fuel Cells - Fundamentals, Technology and Applications, John Wiley & Sons2009, pp. 829 - 843.
[29] E. Billy, F. Maillard, A. Morin, L. Guétaz, F. Emmieux, C. Thurier, P. Doppelt, S. Donet, S. Mailley, Impact of ultra-low Pt loadings on the performance of anode/cathode in a Proton Exchange Membrane Fuel Cell, J. Power Sources, 195 (2010) 2737–2746.
[30] K.C. Neyerlin, W. Gu, J. Jorne, H.A. Gasteiger, Study of the exchange current density for the hydrogen oxidation and evolution reactions, J. Electrochem. Soc., 154 (2007).
[31] K. Sasaki, Y. Mo, J.X. Wang, M. Balasubramanian, F. Uribe, J. McBreen, R.R. Adzic, Pt submonolayers on metal nanoparticles - novel electrocatalysts for H-2 oxidation and O-2 reduction, Electrochim. Acta, 48 (2003) 3841-3849.
[32] J. Zhang, F.H.B. Lima, M.H. Shao, K. Sasaki, J.X. Wang, J. Hanson, R.R. Adzic, Platinum monolayer on nonnoble metal-noble metal core-shell nanoparticle electrocatalysts for O_2 reduction, J. Phys. Chem. B, 109 (2005) 22701-22704.
[33] R.R. Adzic, J. Zhang, K. Sasaki, M.B. Vukmirovic, M. Shao, J.X. Wang, A.U. Nilekar, M. Mavrikakis, J.A. Valerio, F. Uribe, Platinum monolayer fuel cell electrocatalysts, Topics Catal., 46 (2007) 249-262.
[34] J.X. Wang, C. Ma, Y. Choi, D. Su, Y. Zhu, P. Liu, R. Si, M.B. Vukmirovic, Y. Zhang, R.R. Adzic, Kirkendall effect and lattice contraction in nanocatalysts: a new strategy to enhance sustainable activity, J. Am. Chem. Soc., 133 (2011) 13551-13557.
[35] V.R. Stamenkovic, B.S. Mun, M. Arenz, K.J.J. Mayrhofer, C.A. Lucas, G.F. Wang, P.N. Ross, N.M. Markovic, Trends in electrocatalysis on extended and nanoscale Pt-bimetallic alloy surfaces, Nature Mater., 6 (2007) 241-247.
[36] C. Wang, M. Chi, D. Li, D. Strmcnik, D. van der Vliet, G. Wang, V. Komanicky, K.-C. Chang, A.P. Paulikas, D. Tripkovic, J. Pearson, K.L. More, N.M. Markovic, V.R. Stamenkovic, Design and synthesis of bimetallic electrocatalyst with multilayered Pt-Skin surfaces, J. Am. Chem. Soc., 133 (2011) 14396-14403.
[37] D.F. van der Vliet, C. Wang, D. Tripkovic, D. Strmcnik, X.F. Zhang, M.K. Debe, R.T. Atanasoski, N.M. Markovic, V.R. Stamenkovic, Mesostructured thin films as electrocatalysts with tunable composition and surface morphology, Nature Mater., (2012) advance online publication.
[38] C. Chen, Y. Kang, Z. Huo, Z. Zhu, W. Huang, H.L. Xin, J.D. Snyder, D. Li, J.A. Herron, M. Mavrikakis, M. Chi, K.L. More, Y. Li, N.M. Markovic, G.A. Somorjai, P. Yang, V.R. Stamenkovic, Highly crystalline multimetallic nanoframes with three-dimensional electrocatalytic surfaces, Science, 343 (2014) 1339-1343.
[39] C. Cui, L. Gan, M. Heggen, S. Rudi, P. Strasser, Compositional segregation in shaped Pt alloy nanoparticles and their structural behaviour during electrocatalysis, Nature Mater., 12 (2013) 765–771.
[40] M. Oezaslan, F. Hasché, P. Strasser, Pt-based core–shell catalyst architectures for oxygen fuel cell electrodes, J. Phys. Chem. Lett., 4 (2013) 3273-3291.
[41] P. Mani, R. Srivastava, P. Strasser, Dealloyed Pt-Cu core-shell nanoparticle electrocatalysts for use in PEM fuel cell cathodes, J. Phys. Chem. C, 112 (2008) 2770-2778.
[42] M. Oezaslan, M. Heggen, P. Strasser, Size-dependent morphology of dealloyed bimetallic catalysts: linking the nano to the macro scale, J. Am. Chem. Soc., 134 (2011) 514-524.
[43] C. Cui, L. Gan, H.-H. Li, S.-H. Yu, M. Heggen, P. Strasser, Octahedral PtNi nanoparticle catalysts: exceptional oxygen reduction activity by tuning the alloy particle surface composition, Nano Lett., 12 (2012) 5885–5889.
[44] I.E.L. Stephens, A.S. Bondarenko, U. Gronbjerg, J. Rossmeisl, I. Chorkendorff, Understanding the electrocatalysis of oxygen reduction on platinum and its alloys, Energy Environ. Sci., 5 (2012) 6744-6762.
[45] J.R. Kitchin, J.K. Norskov, M.A. Barteau, J.G. Chen, Role of strain and ligand effects in the modification of the electronic and chemical properties of bimetallic surfaces, Phys. Rev. Lett., 93 (2004).

[46] T. Bligaard, J.K. Nørskov, Ligand effects in heterogeneous catalysis and electrochemistry, Electrochim. Acta, 52 (2007) 5512-5516.
[47] C. Cui, L. Gan, M. Heggen, S. Rudi, P. Strasser, Compositional segregation in shaped Pt alloy nanoparticles and their structural behaviour during electrocatalysis, Nat. Mater., 12 (2013) 765-771.
[48] D.F. van der Vliet, C. Wang, D. Li, A.P. Paulikas, J. Greeley, R.B. Rankin, D. Strmcnik, D. Tripkovic, N.M. Markovic, V.R. Stamenkovic, Unique electrochemical adsorption properties of Pt-skin surfaces, Angew. Chem. Int. Ed., 51 (2012) 3139-3142.
[49] J.X. Wang, C. Ma, Y. Choi, D. Su, Y. Zhu, P. Liu, R. Si, M.B. Vukmirovic, Y. Zhang, R.R. Adzic, Kirkendall effect and lattice contraction in nanocatalysts: A new strategy to enhance sustainable activity, J. Am. Chem. Soc., 133 (2011) 13551-13557.
[50] M. Lopez-Haro, L. Dubau, L. Guétaz, P. Bayle-Guillemaud, M. Chatenet, J. André, N. Caqué, E. Rossinot, F. Maillard, Atomic-scale structure and composition of Pt3Co/C nanocrystallites during real PEMFC operation: A STEM–EELS study, Appl. Catal. B, 152–153 (2014) 300-308.
[51] L. Dubau, M. Lopez-Haro, J. durst, L. Guétaz, P. Bayle-Guillemaud, M. Chatenet, F. Maillard, Beyond conventional electrocatalysts: Hollow nanoparticles for improved and sustainable oxygen reduction reaction activity, Journal of Materials Chemistry A, (2014).
[52] F. Rodríguez-Reinoso, The role of carbon materials in heterogeneous catalysis, Carbon, 36 (1998) 159-175.
[53] K. Kinoshita, Carbon: Electrochemical and Physicochemical Properties, John Wiley & Sons, New York, 1988.
[54] W. Mathis, Graphite and carbon powders for electrochemical applications, J. Power Sources, 156 (2006) 142-150.
[55] F. Maillard, P.A. Simonov, E.R. Savinova, Carbon materials as supports for fuel cells electrocatalysts, in: J.L.F. Philippe Serp (Ed.) Carbon Materials for Catalysis, Wiley & Sons, New Jersey, 2009, pp. 429 - 480.
[56] J.-B. Donnet, A. Voet, Carbon black: physics, chemistry and elastomer reinforcement, Marcel Dekker, New York, 1976.
[57] R.D. Heidenreich, W.M. Hess, L.L. Ban, A test object and criteria for high resolution electron microscopy, Journal of Applied Crystallography, 1 (1968) 1 - 19.
[58] K.L. More, K. Perry, M. Chi, S. Reeves, Carbon support structural degradation observed in aged PEM fuel cells, Meeting Abstracts, MA2010-02 (2010) 611.
[59] Z.Y. Liu, J.L. Zhang, P.T. Yu, J.X. Zhang, R. Makharia, K.L. More, E.A. Stach, Transmission electron microscopy observation of corrosion behaviors of platinized carbon blacks under thermal and electrochemical conditions, J. Electrochem. Soc., 157 (2010) B906-B913.
[60] Z.Y. Liu, B.K. Brady, R.N. Carter, B. Litteer, M. Budinski, J.K. Hyun, D.A. Muller, Characterization of carbon corrosion-induced structural damage of PEM fuel cell cathode electrodes caused by local fuel starvation, J. Electrochem. Soc., 155 (2008) B979-B984.
[61] J.B. Donnet, R.C. Bansal, M.J. Wang, Carbon Black, Marcel Dekker, New York, 1993.
[62] O.V. Cherstiouk, A.N. Simonov, N.S. Moseva, S.V. Cherepanova, P.A. Simonov, V.I. Zaikovskii, E.R. Savinova, Microstructure effects on the electrochemical corrosion of carbon materials and carbon-supported Pt catalysts, Electrochim. Acta, 55 (2010) 8453-8460.
[63] K. Malek, M. Eikerling, Q. Wang, T. Navessin, Z. Liu, Self-organization in catalyst layers of polymer electrolyte fuel cells, J. Phys. Chem. C, 111 (2007) 13627-13634.
[64] T. Soboleva, K. Malek, Z. Xie, T. Navessin, S. Holdcroft, PEMFC Catalyst Layers: The Role of Micropores and Mesopores on Water Sorption and Fuel Cell Activity, ACS Applied Materials & Interfaces, 3 (2011) 1827-1837.
[65] Y. Liu, C. Ji, W. Gu, J. Jorne, H.A. Gasteiger, Effects of catalyst carbon support on proton conduction and cathode performance in PEM fuel cells, J. Electrochem. Soc., 158 (2011) B614-B621.
[66] M. Uchida, Y. Fukuoka, Y. Sugawara, N. Eda, A. Ohta, Effects of microstructure of carbon support in the catalyst layer on the performance of polymer-electrolyte fuel cells, J. Electrochem. Soc., 143 (1996) 2245-2252.
[67] M. Uchida, Y. Fukuoka, Y. Sugawara, H. Ohara, A. Ohta, Improved preparation process of very-low-platinum-loading electrodes for polymer electrolyte fuel cells, J. Electrochem. Soc., 145 (1998) 3708-3713.

[68] J. Kaiser, P.A. Simonov, V.I. Zaikovskii, C. Hartnig, L. Jörissen, E.R. Savinova, Influence of carbon support on the performance of platinum based oxygen reduction catalysts in a polymer electrolyte fuel J. Appl. Electrochem., (2007) DOI: 10.1007/s10800-10007-19356-10807.
[69] M. Lee, M. Uchida, H. Yano, D.A. Tryk, H. Uchida, M. Watanabe, New evaluation method for the effectiveness of platinum/carbon electrocatalysts under operating conditions, Electrochim. Acta, 55 (2010) 8504-8512.
[70] M. Lee, M. Uchida, D.A. Tryk, H. Uchida, M. Watanabe, The effectiveness of platinum/carbon electrocatalysts: Dependence on catalyst layer thickness and Pt alloy catalytic effects, Electrochim. Acta, 56 (2011) 4783-4790.
[71] Y. Liu, C. Ji, W. Gu, D.R. Baker, J. Jorne, H.A. Gasteiger, Proton conduction in PEM fuel cell cathodes: Effects of electrode thickness and ionomer equivalent weight, J. Electrochem. Soc., 157 (2010) B1154-B1162.
[72] D. Susac, V. Berejnov, A.P. Hitchcock, J. Stumper, STXM study of the ionomer distribution in the PEM fuel cell catalyst layers, ECS Trans., 41 (2011) 629-635.
[73] T. Soboleva, X. Zhao, K. Malek, Z. Xie, T. Navessin, S. Holdcroft, On the micro-, meso-, and macroporous structures of polymer electrolyte membrane fuel cell catalyst layers, ACS Applied Materials & Interfaces, 2 (2010) 375-384.
[74] J. Xie, K.L. More, T.A. Zawodzinski, W.H. Smith, Porosimetry of MEAs made by "Thin Film Decal" method and its effect on performance of PEFCs, J. Electrochem. Soc., 151 (2004) A1841-A1846.
[75] M. Uchida, Y. Aoyama, N. Eda, A. Ohta, New preparation method for polymer-electrolyte fuel-cells, J. Electrochem. Soc., 142 (1995) 463-468.
[76] M.M. Mench, Polymer Electrolyte Fuel Cells, in: J.W. Sons (Ed.) Fuel Cell Engines2008.
[77] J.M. Morgan, R. Datta, Understanding the gas diffusion layer in proton exchange membrane fuel cells. I. How its structural characteristics affect diffusion and performance, J. Power Sources, 251 (2014) 269-278.
[78] A. Arvay, E. Yli-Rantala, C.H. Liu, X.H. Peng, P. Koski, L. Cindrella, P. Kauranen, P.M. Wilde, A.M. Kannan, Characterization techniques for gas diffusion layers for proton exchange membrane fuel cells – A review, J. Power Sources, 213 (2012) 317-337.
[79] G.O. Mepsted, J.M. Moore, Performance and durability of bipolar plate materials, in: A.L. Wolf Vielstich, Hubert A. Gasteiger (Ed.) Handbook of Fuel Cells - Fundamentals, Technology and Applications, Wiley2013, pp. 286 - 293.
[80] J. Wind, A. LaCroix, S. Braeuninger, P. Hedrich, C. Heller, M. Schudy, Metal bipolar plates and coatings, in: A.L. Wolf Vielstich, Hubert A. Gasteiger (Ed.) Handbook of Fuel Cells - Fundamentals, Technology and Applications, Wiley2013, pp. 294 - 307.
[81] K. Robberg, V. Trapp, Graphite-based bipolar plates, in: A.L. Wolf Vielstich, Hubert A. Gasteiger (Ed.) Handbook of Fuel Cells - Fundamentals, Technology and Applications, Wiley2013, pp. 308 - 314.
[82] D.P. Wilkinson, O. Vanderleeden, Serpentine flow field design, in: A.L. Wolf Vielstich, Hubert A. Gasteiger (Ed.) Handbook of Fuel Cells - Fundamentals, Technology and Applications, Wiley2013, pp. 315 - 324.
[83] L. Dubau, L. Castanheira, F. Maillard, M. Chatenet, O. Lottin, G. Maranzana, J. Dillet, A. Lamibrac, J.-C. Perrin, E. Moukheiber, A. ElKaddouri, G. De Moor, C. Bas, L. Flandin, N. Caqué, A review of PEM fuel cell durability: materials degradation, local heterogeneities of aging and possible mitigation strategies, Wiley Interdisciplinary Reviews: Energy and Environment, (2014) n/a-n/a.
[84] R. Borup, J. Meyers, B. Pivovar, Y.S. Kim, R. Mukundan, N. Garland, D. Myers, M. Wilson, F. Garzon, D. Wood, P. Zelenay, K. More, K. Stroh, T. Zawodzinski, J. Boncella, J.E. McGrath, M. Inaba, K. Miyatake, M. Hori, K. Ota, Z. Ogumi, S. Miyata, A. Nishikata, Z. Siroma, Y. Uchimoto, K. Yasuda, K.-i. Kimijima, N. Iwashita, Scientific Aspects of Polymer Electrolyte Fuel Cell Durability and Degradation, Chem. Rev., 107 (2007) 3904-3951.
[85] N.E. Cipollini, Chemical aspects of membrane degradation, ECS Trans., 11 (2007) 1071-1082.
[86] Y. Tang, M.H. Santare, A.M. Karlsson, S. Cleghorn, W.B. Johnson, Stresses in proton exchange membranes due to hygro-thermal loading, J. Fuel Cell Sci. Tech., 3 (2005) 119-124.

[87] X. Huang, R. Solasi, Y. Zou, M. Feshler, K. Reifsnider, D. Condit, S. Burlatsky, T. Madden, Mechanical endurance of polymer electrolyte membrane and PEM fuel cell durability, Journal of Polymer Science Part B: Polymer Physics, 44 (2006) 2346-2357.
[88] S. Zhang, X.-Z. Yuan, J.N.C. Hin, H. Wang, J. Wu, K.A. Friedrich, M. Schulze, Effects of open-circuit operation on membrane and catalyst layer degradation in proton exchange membrane fuel cells, J. Power Sources, 195 (2010) 1142-1148.
[89] S. Vengatesan, M.W. Fowler, X.-Z. Yuan, H. Wang, Diagnosis of MEA degradation under accelerated relative humidity cycling, J. Power Sources, 196 (2011) 5045-5052.
[90] G. De Moor, C. Bas, N. Charvin, E. Moukheiber, F. Niepceron, N. Breilly, J. André, E. Rossinot, E. Claude, N.D. Albérola, L. Flandin, Understanding membrane failure in PEMFC: Comparison of diagnostic tools at different observation scales, Fuel Cells, 12 (2012) 356-364.
[91] J. Healy, C. Hayden, T. Xie, K. Olson, R. Waldo, M. Brundage, H. Gasteiger, J. Abbott, Aspects of the chemical degradation of PFSA ionomers used in PEM fuel cells, Fuel Cells, 5 (2005) 302-308.
[92] M. Aoki, H. Uchida, M. Watanabe, Decomposition mechanism of perfluorosulfonic acid electrolyte in polymer electrolyte fuel cells, Electrochem. Com., 8 (2006) 1509-1513.
[93] V.A. Sethuraman, J.W. Weidner, A.T. Haug, M. Pemberton, L.V. Protsailo, Importance of catalyst stability vis-à-vis hydrogen peroxide formation rates in PEM fuel cell electrodes, Electrochim. Acta, 54 (2009) 5571-5582.
[94] E. Guilminot, A. Corcella, F. Charlot, F. Maillard, M. Chatenet, Detection of Pt^{z+} ions and Pt nanoparticles inside the membrane of a used PEMFC, J. Electrochem. Soc., 154 (2007) B96-B105.
[95] C. Galeano, C. Baldizzone, H. Bongard, B. Spliethoff, C. Weidenthaler, J.C. Meier, K.J.J. Mayrhofer, F. Schüth, Carbon-based yolk-shell materials for fuel cell applications, Adv. Funct. Mater., 24 (2014) 220-232.
[96] C. Galeano, J.C. Meier, V. Peinecke, H. Bongard, I. Katsounaros, A.A. Topalov, A. Lu, K.J.J. Mayrhofer, F. Schüth, Toward highly stable electrocatalysts via nanoparticle pore confinement, J. Am. Chem. Soc., 134 (2012) 20457-20465.
[97] Y. Shao-Horn, W.C. Sheng, S. Chen, P.J. Ferreira, E.F. Holby, D. Morgan, Instability of supported platinum nanoparticles in low-temperature fuel cells, Topics Catal., 46 (2007) 285-305.
[98] Z. Zhao, L. Dubau, F. Maillard, Evidences of the migration of Pt crystallites on high surface area carbon supports in the presence of reducing molecules, J. Power Sources, 217 (2012) 449-458.
[99] W. Sheng, S. Chen, E. Vescovo, Y. Shao-Horn, Size Influence on the Oxygen Reduction Reaction Activity and Instability of Supported Pt Nanoparticles, J. Electrochem. Soc., 159 (2011) B96-B103.
[100] A.A. Topalov, I. Katsounaros, M. Auinger, S. Cherevko, J.C. Meier, S.O. Klemm, K.J.J. Mayrhofer, Dissolution of platinum: Limits for the deployment of electrochemical energy conversion?, Angew. Chem. Int. Ed., 51 (2012) 12613-12615.
[101] R.M. Darling, J.P. Meyers, Kinetic model of platinum dissolution in PEMFCs, J. Electrochem. Soc., 150 (2003) A1523-A1527.
[102] G. Jerkiewicz, G. Vatankhah, J. Lessard, M.P. Soriaga, Y.S. Park, Surface-oxide growth at platinum electrodes in aqueous H_2SO_4 Reexamination of its mechanism through combined cyclic-voltammetry, electrochemical quartz-crystal nanobalance, and Auger electron spectroscopy measurements, Electrochim. Acta, 49 (2004) 1451-1459.
[103] B.E. Conway, Electrochemical oxide film formation at noble-metals as a surface-chemical process, Prog. Surf. Sci., 49 (1995) 331-452.
[104] D.C. Johnson, D.T. Napp, S. Bruckenstein, A ring-disk electrode study of the current/potential behaviour of platinum in 1.0 M sulphuric and 0.1 M perchloric acids, Electrochim. Acta, 15 (1970) 1493-1509.
[105] S.G. Rinaldo, W. Lee, J. Stumper, M. Eikerling, Model- and theory-based evaluation of Pt dissolution for supported Pt nanoparticle distributions under potential cycling, Electrochem. Solid-State Lett., 14 (2011) B47-B49.
[106] V.I. Birss, M. Chang, J. Segal, Platinum oxide film formation—reduction: an in-situ mass measurement study, J. Electroanal. Chem., 355 (1993) 181-191.
[107] E. Guilminot, A. Corcella, M. Chatenet, F. Maillard, F. Charlot, G. Berthomé, C. Iojoiu, J.-Y. Sanchez, E. Rossinot, E. Claude, Membrane and active layer degradation upon PEMFC steady-state

operation: I. Platinum dissolution and redistribution within the MEA, J. Electrochem. Soc., 154 (2007) B1106-B1114.
[108] L. Dubau, M. Lopez-Haro, L. Castanheira, J. Durst, M. Chatenet, P. Bayle-Guillemaud, L. Guétaz, N. Caqué, E. Rossinot, F. Maillard, Probing the structure, the composition and the ORR activity of Pt3Co/C nanocrystallites during a 3422h PEMFC ageing test, Appl. Catal. B, 142–143 (2013) 801-808.
[109] X. Erler, In-situ investigation of metal nanoparticle stability during electrocatalysis, Von der Fakultät II - Mathematik und Naturwissenschaften, Technical university of Berlin, Berlin, 2012.
[110] H. Binder, A. Köhling, K. Richter, G. Sandstede, Über die anodische oxydation von aktivkohlen in wässrigen elektrolyten, Electrochim. Acta, 9 (1964) 255-274.
[111] K. Kinoshita, J. Bett, Electrochemical oxidation of carbon black in concentrated phosphoric acid at 135°C, Carbon, 11 (1973) 237-247.
[112] K. Kinoshita, J.A.S. Bett, Potentiodynamic analysis of surface oxides on carbon blacks, Carbon, 11 (1973) 403-411.
[113] K. Kinoshita, J.A.S. Bett, Determination of carbon surface oxides on platinum-catalyzed carbon, Carbon, 12 (1974) 525-533.
[114] K. Kinoshita, J.A.S. Bett, Influence of electrochemical treatment in phosphoric acid on the wettability of carbons, Carbon, 13 (1975) 405-409.
[115] K.H. Kangasniemi, D.A. Condit, T.D. Jarvi, Characterization of vulcan electrochemically oxidized under simulated PEM fuel cell conditions, J. Electrochem. Soc., 151 (2004) E125-E132.
[116] L.M. Roen, C.H. Paik, T.D. Jarvi, Electrocatalytic Corrosion of Carbon Support in PEMFC Cathodes, Electrochem. Solid-State Lett., 7 (2004) A19-A22.
[117] J. Willsau, J. Heitbaum, The influence of Pt-activation on the corrosion of carbon in gas diffusion electrodes—A DEMS study, J. Electroanal. Chem. Interfacial Electrochem., 161 (1984) 93-101.
[118] S. Maass, F. Finsterwalder, G. Frank, R. Hartmann, C. Merten, Carbon support oxidation in PEM fuel cell cathodes, J. Power Sources, 176 (2008) 444-451.
[119] R. Makharia, S.S. Kocha, P.T. Yu, M.A. Sweikart, W. Gu, F.T. Wagner, H. Gasteiger, Durable PEM fuel cell electrode materials: requirements and benchmarking methodologies, ECS Trans., 1 (2006) 3-18.
[120] S.C. Ball, S.L. Hudson, D. Thompsett, B. Theobald, An investigation into factors affecting the stability of carbons and carbon supported platinum and platinum/cobalt alloy catalysts during 1.2V potentiostatic hold regimes at a range of temperatures, J. Power Sources, 171 (2007) 18-25.
[121] K. Artyushkova, S. Pylypenko, M. Dowlapalli, P. Atanassov, Structure-to-property relationships in fuel cell catalyst supports: Correlation of surface chemistry and morphology with oxidation resistance of carbon blacks, J. Power Sources, 214 (2012) 303-313.
[122] M.F. Mathias, R. Makharia, H. Gasteiger, J.J. Conley, T.J. Fuller, G.J. Gittleman, S.S. Kocha, D.P. Miller, C.K. Mittelsteadt, T. Xie, S.G. Yan, P.T. Yu, Two fuel cell cars in every garage?, Interface, 14 (2005) 24-35.
[123] E. Passalacqua, P.L. Antonucci, M. Vivaldi, A. Patti, V. Antonucci, N. Giordano, K. Kinoshita, The influence of Pt on the electrooxidation behaviour of carbon in phosphoric acid, Electrochim. Acta, 37 (1992) 2725-2730.
[124] W. Li, A.M. Lane, Investigation of Pt catalytic effects on carbon support corrosion of the cathode catalyst in PEM fuel cells using DEMS spectra, Electrochem. Com., 11 (2009) 1187-1190.
[125] N. Linse, L. Gubler, G.G. Scherer, A. Wokaun, The effect of platinum on carbon corrosion behavior in polymer electrolyte fuel cells, Electrochim. Acta, 56 (2011) 7541-7549.
[126] F. Maillard, A. Bonnefont, F. Micoud, An EC-FTIR study on the catalytic role of Pt in carbon corrosion, Electrochem. Com., 13 (2011) 1109-1111.
[127] S.C. Ball, S.L. Hudson, B. Theobald, D. Thompsett, The effect of dynamic and steady state voltage excursions on the stability of carbon supported Pt and PtCo catalysts, ECS Trans., 3 (2006) 595-605.
[128] P.L. Antonucci, L. Pino, N. Giordano, G. Pinna, A comparative analysis of structural and surface effects in the electrochemical corrosion of carbons, Mater. Chem. Phys., 21 (1989) 495-506.
[129] H.P. Boehm, Surface oxides on carbon and their analysis: a critical assessment, Carbon, 40 (2002) 145-149.

[130] B. Avasarala, R. Moore, P. Haldar, Surface oxidation of carbon supports due to potential cycling under PEM fuel cell conditions, Electrochim. Acta, 55 (2010) 4765-4771.
[131] G. Álvarez, F. Alcaide, O. Miguel, P.L. Cabot, M.V. Martínez-Huerta, J.L.G. Fierro, Electrochemical stability of carbon nanofibers in proton exchange membrane fuel cells, Electrochim. Acta, 56 (2011) 9370-9377.
[132] S.E. Rodil, Infrared spectra of amorphous carbon based materials, Diamond Relat. Mater., 14 (2005) 1262-1269.
[133] N. Giordano, P.L. Antonucci, E. Passalacqua, L. Pino, A.S. Aricò, K. Kinoshita, Relationship between physicochemical properties and electrooxidation behaviour of carbon materials, Electrochim. Acta, 36 (1991) 1931-1935.
[134] H.-S. Choo, T. Kinumoto, S.-K. Jeong, Y. Iriyama, T. Abe, Z. Ogumi, Mechanism for electrochemical oxidation of highly oriented pyrolytic graphite in sulfuric acid solution, J. Electrochem. Soc., 154 (2007) B1017-B1023.
[135] M. Nose, T. Kinumoto, H.S. Choo, K. Miyazaki, T. Abe, Z. Ogumi, Electrochemical oxidation of ighly oriented pyrolytic graphite in sulphuric acid solution under potential pulse condition, Fuel Cells, 9 (2009) 284-290.
[136] C.A. Reiser, L. Bregoli, T.W. Patterson, J.S. Yi, J.D. Yang, M.L. Perry, T.D. Jarvi, A reverse-current decay lechanism for fuel cells, Electrochem. Solid-State Lett., 8 (2005) A273-A276.
[137] T.W. Patterson, R.M. Darling, Damage to the cathode catalyst of a PEM fuel cell caused by localized fuel starvation, Electrochem. Solid-State Lett., 9 (2006) A183-A185.
[138] P.J. Ferreira, G.J. la O, Y. Shao-Horn, D. Morgan, R. Makharia, S. Kocha, H.A. Gasteiger, Instability of Pt/C electrocatalysts in proton exchange membrane fuel cells, J. Electrochem. Soc., 152 (2005) A2256-A2271.
[139] M. Chatenet, E. Guilminot, C. Iojoiu, J.-Y. Sanchez, E. Rossinot, F. Maillard, Pt redistribution within PEMFC MEAs and its consequence on their performances, ECS Trans., 11 (2007) 1203-1214.
[140] J. Xie, D.L. Wood, K.L. More, P. Atanassov, R.L. Borup, Microstructural changes of membrane electrode assemblies during PEFC durability testing at high humidity conditions, J. Electrochem. Soc., 152 (2005) A1011-A1020.
[141] H. Schulenburg, B. Schwanitz, N. Linse, G.n.G. Scherer, A. Wokaun, J. Krbanjevic, R. Grothausmann, I. Manke, 3D Imaging of Catalyst Support Corrosion in Polymer Electrolyte Fuel Cells, J. Phys. Chem. C, 115 (2011) 14236-14243.
[142] K.G. Gallagher, R.M. Darling, T.F. Fuller, Carbon-support corrosion mechanisms and models, in: A.L. Wolf Vielstich, Hubert A. Gasteiger (Ed.) Handbook of Fuel Cells - Fundamentals, Technology and Applications, John Wiley & Sons2009, pp. 819-828.
[143] K.G. Gallagher, T.F. Fuller, Kinetic model of the electrochemical oxidation of graphitic carbon in acidic environments, Phys. Chem. Chem. Phys., 11 (2009) 11557-11567.

Chapter II.

Experimental section

All the glassware accessories used in this thesis were cleaned by soaking in a H_2SO_4:H_2O_2 mixture (Caro acid) overnight and thoroughly washing with ultrapure water.

2.1 Electrocatalysts

The electrocatalysts were Pt nanoparticles supported onto different carbon supports *i.e.* Vulcan XC72 (S_c ~ 250 m² g^{-1}), a high surface area carbon (HSAC) (S_c ~ 800 m² g^{-1}), reinforced graphite (RG) (S_c ~ 110 m² g^{-1}). The electrocatalysts were supplied by Tanaka Kikinzoku (TKK).

In **Chapter III**, the following electrocatalysts were used:

- A Pt/Vulcan XC72 TKK electrocatalyst with a Pt weight fraction (wt. %) of 40 %, and a surface-averaged mean Pt particle size of 2.7 nm (TEC10V40E);
- A Pt/Vulcan XC72 E-TEK with a Pt weight fraction of 40 %, translating into a surface-averaged Pt particle size of 4.7 nm;
- A Pt/HSAC electrocatalyst with a Pt weight fraction of 40 % (TEC10E40E), and a surface-averaged mean Pt particle size of 2.0 nm;
- A Pt/RG electrocatalyst with a Pt weight fraction of 40 % (TEC10EA40E);

In **Chapter IV**, a Pt/HSAC electrocatalyst with a Pt weight fraction of 40 % (TEC10E40E), and a surface-averaged mean Pt particle size of 2.0 nm was used.

In **Chapter V**, the analysed materials are from MEAs which electrocatalysts are proprietary and impossible to disclose their composition.

The electrocatalysts were used as-received without any further treatment.

2.2 Electrochemical measurements

The electrochemical measurements were conducted using an Autolab PGSTAT20. Fresh electrolyte (0.1 M H_2SO_4) was daily prepared from ultrapure water (MQ grade, 18.2 MΩ cm, 1-3 ppb total organic compound (TOC)) and 96 wt. % H_2SO_4 (Suprapur, Merck). For all electrochemical experiments, the electrolyte was purged with argon (Ar, > 99.99 %, Messer).

In **Chapter III**, two separated four-electrode electrochemical cells were used, a "characterization cell" and a "degradation cell" both thermostated at T = 330 K. A homemade rotating disk electrode tip was used as working electrode. A large-area Pt foil was used as counter-electrode for the studies of **sub-chapter 3.4**, **3.5** while a carbon monolith was used as counter-electrode for the study of **sub-chapter 3.6**. A mercury sulphate electrode $Hg|Hg_2SO_4|K_2SO_4$ (saturated, aqueous) - connected to the cell via a Luggin capillary as a reference electrode. This reference electrode was calibrated periodically by measuring the potential difference with a reversible hydrogen electrode (RHE), the latter being systematically 0.72 V *vs*. RHE. All the potentials reported in this study were referenced on the RHE scale. A Pt wire connected to the reference electrode was used to filter the high frequency electrical noise and to avoid disturbing the low frequency electrical measurements. More details on the dual-reference system used in this work can be found in Ref. [1].

In **Chapter IV**, two separated four-electrode electrochemical cells were used, a "characterization cell" and a "degradation cell" both thermostated at T = 330 K. A homemade rotating disk electrode tip was used as working electrode, a large-area Pt foil as counter-electrode and a mercury sulphate electrode $Hg|Hg_2SO_4|K_2SO_4$ (saturated, aqueous) - connected to the cell via a Luggin capillary as a reference electrode.

2.3 Preparation of the catalytic inks and of the porous catalytic layers

The preparation of reproducible porous catalytic layers is extremely important in the field of electrocatalysis of PEMFC materials, the interested reader is referred to the excellent review by Kocha *et al*. on this issue [2].

2.3.1. Preparation of the catalytic inks

Suspensions composed of a 5 wt. % Nafion® solution (Aldrich), MQ-grade water, 20 µL of isopropanol and 5.0 mg of Pt/C powder were ultrasonically treated for 15 minutes and used as catalytic inks. The ionomer/electrocatalyst (I/C) ratio was 0.5. The 40 wt. % Pt/HSAC electrocatalyst inks have a concentration of 0.735 $g_{Pt/C}$ L^{-1}. The inks were used over a period of 1.5 month, such "expiring date" being fixed by the changes in chemistry and structure of the Pt/C electrocatalysts over time (see Ref. [3] for more details).

2.3.2. Preparation of the porous catalytic layers

Home-made rotating disk electrodes (RDE) made of a glassy carbon disk (Sigradur®, 0.196 cm²) embedded in a Kel-F cylinder were firstly manually polished with a 1 μm diamond paste (Mecaprex, Presi) in a "figure eight" pattern for 5 minutes until a mirror finish was obtained. The polished electrode was then rinsed with ultrapure water, and subsequently sonicated in acetone, ethanol and MQ-water solutions to remove the excess of diamond paste (15 minutes for each solution). The electrodes were then stored over-night in a beaker filled with MQ-water sealed with Parafilm®, and placed inside the laboratory cabinet to prevent contamination by air impurities.

On the experiment day, the rotating disk electrodes were air-dried in an oven at T = 383 K for 6 minutes. Meanwhile, the electrocatalyst ink was sonicated to ensure homogenization of the catalyst's ink. An aliquot of 20 μL was then deposited onto the glassy carbon disk of the freshly polished RDE and the ink was dried for 5 minutes in air at T = 383 K to ensure evaporation of the water and the solvents of the Nafion® solution. This resulted in a so-called "porous" RDE. In **Chapter IV** a second aliquot of 20 μL was added yielding a final Pt loading of 11.76 μg_{Pt} (2 × 5.88 μg_{Pt}). The working electrode was always immersed/withdrawn into/from the electrochemical cell at controlled electrode potential E = 0.40 V *vs*. RHE.

2.4 Electrochemical characterization

Before any electrocatalytic measurement, ten cyclic voltammograms at v = 20 mV s^{-1} followed by another one at v =100 mV s^{-1} were firstly recorded to obtain the characteristic voltammetric response of the Pt/C electrocatalysts between 0.05 and 1.23 V *vs*. RHE. Secondly, the electrochemically active surface area (ECSA) was measured using the coulometry required to desorb a monolayer of under-potentially adsorbed H or electrooxidize a monolayer of adsorbed carbon monoxide (CO_{ad} stripping voltammograms). The carbon monoxide (CO) saturation coverage was established by bubbling CO for 6 min and purging the solution with Ar for 45 min, while keeping the electrode potential at E = 0.10 V *vs*. RHE. It was assumed that the electrooxidation of an adsorbed CO monolayer required 420 μC per cm^2 of Pt.

2.5 Accelerated stress tests (ASTs)

Different ASTs were designed to isolate the effect of specific parameters on the degradation mechanisms and the durability of the Pt/C electrocatalysts:

- **Chapter III**

Effect of potential range and gas atmosphere

To test the effect of the potential range and gas atmosphere in the degradation of the electrocatalysts, ASTs defined by the FCCJ organization were performed [4]. The tests consist of two protocols (Figure II - 1):

- Load-cycle protocol: square potential ramp between 0.60 V – 1.00 V *vs.* RHE with a period of 6 s/cycle, which mimic the potential range experienced during PEMFC operation under steady-state;
- Start-up/shutdown protocol: square potential ramp between 1.00 V –1.50 V *vs.* RHE with a period of 6 s/cycle, which mimic the potential range experienced during PEMFC operation under start/stop cycles;

The ASTs protocols are performed in the "degradation cell", during 5000 cycles with 0.1 M H_2SO_4 as electrolyte, under neutral (argon) or oxidising (oxygen) atmosphere.

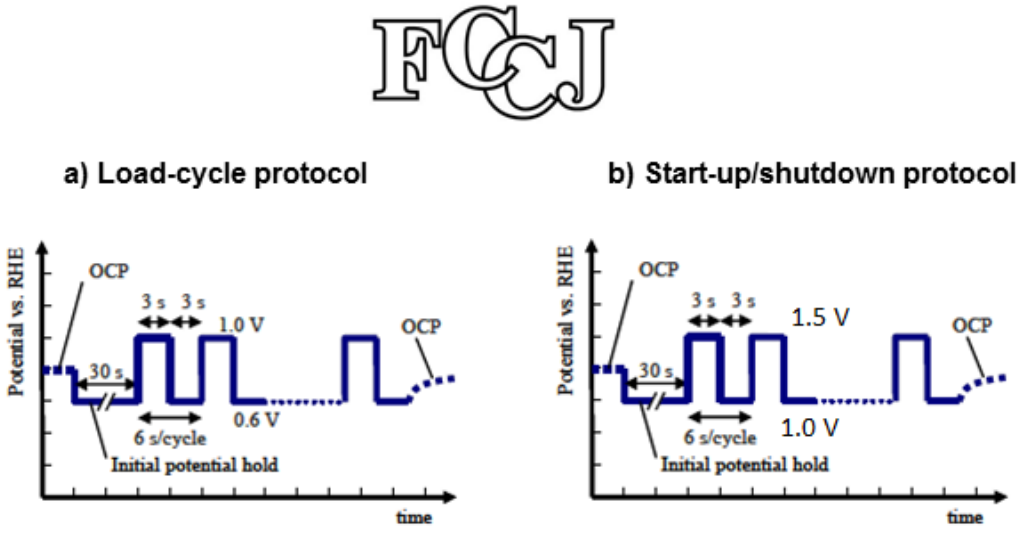

Figure II - 1. FCCJ protocols: a) Load-cycle protocol and b) start-up/shutdown protocol.

- **Chapter IV**

The accelerated stress tests performed in this chapter consisted of potentiostatic measurements performed at E = 0.40, 0.50, 0.60, 0.70, 0.80, 0.90, 1.00, 1.20, 1.30, or 1.40 V *vs*. RHE for 96 hours. The changes in ECSA were monitored via CO_{ad} stripping coulometry (after 6, 24, 48, 72 and 96 h) in the characterization cell. Before the CO_{ad} stripping, five cyclic voltammograms at v = 100 mV s^{-1} and a cyclic voltammogram at v = 20 mV s^{-1} were recorded to characterize the surface reactivity of the Pt/HSAC electrocatalyst.

2.6 PEMFC testing

A 110-cell PEMFC stack using Pt/C at the anode and at the cathode was operated at constant current density (j = 0.25 A cm^{-2}) for t = 12,860 h at T = 333 to 338 K by Axane (Isère, France). The electrocatalytic materials, the chemical nature of the ionomer contained in the catalytic layers and the proton-exchange membrane are proprietary and cannot be described. The catalytic layers were catalyst-coated membranes (geometric area 86 cm^2). The cathode was fed with humidified air (60 to 75% relative humidity (RH), close to the atmospheric pressure, gas stoichiometry of 2.5), and the anode was fuelled with dry pure dihydrogen (0 % RH, 1.35 bar abs., dead-end mode, corresponding to an average H_2 stoichiometry of *ca*. 1.1). Air and H_2 purges were performed intermittently to remove the water produced at the cathode and the water and nitrogen that accumulate at the anode, respectively. Practically speaking, the air RH was fixed at the gas inlet by an adequate choice of the humidifier and cell temperature, and the air stoichiometry was doubled intermittently to allow air purges. The frequency and the duration of the air purge are proprietary and cannot be mentioned. The stack was disassembled at the end of life, and used for physical, chemical and electrochemical characterization. All the data presented in this study were obtained for electrocatalysts sampled in different regions of the cathode: cathode inlet/outlet and regions corresponding to segment 5 and segment 8 of LEMTAs segmented cell (see **Chapter V**).

2.7 *Ex situ* preparation of the fresh/aged MEAs cathode electrocatalysts

For the post-mortem analysis of the cathode electrocatalyst of a catalyst-coated backing (CCB) MEA, it is not possible to detach the gas diffusion-layer (GDL) from the proton-exchange membrane (PEM) without affecting the electrode structure. Small pieces of the MEA were then cut with a punch, and some droplets of ethanol were added onto the surface

of the GDL (anode and cathode) to facilitate its detachment from the PEM. It was possible to observe that a fraction of electrocatalyst remained on the PEM surface (middle circle in step 6 of Figure II - 2), but most of the catalytic powder was attached to the GDL. For TEM imaging, the remaining electrocatalyst present in the Nafion® membrane (cathode side) was scraped with a metallic spatula, dispersed in MQ-grade water and deposited on a TEM grid. The cathode side of the GDL, which was covered with the fresh/aged catalytic powder, was used for Raman spectroscopy and X-ray photoelectron spectroscopy (XPS) measurements without any further treatment. The reliability of such procedure is shown in Figure II - 3, where a Raman spectra of aged Pt/C on the GDL and on the PEM are presented, revealing identical features.

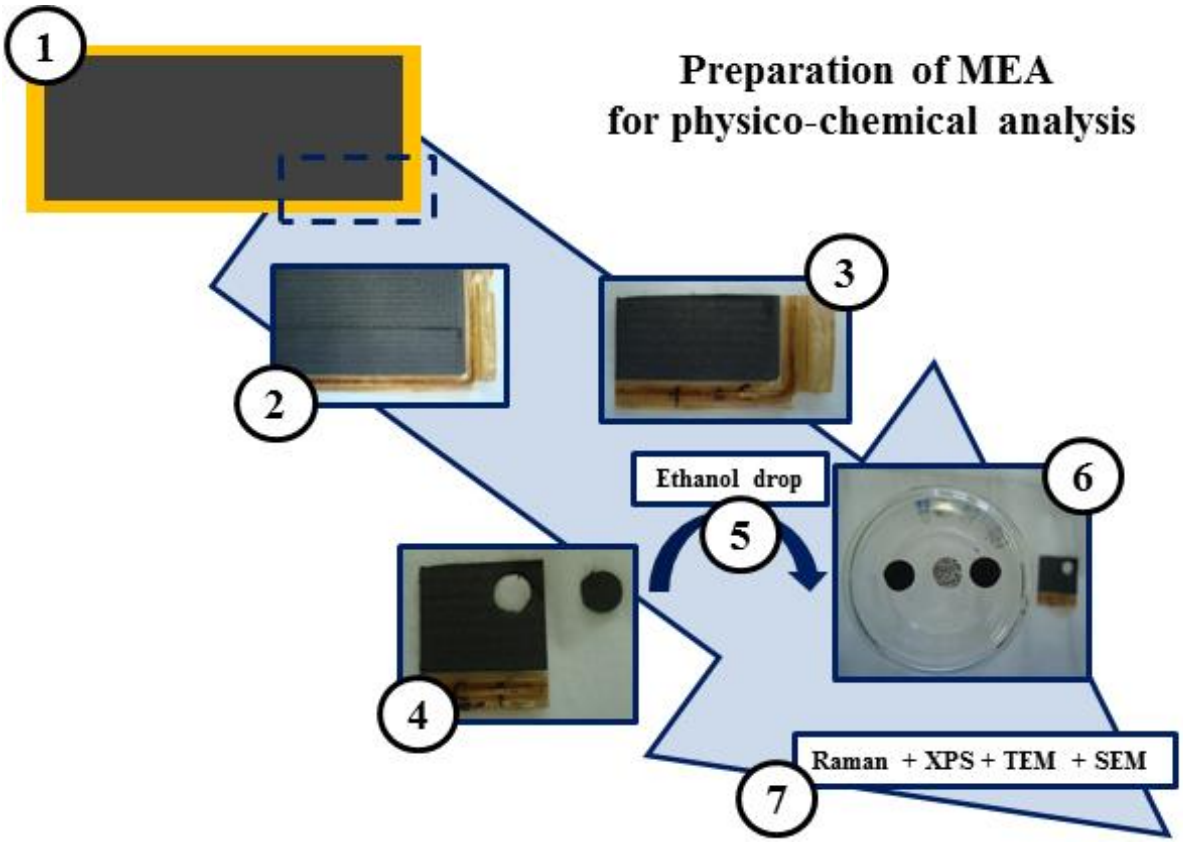

Figure II - 2. Sequence for the MEA sample preparation for physico-chemical analysis.

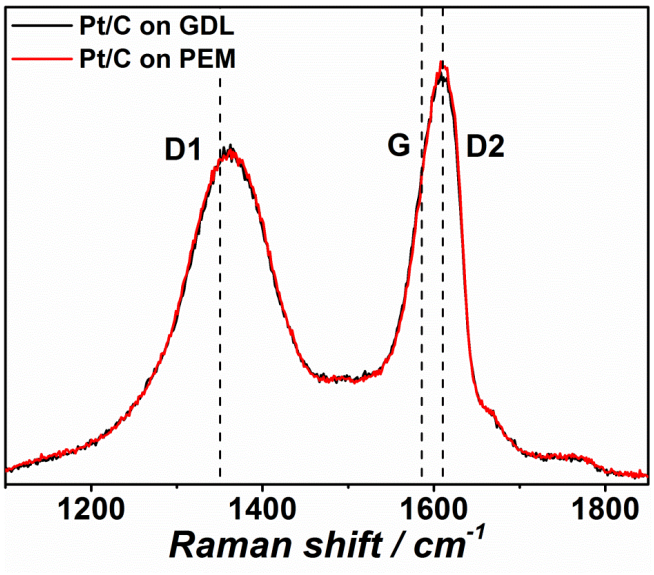

Figure II - 3. Raman spectrum of the Pt/C electrocatalyst present on the GDL and on the PEM.

2.8 Characterization of the fresh and aged electrocatalysts

2.8.1 Physical techniques

Electron microscopes use a beam of highly energetic electrons to examine nanometre scale objects on a very fine scale. This examination provides information about the topography (surface features of an object), the morphology (shape and size of the particles making up the object), the composition (the elements and compounds that the object is composed of and the relative amounts of them) and the crystallographic information (how the atoms are arranged in the object). The advantage of such microscopes is the use of electrons beam (shorter wavelength than white light), which provides them the possibility to distinguish "atomic" features.

Most electron microscopy rely on the same principle: (*i*) firstly, a beam of electrons is formed in high vacuum (by electron guns), (*ii*) secondly the electron beam is focused using metal apertures and magnetic lenses into a thin, focused, monochromatic beam, (*iii*) thirdly the sample is irradiated by the beam and interactions occur inside the irradiated sample, affecting the electron beam and finally (*iv*) these interactions are detected and transformed into an image.

Electron microscopy techniques used in this thesis were valuable tools to:

- characterize the particle size distribution (PSD) of the studied Pt/C electrocatalysts and follow their degradation mechanisms in identical regions (TEM and IL-TEM);
- follow the structural changes of the MEAs electrodes and Nafion® membrane during PEMFC stack operation (FEG-SEM);

The reader is referred to Ref. [5] for more details on the use of electron microscopy for characterization of PEMFC electrode materials.

a. Transmission Electron Microscopy (TEM)

A TEM is a microscopy technique where an incident beam of high energy electrons is transmitted through a sample. For the electron beam to penetrate the sample, it is required that the thickness of the sample is in the order of a few hundred nanometres. The electron beam is under vacuum and the presence of electromagnetic lenses allows the operator to control the convergence of the beam and the magnification of the microscope. The interaction of the electron beam with the sample forms a projection, allowing the operator to select the interest zones for imaging and the image results from either a mass/thickness contrast or a diffraction contrast. As for any experimental technique, the operator sensibility is extremely important to control the image properties (brightness and/or contrast) in order to obtain comparable images, once the interaction of the electron beam with the sample may provide measure artefacts [6].

For TEM experiments, the electrocatalysts were deposited onto a copper or a gold grid baring a Lacey carbon membrane (300 mesh, Lacey Carbon; Agar Sc. UK) and examined with a Jeol 2010 TEM operated at 200 kV with a point to point resolution of 0.19 nm located at the Centre des Moyens Technologiques Communs (CMTC) of Grenoble INP. The images were used to build the PSD of the electrocatalysts and to follow the structural changes of the Pt/C electrocatalysts before/after degradation test. From these observations, the number-averaged mean-particle size:

$$\overline{d}_N = \frac{\sum_{i=1}^{n} n_i d_i}{\sum_{i=1}^{n} n_i} \qquad \text{(Eq. II - 1)}$$

and the surface-averaged mean particle size:

$$\overline{d}_S = \frac{\sum_{i=1}^{n} n_i d_i^3}{\sum_{i=1}^{n} n_i d_i^2} \qquad \text{(Eq. II - 2)}$$

were determined by eye-counting over *ca*. 400 particles (n_i stands for the number of particles having a diameter d_i). Only "isolated" particles (that is non-agglomerated, single grain spherical particles) were counted to build the particle size distribution. Any other Pt nanoparticle whatever its shape or its structure (a single crystallite or a combination of individual nanocrystallites) was considered an "agglomerated" Pt nanoparticle.

b. Identical-Location TEM (IL-TEM)

The degradation mechanisms of PEMFC electrocatalysts were also determined using Identical-location Transmission Electron Microscopy (IL-TEM) [7-9]. In this technique, first introduced by Mayrhofer and co-workers, a TEM grid made of Au is loaded with a given electrocatalyst, used as a working electrode in a conventional electrochemical cell, and finally, the "same exactly locations" that were previously observed are imaged again in TEM.

Technically speaking, the electrocatalyst suspension was diluted by a factor of 4 with MQ-grade water (Millipore). A 5 μL aliquot was then deposited over a gold TEM grid (300 mesh, Lacey Carbon; Agar Sc. UK), and dried in air. Five randomly selected carbon particles located at different places of the grid were imaged at low (80 k) and high (150 k) magnification. Then, the grid was carefully clamped between two carbon plates, which served as a mechanical support and current collectors for the electrochemistry experiments. After the electrochemical experiments, the TEM grid was rinsed with MQ-grade water, dried in air, and TEM images were acquired in exactly the same position (identical-location TEM). The experimental steps of such technique are exemplified in Figure II - 4. The IL-TEM images were used to build the particle size distribution of the electrocatalysts before/after degradation test and to determine the number-averaged mean-particle size ($\overline{d}_N$) and the surface-averaged mean particle size ($\overline{d}_S$).

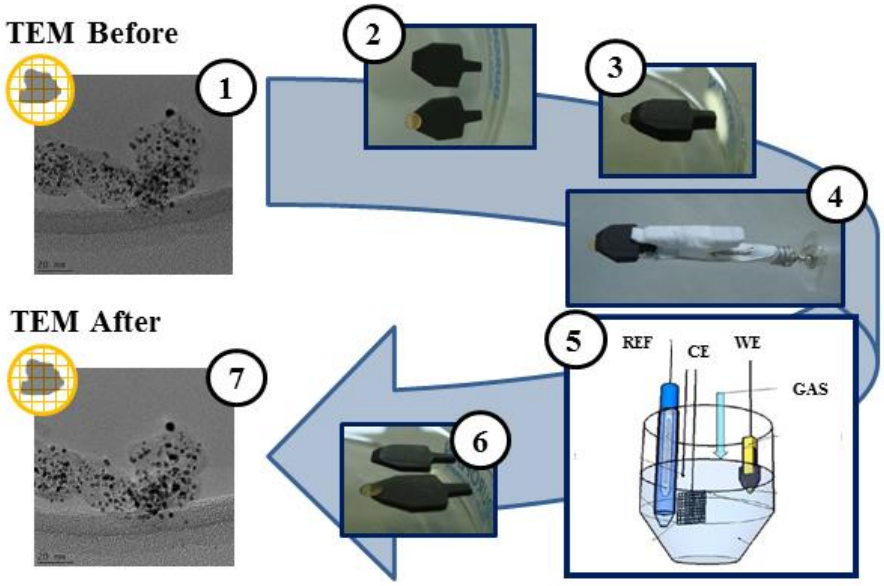

Figure II - 4. Sequence for IL-TEM experiments: 1) Deposition of the electrocatalyst suspension and TEM observation, 2 and 3) Clamping TEM grid between carbon plates 4) Fixation of the carbon plates with working-electrode contact 5) Electrochemical tests 6) Disassembling of the carbon plates 7) Observation of the same locations as in step 1.

c. Field-Emission Gun-Scanning Electron Microscopy (FEG-SEM)

In SEM, a finely focused electron beam is scanned over a conducting sample with the help of deflector coils. The interaction of the focused beam with the surface of the sample creates different signals among of which are: (*i*) secondary electrons (SE) (*ii*) backscattered electrons (BSE) (*iii*) characteristic X-rays and (*iv*) fluorescence X-rays. The signals used to form images are the secondary electrons and the backscattered electrons. Secondary electrons are sensitive to the topographical contrast given by the shape and morphology of the surface of the sample; while backscattered electrons provide compositional contrast due to the difference in the intensity of the signal with the atomic number of the scanned area (regions of high atomic number will be brighter relative to regions of low atomic number).

FEG-SEM images were obtained on a Zeiss Ultra 55 microscope designed to maximize the image resolution at low beam energies. In contrast to the V-shaped filaments made of tungsten (W) or lanthanum hexaboride (LaB_6), the FEG allows the production of an electron beam that is smaller in diameter resulting in an improved signal-to-noise ratio and spatial resolution. The Ultra 55 is equipped with a secondary electron detector inside the lens (in-lens detector) and a backscattered electron detector. Both are engineered to image electrons at low accelerating voltage (less than 5 kV). The samples consisted of circular or

square zones cut fresh/aged active layers of MEAs. The measurement of the component thickness was done by integrating the overall thickness of the electrodes or membrane with ImageJ® freeware.

2.8.2 Chemical techniques

a. Raman spectroscopy

Raman spectroscopy is a non-destructive technique used to identify the chemical composition, characterize the molecular structure and quantify the elements present in a material. Raman spectroscopy is a very versatile technique: it requires minimal sample preparation, allows the characterization of materials in different phases (solid, liquid or gases), pure chemical elements or solutions, and is used in several fields of research from pharmaceutics [10], medicine [11] and characterization of carbon materials [12-14], among others.

During Raman spectroscopy measurements, the sample is irradiated with monochromatic light, which produces reflected, adsorbed and scattered radiation (Raman scatter) of different wavelengths. The scattered phonons provide information on the vibrational modes, chemical and structural nature of the material. A Raman spectrum is a plot of the intensity of Raman scattered radiation as a function of its frequency difference from the incident radiation (usually in units of wavenumbers, cm^{-1}), featuring characteristic peaks that are specific of molecular bonds.

Raman spectroscopy was used to examine the structure of the fresh/aged carbon supports. The Raman spectra were recorded *ex situ* using either a Renishaw RM1000 or a Renishaw In-Via spectrometer. The Raman spectra were obtained by excitation with the radiation from an argon LASER (514 nm) operated at approximately 5 mW. The detector was a Peltier-cooled charge coupled device camera (CCD) and the spectral resolution was about 1 cm^{-1}. The measurements were performed with a x 50 ULWD objective and a 100 µm confocal aperture for both the sample illumination and collection of the scattered photons. For the sake of comparison between the samples, the Raman spectra of the Pt/C electrocatalysts were normalized by the intensity of the peak at *ca*. 1600 cm^{-1}, which corresponds to the band of the graphitic lattice. Curve fitting for the determination of spectral parameters was performed with the software LabSpec. An accurate fitting of the Raman spectra considers the presence of 5 bands (Table II - 1).

Table II - 1. Vibration modes observed on high surface area carbon supports with Raman spectroscopy.

Band	Raman Shift	Vibration Mode
G	*ca.* 1585 cm^{-1}	Ideal graphitic lattice
D1	*ca.* 1350 cm^{-1}	Disordered graphitic lattice-graphene layer edge
D2	*ca.* 1610 cm^{-1}	Disordered graphitic lattice – surface graphene layer
D3	*ca.* 1495 cm^{-1}	Amorphous carbon
D4	*ca.* 1190 cm^{-1}	Polyenes, ionic impurities

The changes in structure of the carbon support were followed by the evolution of the mean crystallite size of the carbon particles, obtained with the Knight and White formula [15]:

$$L_a \text{ (nm)} = 4.4 \times (I_{D1}/I_G)^{-1} \quad \text{(Eq. II - 3)}$$

b. X-ray Photoelectron Spectroscopy (XPS)

XPS allows determining the elemental composition, the chemical state and the electronic state of the top-most surface layers of a material (1-10 nm) [16]. XPS experiments are carried out in an ultra-high vacuum (UHV) chamber and the technique is based in the irradiation of the sample surface with a beam of X-rays, inducing the ejection of electrons due to the photoelectric effect. The kinetic energy of the ejected photoelectrons is measured, amplified and the spectrum is acquired. The fundamental relation of XPS is:

$$E_b = hv - E_k - e^{\Phi} \quad \text{(Eq. II - 4)}$$

where E_b is the binding energy of an electron, hv is the X-ray excitation energy, E_k the kinetic energy measured, e^{Φ} the work function of the spectrometer. Since each element has an individual set of binding energies, it is possible to identify the composition of the material surface. The spectrum represents the number of electrons detected as a function of their binding energy, and only those who escape without energy loss contribute to the characteristic peaks. This puts in evidence why XPS is extremely sensitive to the outer-most atomic layers of the surface of a material. X-ray photoelectron spectroscopy proved to be a precious tool to characterize the oxidation state of Pt/C electrocatalysts at different states of ageing.

In XPS experiments, electrodes were prepared as for electrochemical experiments *i.e.* the electrocatalyst was deposited onto a home-made RDE made of glassy carbon tip (Sigradur, 0.196 cm^2) and Teflon®. This tip was then removed from the RDE, fixed onto a molyblock and introduced into the XPS chamber within one hour after the end of the AST. The XPS patterns were obtained on a XR3E2 spectrometer (Vacuum Generator) equipped with an Mg Kα (1253.6 eV) X-ray source powered at 300 W (15 kV – 20 mA). The kinetic energies of the photoelectrons were measured using a hemispherical electron analyser working in the constant pass energy mode (30.0 eV). The background pressure in the analysis chamber was kept below 10^{-9} - 10^{-10} mbar during data acquisition. The XPS data signals were taken in increments of 0.1 eV with dwelling times of 50 ms. Analyses were carried out at an angle 90° between the sample surface and the analyser. High resolution spectra envelopes were obtained by curve fitting of the XPS multiplex peaks using the software "Avantage" from ThermoScientific. Symmetric Gaussian–Lorentzian (90:10) product functions were used to approximate the line shapes of the fitting components with Shirley background corrections. The full width at half maximum of the XPS envelopes was arbitrarily fixed at 1.7 ± 0.1 eV. To correct for any charging effect, all the binding energies were referenced to the graphene component (C-C) of the carbon C1s peak at 284.3 eV. The evolution of the oxygen content during the AST was monitored by dividing the peak areas of the O1s and the C1s signal (without the contribution of Nafion®-related envelopes), after proper background subtraction, by their respective atomic sensitivity factors:

$$\text{Ratio (O1s/C1s)} = \frac{I_{O1s}}{0.63} X \frac{0.205}{I_{C1s}} \qquad \text{(Eq. II - 5)}$$

2.8.3 Electrochemical techniques

a. Cyclic Voltammetry (CV)

Cyclic voltammetry was employed to study redox reactions occurring at the surface of the working electrode [17, 18]. In cyclic voltammograms (CVs), the electrode potential (E) is swept linearly with time between two potential limits (E_1 and E_2), while recording the current variation (I). The ratio potential/time defines the scan rate (V s^{-1}), and is chosen according to the kinetics of the electrochemical reaction in study. Two types of contributions are responsible for a variation of the current variation in a CV: (*i*) a faradaic contribution arising

from charge transfer at the working electrode surface and (*ii*) a capacitive contribution, which is caused by accumulation (or removal) of species at the electrode/electrolyte interface.

Due to the strong surface sensitivity of H, and O chemisorption and CO_{ads} monolayer electrooxidation on Pt, CVs provide information on the crystalline orientation, the mean nanoparticle size and the degree of agglomeration of the pristine and aged PEMFC electrocatalysts. Figure II - 5a shows a characteristic cyclic voltammogram of the 40 wt. % Pt/HSAC electrocatalyst measured in 0.1 M H_2SO_4 at T = 330 K. In the potential region 0.05 V < E < 0.40 V vs RHE, the adsorption/desorption of protons proceeds onto/from Pt nanoparticles. The number and the intensity of peaks in this potential region are related to the crystalline orientation and the texture of the Pt nanoparticles. For example, the peaks located at E = 0.22 – 0.28 V *vs*. RHE are ascribed to the adsorption/desorption of H on/from Pt(100) and Pt(111) sites [19]. Therefore, an increase of the intensity of the under-potentially deposited H peaks is indicative of larger terraces (larger Pt nanoparticles). In the potential region 0.4 V < E < 0.70 V *vs* RHE, pseudo capacitive currents associated with the carbon support are observed. At E > 0.85 V *vs* RHE, water molecules are dissociated on Pt, yielding the formation of surface oxides [20], and their reduction in the cathodic scan at ~ 0.80 V *vs* RHE. The position of the reduction peak of Pt oxides strongly depends on the size distribution of the Pt nanoparticles [21] and its change in shape/intensity during an AST provides information on the mean particle size/degree of agglomeration of the Pt/C nanoparticles.

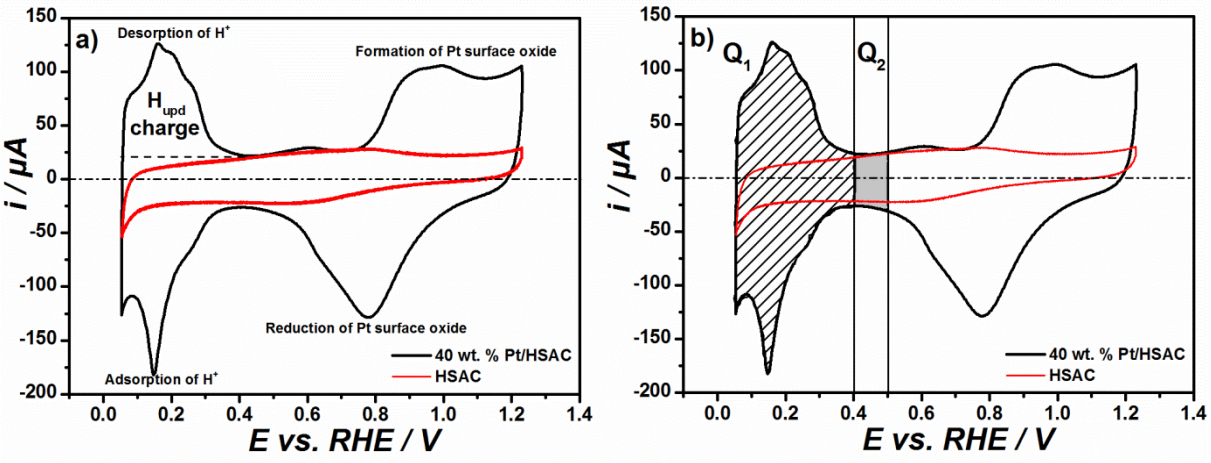

Figure II - 5. a) Characteristic voltammogram of a 40 wt. % Pt/HSAC electrocatalyst and HSAC support b) Integration of H adsorption/desorption charge (Q_1) and capacitive charge of the HSAC support (Q_2) to obtain the correct value of Q_H. Electrolyte: 0.1 M H_2SO_4; v = 0.020 V s^{-1}; T = 330 K.

The ECSA of the Pt/C nanoparticles can be accessed electrochemically by integrating the coulometry required to desorb under-potentially deposited hydrogen ($Q_{H,des}$) or oxidize a monolayer of CO (Q_{CO}). When using $Q_{H,des}$ (**Chapter III sub-chapter 3.6**), if the pseudo-capacitive contribution of the Pt/C nanoparticles is assumed to follow a straight line (Figure II - 5a), the $Q_{H,des}$ will be under-estimated. Indeed, the "straight-line" profile does not reflect the shape of the CVs measured onto high surface area carbon supports (in particular the pronounced current decrease below 0.20 V *vs.* RHE). To correctly calculate the $Q_{H,des}$ the charges corresponding to the absorption/desorption of hydrogen (Q_1 in Figure II - 5b) and the capacitive charge of the HSAC support (Q_2 in Figure II - 5b) were calculated and the value of Q_H is obtained with the relation:

$$Q_H - 3{,}5 \times Q_2 = 2Q_H \qquad \text{(Eq. II – 6)}$$

$$Q_{H,des} = 2Q_H/2 \qquad \text{(Eq. II - 7)}$$

Assuming a charge density of 210 μC cm^{-2} to adsorb/desorb a saturated monolayer of adsorbed H, the ECSA can be obtained by the formula:

$$\mathrm{ECSA_H} = \frac{\mathrm{Q_{H,des}}}{210} \qquad \text{(Eq. II - 8)}$$

The cyclic voltammograms also provide information about the changes of the structure and the surface chemistry (development of quinone/hydroquinone peak, increase in the double layer capacitance) of the carbon supports. Figure II - 6a displays the characteristic CV profiles of Pt nanoparticles loaded onto different carbon supports - a high surface area carbon support (*S*c ~ 800 $m^2\ g^{-1}$), Vulcan XC72 (*S*c ~ 250 $m^2\ g^{-1}$) and a reinforced graphite (*S*c ~ 110 $m^2\ g^{-1}$) - but featuring identical Pt weight percentage. It is clear that the current measured in the potential region 0.40 < *E* < 0.70 V *vs*. RHE is essentially determined by the type of carbon support, higher currents being monitored on carbon support featuring high specific surface area.

The changes of the CV profile during an AST (in this case a potentiostatic polarization at E_{AST} = 1.30 V *vs.* RHE during 24 h in 0.1 M H_2SO_4 at *T* = 330 K) are shown in Figure II - 6b. In parallel with the decrease of the ECSA (decrease of the H_{upd} charge), an increase of the electrochemical charge (hatched area) is observed in the potential region 0.40 V < *E* < 0.80 V

vs. RHE compared to the fresh Pt/HSAC electrocatalyst. This signs (*i*) changes of the double layer capacitance most likely due to the increasing porosity of the carbon support and (*ii*) the formation of carbon surface oxides (CO_{surf}) such as quinone – hydroquinone surface groups (Q/HQ). Only Q/HQ carbon surface oxide groups are assumed to be electrochemically active in the region 0.40 V < *E* < 0.80 V *vs.* RHE, and to give a redox peak centred at *ca*. 0.60 V *vs.* RHE [22].

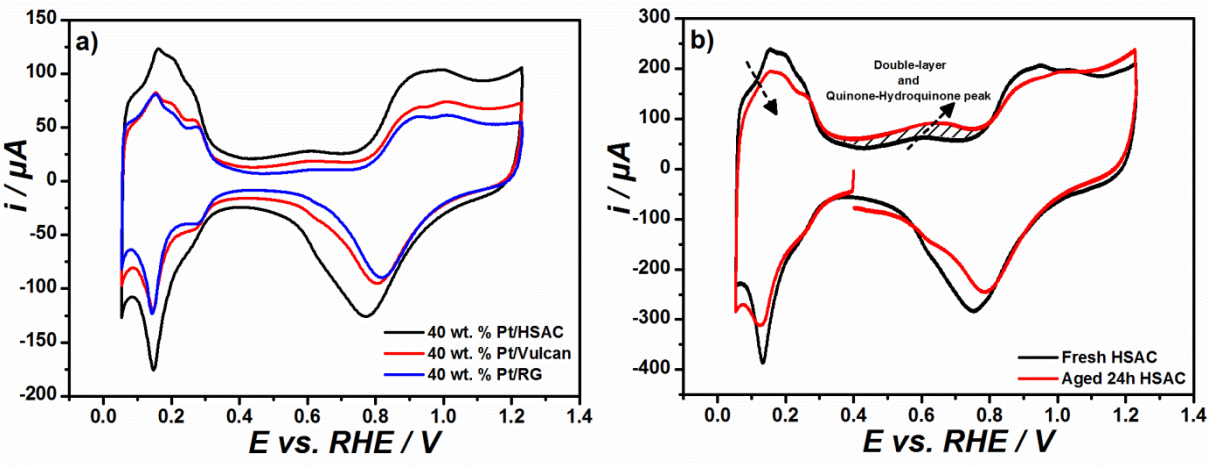

Figure II - 6. Characteristic voltammogram of different Pt/C 40 wt. % electrocatalysts supported on different carbon supports b) Change of the CV profile after polarization at E = 1.3 V vs. RHE during 24 h .Electrolyte: 0.1 M H_2SO_4; v = 0.020 V s-1; T = 330 K.

To calculate the charges over the Q/HQ peak, in this PhD thesis a straight-line is subtracted between 0.40 V < *E* < 0.77 V *vs.* RHE and the Q/HQ oxidation charge is integrated. In **Chapter IV** a comparison with another method presented in the literature is presented, which measures the oxidation current at the Q/HQ peak at *E* = 0.55 V [23].

b. CO_{ad} stripping voltammograms

The CO_{ad} stripping is a widely used method to accurately measure the ECSA of Pt nanoparticles. In the present work, the saturation coverage of the Pt nanoparticles was firstly established by bubbling CO for 6 min in the electrolyte. Then, to eliminate the excess CO that was not adsorbed, the electrolyte was purged with Ar for 45 min, while keeping the electrode potential at *E* = 0.10 V *vs.* RHE. The value of potential has to be sufficiently low to allow the adsorption of CO molecules on the surface of Pt nanoparticles and significantly below the onset potential of carbon monoxide oxidation. A classical CO_{ad} stripping procedure consists in performing three cyclic voltammograms at *v* =100 mV s^{-1} between 0.05 and 1.23 V *vs.* RHE (see Figure II - 7). The first CO_{ad} stripping voltammogram displays a marked peak

associated with the oxidation of adsorbed CO, and the two following cycles serve as baseline for integration of the main stripping peak (Q_{CO}) and to confirm that the electrolyte has been correctly purged from dissolved CO. The CO_{ad} stripping was used in **Chapter III** and **IV** to calculate the initial ECSA and **Chapter III sub-chapter 3.5** for the intermediate characterizations.

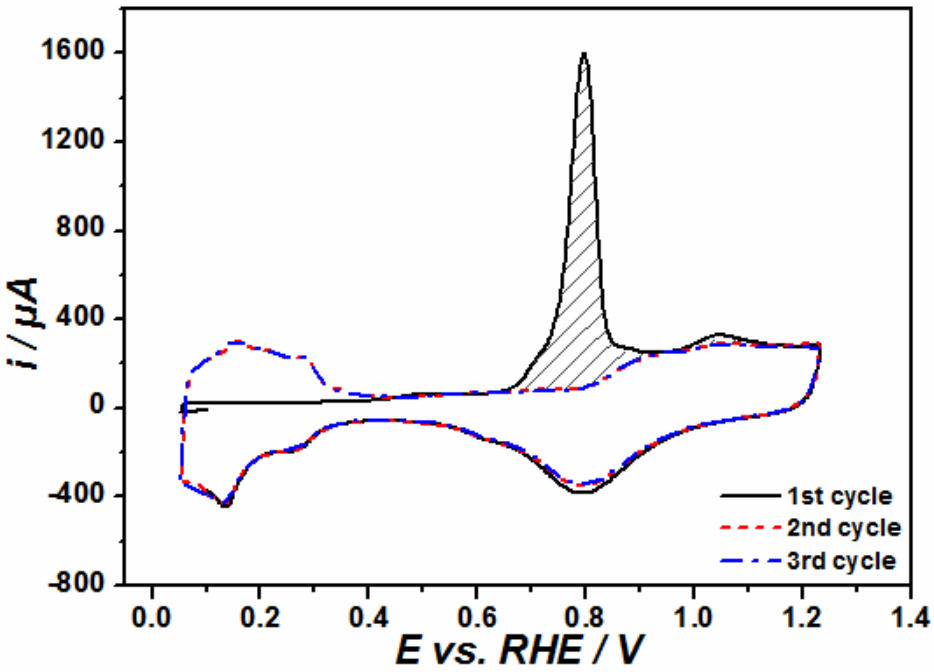

Figure II - 7. COad stripping voltammograms: 1st, 2nd and 3rd cycle. Electrolyte: 0.1 M H2SO4; v = 0.100 V s-1; T = 330 K.

Considering that all Pt nanoparticles are covered with adsorbed CO molecules in a-top configuration, the oxidation charge is proportional to the number of Pt surface atoms. For the calculation of the ECSA, the third cycle was subtracted to the first one and it was assumed that the electrooxidation of an adsorbed CO monolayer requires a charge density of 420 μC per cm^2 of Pt, resulting in:

$$\mathrm{ECSA_{CO}} = \frac{\mathrm{Q_{CO}}}{420} \qquad \text{(Eq. II - 9)}$$

In addition, the electrochemical oxidation of carbon monoxide (CO) on Pt is highly sensitive to the structure of the surface. Previous studies in the field have unveiled the non-monotonic dependence of the main electrooxidation peak on the size distribution (position and shape of the main CO_{ad} stripping peak) and the degree of agglomeration (presence of a

CO_{ad} pre-oxidation peak) of the Pt nanoparticles. These fingerprints were also used to gain some insights on the Pt/C degradation mechanisms [21, 24-27].

c. Pseudo CO_{ad} stripping voltammograms

The effect of oxidizing, reducing or neutral molecules present in the electrolyte molecules on the degradation mechanism of Pt/C nanoparticles has recently been pointed out. Dubau *et al.* [28] underlined that dissolved gases have an effect on the preferential degradation mechanism at work. Whereas minor changes of the Pt/C nanoparticles were detected after an AST under neutral atmosphere (Ar), the migration/aggregation of Pt nanocrystallites was strongly accelerated in the presence of a reducing atmosphere, such as CO. Carbon corrosion and Pt nanoparticle detachment were more frequently observed under oxidizing atmosphere (O_2). In a similar study, Topalov *et al.* [29] showed that adsorbed CO molecules delay surface oxide formation on Pt, and hence the amount of dissolved Pt during an AST. To gain further insights on the effect of carbon monoxide, "pseudo" CO_{ad} stripping experiments were realised. In this procedure, the exactly same steps as for a real CO_{ad} stripping are performed but Ar is used instead of CO.

References

[1] C.C. Herrmann, G.G. Perrault, A.A. Pilla, Dual reference electrode for electrochemical pulse studies, Anal. Chem., 40 (1968) 1173-1174.
[2] Y. Garsany, O.A. Baturina, K.E. Swider-Lyons, S.S. Kocha, Experimental methods for quantifying the activity of platinum electrocatalysts for the oxygen reduction reaction, Anal. Chem., 82 (2010) 6321-6328.
[3] Z. Zhao, L. Castanheira, L. Dubau, G. Berthomé, A. Crisci, F. Maillard, Carbon corrosion and platinum nanoparticles ripening under open circuit potential conditions, J. Power Sources, 230 (2013) 236-243.
[4] A. Ohma, K. Shinohara, A. Iiyama, T. Yoshida, A. Daimaru, Membrane and catalyst performance targets for automotive fuel cells by FCCJ membrane, catalyst, MEA WG, ECS Trans., 41 (2011) 775-784.
[5] M. Chatenet, L. Guétaz, F. Maillard, Electron microscopy to study MEA materials and structure degradation, in: W. Vielstich, H. Yokokawa, H.A. Gasteiger (Eds.) Handbook of Fuel Cells, John Wiley & Sons, Ltd., New York, 2009, pp. 844-860.
[6] B. Vion-Dury, Mécanismes de vieillissement des électrocatalyseurs de pile à combustible de type PEMFC, Grenoble INP, Grenoble INP, 2011.
[7] L. Dubau, J. Durst, F. Maillard, M. Chatenet, L. Guétaz, J. André, E. Rossinot, Heterogeneities of aging within a PEMFC MEA, Fuel Cells, 12 (2012) 188-198.
[8] K.J.J. Mayrhofer, S.J. Ashton, J.C. Meier, G.K.H. Wiberg, M. Hanzlik, M. Arenz, Non-destructive transmission electron microscopy study of catalyst degradation under electrochemical treatment, J. Power Sources, 185 (2008) 734-739.
[9] K. Schlögl, K.J.J. Mayrhofer, M. Hanzlik, M. Arenz, Identical-location TEM investigations of Pt/C electrocatalyst degradation at elevated temperatures, J. Electroanal. Chem., 662 (2011) 355-360.
[10] S. Wartewig, R.H.H. Neubert, Pharmaceutical applications of Mid-IR and Raman spectroscopy, Advanced Drug Delivery Reviews, 57 (2005) 1144-1170.
[11] E.B. Hanlon, R. Manoharan, T.W. Koo, K.E. Shafer, J.T. Motz, M. Fitzmaurice, J.R. Kramer, I. Itzkan, R.R. Dasari, M.S. Feld, Prospects for in vivo Raman spectroscopy, Phys. Med. Biol., 45 (2000) R1.
[12] A.C. Ferrari, J. Robertson, Interpretation of Raman spectra of disordered and amorphous carbon, Phys. Rev. B, 61 (2000) 14095-14107.
[13] M.S. Dresselhaus, G. Dresselhaus, R. Saito, A. Jorio, Raman spectroscopy of carbon nanotubes, Phys. Rep., 409 (2005) 47-99.
[14] M.A. Pimenta, G. Dresselhaus, M.S. Dresselhaus, L.G. Cancado, A. Jorio, R. Saito, Studying disorder in graphite-based systems by Raman spectroscopy, Phys. Chem. Chem. Phys., 9 (2007) 1276-1290.
[15] D.S. Knight, W.B. White, Characterization of diamond films by Raman spectroscopy, J. Mater. Res., 4 (1989) 385-393.
[16] J.C.R.S. Myrha, Handbook of surface and interface analasys: Methods for problem-solving, CRC Press2009.
[17] A.J.B.L.R. Faulkner, Electrochemical methods: Fundamentals and applications, John Wiley & Sons Inc.2000.
[18] G.Z. Cynthia, Handbook of electrochemistry, Elsevier, Amsterdam, 2007.
[19] N.M. Marković, B.N. Grgur, P.N. Ross, Temperature-dependent hydrogen electrochemistry on platinum low-index single-crystal surfaces in acid solutions, J. Phys. Chem. B, 101 (1997) 5405-5413.
[20] G. Jerkiewicz, G. Vatankhah, J. Lessard, M.P. Soriaga, Y.-S. Park, Surface-oxide growth at platinum electrodes in aqueous H2SO4: Reexamination of its mechanism through combined cyclic-voltammetry, electrochemical quartz-crystal nanobalance, and Auger electron spectroscopy measurements, Electrochim. Acta, 49 (2004) 1451-1459.
[21] F. Maillard, S. Schreier, M. Hanzlik, E.R. Savinova, S. Weinkauf, U. Stimming, Influence of particle agglomeration on the catalytic activity of carbon-supported Pt nanoparticles in CO monolayer oxidation, Phys. Chem. Chem. Phys., 7 (2005) 385-393.
[22] K. Kinoshita, Carbon: Electrochemical and physicochemical properties, John Wiley & Sons, New York, 1988.

[23] Y.-C. Park, K. Kakinuma, M. Uchida, H. Uchida, M. Watanabe, Deleterious effects of interim cyclic voltammetry on Pt/carbon black catalyst degradation during start-up/shutdown cycling evaluation, Electrochimica Acta, 123 (2014) 84-92.
[24] F. Maillard, M. Eikerling, O.V. Cherstiouk, S. Schreier, E. Savinova, U. Stimming, Size effects on reactivity of Pt nanoparticles in CO monolayer oxidation: The role of surface mobility, Faraday Discuss., 125 (2004) 357-377.
[25] F. Maillard, E.R. Savinova, P.A. Simonov, V.I. Zaikovskii, U. Stimming, Infrared spectroscopic study of CO adsorption and electro-oxidation on carbon-supported Pt nanoparticles: Interparticle versus intraparticle heterogeneity, J. Phys. Chem. B, 108 (2004) 17893-17904.
[26] K.J.J. Mayrhofer, M. Arenz, B.B. Blizanac, V. Stamenkovic, P.N. Ross, N.M. Markovic, CO surface electrochemistry on Pt-nanoparticles: A selective review, Electrochim. Acta, 50 (2005) 5144-5154.
[27] P. Urchaga, S. Baranton, C. Coutanceau, G. Jerkiewicz, Electro-oxidation of COchem on Pt nanosurfaces: Solution of the peak multiplicity puzzle, Langmuir, 28 (2011) 3658-3663.
[28] L. Dubau, L. Castanheira, G. Berthomé, F. Maillard, An identical-location transmission electron microscopy study on the degradation of Pt/C nanoparticles under oxidizing, reducing and neutral atmosphere, Electrochim. Acta, 110 (2013) 273-281.
[29] A.A. Topalov, A.R. Zeradjanin, S. Cherevko, K.J.J. Mayrhofer, The impact of dissolved reactive gases on platinum dissolution in acidic media, Electrochem. Com., 40 (2014) 49-53.

Chapter III.

From Pt/C electrocatalysts suspensions to accelerated stress tests

Parts of the results discussed in this chapter have been published in:

Z. Zhao, **L. Castanheira**, L. Dubau, G. Berthomé, A. Crisci, F. Maillard
Carbon corrosion and platinum nanoparticles ripening under open circuit potential conditions
Journal of Power Sources 230 (2013) 236 – 243. DOI: 10.1016/j.jpowsour.2012.12.053

The contribution of the author of this thesis includes the part of the experimental part (preparation of the catalytic layers for Raman and XPS, preparation and measurements of the properties of the catalytic layers in EC-FTIR), the treatment and the analysis of the Raman and X-ray photoelectron spectroscopy data and the preparation of the manuscript for the publication.

L. Castanheira, L. Dubau, F. Maillard
Accelerated Stress Tests of Pt/HSAC Electrocatalysts: an Identical-Location Transmission Electron Microscopy Study on the Influence of Intermediate Characterizations
Electrocatalysis 5 (2) (2014) 125 – 135. DOI: 10.1007/s12678-013-0173-y

The contribution of the author of this thesis includes the entirety of the experimental part (preparation and measurements of the properties of the catalytic layers and IL-TEM setup), the treatment and the analysis of the Transmission Electron Microscopy and Raman spectroscopy data and the preparation of the manuscript for the publication.

3.1 Introductory note to Raman spectroscopy of carbon materials and accelerated stress tests protocols

In 1969, F. Tuinstra and J. L. Koenig reported the Raman spectra of graphite and graphite-like materials [1]. The Raman spectrum of graphite single crystal presented a single band centred at $\overline{\upsilon} \sim 1575$ cm^{-1} (G-band, assigned to ordered graphite domains) while graphite-like materials featured a second band centred at $\overline{\upsilon} \sim 1350$ cm^{-1} (D1-band, assigned to defects in graphite domains, also referred to as D or D'-band in some publications, see Figure III - 1 a) to d)). The intensity of the D1-band increased with (*i*) an increase of the structural disorder of the carbon material and with (*ii*) a decrease of the graphite crystallite size. Tuinstra and Koenig evidenced that the ratio between the intensities of the D1 and G-bands (I_D/I_G) is linearly proportional to the inverse of the carbon crystallite size L_a. Later on, Nakamizo *et al.* [2, 3] provided evidence of the appearance of another band centred at $\overline{\upsilon} \sim 1620$ cm^{-1} (D2-band, assigned to disordered graphitic lattice – surface graphene defects) on natural graphite subjected to grinding and air-oxidation (Figure III - 1e)). The sensitivity of the frequency, the shape and the relative intensities of the Raman bands to the structure of carbon materials make Raman spectroscopy a powerful technique for their characterization.

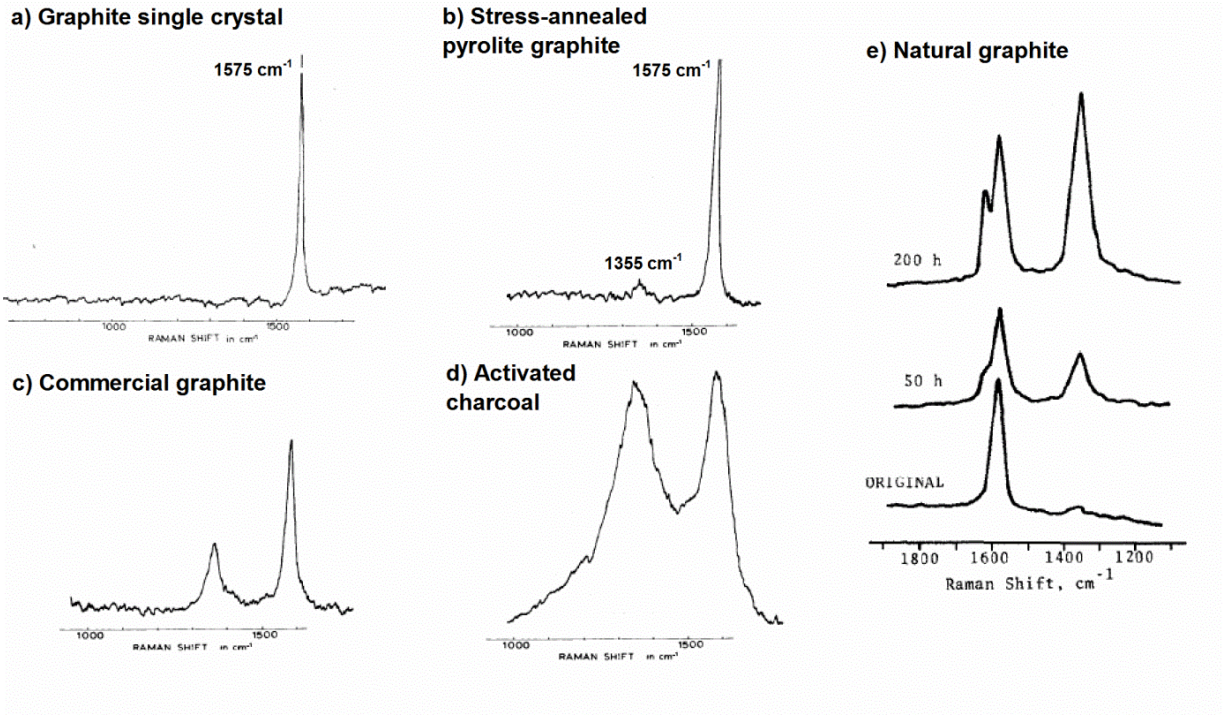

Figure III - 1. Raman spectrum of a) graphite single crystal, b) stress-annealed pyrolite graphite, c) commercial graphite, d) activated charcoal and e) effect of grinding of natural graphite. a), b), c) and d) reprinted from [1] and e) reprinted from [2].

More recently, Cançado [4, 5] bridged the G and D-band features to the structure of the carbon materials. Figure III - 2 shows two confocal Raman images of a highly-oriented pyrolytic graphite (HOPG) crystallite deposited onto a glass substrate. Two Raman spectra were recorded: one at the interior (spot 1) and another one at the edge of the crystallite (spot 2) (Figure III - 2 c)). It is explicit that the G-band intensity originates from the surface of the graphite crystallite while the D-band intensity results from its edge. This is best illustrated in Figure III - 2 a) and Figure III - 2 b), which plot the spatial dependence of the G-band and the D-band intensity, respectively.

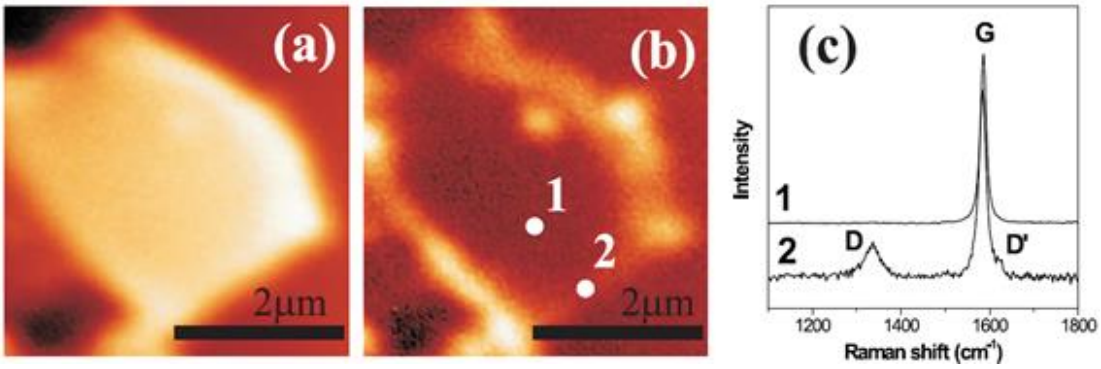

Figure III - 2. Confocal (600 nm resolution) Raman images of an HOPG crystallite deposited on a glass substrate: a) G-band intensity and b) D-band intensity. c) Raman spectra of spot 1 and 2 (white circles in b)). Reprinted from [4].

By measuring the Raman spectra of various graphitic materials, Knight and White [6] established an empirical formula, which allowed for the calculation of the in-plane crystallite size (L_a). The formula is based on the I_D/I_G ratio but is only valid for Raman spectra recorded with a laser wavelength of λ = 514.5 nm (E_l = 2.41 eV), since the position and the intensity of the D1-band depend on the excitation laser energy (E_l) [7-9]. Since that, the I_D/I_G ratio is a useful tool to characterize the graphitic character of carbon materials [10, 11]. However, the validity of the Knight and White formula for amorphous carbons, the spectra fitting parameters [12-17] and a possible generalization of the empirical formula for all excitation laser energies [18] are still debated. In this work, the Raman measurements were performed with an excitation laser energy of E_l = 2.41 eV (λ = 514.5 nm), in agreement with the conditions of the Knight and White formula. Five bands were considered to fit the Raman spectra [15] (Figure III - 3): the D1 and the G-band at $\bar{\upsilon}$ ~ 1350 cm^{-1} and $\bar{\upsilon}$ ~ 1585 cm^{-1}, respectively, the D2-band (at $\bar{\upsilon}$ ~ 1610 cm^{-1}) which is assigned to the defects present in the surface of the graphite crystallites, the D3-band (at $\bar{\upsilon}$ ~ 1495 cm^{-1}) and the D4-band (at $\bar{\upsilon}$ ~ 1190 cm^{-1}), which are ascribed to maxima in the vibrational density of states or to polyenes and ionic impurities present in carbon blacks (see **Chapter II table II- 3**). Such a fitting is of

great interest to understand the structural changes of model carbon supports having well-defined structure. However, the reader must be aware that the high incertitude associated with the deconvolution of the Raman spectra into five bands is poorly useful for disordered HSAC supports. Consequently, in what follows, only the variations in intensity/shape for the D1, the D2 and the G-band, which dominate the Raman spectra, will be discussed.

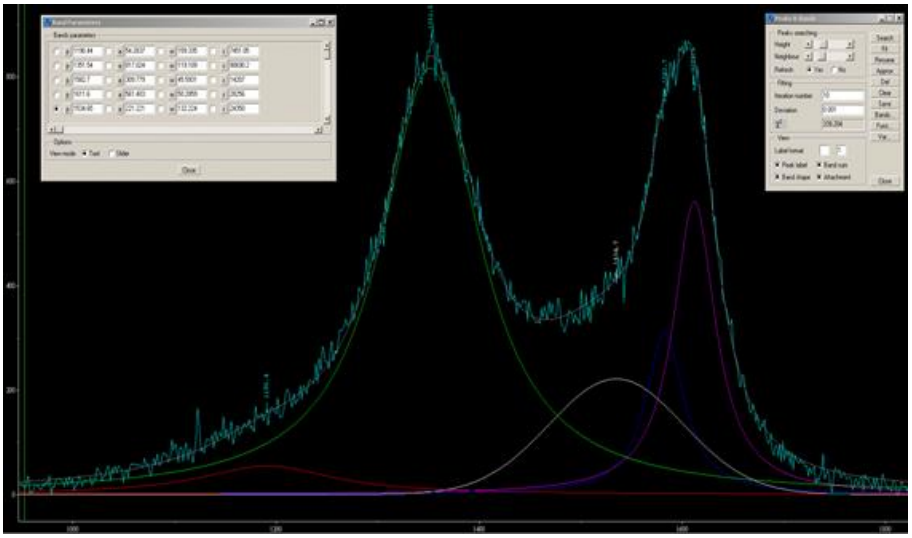

Figure III - 3. Example of curve fitting based in the combination of bands given in **Chapter II Table II- 3.**

As reviewed in **Chapter I**, cost and durability of the catalytic materials are the major issues to be overcome for the widespread commercialization of PEMFC systems. The current R&D programs worldwide focus on finding cheaper and more robust carbon materials. To test their ability to withstand the harsh PEMFC operating conditions, long-term durability tests are the "ideal case". However, operating a PEMFC during thousands of hours inside a laboratory is time and cost consuming. To bypass these tests, accelerated stress tests (ASTs) are commonly employed. Different organizations such as the American Department of Energy (DoE) and the Fuel Cell Commercialization Conference of Japan (FCCJ) have their own AST protocols [19, 20]. In the "Electrocatalyst Cycle and Metrics" test from the American DOE, a 30,000 triangle sweep cycle between 0.6 V – 1.0 V *vs.* RHE is used. A polarization curve is performed after 1,000 / 5,000 / 10,000 / 30,000 cycles and cyclic voltammograms (CV*s.*) are recorded every 10 / 100 / 1,000 / 3,000 / 10,000 / 20,000 / 30,000 cycles to monitor changes in ECSA and ORR catalytic activity. In the "Catalyst Support Cycle and Metrics" test from the American DOE, which consists in a potentiostatic hold at E = 1.2 V for t = 400 h in a 25-50 cm² single cell, a polarization curve and a CV are recorded every 24 h. The Japanese FCCJ mimics start/stop cycles by a triangular wave potential cycle between 1.0 V – 1.5 V *vs.* RHE,

and load cycles by a potentiostatic square-wave pulse with a repeating pattern of 3 s at 0.6 V *vs.* RHE followed by another pattern of 3 s at 1.0 V *vs.* RHE. CVs and polarization curves are recorded every 10 to 1,000 cycles. In these ASTs, the evolution of the ECSA is the main descriptor of the catalyst's stability but the variation of the charge ascribed to the quinone/hydroquinone (Q/HQ) redox couple is also monitored [21-24] if different carbon supports are evaluated.

These intermediate characterizations are considered to contribute only a minor part to the ageing of the Pt/C electrocatalysts. However, since degradation processes are sensitive to the potential modulation mode (potential cycling *vs.* potential holding) [25, 26] and the potential range [26, 27], the ECSA and the Q/HQ variations are likely to be influenced by these intermediate characterizations. Similarly, it should be remarked that electrochemical measurements with Pt/C electrocatalysts involve the prior preparation of a suspension composed of Pt/C, solid ionomer and water in flasks into which air can permeate. In these conditions, local galvanic cells are likely to develop: the carbon support may be oxidized (anode) and the oxygen from the air reduced at the Pt surface (cathode). In consequence, the quantity of Nafion® ionomer (used as binder in the catalyst suspension), the Pt mass-fraction and the age of the suspension are believed to be important parameters, which may influence the long-term stability of the Pt/C electrocatalysts.

These issues are those that we want to address in this chapter. Firstly, Pt nanoparticles with nearly constant mean particle size supported on carbon supports featuring different structure/chemistry will be characterized by physical and chemical techniques. Secondly, we will investigate how the preparation of the catalyst suspension and the characterization protocols affect these properties. The surface chemistry of the Pt/C electrocatalysts will be monitored by X-ray photoelectron spectroscopy and the effect of Nafion® ionomer will be discussed. Thirdly, the effect of the storage of Pt/C suspensions will be investigated. Finally, the influence the number of intermediate electrochemical characterizations, the gas atmosphere and the upper potential limit used in ASTs will be quantified.

3.2 Structural properties of carbon supports

As previously discussed in Chapter I, the structural parameters (L_a, L_c and d_{002}), the specific surface area, the pore volume and the surface chemistry of the carbon support exert strong influence on its oxidation kinetics. Some of these characteristics were determined by

physico-chemical techniques such as Raman spectroscopy, Brunauer-Emett-Teller (BET) surface area and porosity measurements, transmission electron microscopy (TEM) and X-ray photoelectron spectroscopy (XPS) for the studied Pt/C electrocatalysts.

Figure III - 4 and Table III - 1 display the normalized Raman spectra of the different carbon supports evaluated and their respective mean crystallite size (L_a, determined from the Knight and White formula) as well as some or their textural and sub-structural properties.

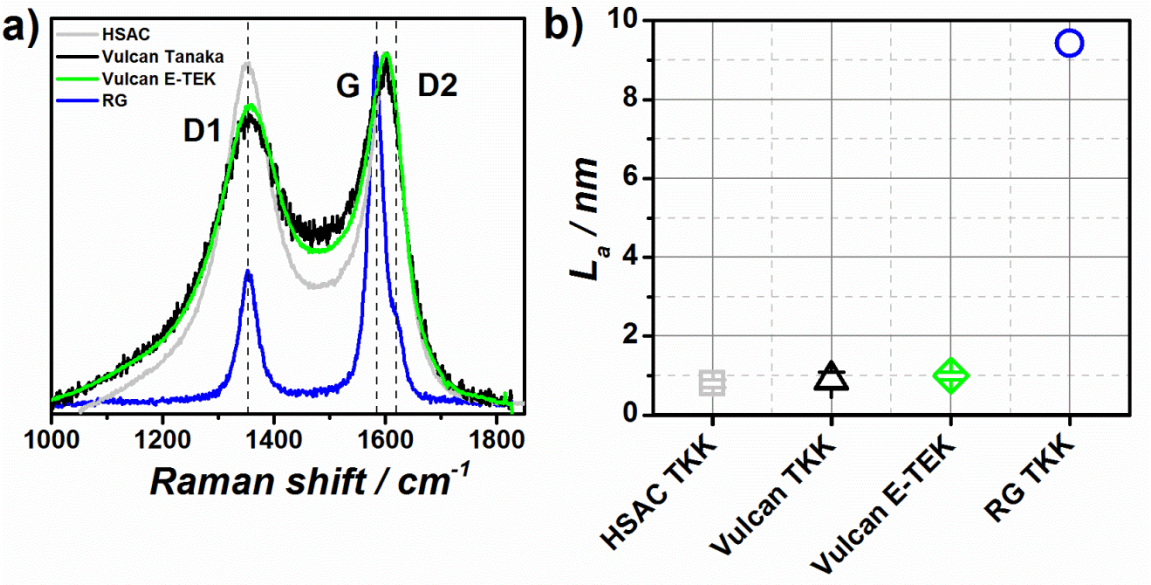

Figure III - 4. a) Normalized Raman spectra of HSAC TKK, Vulcan TKK and reinforced graphite (RG) carbon supports b) carbon mean crystallite size (L_a) determined using the Knight and White formula.

The vibrational band appearing at *ca*. 1350 cm^{-1}, namely the D1-band, is assigned to amorphous carbon domains and edge-defects of the graphite crystallites, and the G-band at *ca* 1585 cm^{-1} is ascribed to the ordered graphite crystallites. The Raman spectra are normalized to the intensity of the G-band. Therefore, any changes in the proportion of ordered/disordered carbon domains graphically results into modified D1 and G-band frequency/shape. Pronounced differences are noticed between the carbon blacks and the RG support. The superior intensity and the broader D1-band for the HSAC TKK and the Vulcan TKK supports reflect their larger structural disorder level relative to RG. The position and the shape of the G-band depend on the analysed carbon material: the G-band of the RG support is sharp and centred at $\bar{\upsilon}$ ~1585 cm^{-1} *i.e.* close to the value reported for graphite single crystal ($\bar{\upsilon}$ ~ 1575 cm^{-1}); [1] while for HSAC and Vulcan this band is broader and red-shifted (*i.e.* shifted to higher frequency values). Moreover, a shoulder at *ca*. $\bar{\upsilon}$ ~ 1615 cm^{-1} indicates the presence of structural defects in the surface of the graphite crystallites. These observations agree with

previous literature findings for the same carbon support [28]. The superposition of the Raman spectra for the three carbon supports (Figure III-4a) shows that the D2-band (surface defects of graphite crystallites) contributes to the broadening of the G-band: this is a characteristic of highly disordered carbons [10]. Finally, the less organized carbon supports, namely the HSAC TKK and the two Vulcan, possess carbon crystallites with sizes in the order of 0.8 nm and 1.0 nm, respectively. The graphitized carbon support (RG) features larger-sized carbon crystallites in the order of 9.4 nm.

The textural properties of the different carbon supports are listed in Table III - 1. For the HSAC TKK and the Vulcan TKK supports, the experimentally determined values of the BET surface area (S_{BET}) are smaller than expected (see S_{BET} values provided by the supplier). The difference may arise from the fact that part of the porosity of the support is occupied by the deposited Pt nanoparticles [29]. The RG support has the smaller S_{BET}, as a consequence of the graphitization process. The total pore volume ($V_{\sum}$) is not directly related to the S_{BET} of the support, once the HSAC TKK and the RG support present close values of total pore volumes while their S_{BET} is distinctively different.

Table III - 1. Textural and substructural properties of the HSAC supports investigated in this study. [a] Values obtained from ref [30].

	40 wt. % Pt/HSAC TKK	40 wt. % Pt/Vulcan TKK	Vulcan XC72[a]	40 wt. % Pt/RG TKK
Specific surface area from supplier ($S_{BET, supplier}$) / $m^2\ g^{-1}_{carbon}$	800	250	-	-
Surface area measured ($S_{BET, measured}$) / $m^2\ g^{-1}_{carbon}$	462	136	252	110
Pore volume / $cm^3\ g^{-1}$ **Total pore volume ($V_{\sum}$)**	0.497	0.188	0.63	0.307
Mean pore diameter (D_{BET}) / nm	4.3	5.5	15.9	11.1
Mean carbon crystallite size (L_a) / nm	0.8	0.9	1.6	9.4

Transmission electron microscopy was used to determine the dispersion and the degree of agglomeration of the Pt/C nanoparticles. Figure III - 5 and Figure III - 6 show representative TEM images of the different electrocatalysts and the associated particle size

distributions (PSD), respectively for 40 wt. % Pt/HSAC and 40 wt. % Pt/ Vulcan TKK. Due to the severe aggregation of the Pt/RG crystallites (see Figure III - 5e and f), the PSD could not be established. The number-averaged mean Pt particle size determined for Vulcan TKK is superior ($\bar{d}_N$ = 2.7 nm) to that estimated for the HSAC support ($\bar{d}_N$ = 2.0 nm). Also, Pt aggregates are visible on the Vulcan TKK and the RG supports but not on the HSAC support. The higher dispersion of the Pt nanoparticles and their lower degree of agglomeration are direct consequences of the differences in S_{BET} values [31, 32].

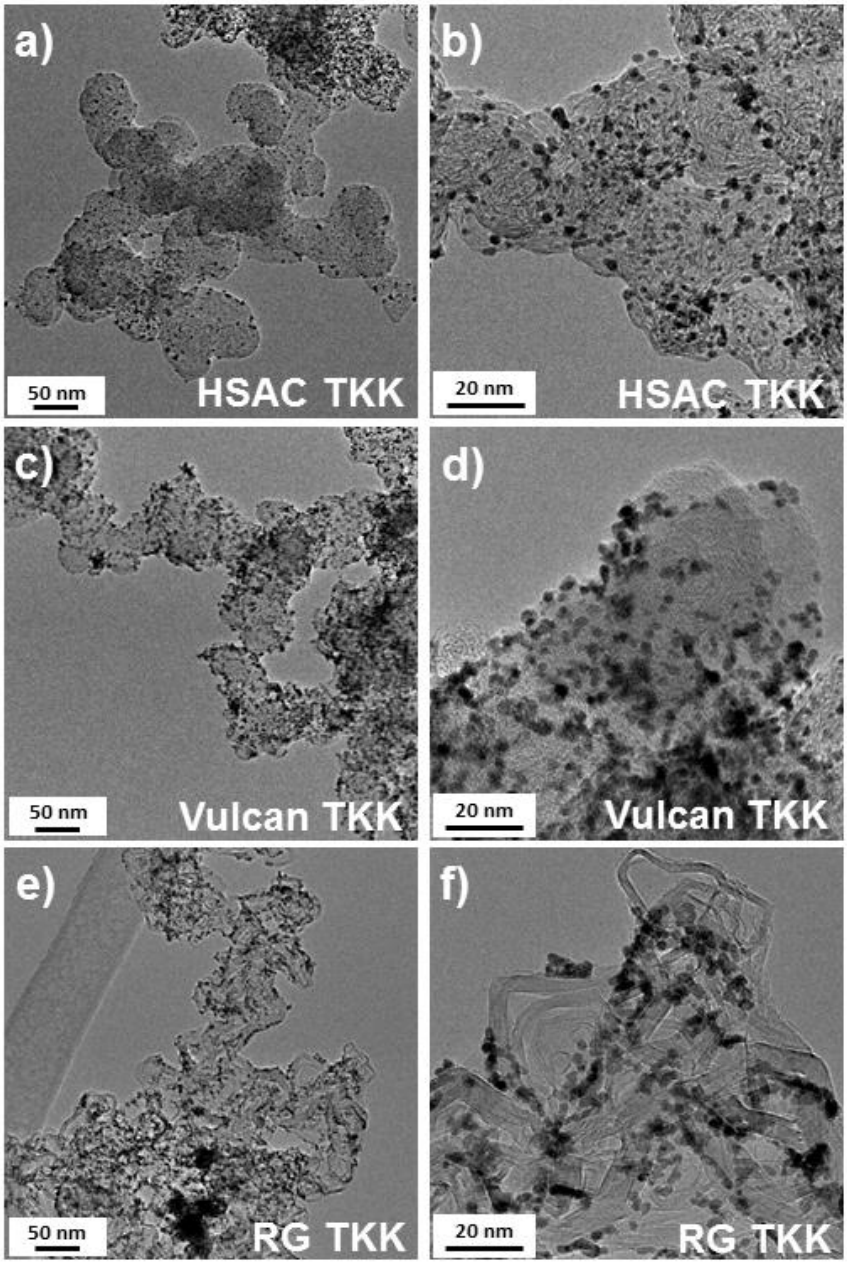

Figure III - 5. TEM images of the different carbon supports used in this thesis: a) and b) HSAC TKK, c) and d) Vulcan TKK, e) and f) RG TKK.

Different morphologies are observed for the studied carbon supports. For HSAC and Vulcan (Figure III - 5b and d), the graphite crystallites are arranged into round-shaped primary particles with size between 10 and 100 nm. In contrast, the RG support (Figure III - 5f) features highly oriented and parallel graphitic crystallites at their edges. The larger carbon crystallite size resulting from the graphitization process is clearly seen in the TEM images, in agreement with previous literature findings [33-35].

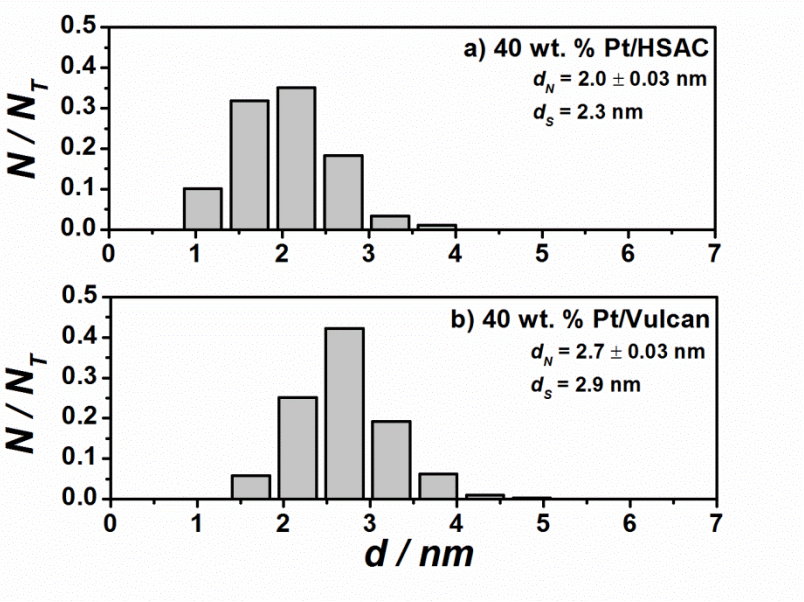

Figure III - 6. Particle size distribution, number-averaged diameter ($\bar{d}_N$) and surface-average diameter ($\bar{d}_S$) for the fresh 40 wt. % Pt/Vulcan and 40 wt. % Pt/HSAC electrocatalysts.

3.3 Preparation of catalysts' suspensions

In order to perform electrochemical measurements, a defined quantity of Pt/C electrocatalyst was first mixed with MQ-grade water, alcohol and Nafion® solution to form a suspension. An aliquot of this ink was then deposited onto a glassy carbon rotating disk electrode and cast to prepare a thin-film porous electrode. The quality of the thin film strongly influence the electrocatalytic activity, as first shown by Kocha *et al*. [36]. In the same line of thought, the presence of Nafion® used as a binder in the catalysts suspension and the storage conditions of the suspensions are important parameters to the COR kinetics, which were not previously investigated in the literature.

3.3.1 Definition of the initial surface state and effect of Nafion® on the carbon support

The physicochemical properties of carbon materials, such as the wettability and the electrical conductivity, highly depend on the nature and the amount of oxygen-containing groups present on their surface (CO_{surf}). The CO_{surf} groups include but are not limited to

phenols, ethers, ketones, and carboxylic acids [37, 38]. Moreover, CO_{surf} groups are intermediates of the carbon oxidation reaction (COR) [34, 39-41]. Therefore, an accurate determination of the oxygen content of the carbon supports is of prime importance to this study.

The surface chemistry of the carbon supports can be accessed by X-ray photoelectron spectroscopy (XPS), a surface sensitive technique which allows a qualitative and quantitative analysis. Figure III - 7 shows the C1s XPS spectra, the O1s/C1s atomic ratio (see Table III - 2) and the CO_{surf} composition (obtained by deconvolution of the XPS spectra,
Table III - 3) of electrodes prepared from different suspensions containing: (i) MQ-grade water + Pt/HSAC; (ii) MQ-grade water + Pt/HSAC + Nafion®, (iii) MQ-grade water + Pt/HSAC + Nafion®, this electrode being pre-cycled in support electrolyte (ten potential cycles at v = 20 mV s^{-1} followed by one potential cycle at v = 100 mV s^{-1} and a CO_{ad} stripping voltammogram at v = 100 mV s^{-1}). The O1s/C1s ratio on the Pt/HSAC surface, which contacted only MQ-grade water (0.11) is close to that monitored for reference samples in the literature (0.01- 0.07) [41-44]. However, it increases to 0.52 in the presence of Nafion® in the catalyst ink. As explained previously, this can be rationalized by considering the formation of local galvanic cells in the catalyst suspension, which yield the formation of a mixed potential close to 0.95 V *vs.* RHE produced by the oxidation of the HSAC support (anode) and the ORR at the Pt nanoparticles (cathode). On the contrary, in the absence of Nafion®, the negligible ion conductivity of MQ-grade water prevents the formation of these cells, and limits the corrosion of the HSAC surface. Recently, Cherstiouk *et al*. [45] proposed another scenario, which also accounts for the more facile corrosion of carbon materials in the presence of Nafion®. The authors proposed that the Nafion® ionomer blocks the micro and meso-porosity of the carbon support and, at high-loadings, deform the carbon aggregates. This deformation leads to strained zones, which become preferential sites for the COR. To the best of the author knowledge, the literature is rather scarce on this issue and most of the studies dealing with the interaction of Nafion® with the carbon support focused on the distribution of the ionomer on the carbon surface and its effect on the preparation of catalytic layers [46-48]. In particular, many efforts were devoted to determine the optimal ionomer/carbon ratio for PEMFC electrodes [49-53].

The effect of initial characterization CVs on the extent of oxidation of the HSAC surface is also worth noting. The O1s/C1s ratio measured on Pt/HSAC electrodes decreases from 0.52 to 0.33 after electrochemical characterizations, such as base or CO_{ads} stripping voltammograms. This result suggests that intermediate electrochemical characterization affect the surface state of Pt/HSAC electrocatalysts, as it will be further shown in **sub-chapter 3.5.1.**

Table III - 2. Values of the O1s/C1s ratio monitored by X-ray photoelectron spectroscopy, and comparison to literature values.

Sample / Reference	Description	Ratio O1s/C1s
A	40 wt. % Pt/HSAC TKK	0.11
B	47 wt. % Pt/HSAC TKK + water suspension + Nafion®	0.52
C	40 wt. % Pt/HSAC + water suspension + Nafion® + potential sweeping	0.33
D	Fresh MEA cathode	0.17
[39]	Kangasniemi, K. H.; Condit, D. A.; Jarvi, T. D. J. Electrochem. Soc. 2004, 151, E125.	0.07
[42]	Shao, Y.; Yin, G.; Gao, Y.; Shi, P. J. Electrochem. Soc. 2006, 153, A1093.	0.03
[40]	Avasarala, B.; Moore, R.; Haldar, P. Electrochim. Acta 2010, 55, 4765.	0.01
[41]	Álvarez, G.; Alcaide, F.; Miguel, O.; Cabot, P. L.; Martínez-Huerta, M. V.; Fierro, J. L. G. Electrochim. Acta 2011, 56, 9370.	0.07

Table III - 3. Assignments of the deconvoluted peaks of the high resolution C1s XP spectra.

Assignment	C1s binding energy (eV)	Functional group
C–C	284.3	sp^2 and sp^3-hydribized carbon atoms
C–O	286.0	Hydroxyl, epoxy, ether-like, alcoholic and phenolic
C=O	287.7	Carbonyl and/or quinone-like
O=C–O	289.4	Carboxylic acid, lactone, anhydride
C–F	291.3	$C–F_2$ (Nafion® ionomer)
C–F	293	$C–OF_2$ and/or $C-F_3$ groups (Nafion® ionomer)

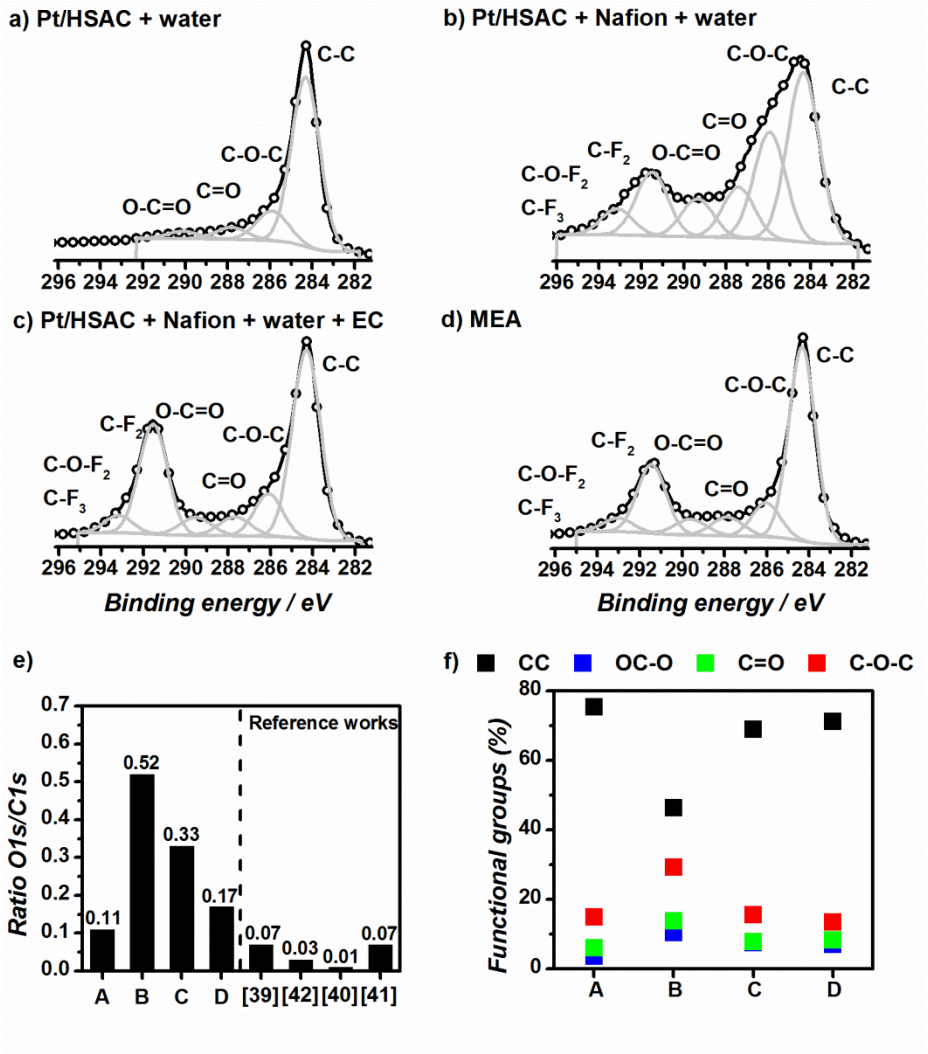

Figure III - 7. C1s XP spectra for electrodes prepared from different inks containing: a) MQ-grade water + Pt/HSAC, b) MQ-grade water + Pt/HSAC + Nafion®, c) MQ-grade water + Pt/HSAC + Nafion® this electrode being pre-cycled in support electrolyte (ten potential cycles at v = 20 mV s^{-1} followed by one potential cycle at v = 100 mV s^{-1} and a CO_{ad} stripping voltammogram at v = 100 mV s^{-1}), d) MEA support , their e) O1s/C1s atomic ratio and e) concentration of the functional groups.

3.4 Effect of storage of the ink under air atmosphere on the carbon support

3.4.1 Effect of short-term storage of the ink

The electrocatalyst suspensions used in this Ph.D. thesis were prepared in non-hermetic glass flasks. After deposition of an aliquot of the ink onto the glassy carbon rotating disk electrode (a Pt loading of 30 $\mu g_{Pt}\,cm^{-2}$ was targeted), the thin-film porous electrodes were subjected to a routine electrochemical characterization protocol, which consisted of 10 cyclic voltammograms at 20 mV s^{-1}, 1 cyclic voltammogram at 100 mV s^{-1} and a final CO stripping voltammogram at 100 mV s^{-1}, in 0.1 M H_2SO_4 at T = 330 K. Figure III - 8 displays the CO_{ad} stripping voltammograms recorded on thin-film porous rotating disk electrodes made from

two independent inks composed of 40 wt. % Pt/HSAC dispersed in MQ-grade water, isopropanol and Nafion® as a function of their age. The CO_{ad} stripping coulometry determined from these experiments was used to monitor the change in Pt specific surface area during the storage on the suspension (Figure III - 9).

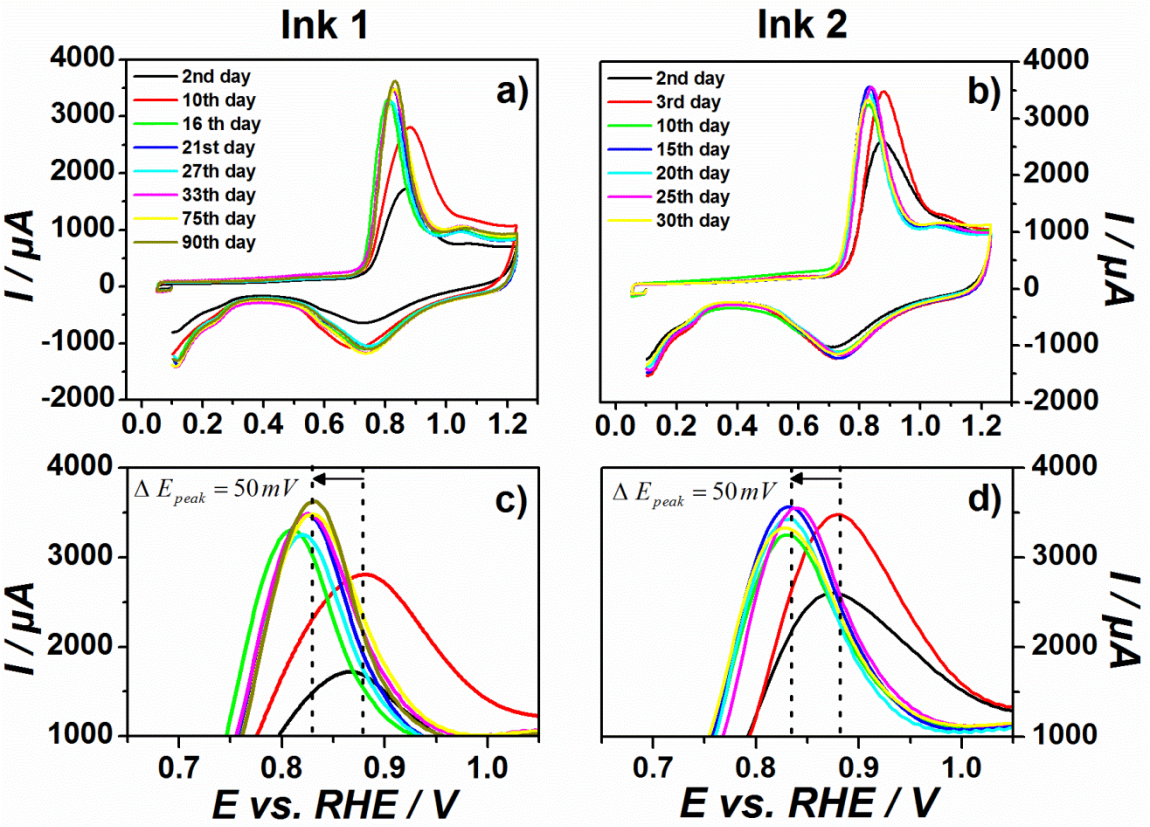

Figure III - 8. CO_{ad} stripping voltammograms of 40 wt. % Pt/HSAC as a function of the age of the ink suspension. Electrolyte: 0.1 M H_2SO_4; v = 0.100 V s^{-1}; T = 330 K.

A change in the position and shape of the CO_{ad} stripping peak is noticed for ink suspensions older than 10-15 days. The CO_{ad} stripping peak becomes more symmetric and a decrease of ~50 mV of its original position (E_{peak}) is observed. Concomitantly, a change of the Pt surface area is monitored over time: a slight but discernible change is noticed when the catalyst suspension gets older (Figure III - 9). As verified from measurements on two independent inks prepared with the exact same composition, the observed trends are reproducible.

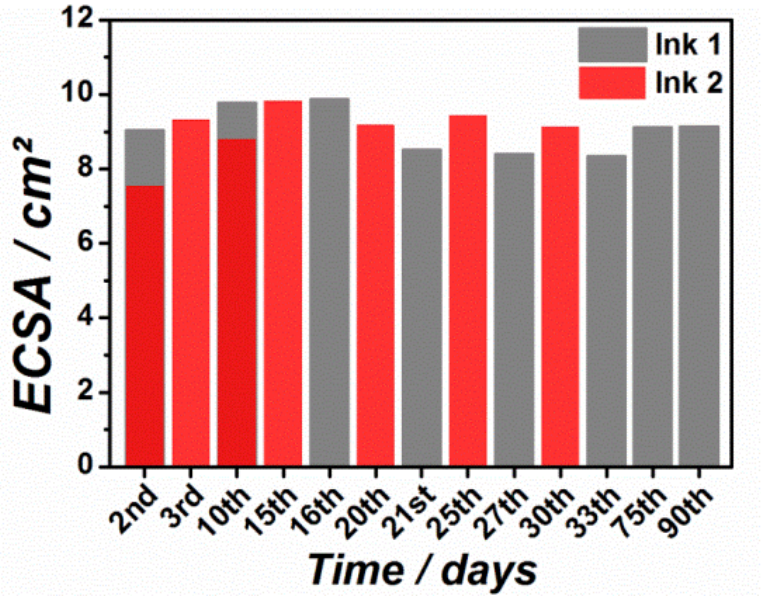

Figure III - 9. Change of the ECSA for electrodes based on 40 wt. % Pt/HSAC as a function of the age of the ink suspension. The ECSA was determined using the CO_{ad} stripping coulometry. Electrolyte: 0.1 M H_2SO_4; v = 0.100 V s^{-1}; T = 330 K.

The changes observed in the CO_{ad} stripping voltammogram may be rationalized by considering the structure sensitivity of the CO_{ad} monolayer electrooxidation. Indeed, it is well-established that the position and the shape of a CO_{ad} stripping voltammogram depend on the size distribution and the degree of agglomeration of the Pt nanoparticles [54-58]. As previously shown, the main CO_{ad} electrooxidation peak shifts towards negative potential and becomes more symmetric when the Pt nanoparticle size increases. In the present study, the average Pt nanoparticle size was estimated to be 2.0 nm but the histogram of Figure III - 6 indicates the presence of smaller nanoparticles in the order of 1.5 nm in the fresh 40 wt. % Pt/HSAC. The broad shape of the CO_{ad} oxidation peak, in particular the pronounced tailing at potential larger than that of the current peak, observed during the first days of the storage of the inks confirms by electrochemical means the existence of Pt nanoparticles with size below 2.5 nm [54-58]. However, the disappearing of the tailing and the negative potential shift of the main CO_{ad} stripping peak suggest that the smallest Pt nanoparticles are lost over time, most likely because of their detachment from the carbon support.

These results can be rationalized by considering that the HSAC support is corroded during its storage in the suspension. Indeed, the Pt/HSAC catalyst suspensions were prepared in glass flask, which were not completely hermetically closed, and allowed the permeation of oxygen from the air. Such storage conditions caused a mixed potential produced by simultaneous HSAC support corrosion and the oxygen reduction on Pt, and basically

reproduce what happens in a PEMFC cathode at open-circuit potential (OCP) or under idling conditions. The detachment of the Pt nanoparticles induced by the corrosion of the HSAC support nicely explains the modification of the CO_{ad} stripping voltammograms and the observed decrease of the Pt specific surface area. However, this scenario is contradicted by the normalized Raman spectra measured periodically on ink 2 (Figure III - 10). No significant changes neither of the shape nor of the intensity of the D1-band are noticed (inset of Figure III - 10), all spectra being superposed to that measured on the native HSAC support.

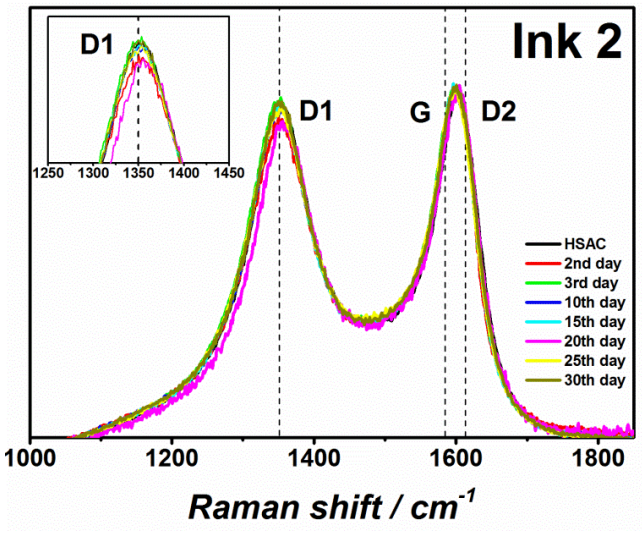

Figure III - 10. Normalized Raman spectra of ink 2.

Interestingly, pronounced changes of the carbon surface chemistry are noticed when Vulcan XC 72 is used. Figure III - 11 shows the C1s XP spectra, the O1s/C1s atomic ratio and the carbon surface oxide (CO_{surf}) composition measured on electrodes prepared from 40 wt. % Pt/Vulcan E-TEK after different periods of time. The variation of the O1s/C1s atomic ratio during the first two weeks of storage shows that the carbon surface chemistry is strongly modified during the preparation steps. It suggests a pronounced corrosion of the Vulcan support, which nicely account for the detachment of the Pt nanoparticles, and the changes of the CO_{ad} stripping voltammograms and of the Pt specific surface area observed on Pt/HSAC (Figure III - 8).

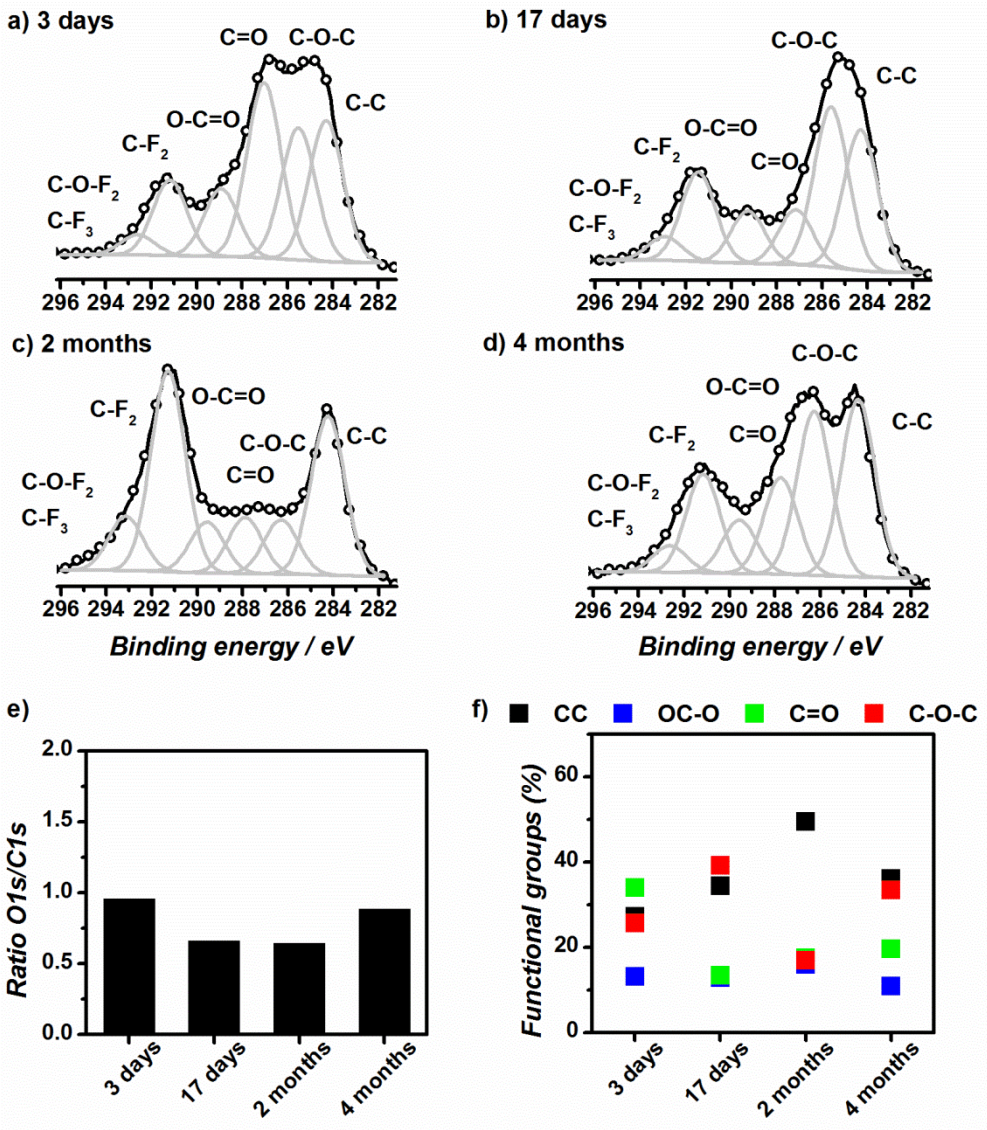

Figure III - 11. XPS C1s spectra measured on inks based on Pt/ Vulcan XC-72 E-TEK after a) 3 days, b) 17 days, c) 2 months and d) 4 months and their respective e) O1s/C1s atomic ratio and f) concentration of the functional groups in the suspensions.

3.4.2 Effect of long-term storage of the ink

We now investigate the structural changes of the Vulcan E-TEK support over a longer period of time. To that purpose, inks composed of Pt/Vulcan E-TEK, water, isopropanol and Nafion® were evaluated after 1.5, 2.5 and 3.5 years of storage into non-hermetic glass flasks. The structural changes experienced by the Vulcan carbon support are presented in Figure III - 12.

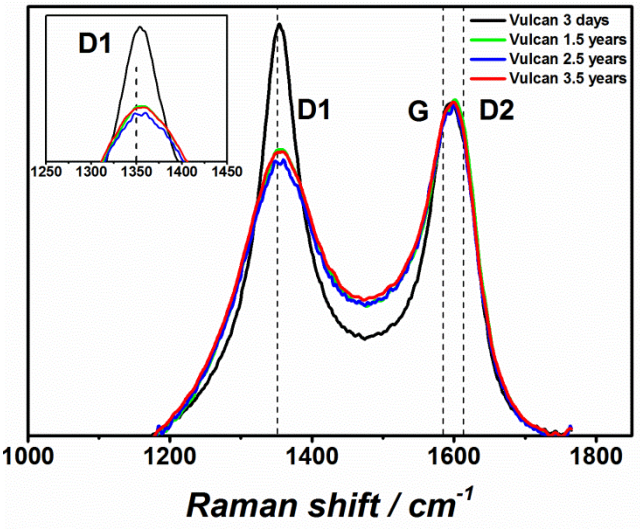

Figure III - 12. Normalized Raman spectra of Vulcan XC-72 carbon support after 3 days, 1.5 years, 2.5 years and 3.5 years under OCP conditions.

The decreased intensity of the D1-band in Raman spectra observed after 1.5 years of aging at OCP suggests that the disordered domains of the Vulcan support were preferentially oxidized. This trend is very fast in the first year of storage and then slows down most likely because the remaining carbon particles possess a better ordered and more robust graphitic structure. The XPS results of Figure III - 13 provide evidence that the CO_{surf} species were preferentially oxidized during the first 1.5 year of storage (decrease of the O1s/C1s ratio). The decrease of the graphitic contribution and the formation of new CO_{surf} species observed in the following two years (Figure III - 13 f)) are believed to result from the corrosion of the organized graphite crystallites.

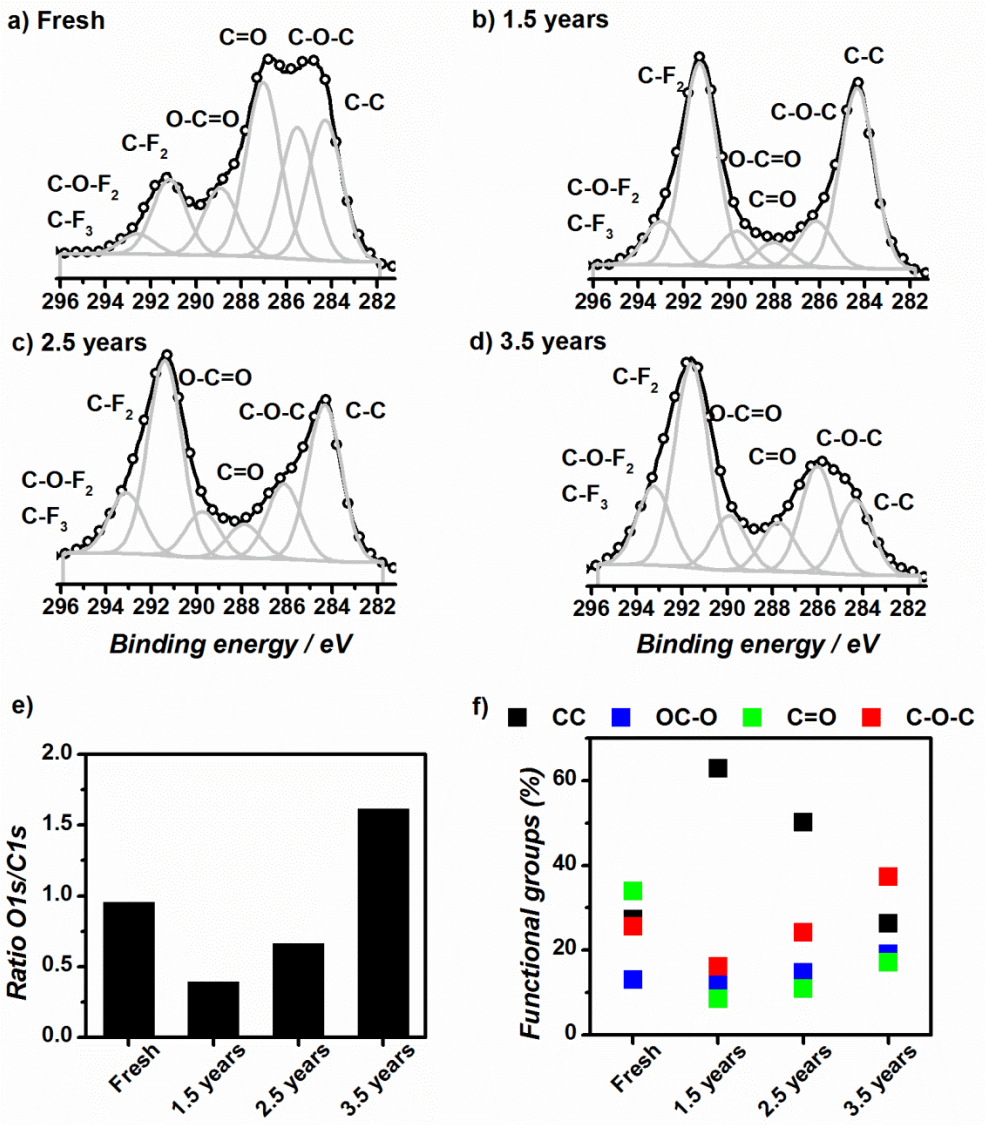

Figure III - 13. C1s X-ray photoelectron spectra of a) fresh and after b) 1.5 years, c) 2.5 years and d) 3.5 years of ageing and their respective e) O1s/C1s atomic ratio and f) concentration of the functional groups of suspension with Vulcan E-TEK, solid ionomer and water stored under air atmosphere at room temperature.

3.5 Role of intermediate characterizations, nature of the carbon support, gas atmosphere and potential limits on ECSA and Q/HQ redox couple during ASTs

We now investigate the role of different experimental parameters such as the number and the nature of intermediate characterizations, the gas atmosphere and the upper potential limit used during ASTs.

3.5.1 Electrochemical evidences on the influence of intermediate characterizations on ECSA and Q/HQ redox couple evolution

In this sub-chapter, a new catalyst suspension composed of 5 wt. % Nafion® solution, MQ-grade water and 40 wt. % Pt/HSAC were used to prepare porous thin-film working electrodes. As referred in **Chapter II 2.3.1** the inks were used for a maximal period of time of 1.5 months. The ECSA was measured using the coulometry of a CO_{ad} stripping voltammogram performed at v = 100 mV s^{-1}. After their characterization in a conventional electrochemical cell, the electrodes were withdrawn from the solution at controlled electrode potential E = 0.40 V *vs.* RHE, and then transferred into a degradation cell with the electrode surface protected by a drop of electrolyte (the overall procedure takes less than a minute).

The benchmark AST used in this sub-chapter was a potential hold at E = 1.0 V *vs.* RHE for t = 96 hours in deaerated electrolyte at T = 330 K. Five cyclic voltammograms at v = 100 mV s^{-1}, one cyclic voltammogram at v = 20 mV s^{-1} and one CO_{ad} stripping voltammogram were recorded at the beginning and at the end of the AST to monitor the changes in Pt surface reactivity and ECSA. These experimental conditions are referred to as "AST 0" in what follows. The effect of intermediate characterizations, such as base or CO_{ad} stripping voltammograms, was investigated by adding different steps to the benchmark AST:

- **AST 1.** In this aging test, five cyclic voltammograms at v = 100 mV s^{-1}, one cyclic voltammogram at v = 20 mV s^{-1} and a CO_{ad} stripping voltammogram were additionally performed after 6 h, 24 h, 48 h and 72 h to monitor the variations of ECSA over time.

- **AST 2.** In this aging test, five cyclic voltammograms at v = 100 mV s^{-1} and one cyclic voltammogram at v = 20 mV s^{-1} were additionally performed after 6 h, 24 h, 48 h and 72 h to monitor the variations of ECSA over time.

- **AST 3.** In this aging test, CO_{ad} stripping experiments were additionally performed after 6 h, 24 h, 48 h, and 72 h to monitor the change of ECSA over time.

- **AST 4.** In this aging test, five cyclic voltammograms at v = 100 mV s^{-1}, one cyclic voltammogram at v = 20 mV s^{-1} and a "pseudo" CO_{ad} stripping voltammogram were performed to monitor the changes in surface reactivity and ECSA. A "pseudo" CO_{ad}

stripping experiment consisted of all the steps involved in a normal CO_{ad} stripping but used Ar instead of CO. Two real CO_{ad} stripping experiments (that is with CO) were performed to monitor the changes in ECSA after polarization at E = 1.0 V *vs.* RHE for 96 h in deaerated electrolyte.

Figure III - 14 and Table III - 4 show the ECSA changes recorded as a function of the polarization time at E = 1.0 V *vs.* RHE for the different aging tests. It is obvious that intermediate characterizations are the major contributor to the decrease in ECSA. Indeed, while the benchmark aging test (t = 96 h at E = 1.0 V *vs.* RHE) displays only 5 % ECSA loss (AST 0), the same aging test with the full set of intermediate characterizations features 18 % of ECSA loss (AST 1). It is also clear from Figure III-15 that, when only a part of the full characterization protocol is realized (*i.e.* potential cycling or CO_{ad} stripping), ECSA losses are kept at intermediate values. The most degrading characterization protocols in terms of ECSA losses can be ranked as: Intermediate CVs (AST 2) < Intermediate CVs + "pseudo" CO_{ad} stripping (AST 4) < intermediate CO_{ad} stripping (AST 3) ~ intermediate CVs + intermediate CO_{ad} stripping (AST 1).

The results suggest that excursions or extended polarization at reducing potentials, such as that used during the adsorption of a CO monolayer, accelerate the ECSA losses. They can be understood in view of the breakdown of the passivation layer formed on the Pt/HSAC electrocatalyst during the polarization at E = 1.0 V *vs.* RHE. Indeed, it is well-documented that a passivating oxide layer forms on the surface of the Pt nanoparticles at electrode potential above 1.0 V *vs.* RHE [59-61]. The reduction of this oxide layer facilitates the dissolution of the Pt nanoparticles [59, 62, 63], the quantity of Pt^{z+} ions released in solution increasing with an increase in the duration of a potential cycle [25]. Similarly, extended polarization at high electrode potential causes the formation of stable CO_{surf} groups, but potential excursions below 0.65 V *vs.* RHE renew the carbon surface, and intensify the carbon corrosion rate [27].

In consequence, a proper evaluation of the ECSA losses would require minimal perturbation of the system, and ideally individual electrodes should then be used (for example, in the benchmark AST considered here, five electrodes: the first one being aged for 6 h, the second for 24 h and so on until 96 h). This is an important aspect that should be kept in mind when investigating the degradation of PEMFC electrode materials.

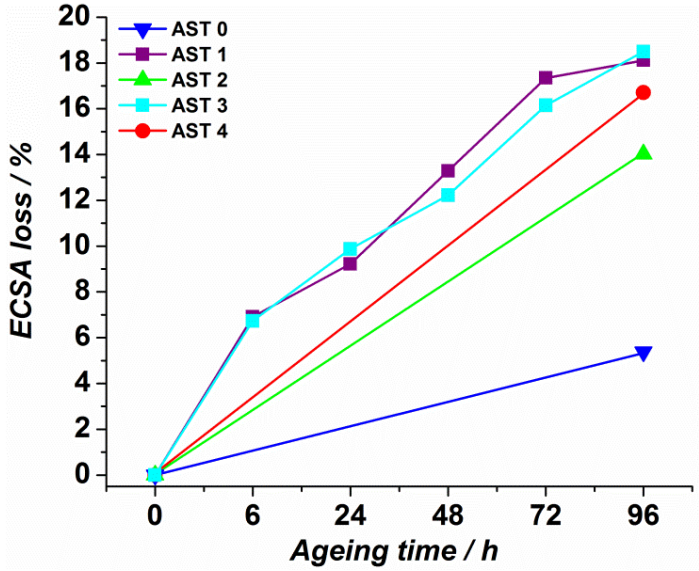

Figure III - 14. Evolution of the ECSA for different intermediate characterization protocols. The ECSA was estimated from the CO_{ad} stripping coulometry. Electrolyte: 0.1 M H_2SO_4; v = 0.100 V s^{-1}; T = 330 K.

Table III - 4. Evolution of the ECSA for the different ASTs.

Accelerated stress test	Fresh ECSA (cm^2)	Aged ECSA (cm^2)	ECSA loss in %
0	8.74	8.27	5.4 %
1	9.11	7.46	18.1 %
2	9.27	7.96	14.1 %
3	9.55	7.81	18.2 %

Figure III - 15 shows the cyclic voltammograms measured before/after the ASTs for the different characterization protocols. In their fresh state, all the electrodes present similar H_{upd} features (under-potential adsorption/desorption of protons onto/from Pt nanoparticles) and comparable ECSA values (Table III - 4) indicating a reproducible preparation. However, a more pronounced decrease of the H_{upd} charge density is noticed for AST 0. This result firstly indicates that integration of the H_{upd} charge is inappropriate for the measurement of the real surface area of the Pt/HSAC electrocatalysts during ASTs. It may also indicate that the liquid electrolyte of the "degradation cell" is slowly contaminating over time or that the Pt catalytic sites were contaminated by oxygen-containing surface groups (CO_{surf}) produced during the electrochemical corrosion of the HSAC. Indeed, previous work [64] evidenced that CO_{surf} species may back-spillover from the carbon support to Pt, where they dehydrogenate into adsorbed CO molecules. Last but not least, the decrease in H_{upd} charge density may

simply be a consequence of the strong oxidation of the Pt surface during the 96 h potential step at E = 1.0 V *vs.* RHE.

There is also clear evidence that the charge contained under the Q/HQ redox couple [34] (0.50 < E < 0.80 V) increases during the 96 h polarization at E = 1.0 V *vs.* RHE (Figure III - 16). This trend is particularly marked for the ASTs where no intermediate CV or CO_{ad} stripping voltammogram was performed (AST 0), and suggests that cyclic voltammogramms favour the electrooxidation of CO_{surf} groups in CO_2 or their reduction Similar results were recently reported by Park *et al.* [65] in MEA configuration during a FCCJ AST protocol.

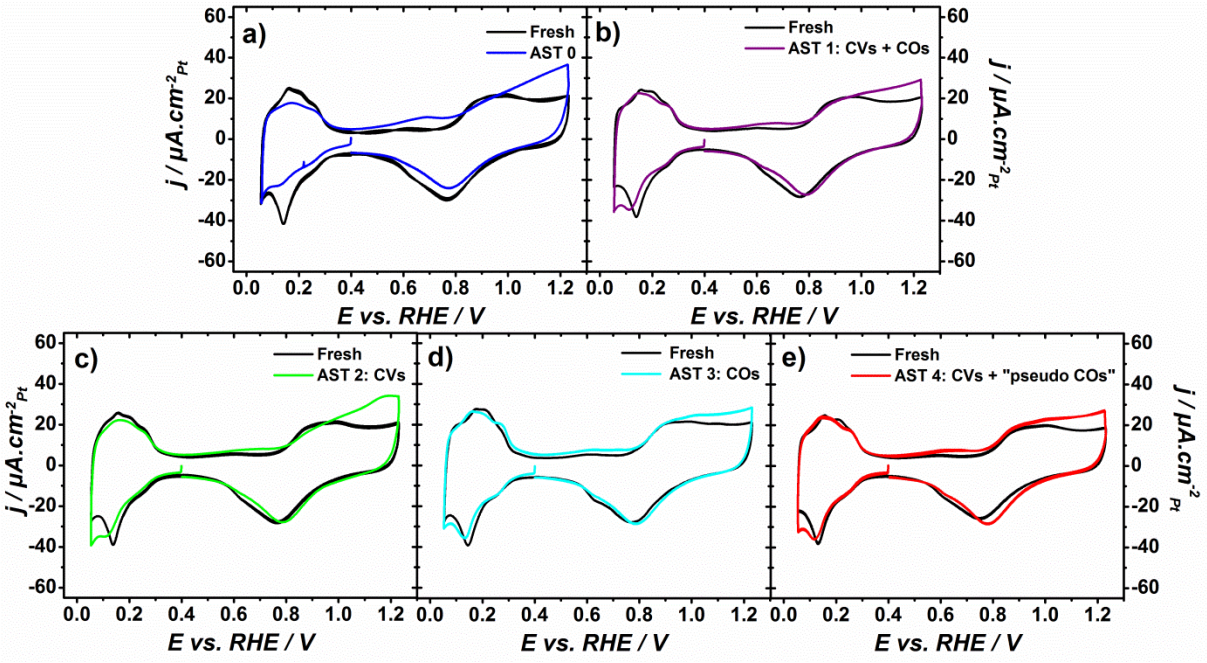

Figure III - 15. Cyclic voltammograms measured after the ASTs for different intermediate characterization protocols. The current is normalized to the real surface area estimated from the CO_{ad} stripping coulometry. Electrolyte: 0.1 M H_2SO_4; v = 0.020 V s^{-1}; T = 330 K.

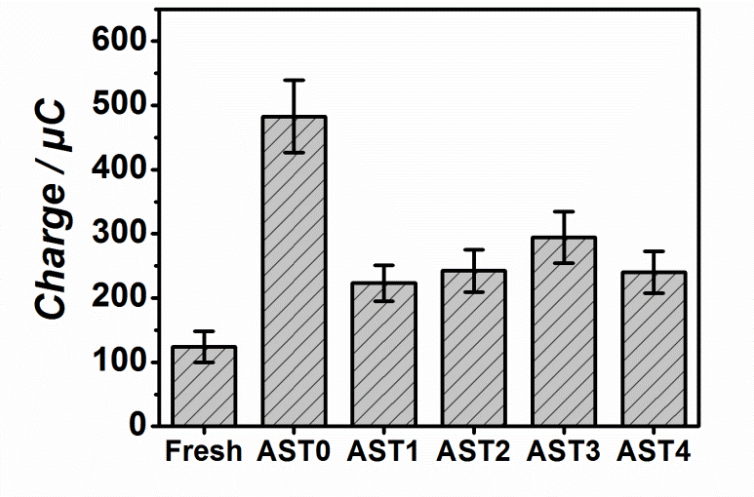

Figure III - 16. Coulometry of the quinone-hydroquinone (Q/HQ) redox couple determined after 96 h of polarization for the different ASTs. Integration of the current between E = 0.40 and 0.75 V *vs.* RHE corrected from the interfacial double-layer contribution measured at E = 0.40 V *vs.* RHE.

3.5.2 Structural modifications of the Pt/HSAC electrocatalyst induced by intermediate characterizations followed by IL-TEM

The morphological changes of the Pt/HSAC electrocatalyst induced by the intermediate characterizations were investigated by identical location transmission electron microscopy (IL-TEM). The comparison of the TEM images recorded for the Pt/HSAC samples aged in AST 0 or AST 1 conditions allowed a direct quantification of the effect of the intermediate characterizations. The AST 3 explored the influence of CO_{ad} stripping voltammograms, and the AST 4 investigated whether this effect is due to the electrochemically reducing potential or to the CO atmosphere. Recently, a possible limitation of the IL-TEM technique was discussed by Schlögl *et al*. [66]. The authors argued that, at temperature close to T = 330 K, the dissolution of the gold TEM grid initiates at E ~ 1.3 V *vs.* RHE. However, since this upper potential limit was never exceeded during the ASTs, this phenomenon is very unlikely to have occurred here.

a. Effect of the number of intermediate characterizations

Figure III - 17 and Figure III - 18 display IL-TEM micrographs recorded before/after AST 0 and AST 1, respectively. In both case, well-known degradation mechanisms appear: (*i*) the migration of Pt nanocrystallites, resulting in an increased degree of agglomeration (white rectangles), (*ii*) the electrochemical Ostwald ripening, that is the preferential dissolution of the smallest Pt nanocrystallites over time (production of Pt^{z+} ions) and the increase of the mean particle size due to redeposition of these ions (green circles), (*iii*) the

thinning/shrinking/collapsing of the carbon particles due to electrochemical corrosion (white arrows) or the structural re-arrangement of the carbon particles (red line).

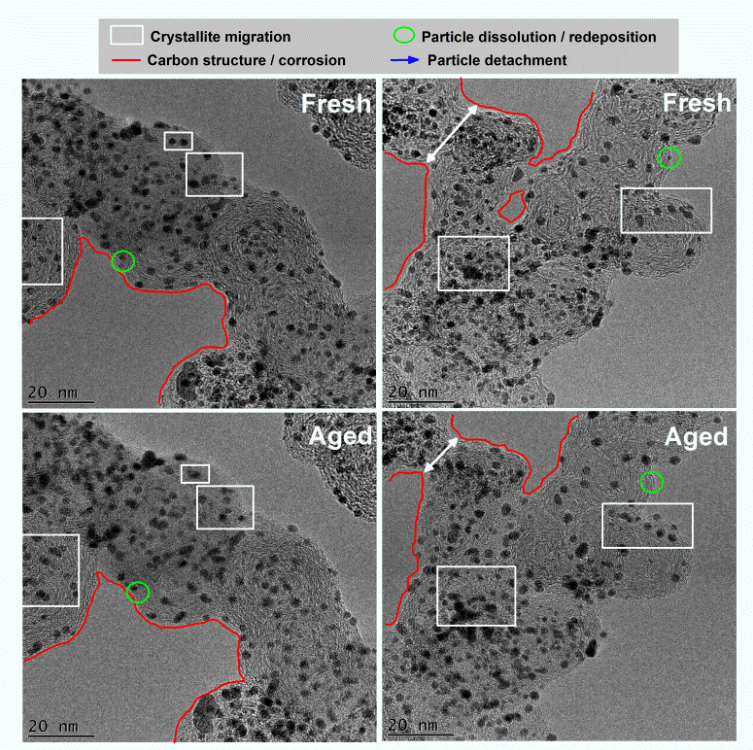

Figure III - 17. IL-TEM images of the Pt/HSAC electrocatalyst after AST 0 (96 h polarization at E = 1.0 V *vs.* RHE and T = 330 K in 0.1 M H_2SO_4).

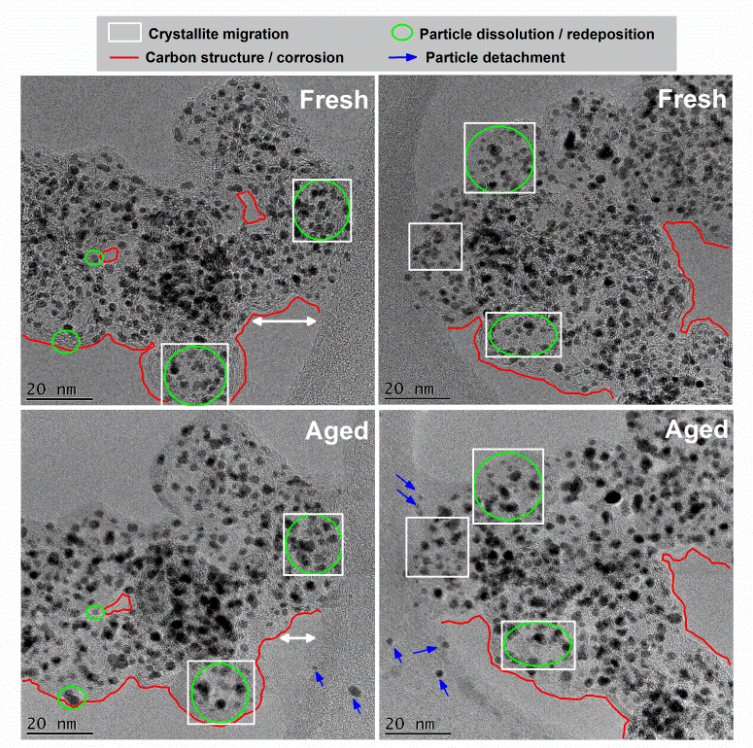

Figure III - 18. IL-TEM images of the Pt/HSAC electrocatalyst after AST 1 (96 h polarization at E = 1.0 V *vs.* RHE and T = 330 K in 0.1 M H_2SO_4 + intermediate characterizations).

It is clear from these micrographs that the extent of degradation of the Pt/HSAC nanoparticles increases with an increase in the number of intermediate characterizations. These observations are quantified in Figure III - 19 and in Figure III - 20 where the particle size distributions, the surface-averaged mean particle size and the density of "isolated" particles are displayed, respectively. The Pt nanoparticles increase in size more significantly, and there is a more pronounced decrease in the fraction of the smallest Pt nanocrystallites when intermediate characterizations are implemented in the AST: + 38 % in size for AST 1 *vs.* + 32 % in size for AST 0. This may be explained by the redeposition of Pt^{z+} ions produced by electrochemical Ostwald ripening during the negative-going potential sweep in cyclic voltammetry experiments.

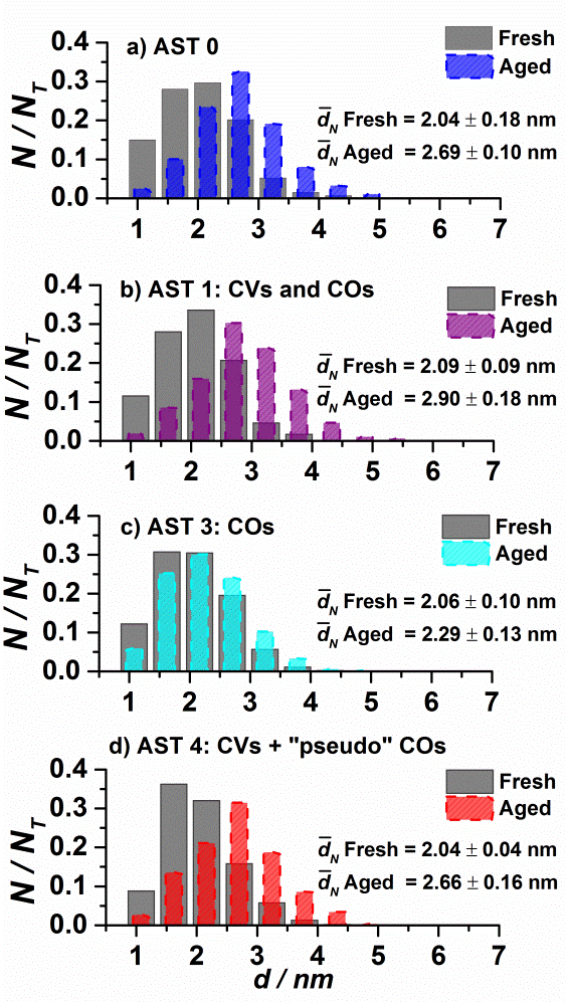

Figure III - 19. Particle size distribution and number-averaged diameter ($\bar{d}_N$) for the different ASTs.

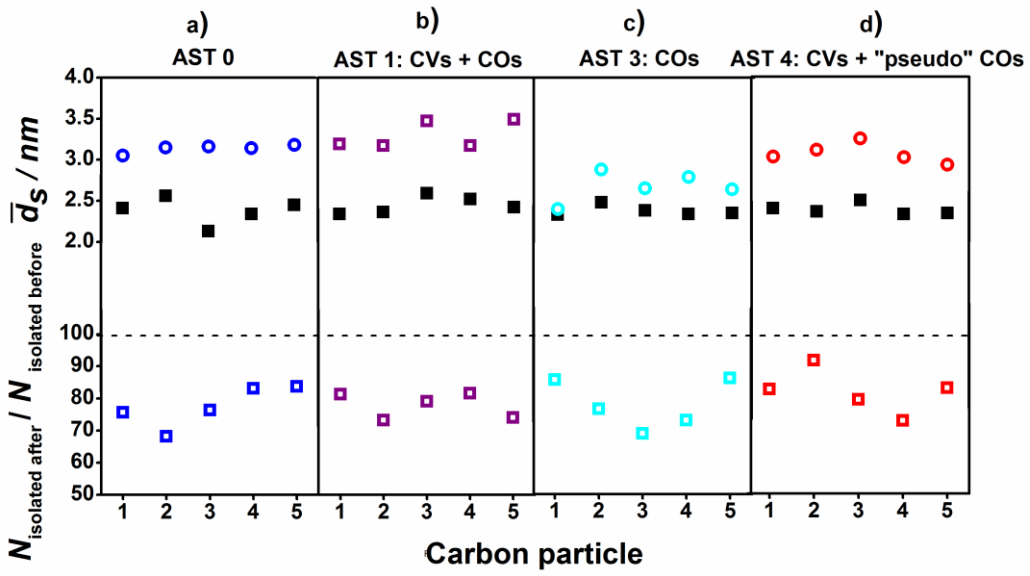

Figure III - 20. Surface-averaged mean particle size ($\bar{d}_S$) and density of isolated (non-agglomerated and spherical) Pt nanoparticles before (filled symbols) and after (open symbols) different ASTs.

Furthermore, Figure III - 21 illustrates that the changes of the HSAC structure are more severe when intermediate characterizations are included in the AST. For both AST 0 (left-hand side) and AST 1 (right-hand side), the borders of the primary carbon particles are modified, but the brighter contrast of IL-TEM micrographs recorded after AST 1 suggests more pronounced corrosion of the HSAC in AST1. Further evidence is provided in Figure III - 22: the greater depreciation of the D1-band intensity in Raman spectra following AST1 provides evidence of the harsher corrosion of the organized domains of the HSAC support, in agreement with previous reports [67, 68]. Considering the above, it is not surprising that Pt nanoparticles detach from the carbon support (blue arrows) during AST 1 (Figure III - 18) and not in AST 0 (Figure III - 17). It is also possible to provide evidences of this phenomenon because certain detached Pt nanoparticles are trapped in the Lacey carbon membrane of the TEM grid. The detachment of the Pt nanoparticles likely accounts for the 13% difference in the ECSA loss monitored between AST 0 and AST 1.

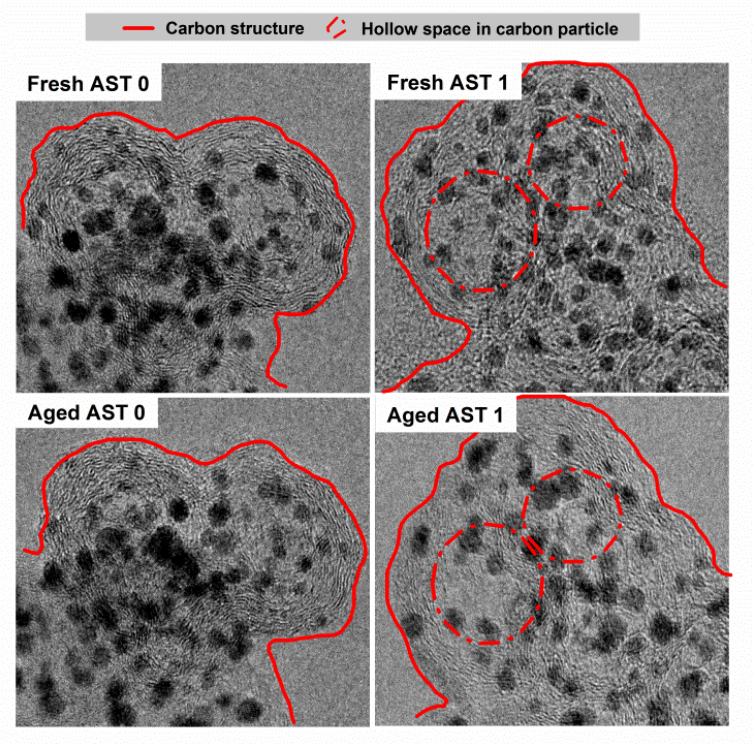

Figure III - 21. IL-TEM images of the Pt/HSAC electrocatalyst after AST 0 (96 h polarization at E = 1.0 V *vs.* RHE and T = 330 K in 0.1 M H_2SO_4) and AST 1 (96 h polarization at E = 1.0 V *vs.* RHE and T = 330 K in 0.1 M H_2SO_4 + intermediate characterizations).

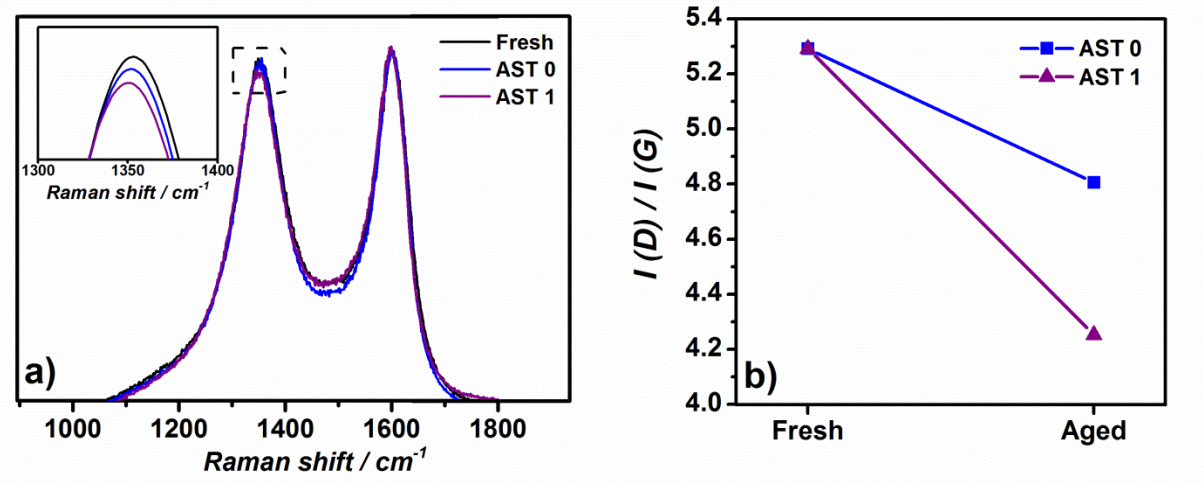

Figure III - 22. a) Raman spectra and b) ratio I(D)/I(G) for AST 0 and AST 1.

b. Effect of the nature of intermediate characterizations

Finally, the effect of the nature of the intermediate characterizations (cyclic and CO_{ad} stripping voltammograms) used during ASTs was investigated. For that purpose, AST 1 that includes four intermediate CVs and four CO_{ad} intermediate stripping voltammograms, AST 3 that includes four CO_{ad} intermediate stripping voltammograms and AST 4 that includes four intermediate CVs and four "pseudo" CO_{ad} stripping voltammograms were compared.

Figure III - 23 shows the IL-TEM images recorded before/after AST 3. In these experimental conditions, crystallite migration/agglomeration appears to be the predominant degradation mechanisms (see inset). Indeed, the mean diameter of the isolated Pt nanoparticles is only slightly altered ($\overline{d}_N$ aged = 2.29 nm *vs.* $\overline{d}_N$ fresh = 2.06 nm in Figure III - 19) and the population of small Pt nanoparticles (between 1 nm and 1.5 nm) is preserved (Figure III - 20). As proposed in our former study [69], this can be explained by considering that CO molecules partially reduce the CO_{surf} species present on the carbon support, thereby facilitating their movement. A striking result is the absence of Pt nanocrystallite growth in these AST conditions: this suggests that CO molecules inhibit the dissolution of Pt into the electrolyte or the redeposition of Pt^{z+} ions onto larger Pt crystallites. Note however that, in the last scenario, a decrease in the mean Pt/HSAC crystallite growth would have been observed.

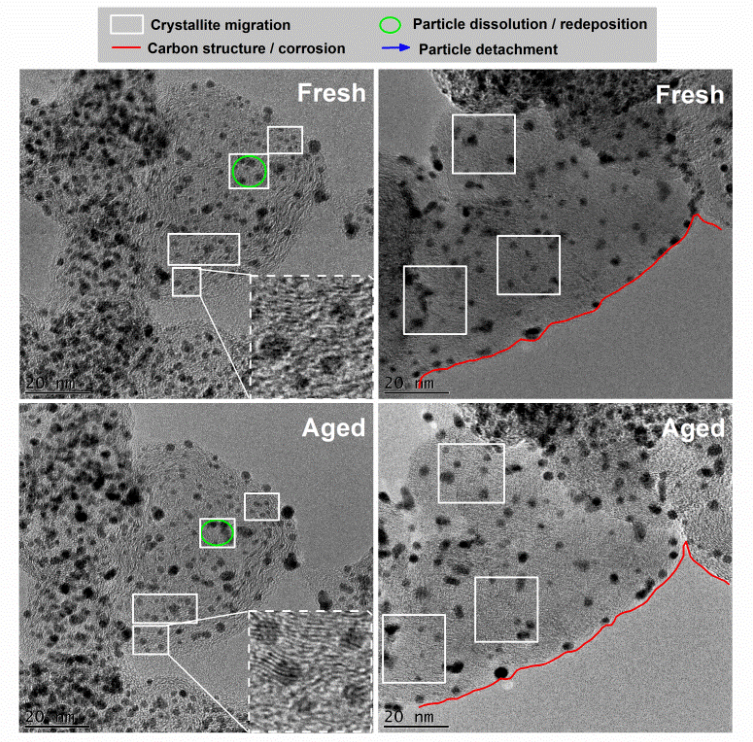

Figure III - 23. IL-TEM images of the Pt/HSAC electrocatalysts after AST 3 (96 h polarization at E = 1.0 V *vs.* RHE and T = 330 K in 0.1 M H_2SO_4 + CO_{ad} stripping voltammograms**).**

Further evidence of the influence of CO molecules can also be clearly seen in Figure III - 24, which presents representative IL-TEM images for AST 4. The AST 4 is essentially similar to AST 1, except the fact that Ar was bubbled in solution during the CO_{ad} stripping experiments (”pseudo” CO_{ad} stripping voltammograms). After pseudo CO_{ad} stripping voltammograms, IL-TEM images feature Pt nanoparticles that were not present at fresh state

or flat rafts between individual Pt nanocrystallites (Figure III - 24 inset). Since similar variations of the density of isolated Pt nanoparticles and of the mean Pt nanoparticle size were observed during AST 4 as in AST 1 (Figure III - 19 and Figure III - 20), this confirms that CO molecules prevent the dissolution of Pt nanoparticles into Pt^{z+} ions. The interested reader is referred to Ref. [69] for a more detailed discussion.

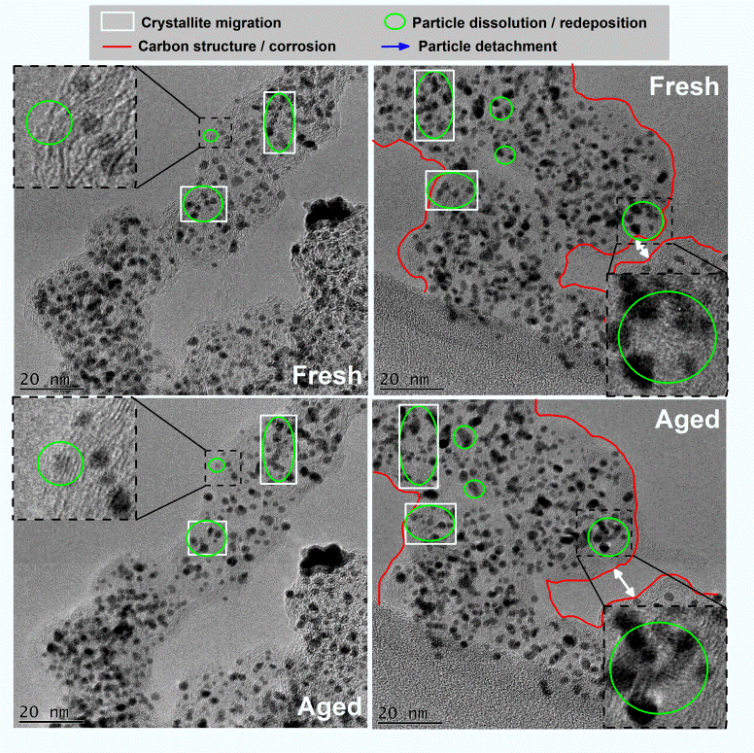

Figure III - 24. IL-TEM images of the Pt/HSAC electrocatalyst after AST 4 (96 h polarization at E = 1.0 V *vs.* RHE and T = 330 K in 0.1 M H_2SO_4 + CVs + "pseudo" CO_{ad} stripping voltammograms).

3.6 Influence of the nature of the carbon support, the gas atmosphere and the potential limits used in ASTs

Under steady-state PEMFC operation, the potential of a PEMFC cathode varies between 0.60 V and 1.0 V *vs.* RHE (depending on the current density), while under start-up/shutdown conditions, the electrode potential may reach up to 1.5 V *vs.* the RHE [20, 70, 71]. The degradation of the carbon support may also be different in different gas atmospheres.

To investigate the effect of these parameters, different ASTs were performed on HSAC, Vulcan TKK and RG carbon supports under neutral (argon) and oxidative (oxygen) atmosphere. Two distinct protocols were used: a load-cycle protocol with a square potential

ramp between 0.60 V – 1.00 V and a start-up/shutdown protocol with a square potential ramp between 1.00 V –1.50 V *vs*. RHE, which mimic the potential range experienced during steady-state and start-up/shutdown cycles, respectively. These ASTs are based on the Fuel Cell Commercialization Conference of Japan (FCCJ) protocols [20].

In the potential range used in the load-cycle protocol, simultaneous degradations may occur: (*i*) the electrochemical oxidation of the HSAC support (*ii*) the Pt-catalysed carbon corrosion (*iii*) the formation/reduction of Pt surface oxide, which facilitates (*iv*) the dissolution/redeposition of the Pt nanocrystallites, (*v*) the reduction of oxygen to water or hydrogen peroxide (H_2O_2). In start-up/shutdown conditions, (*i*) the strong oxidation of the HSAC support and (*ii*) the electrochemical oxidation of the Pt surface, which results into the penetration of oxygen into the Pt lattice (place-exchange), are likely to occur [72].

3.6.1 Electrochemical results

Figure III - 25 shows the ECSA losses monitored for the 40 wt. % Pt/HSAC, the 40 wt. % Pt/Vulcan TKK and the 40 wt. % Pt/RG electrocatalysts under the different AST conditions. Three general observations outstand from the following results: firstly, oxygen has a negligible effect on the ECSA losses both in load-cycle and start-up/shutdown protocols, secondly, the ECSA losses depend on the electrochemical potential range experienced by the Pt/C electrocatalyst; and thirdly, the ECSA losses depend on the structure of the carbon support, more particularly during the start-up/shutdown protocol.

For the different carbon supports and for all AST protocols, similar ECSA losses are monitored in neutral (Figure III - 25 a and Figure III - 25 b) and in oxidizing atmosphere (Figure III - 25 c and Figure III - 25 d). This result suggests that water is the main oxidizing agent when the ASTs are performed in aqueous solution. The strong effect of water partial pressure on the extent of degradation of the metal nanoparticles [73, 74] and the carbon support [74, 75] is well-documented in the literature.

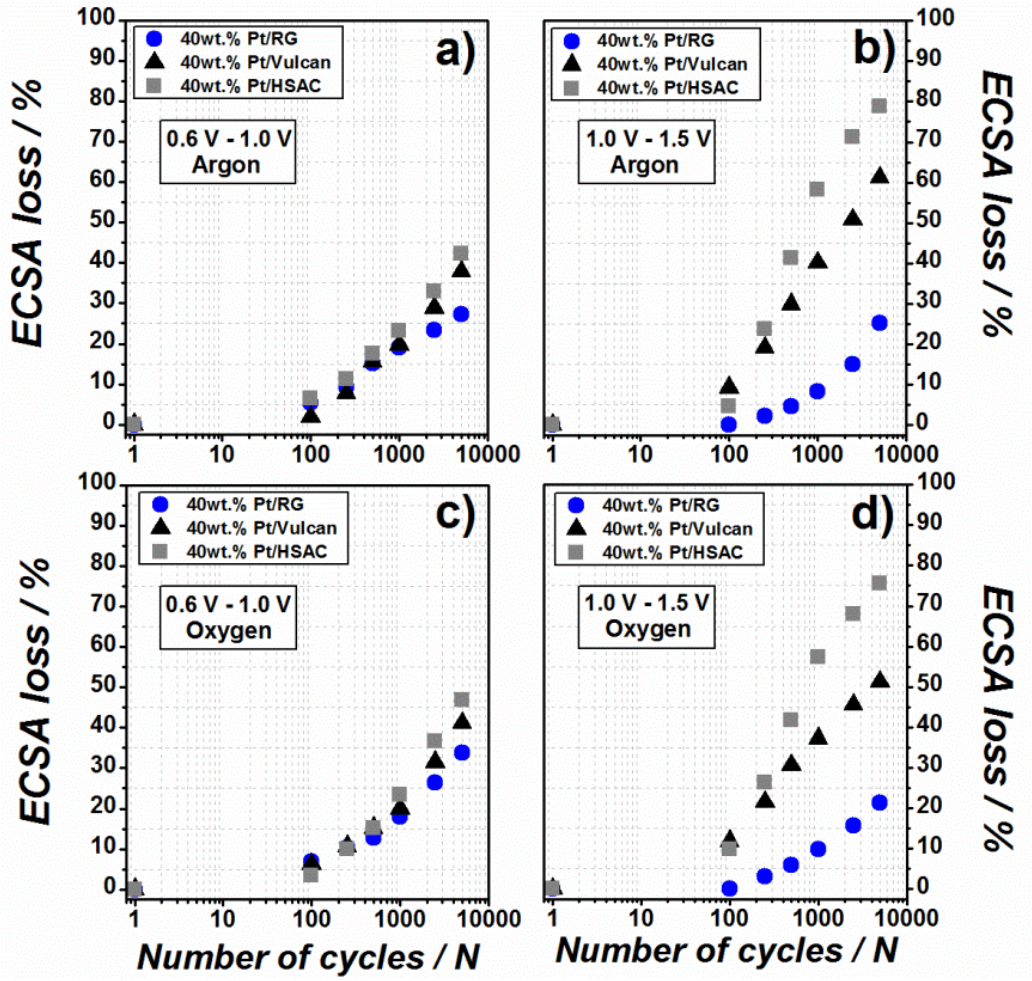

Figure III - 25. ECSA losses monitored for the 40 wt. % Pt/HSAC, the 40 wt. % Pt/Vulcan and the 40 wt. % Pt/RG electrocatalysts tested with FCCJ protocols under argon (a) and b)) or oxygen (c) and d)) atmosphere. To avoid the detrimental effect of intermediate characterizations, the ECSA losses were estimated as described in Chapter II. Electrolyte: 0.1 M H_2SO_4; $v = 0.100$ V s^{-1}; $T = 330$ K.

The superior ECSA losses monitored during the start-up/shutdown protocol reflect the Nernstian activation of the COR. The ECSA losses for the 40 wt. % Pt/HSAC electrocatalyst amount to *ca*. 45 % , and *ca*. 80 % after 5,000 potential cycles in the load-cycle and the start-up/shutdown protocol, respectively. This result confirms that transients to high electrode potential are extremely aggressive for the electrocatalyst, in agreement with former literature reports [76-78]. As a consequence, during the load-cycle protocol, the ECSA losses for the three Pt/C electrocatalysts start to diverge after ~2,500 cycles, while for the start-up/shutdown protocol different tendencies are already observed after ~100 cycles.

Since the studied electrocatalysts have the same Pt mass fraction, the disparate tendencies observed in this sub-chapter point towards a strong effect of the structure of the carbon support. The ECSA losses for the Vulcan and HSAC carbon supports amount to *ca.* 40

% for the load-cycle protocol, and *ca* 60/80 % for the start-up/shutdown protocol, respectively. Meanwhile, they reach only 25 % for the RG carbon support for both load-cycle and start-up/shutdown protocols. These conclusions agree with literature reports that highly graphitized carbon supports are more robust than disordered carbon supports (such as HSAC and Vulcan) [35, 79-81]. Moreover, the different ECSA losses monitored during the load-cycle and the start-up/shutdown protocols suggest that the structure of the carbon support dominates the rate of degradation of the Pt/C electrocatalysts at electrode potential $E > 1.0$ V *vs.* RHE. This will be confirmed in the forthcoming chapter.

To better understand the impact of the AST protocols on the different carbon supports, the variations of the electrical charge of the quinone-hydroquinone (Q/HQ) peak were monitored over time. Figure III - 26 shows that the Q/HQ charge strongly depends on the applied AST protocol and on the structure of the carbon support. Contrary to what was observed in terms of ECSA losses, the oxygen atmosphere significantly affects the charge of the Q/HQ peak. Under neutral atmosphere, a slight increase of the Q/electrical charge is observed during the load-cycle protocol for the less organized supports, while no variation is visible on the RG support. During the start-up/shutdown protocol, a gradual increase of the Q/HQ charge is observed for the three carbon supports until a maximum is reached after which the charge is decreasing. Interestingly, the number of potential cycles needed to reach this maximum is inversely proportional to the specific surface area/mean crystallite size of the carbon support (see Table II-1): a maximal value of the Q/HQ charge is observed at ~500 cycles for the HSAC and the Vulcan TKK carbon supports and a continuous increase is observed on the RG support. Performing the ASTs under oxidizing atmosphere slightly modifies the experimental trends observed in neutral atmosphere. During the load-cycle protocol, no increase of the Q/HQ charge is observed for the Vulcan support, contrary to the HSAC support, for which a continuous increase is monitored until ~500 potential cycles followed by a loss until the end of the AST. During the start-up/shutdown cycles, the effect of oxygen is most significant for the HSAC TKK and the RG carbon supports: the Q/HQ charge increased drastically in comparison to the same test performed under neutral atmosphere.

In summary, the results indicate that oxygen effectively changes the surface chemistry of the carbon supports, but such changes do not significantly influence the ECSA losses.

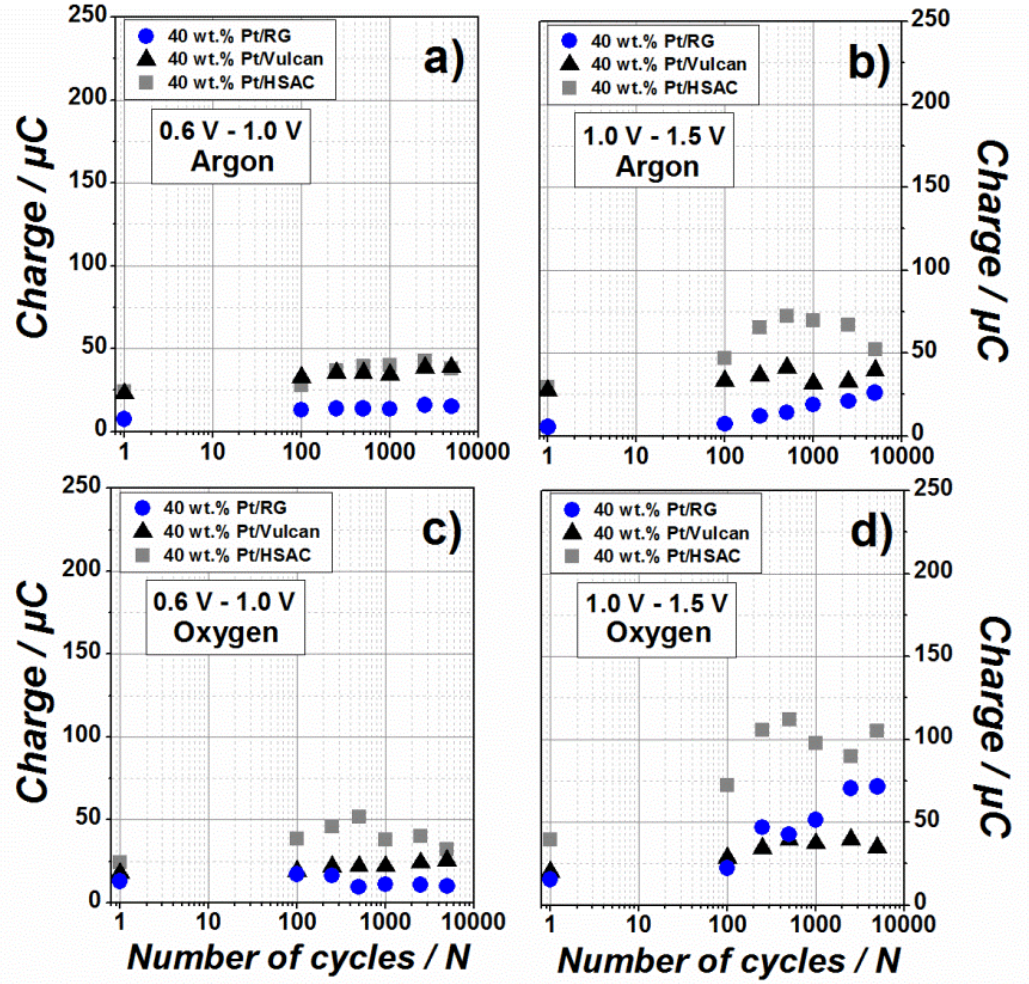

Figure III - 26. Variation of the electrical charge of the quinone-hydroquinone redox peak monitored for the 40 wt. % Pt/HSAC, the 40 wt. % Pt/Vulcan and the 40 wt. % Pt/RG electrocatalysts during the FCCJ protocols under argon (a) and b)) or oxygen (c) and d)) atmosphere. The current monitored between E = 0.40 and 0.77 V *vs.* RHE corrected from the interfacial double-layer contribution measured at E = 0.40 V *vs.* RHE.

3.6.2 Structural modifications of the carbon supports after the ASTs

Figure III - 27 shows normalized Raman spectra monitored on the carbon supports after the FCCJ protocols under neutral and oxidizing atmosphere. On the basis of the ratio between the intensities of the D1 and G-bands, the start-up/shutdown protocol appears to be the most harmful towards the structure of the carbon supports, independently of the nature of the atmosphere.

While no significant change is evidenced in the Raman spectra of the HSAC supports subjected to the load-cycle protocol, a pronounced decrease in the intensity of the D1-band is observed during the start-up/shutdown protocol. This variation suggests that the disorganized domains of the HSAC support are preferentially oxidized during the start-up/shutdown protocol, in agreement with our previous findings (see sub-chapter 3.4). A shoulder appears at $\overline{\upsilon} \sim 1760$ cm^{-1} after this AST under argon atmosphere, the intensity of which is minored

under oxidizing atmosphere. This band is active both in infrared [68] and Raman spectroscopy [13, 28, 82], and is ascribed to the C=O stretch vibration of carbonyl groups of carboxylic acids, or lactone groups. This experimental trend suggests that the HSAC surface becomes more oxidized under the start-up/shutdown protocol. Interestingly, the formed CO_{surf} species are irreversibly oxidized under oxygen atmosphere (see the decrease in intensity of the 1760 cm^{-1} Raman band in oxygen *vs.* argon atmosphere). It is surprising to note that similar changes of the shape and of the intensity of the D1 and G bands are observed for the Vulcan TKK during the load-cycle and the start-up/shutdown protocols (the I_D/I_G ratio does not change and a slight thinning of the G-band is observed). On the contrary, for the RG carbon support, different experimental trends are observed depending on the applied ageing protocol and on the atmosphere used. When the load-cycle protocol is performed under neutral atmosphere, a pronounced increase of D1-band intensity is observed: this indicates that edge-type defects are formed in the graphite crystallites. The formation of the edge-defects is intensified during the start-up/shutdown protocol (further increase of D1-band intensity) and, at the same time, is accompanied by the formation of surface-defects (appearance of a Raman band at $\bar{\upsilon} \sim 1620$ cm^{-1}). These trends are maintained under oxidizing atmosphere; however, the lower intensities of D1 and the D2 Raman bands monitored for this test confirm that the CO_{surf} groups are unstable under oxidizing atmosphere.

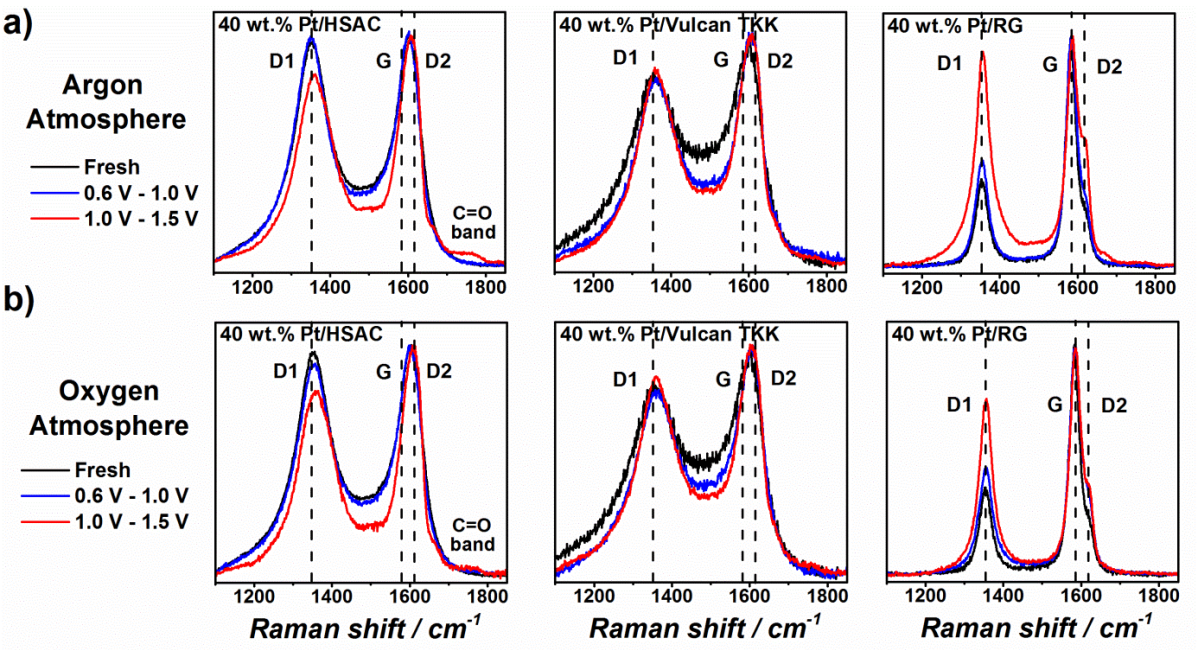

Figure III - 27. Normalized Raman spectra of the HSAC, Vulcan and RG carbon supports before/after the FCCJ protocols under a) argon or b) oxygen atmosphere.

3.6.3 Structural modifications of the Pt nanoparticles after the ASTs

In the following, the TEM characterization of the carbon supports tested under neutral atmosphere are discussed. Figure III - 28 and Figure III - 29 show representative TEM images obtained after 5,000 potential cycles under the load-cycle and the start-up/shutdown protocols, respectively. The reader is referred to **sub-chapter 3.2 (Figure III - 5)** for TEM images of the fresh electrocatalysts.

After the load-cycle protocol, individual (*i.e.* non-agglomerated) Pt nanoparticles are present in large quantity on the carbon supports, more particularly on the HSAC. The mean Pt particle size increased for all the electrocatalysts, following the electrochemical Ostwald ripening *i.e.* the preferential dissolution of the smallest Pt crystallites, yielding the formation of Pt^{z+} ions and their redeposition onto larger particles. Although it is difficult to judge from TEM images, minor morphological changes of the primary carbon nanoparticles are observed after this protocol (Figure III - 28 d) to i)). Combined with the observations derived from Raman spectra, these results suggest that the load-cycle protocol is essentially deleterious for the Pt nanoparticles.

On the contrary, after the start-up/shutdown protocol, significant agglomeration of the Pt nanoparticles and severe degradation of the carbon support are witnessed. This holds especially true for less organized carbon supports. The density of individual – non-agglomerated – Pt nanoparticles drastically decreased relative to what was observed after the load-cycle protocol, suggesting that their detachment was promoted by the corrosion of the carbon support [78]. This is confirmed by the emergence of complex Pt nanoparticle shapes and massive Pt agglomerates in the TEM images of the aged Pt/HSAC and Pt/Vulcan TKK electrocatalysts (Figure III - 29a and b). It is clear from TEM images how the structure of the carbon supports is affected during the excursions at high electrode potentials. For the HSAC carbon support, the classical organization of the carbon blacks (*i.e.* primary carbon particles – aggregates - agglomerates) is blurred, and the remaining carbon particles appear amorphous (Figure III - 29d and g). Part of this organization is maintained for the Vulcan TKK support, but large areas are now depleted from Pt particles. Due to its highly-ordered graphitic nature, the RG support feature minor changes. The highly oriented and parallel graphitic crystallites present at the edges of the carbon particles, which were observed on the fresh Pt/RG electrocatalyst are still present (Figure III - 29f), but some zones start to evidence structural changes possibly due to amorphization of the support (see Figure III - 29i).

It is interesting to link the ECSA losses (Figure III - 25) to the morphological changes of the Pt/C electrocatalysts. The moderate losses monitored during the load-cycle protocol are mainly due to Pt nanoparticle coalescence/agglomeration or dissolution/re-deposition of Pt nanocrystallites (electrochemical Ostwald ripening) as shown by the Raman spectra and the TEM images. During the start-up/shutdown protocol, the inherent corrosion resistance of the carbon supports appears to be key.

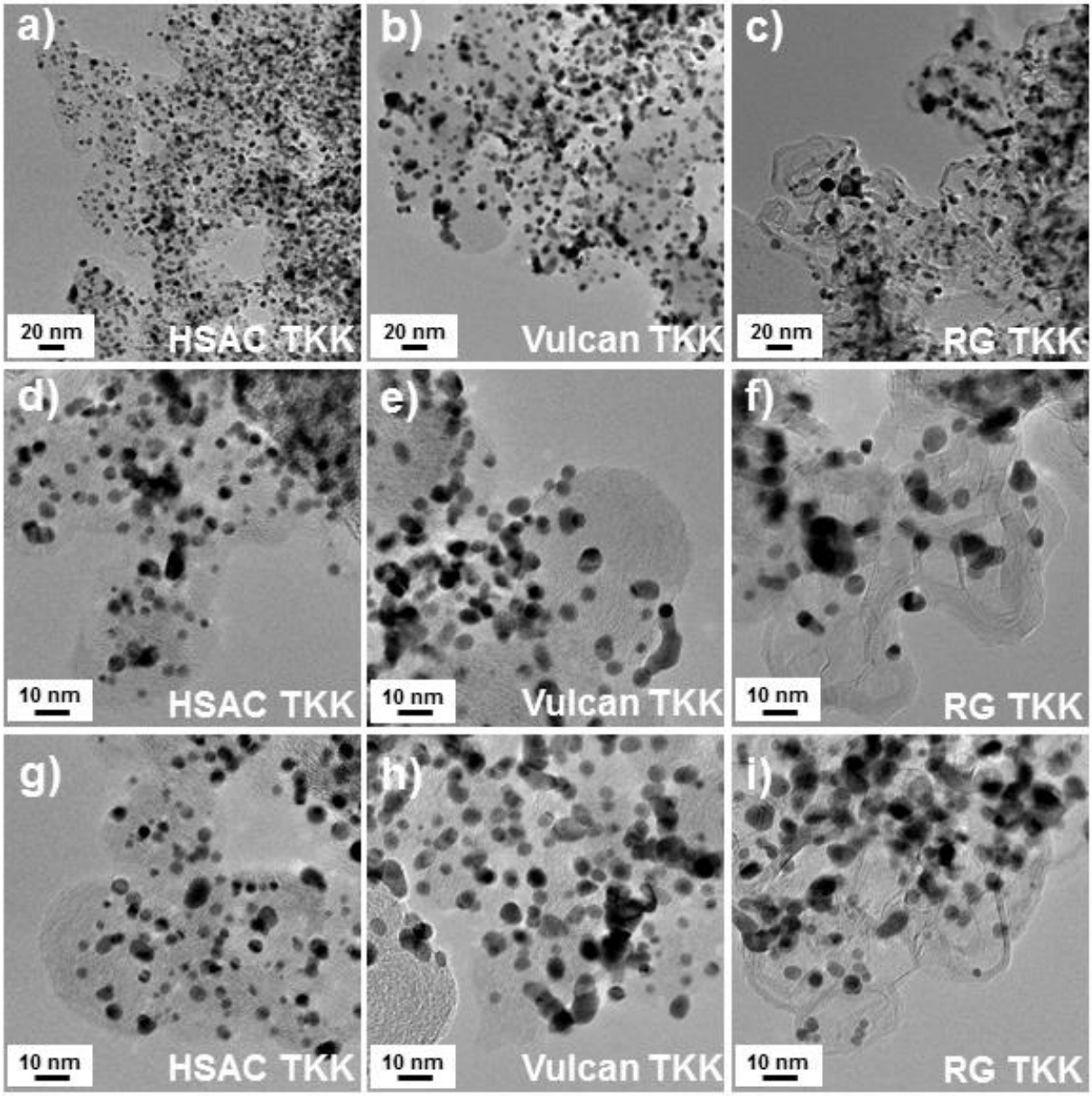

Figure III - 28. TEM images of the different carbon supports before/after 5,000 FCCJ load-cycles under argon atmosphere: a), d) and g) HSAC, b), e) and h) Vulcan TKK, c), f) and i) RG.

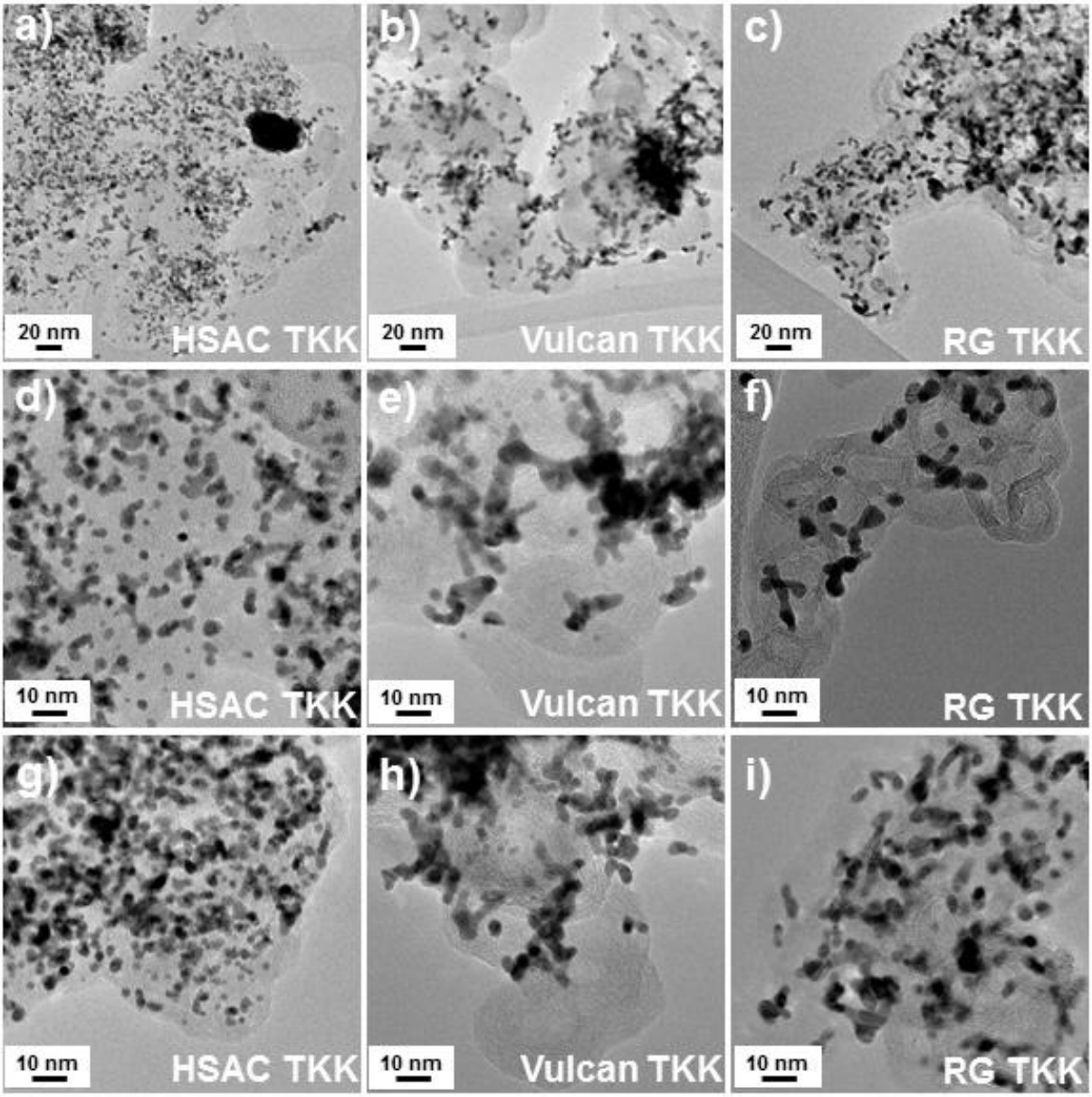

Figure III - 29. TEM images of the different carbon supports before/after 5,000 FCCJ start-up/shutdown cycles under argon atmosphere: a), d) and g) HSAC, b), e) and h) Vulcan TKK, c), f) and i) RG.

3.7 Conclusion

In this chapter, the structural properties of different state-of-the-art carbon supports used in PEMFCs were characterized. The HSAC and the Vulcan are the less organized supports, due to the coexistence of disordered and ordered graphitic domains in their primary carbon nanoparticles. The RG carbon support is the most organized support, presenting mainly ordered graphitic domains in its structure.

In a second point, different issues concerning the effect of experimental procedures were addressed, with the objective of understanding their effect on the surface chemistry of the carbon support:

- The influence of Nafion® as the binder of the catalyst and the storage conditions of the suspensions were studied. It was revealed that the surface chemistry of the carbon supports is sensible to the presence of Nafion® and the initial electrochemical characterization. In addition, the storage conditions of the electrocatalyst inks induces a non-monotonical evolution of the carbon support. At short-term, the surface chemistry of the carbon support changes and at long-term, the structure of the carbon support is modified.

- The introduction of "measure-artefacts" by electrochemical techniques to the final degradation of the ASTs was demonstrated. Intermediate characterizations performed during accelerated stress tests intensify the ECSA losses. These characterizations are required to access the ECSA changes during the AST but actually level off the "real" degradation rate of the Pt/HSAC. The results highlight that the number and the nature of intermediate characterizations should be controlled when designing new ASTs. Ideally, individual electrodes should be used to get an accurate evaluation of the ECSA variations over time during ASTs.

- The influence of the potential limits, the gas atmosphere and the carbon surface chemistry were investigated by applying the FCCJ protocols. The ECSA losses are dependent on the electrochemical potential range and of the structure of the carbon support. The oxidizing atmosphere has no significant effect on the ECSA loss but affects the Q/HQ peak and consequently the CO_{surf} species. The load-cycle protocol induces Pt nanoparticle degradation while the start-up/shutdown protocol induces corrosion of the carbon support.

References

[1] F. Tuinstra, J.L. Koenig, Raman spectrum of graphite, The Journal of Chemical Physics, 53 (1970) 1126-1130.
[2] M. Nakamizo, H. Honda, M. Inagaki, Raman spectra of ground natural graphite, Carbon, 16 (1978) 281-283.
[3] M. Nakamizo, K. Tamai, Raman spectra of the oxidized and polished surfaces of carbon, Carbon, 22 (1984) 197-198.
[4] L.G.d.O.L. Cançado, Raman spectroscopy of nanographites, Universidade Federal de Minas Gerais, Brasil, 2006.
[5] M.A. Pimenta, G. Dresselhaus, M.S. Dresselhaus, L.G. Cancado, A. Jorio, R. Saito, Studying disorder in graphite-based systems by Raman spectroscopy, Physical Chemistry Chemical Physics, 9 (2007) 1276-1290.
[6] D.S. Knight, W.B. White, Characterization of diamond films by Raman spectroscopy, Journal of Materials Research, 4 (1989) 385-393.
[7] R.P. Vidano, D.B. Fischbach, L.J. Willis, T.M. Loehr, Observation of Raman band shifting with excitation wavelength for carbons and graphites, Solid State Communications, 39 (1981) 341-344.
[8] T.P. Mernagh, R.P. Cooney, R.A. Johnson, Raman spectra of Graphon carbon black, Carbon, 22 (1984) 39-42.
[9] M.J. Matthews, M.A. Pimenta, G. Dresselhaus, M.S. Dresselhaus, M. Endo, Origin of dispersive effects of the Raman D band in carbon materials, Physical Review B, 59 (1999) R6585-R6588.
[10] T. Gruber, T.W. Zerda, M. Gerspacher, Raman studies of heat-treated carbon blacks, Carbon, 32 (1994) 1377-1382.
[11] T. Jawhari, A. Roid, J. Casado, Raman spectroscopic characterization of some commercially available carbon black materials, Carbon, 33 (1995) 1561-1565.
[12] J. Schwan, S. Ulrich, V. Batori, H. Ehrhardt, S.R.P. Silva, Raman spectroscopy on amorphous carbon films, Journal of Applied Physics, 80 (1996) 440-447.
[13] S.K. Sze, N. Siddique, J.J. Sloan, R. Escribano, Raman spectroscopic characterization of carbonaceous aerosols, Atmospheric Environment, 35 (2001) 561-568.
[14] T. Ungár, J. Gubicza, G. Ribárik, C. Pantea, T.W. Zerda, Microstructure of carbon blacks determined by X-ray diffraction profile analysis, Carbon, 40 (2002) 929-937.
[15] A. Sadezky, H. Muckenhuber, H. Grothe, R. Niessner, U. Pöschl, Raman microspectroscopy of soot and related carbonaceous materials: Spectral analysis and structural information, Carbon, 43 (2005) 1731-1742.
[16] G.A. Zickler, B. Smarsly, N. Gierlinger, H. Peterlik, O. Paris, A reconsideration of the relationship between the crystallite size La of carbons determined by X-ray diffraction and Raman spectroscopy, Carbon, 44 (2006) 3239-3246.
[17] M.R. Baldan, E.C. Almeida, A.F. Azevedo, E.S. Gonçalves, M.C. Rezende, N.G. Ferreira, Raman validity for crystallite size La determination on reticulated vitreous carbon with different graphitization index, Applied Surface Science, 254 (2007) 600-603.
[18] L.G. Cancado, K. Takai, T. Enoki, M. Endo, Y.A. Kim, H. Mizusaki, A. Jorio, L.N. Coelho, R. Magalhaes-Paniago, M.A. Pimenta, General equation for the determination of the crystallite size La of nanographite by Raman spectroscopy, Applied Physics Letters, 88 (2006) 163106-163103.
[19] U.S.C.f.A.R. LLC, Cell component accelerated stress test and polarization curve protocols for polymer electrolyte membrane fuel cells, (2011) Accesible at: www.uscar.org/guest/view_team.php?teams_id=17.
[20] A. Ohma, K. Shinohara, A. Iiyama, T. Yoshida, A. Daimaru, Membrane and catalyst performance targets for automotive fuel cells by FCCJ membrane, catalyst, MEA WG, ECS Transactions, 41 (2011) 775-784.
[21] S.C. Ball, S.L. Hudson, D. Thompsett, B. Theobald, An investigation into factors affecting the stability of carbons and carbon supported platinum and platinum/cobalt alloy catalysts during 1.2 V potentiostatic hold regimes at a range of temperatures, Journal of Power Sources, 171 (2007) 18-25.
[22] J. Wang, G. Yin, Y. Shao, S. Zhang, Z. Wang, Y. Gao, Effect of carbon black support corrosion on the durability of Pt/C catalyst, Journal of Power Sources, 171 (2007) 331-339.

[23] C.-C. Hung, P.-Y. Lim, J.-R. Chen, H.C. Shih, Corrosion of carbon support for PEM fuel cells by electrochemical quartz crystal microbalance, Journal of Power Sources, 196 (2011) 140-146.
[24] K.G. Gallagher, T.F. Fuller, Kinetic model of the electrochemical oxidation of graphitic carbon in acidic environments, Physical Chemistry Chemical Physics, 11 (2009) 11557-11567.
[25] A.A. Topalov, I. Katsounaros, M. Auinger, S. Cherevko, J.C. Meier, S.O. Klemm, K.J.J. Mayrhofer, Dissolution of platinum: Limits for the deployment of electrochemical energy conversion?, Angewandte Chemie International Edition, 51 (2012) 12613-12615.
[26] K. Kinoshita, J.T. Lundquist, J. Bett, Potential cycling effects on platinum electrocatalyst surfaces, Electroanalytical Chemistry and InterJacial Electrochemistry, 48 (1973) 157-166.
[27] N. Linse, L. Gubler, G.G. Scherer, A. Wokaun, The effect of platinum on carbon corrosion behavior in polymer electrolyte fuel cells, Electrochimica Acta, 56 (2011) 7541-7549.
[28] M. Hara, M. Lee, C.-H. Liu, B.-H. Chen, Y. Yamashita, M. Uchida, H. Uchida, M. Watanabe, Electrochemical and Raman spectroscopic evaluation of Pt/graphitized carbon black catalyst durability for the start/stop operating condition of polymer electrolyte fuel cells, Electrochimica Acta, 70 (2012) 171-181.
[29] G.-G. Park, T.-H. Yang, Y.-G. Yoon, W.-Y. Lee, C.-S. Kim, Pore size effect of the DMFC catalyst supported on porous materials, International Journal of Hydrogen Energy, 28 (2003) 645-650.
[30] F. Maillard, P.A. Simonov, E.R. Savinova, Carbon Materials for Catalysis, in: P. Serp, J.L. Figueiredo (Eds.) Carbon Materials for Catalysis, John Wiley & Sons2009, pp. 429 - 480.
[31] F. Rodríguez-Reinoso, I. Rodríguez-Ramos, C. Moreno-Castilla, A. Guerrero-Ruiz, J.D. López-González, Platinum catalysts supported on activated carbons: I. Preparation and characterization, Journal of Catalysis, 99 (1986) 171-183.
[32] A.E. Aksoylu, M. Madalena, A. Freitas, M.F.R. Pereira, J.L. Figueiredo, The effects of different activated carbon supports and support modifications on the properties of Pt/AC catalysts, Carbon, 39 (2001) 175-185.
[33] R.D. Heidenreich, W.M. Hess, L.L. Ban, A test object and criteria for high resolution electron microscopy, Journal of Applied Crystallography, 1 (1968) 1.
[34] K. Kinoshita, Carbon: Electrochemical and physicochemical properties, John Wiley & Sons, New York, 1988.
[35] K. Miyazaki, H. Shirakata, T. Abe, N. Yoshizawa, Z. Ogumi, Novel graphitised carbonaceous materials for use as a highly corrosion-tolerant catalyst support in polymer electrolyte fuel cells, Fuel Cells, 10 (2010) 960-965.
[36] Y. Garsany, O.A. Baturina, K.E. Swider-Lyons, S.S. Kocha, Experimental methods for quantifying the activity of platinum electrocatalysts for the oxygen reduction reaction, Analytical Chemistry, 82 (2010) 6321-6328.
[37] H.P. Boehm, Surface oxides on carbon and their analysis: a critical assessment, Carbon, 40 (2002) 145-149.
[38] T.J. Bandosz, Surface Chemistry of Carbon Materials, in: P. Serp, J. Figueiredo (Eds.) Carbon Materials for Catalysis, John Wiley & Sons, Inc2009, pp. 45 - 92.
[39] K. Kinoshita, J.A.S. Bett, Potentiodynamic analysis of surface oxides on carbon blacks, Carbon, 11 (1973) 403-411.
[40] N. Giordano, P.L. Antonucci, E. Passalacqua, L. Pino, A.S. Aricò, K. Kinoshita, Relationship between physicochemical properties and electrooxidation behaviour of carbon materials, Electrochimica Acta, 36 (1991) 1931-1935.
[41] K.H. Kangasniemi, D.A. Condit, T.D. Jarvi, Characterization of vulcan electrochemically oxidized under simulated PEM fuel cell conditions, Journal of The Electrochemical Society, 151 (2004) E125-E132.
[42] B. Avasarala, R. Moore, P. Haldar, Surface oxidation of carbon supports due to potential cycling under PEM fuel cell conditions, Electrochimica Acta, 55 (2010) 4765-4771.
[43] G. Álvarez, F. Alcaide, O. Miguel, P.L. Cabot, M.V. Martínez-Huerta, J.L.G. Fierro, Electrochemical stability of carbon nanofibers in proton exchange membrane fuel cells, Electrochimica Acta, 56 (2011) 9370-9377.
[44] Y. Shao, G. Yin, Y. Gao, P. Shi, Durability study of Pt/C and Pt/CNTs satalysts under simulated PEM fuel cell conditions, Journal of The Electrochemical Society, 153 (2006) A1093-A1097.

[45] O.V. Cherstiouk, P.A. Simonov, V.B. Fenelonov, E.R. Savinova, Influence of Nafion® ionomer on carbon corrosion, J Appl Electrochem, 40 (2010) 1933-1939.
[46] M. Uchida, Y. Aoyama, N. Eda, A. Ohta, Investigation of the microstructure in the catalyst layer and effects of both perfluorosulfonate ionomer and PTFE loaded carbon on the catalyst layer of polymer electrolyte fuel cells, Journal of The Electrochemical Society, 142 (1995) 4143-4149.
[47] M. Uchida, Y. Fukuoka, Y. Sugawara, N. Eda, A. Ohta, Effects of microstructure of carbon support in the catalyst layer on the performance of polymer electrolyte fuel cells, Journal of The Electrochemical Society, 143 (1996) 2245-2252.
[48] M. Uchida, Y. Fukuoka, Y. Sugawara, H. Ohara, A. Ohta, Improved preparation process of very low platinum loading electrodes for polymer electrolyte fuel cells, Journal of The Electrochemical Society, 145 (1998) 3708-3713.
[49] T. Soboleva, X. Zhao, K. Malek, Z. Xie, T. Navessin, S. Holdcroft, On the micro-, meso-, and macroporous structures of polymer electrolyte membrane fuel cell catalyst layers, ACS Applied Materials & Interfaces, 2 (2010) 375-384.
[50] T. Soboleva, K. Malek, Z. Xie, T. Navessin, S. Holdcroft, PEMFC catalyst layers: The role of micropores and mesopores on water sorption and fuel cell activity, ACS Applied Materials & Interfaces, 3 (2011) 1827-1837.
[51] M. Lee, M. Uchida, H. Yano, D.A. Tryk, H. Uchida, M. Watanabe, New evaluation method for the effectiveness of platinum/carbon electrocatalysts under operating conditions, Electrochimica Acta, 55 (2010) 8504-8512.
[52] M. Lee, M. Uchida, D.A. Tryk, H. Uchida, M. Watanabe, The effectiveness of platinum/carbon electrocatalysts: Dependence on catalyst layer thickness and Pt alloy catalytic effects, Electrochimica Acta, 56 (2011) 4783-4790.
[53] H. Uchida, J.M. Song, S. Suzuki, E. Nakazawa, N. Baba, M. Watanabe, Electron tomography of Nafion ionomer coated on Pt/Carbon black in high utilization electrode for PEFCs, The Journal of Physical Chemistry B, 110 (2006) 13319-13321.
[54] F. Maillard, M. Eikerling, O.V. Cherstiouk, S. Schreier, E. Savinova, U. Stimming, Size effects on reactivity of Pt nanoparticles in CO monolayer oxidation: The role of surface mobility, Faraday Discussions, 125 (2004) 357-377.
[55] F. Maillard, E.R. Savinova, P.A. Simonov, V.I. Zaikovskii, U. Stimming, Infrared spectroscopic study of CO adsorption and electro-oxidation on carbon-supported Pt nanoparticles: Interparticle versus intraparticle heterogeneity, The Journal of Physical Chemistry B, 108 (2004) 17893-17904.
[56] F. Maillard, S. Schreier, M. Hanzlik, E.R. Savinova, S. Weinkauf, U. Stimming, Influence of particle agglomeration on the catalytic activity of carbon-supported Pt nanoparticles in CO monolayer oxidation, Physical Chemistry Chemical Physics, 7 (2005) 385-393.
[57] K.J.J. Mayrhofer, M. Arenz, B.B. Blizanac, V. Stamenkovic, P.N. Ross, N.M. Markovic, CO surface electrochemistry on Pt-nanoparticles: A selective review, Electrochimica Acta, 50 (2005) 5144-5154.
[58] P. Urchaga, S. Baranton, C. Coutanceau, G. Jerkiewicz, Electro-oxidation of COchem on Pt nanosurfaces: Solution of the peak multiplicity puzzle, Langmuir, 28 (2011) 3658-3663.
[59] V.I. Birss, M. Chang, J. Segal, Platinum oxide film formation—reduction: an in-situ mass measurement study, Journal of Electroanalytical Chemistry, 355 (1993) 181-191.
[60] Z. Nagy, H. You, Applications of surface X-ray scattering to electrochemistry problems, Electrochimica Acta, 47 (2002) 3037-3055.
[61] X.P. Wang, R. Kumar, D.J. Myers, Effect of voltage on platinum dissolution relevance to polymer electrolyte fuel cells, Electrochem. Solid State Lett., 9 (2006) A225-A227.
[62] S.G. Rinaldo, W. Lee, J. Stumper, M. Eikerling, Model- and theory-based evaluation of Pt dissolution for supported Pt nanoparticle distributions under potential cycling, Electrochemical and Solid-State Letters, 14 (2011) B47-B49.
[63] D.C. Johnson, D.T. Napp, S. Bruckenstein, A ring-disk electrode study of the current/potential behaviour of platinum in 1.0 M sulphuric and 0.1 M perchloric acids, Electrochimica Acta, 15 (1970) 1493-1509.
[64] F. Maillard, A. Bonnefont, F. Micoud, An EC-FTIR study on the catalytic role of Pt in carbon corrosion, Electrochemistry Communications, 13 (2011) 1109-1111.

[65] Y.-C. Park, K. Kakinuma, M. Uchida, H. Uchida, M. Watanabe, Deleterious effects of interim cyclic voltammetry on Pt/carbon black catalyst degradation during start-up/shutdown cycling evaluation, Electrochimica Acta, 123 (2014) 84-92.
[66] K. Schlögl, K.J.J. Mayrhofer, M. Hanzlik, M. Arenz, Identical-location TEM investigations of Pt/C electrocatalyst degradation at elevated temperatures, Journal of Electroanalytical Chemistry, 662 (2011) 355-360.
[67] L. Dubau, M. Lopez-Haro, L. Castanheira, J. Durst, M. Chatenet, P. Bayle-Guillemaud, L. Guétaz, N. Caqué, E. Rossinot, F. Maillard, Probing the structure, the composition and the ORR activity of Pt3Co/C nanocrystallites during a 3422h PEMFC ageing test, Applied Catalysis B: Environmental, 142-143 (2013) 801-808.
[68] Z. Zhao, L. Castanheira, L. Dubau, G. Berthomé, A. Crisci, F. Maillard, Carbon corrosion and platinum nanoparticles ripening under open circuit potential conditions, Journal of Power Sources, 230 (2013) 236-243.
[69] L. Dubau, L. Castanheira, G. Berthomé, F. Maillard, An identical-location transmission electron microscopy study on the degradation of Pt/C nanoparticles under oxidizing, reducing and neutral atmosphere, Electrochimica Acta, (2013).
[70] A. Lamibrac, G. Maranzana, O. Lottin, J. Dillet, J. Mainka, S. Didierjean, A. Thomas, C. Moyne, Experimental characterization of internal currents during the start-up of a proton exchange membrane fuel cell, Journal of Power Sources, 196 (2011) 9451-9458.
[71] S. Didierjean, A. Lamibrac, T. Geneston, A. Rakotondrainibe, G. Maranzana, E. Rozier, F. Beille, O. Lottin, Internal currents in response to a load change during fuel cell start-up, International Journal of Hydrogen Energy, 37 (2012) 6798-6807.
[72] B.E. Conway, Electrochemical oxide film formation at noble metals as a surface-chemical process, Progress in Surface Science, 49 (1995) 331-452.
[73] J. Xie, D.L. Wood , D.M. Wayne, T.A. Zawodzinski, P. Atanassov, R.L. Borup, Durability of PEFCs at high humidity conditions, Journal of The Electrochemical Society, 152 (2005) A104-A113.
[74] F.R. Nikkuni, B. Vion-Dury, L. Dubau, F. Maillard, E.A. Ticianelli, M. Chatenet, The role of water in the degradation of Pt3Co/C nanoparticles: An identical location transmission electron microscopy study in polymer electrolyte environment, Applied Catalysis B: Environmental, 156–157 (2014) 301-306.
[75] N. Takeuchi, T.F. Fuller, Investigation of carbon loss on the cathode during PEMFC operation, ECS Transactions, 16 (2008) 1563-1571.
[76] C.A. Reiser, L. Bregoli, T.W. Patterson, J.S. Yi, J.D. Yang, M.L. Perry, T.D. Jarvi, A reverse-current decay mechanism for fuel cells, Electrochemical and Solid-State Letters, 8 (2005) A273-A276.
[77] Y. Ishigami, K. Takada, H. Yano, J. Inukai, M. Uchida, Y. Nagumo, T. Hyakutake, H. Nishide, M. Watanabe, Corrosion of carbon supports at cathode during hydrogen/air replacement at anode studied by visualization of oxygen partial pressures in a PEFC—Start-up/shut-down simulation, Journal of Power Sources, 196 (2011) 3003-3008.
[78] Y.-C. Park, K. Kakinuma, M. Uchida, D.A. Tryk, T. Kamino, H. Uchida, M. Watanabe, Investigation of the corrosion of carbon supports in polymer electrolyte fuel cells using simulated start-up/shutdown cycling, Electrochimica Acta, 91 (2013) 195-207.
[79] O.V. Cherstiouk, A.N. Simonov, N.S. Moseva, S.V. Cherepanova, P.A. Simonov, V.I. Zaikovskii, E.R. Savinova, Microstructure effects on the electrochemical corrosion of carbon materials and carbon-supported Pt catalysts, Electrochimica Acta, 55 (2010) 8453-8460.
[80] S. Vinod Selvaganesh, G. Selvarani, P. Sridhar, S. Pitchumani, A.K. Shukla, Graphitic carbon as durable cathode-catalyst support for PEFCs, Fuel Cells, 11 (2011) 372-384.
[81] H.-S. Oh, K.H. Lim, B. Roh, I. Hwang, H. Kim, Corrosion resistance and sintering effect of carbon supports in polymer electrolyte membrane fuel cells, Electrochimica Acta, 54 (2009) 6515-6521.
[82] Y. Hiramitsu, H. Sato, H. Hosomi, Y. Aoki, T. Harada, Y. Sakiyama, Y. Nakagawa, K. Kobayashi, M. Hori, Influence of humidification on deterioration of gas diffusivity in catalyst layer on polymer electrolyte fuel cell, J. Power Sources, 195 (2010) 435-444.

Chapter IV.

Carbon corrosion in PEMFCs: from model experiments to real-life operation in MEAs

The results discussed in this chapter have been published in:

Luis Castanheira, Laetitia Dubau, Michel Mermoux, Gregory Berthomé, Nicolas Caqué, Elisabeth Rossinot, Marian Chatenet and Frédéric Maillard
Carbon Corrosion in Proton-Exchange Membrane Fuel Cells: From Model Experiments to Real-Life Operation in Membrane Electrode Assemblies
ACS Catalysis 2014, 4, 2258 – 2267. DOI: 10.1021/cs500449q

The contribution of the author of this thesis includes the entirety of the experimental part (preparation and measurements of the properties of the catalytic layers), the treatment and the analysis of the Transmission Electron Microscopy, Raman and X-ray photoelectron spectroscopy data and the preparation of the manuscript for the publication.

4.1 Introduction

Early studies dealing with COR have been made in the context of phosphoric acid fuel cells (phosphoric acid electrolyte, 423 < *T* < 493 K) [1-4]. Because PEMFC systems operate at much lower temperature (*T* = 343 - 353 K), the COR was believed to be insignificant in PEMFC operating conditions, which was proven incorrect [5, 6]. Indeed, the low carbon dioxide/carbon standard potential E^0_{C/CO_2}= 0.207 V *vs* the normal hydrogen electrode (NHE) renders it thermodynamically possible in a PEMFC. The COR is mostly a concern at the cathode, [7, 8] in particular during start/stop or fuel starvation events, where the electrode potential may reach up to 1.5 V *vs*. the reversible hydrogen electrode (RHE) [9-11]. The localized fuel starvation events, such as those caused by blocking of a fuel channel or differences in H_2 partial pressure under the channel or the land during PEMFC start-up, also cause localized but severe carbon corrosion in PEMFC cathode electrode [12].

The mechanism of the COR is still not fully established but is believed to occur via the formation of carbon surface oxides and the evolution of CO_2 [2, 5, 13, 14]. The carbon surface oxide groups include but are not limited to phenols, ethers, ketones, carboxylic acids, and are referred to as CO_{surf} in what follows [1, 15]. Due to the observed power-law dependence of the COR rate and the increasing faradaic efficiency of CO_2 evolution over time, [2] Kinoshita *et al.* suggested that these groups act as passivation species for the reaction. The COR kinetics is strongly affected by the potential, the temperature, the morphology, the structure and the surface properties of carbon material [14, 16-18]. It is catalysed by the presence of Pt nanoparticles [6, 7, 19, 20], most likely through the spill-over of CO_{surf} species to the surface of the Pt nanoparticles and their further oxidation into CO_2 at potentials between 0.60 V and 0.80 V *vs.* RHE, where oxygenated species are nucleated on the catalytic surface [8]. The consequences of the COR involve (i) the agglomeration and/or detachment of the metal nanoparticles, which result into lower catalyst utilization and decrease the ECSA, [21-23] (ii) the decrease of the electrode porosity,[22] and (iii) the emergence of water management difficulties due to the growth of hydrophilic CO_{surf} groups [5]. The two latter processes yield increased mass-transport issues in the electrodes and are therefore particularly detrimental to their long-term performance [24].

The COR is currently studied by applying potentiostatic polarisation for several hours at electrode potentials ≥ 1.4 V *vs*. RHE [18, 25, 26], so as to mimic the excursion to high potential that a PEMFC cathode experiences during start/stop or fuel starvation events. These ASTs provide an efficient way to screen different carbon supports but they level-off their

resistance to corrosion, and provide poor mechanistic perspective. In addition, these excursions to high potential are far from the conditions that a PEMFC cathode experiences during the major part of its life: for example, during automotive fuel cell operation, the cathode potential lies between 0.70 V *vs.* RHE and the open-circuit potential (0.95 V *vs.* RHE) [27], *i.e.* a much narrower potential range than the one investigated in ASTs. This statement is particularly true during stationary operating conditions, for which the cathode mostly experiences electrode potentials lower than 0.90 V *vs*. RHE [28-31]. To the best of our knowledge, the degradation mechanisms of HSAC supports in these operating conditions have never been investigated, and are the focus of the present study.

Herein, a state-of-the-art Pt/HSAC electrocatalyst was subjected to long-term (96 h) polarization at different electrode potentials ranging from 0.40 V to 1.40 V *vs*. RHE and T = 330 K. The structural changes of the Pt/HSAC electrocatalyst were followed by Raman spectroscopy, while X-ray photoelectron spectroscopy (XPS) provided a chemical analysis of their surface. Finally, the observations made in model conditions were compared to those obtained during a long-term stationary PEMFC test (i = 0.25 A.cm^{-2}, 0.65 V < E_{cell} < 0.77 V, T = 335 K, t = 12,860 h, 250 start/stop events).

4.2 Results and Discussion

4.2.1 Electrochemical characterization

Figure IV - 1 displays intermediate cyclic voltammograms (CVs) recorded during the ASTs.

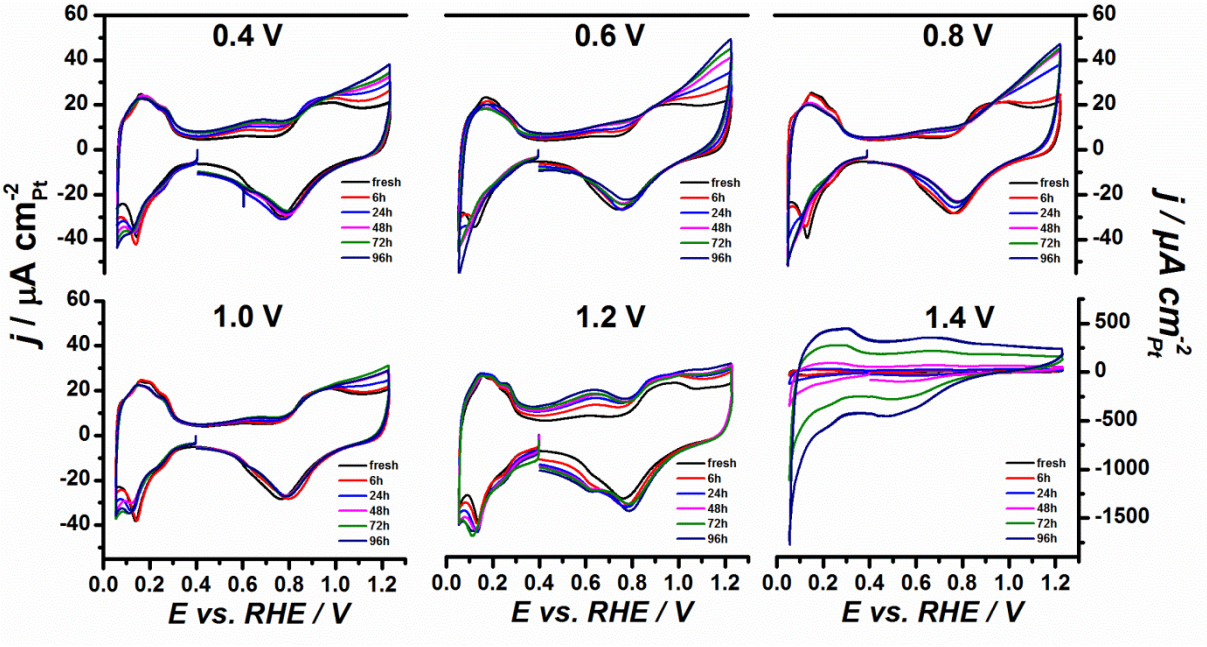

Figure IV - 1. Intermediate characterization cyclic voltammograms measured on the Pt/HSAC electrocatalysts during the ASTs. The current is normalized to the real surface area estimated by COad stripping coulometry. Electrolyte: 0.1 M H_2SO_4; v = 0.020 V s^{-1}; T = 330 K.

The electrochemical features obtained in the CVs depend on the polarization potential. When the potentiostatic AST was performed at E_{AST} = 0.40 V *vs*. RHE, a broad oxidation peak ($I > 0$) can be distinguished in the potential range $0.5 < E < 0.8$ V *vs*. RHE. This redox peak is ascribed to the one-electron transfer on quinone/hydroquinone (Q/HQ) groups [1]:

$$C = O_{(s)} + H^+ + e^- \leftrightarrow C - OH_{(s)} \qquad \text{(Eq. IV - 1)}$$

The larger electrical charge under this peak (positive-going potential sweep) relative to that measured on the pristine material points towards higher concentration of hydroquinone groups on the aged Pt/HSAC electrocatalyst surface. Similarly, "extra current" in the Pt surface oxide formation region (positive-going potential sweep, $E > 0.80$ V *vs*. RHE) relative to what is observed on the fresh Pt/HSAC indicates that other COR intermediates were formed during the 96 h-polarization at E_{AST} = 0.40 V *vs*. RHE (the under-potentially deposited

hydrogen region of Pt ($0.05 < E < 0.40$ V *vs*. RHE) being unchanged, this extra current does not originate from any Pt surface roughening).

Increasing the polarization potential to more positive values ($0.40 < E_{AST} < 0.80$ V *vs*. RHE) results in a decrease of the currents related to electron transfer on Q/HQ groups, and suggests that these functional groups were oxidized during the 96h polarization. Concomitantly, the "extra-current" in the potential region of $E > 0.80$ V *vs*. RHE is magnified, suggesting a larger surface concentration of CO_{surf} groups (that are not of the Q/HQ family). It is also interesting to note that the charge density associated with the under-potential deposition/desorption of protons on Pt depreciates with increasing values of E_{AST}. This may be rationalized by considering that CO_{surf} groups spill-over from the HSAC support to the Pt nanoparticles, where they dehydrogenate, and form CO molecules which adsorb on Pt [8]. When the AST was performed in the potential interval of $0.80 < E_{AST} < 1.00$ V *vs*. RHE, the formation of surface oxides on Pt (via water splitting) facilitated the removal of the adsorbed CO molecules. Consequently, no change of the charge density in the H_{upd} adsorption/desorption region was observed in the intermediate characterization CVs. For $E_{AST} > 1.00$ V, remarkable features emerged in the CVs: (i) the increase of the current in the potential region $0.50 < E < 0.80$ V *vs*. RHE (re-appearance of current ascribed to Q/HQ groups), (ii) the disappearance of the "extra-current" at $E > 0.80$ V *vs*. RHE and (iii) the increase of the interfacial double-layer capacitance. Since the capacitance of a Pt/HSAC-based electrode is essentially fixed by the HSAC support, the larger double-layer capacitance points towards more hydrophilic surface, and a possible increase of the carbon support roughness (creation of structural defects) [29, 32]. Summing up, the electrochemical characterizations suggest that the nature and the concentration of oxygen-containing surface groups formed as COR intermediates strongly depend on the applied potential during the stationary AST. Structural and chemical changes were noticed in the intermediate characterization CVs at potentials as low as $E_{AST} = 0.40$ V *vs*. RHE. These changes were magnified at $E_{AST} \geq 1.00$ V *vs*. RHE in the present experimental conditions (0.1 M H_2SO_4, $T =$ 330 K).

Figure IV - 2 displays the electrical charge of the quinone/hydroquinone (Q/HQ) peak for the fresh and the aged Pt/HSAC electrocatalysts.

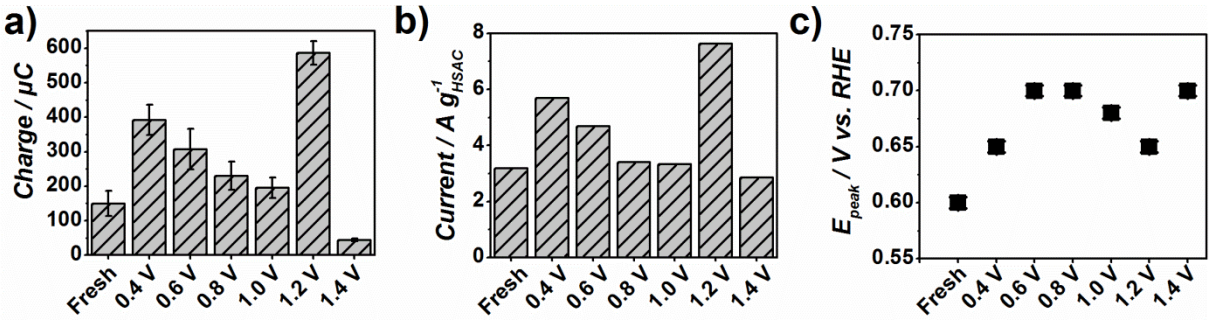

Figure IV - 2. Characteristic features of the quinone – hydroquinone (Q/HQ) redox couple after 96 h of polarization at different electrode potentials: (a) coulometry corrected from the interfacial double-layer contribution measured at E = 0.40 V *vs.* RHE (integration of the current between E = 0.40 and 0.75 V *vs*. RHE) b) mass-normalized oxidation current and c) peak potential. Electrolyte: 0.1 M H_2SO_4; v = 0.020 V s^{-1}; T = 330 K.

This charge was calculated from the positive-going potential sweep of the CV performed just before the CO_{ads} stripping characterization, and it was corrected from the double-layer contribution measured at E = 0.40 V *vs*. RHE. For the sake of comparison, the electrical charge of the Q/HQ peak was also calculated using the methodology developed by Park *et al.* (Figure IV - 2 b) [33, 34]. Whatever the calculation procedure, an increased Q/HQ electrical charge was observed after 96 h of polarization at E_{AST} = 0.40 V *vs*. RHE, followed by a progressive decrease for 0.40 < E_{AST} < 1.00 V *vs*. RHE. Interestingly, the same trend is found above 1.00 V: a sharp increase was observed for E_{AST} = 1.2 V *vs*. RHE, and a further increase in potential resulted into a decreased Q/HQ electrical charge. Figure IV - 2 c) illustrates the dependence of the position of the Q/HQ peak on the AST polarization potential. Here again, the relationship is not monotonous: the peak potential first increased for 0.40 < E_{AST} < 0.80 V *vs*. RHE, and then decreased until E_{AST} = 1.2 V *vs*. RHE. Since CV is a dynamic technique, this trend is, to some extent, related to the dependence of the surface concentration of Q/HQ groups on the polarization potential. Previous studies also suggested that the peak potential of the Q/HQ redox couple varies with the number of aromatic rings neighbouring these functional groups [1].

These results hold significant importance for the understanding of HSAC degradation mechanisms. Indeed, they challenge the current view in the field that electrochemical oxidation of HSAC supports necessarily results in increasing concentration of Q/HQ groups. As shown in this study, the surface concentration with Q/HQ groups at a given time depends (among others) on the polarization potential, and the duration of the polarization. In some circumstances, such as a 96 h polarization at E_{AST} = 1.4 V *vs*. RHE and T = 330 K, the surface concentration with quinone/hydroquinone groups was found to be smaller after the AST relative to the fresh sample.

4.2.2 Physical characterization

The HSAC supports used in PEMFCs are composed of primary carbon particles (ranging from 10 to 100 nm) that are fused together via covalent bonds to form aggregates (100 – 800 nm), that finally pack into loosely bond agglomerates (1 – 100 μm) [15]. Ordered (graphite-like), and disordered (defective graphite crystallites and amorphous carbon) domains are present within the primary carbon particles [1, 35, 36]. Figure IV - 3 displays normalized Raman spectra, and the carbon mean crystallite size (L_a) estimated using the Knight and White formula [37, 38]. The vibrational band appearing at *ca*. 1350 cm^{-1}, namely the D1-band, is assigned to amorphous carbon domains and edges of the graphite crystallites, and the G-band at *ca*. 1585 cm^{-1} is ascribed to the ordered graphite crystallites [37]. By means of deconvolution, the D2-band (at *ca* 1610 cm^{-1}) that is assigned to the defects present in the surface of the graphite crystallites, the D3-band (at *ca* 1495 cm^{-1}) and the D4-band (at *ca* 1190 cm^{-1}), which are ascribed to maxima in the vibrational density of states [39, 40] or to polyenes and ionic impurities present in carbon blacks, [41] can be observed (see **Chapter II Table II - 3 and Chapter III Figure III - 3**). These bands are of great interest to the understanding of the structural changes of model carbon supports having well-defined structure [38, 42-45]. However, the high incertitude associated with the deconvolution of the Raman spectra into five bands make them poorly useful for disordered HSAC supports such as that used in this study. Consequently, in what follows, only the variations in shape and in intensity of the D1-band, and the G-band will be discussed. Therefore, any changes in the proportion of order/disordered domains in the sample will graphically result into modified D1-band intensity.

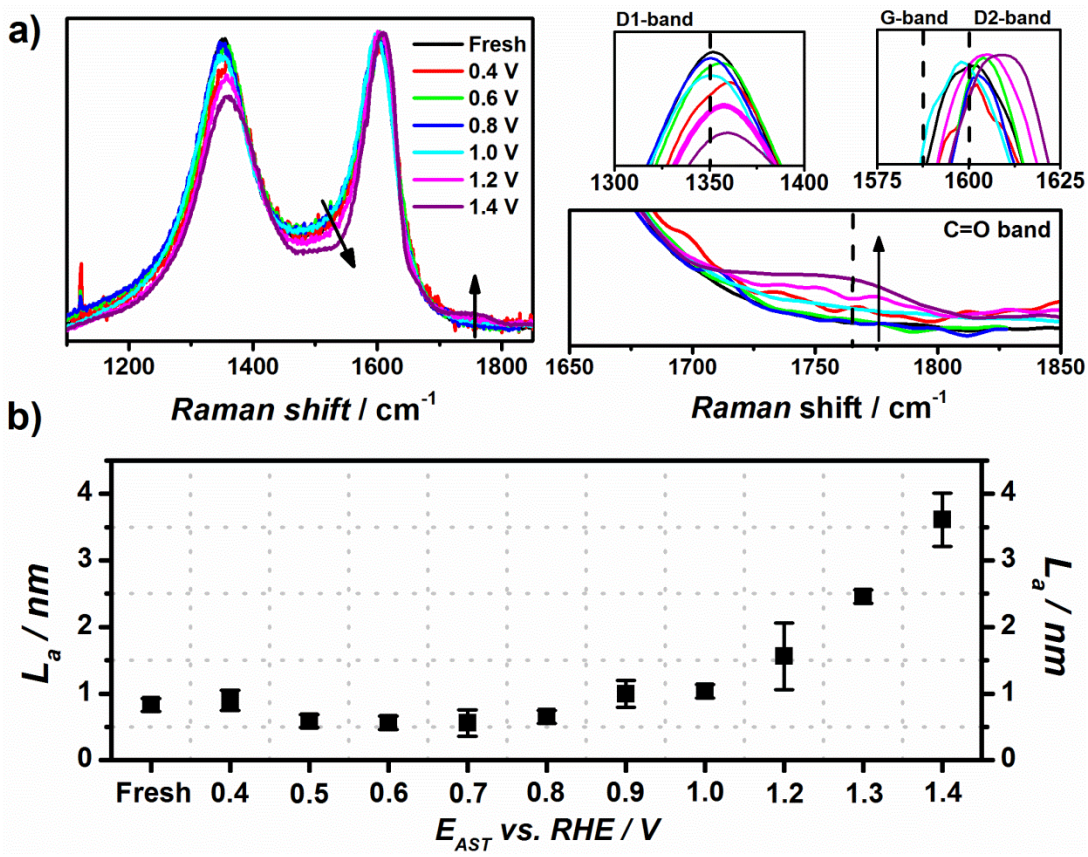

Figure IV - 3. a) Normalized Raman spectra of the fresh and aged Pt/HSAC electrocatalysts. Inset: D1-band, G-band, D2-band and carbonyl band, b) Variation of the carbon mean crystallite size (*La*) as function of the polarization potential. Electrolyte: 0.1 M H_2SO_4; T = 330 K.

After 96 h of potentiostatic hold at 0.40 < E_{AST} < 1.00 V *vs*. RHE, the Raman spectra feature a slow but continuous decrease of the D1-band intensity, and a small decrease of the G band intensity (Figure IV - 3 a), which suggest preferential oxidation of the more disordered domains of the HSAC support. At E_{AST} = 1.00 V *vs*. RHE, the development of the D2-band intensity at *ca*. 1600 cm^{-1} [43, 44] suggests the formation of surface defects within the graphite crystallites. Along with this, a new Raman band appears at *ca*. 1760 cm^{-1} (inset of Figure IV - 3 a). This band is active in both infrared [46] and Raman spectroscopy, [47-49] and is ascribed to the C=O stretch vibration of carbonyl groups of carboxylic acids, or lactone groups. Its intensity increases with an increase in the polarization potential above 1.00 V *vs*. RHE, suggesting that the HSAC surface becomes more oxidized. Along with the development of the C=O band, an increase in the polarization potential also causes a blue-shift of the D1 and D2-band maxima relative to the fresh sample (5 cm^{-1} at maximum). This blue-shift translates changes in the effective force constant of the atomic vibrations, and may be rationalized by considering the adsorption of oxygen atoms on structural defects (oxygen

atoms being more electronegative than carbon atoms, electron density will be transferred from the carbon atoms to the chemisorbed oxygen atoms). Similar results were reported for fluorinated graphene samples [50].

In an early study, Tuinstra and Koenig [42] showed that the ratio of the D1 and G Raman band intensities (I_{D1}/I_G) is inversely proportional to the mean crystallite size L_a. Their results were confirmed later and generalized for different excitation wavelengths [51, 52]. Using the Knight and White formula [37], and the I_{D1}/I_G ratio determined from the best fits of the Raman spectra, the changes in the average carbon crystallite size (L_a) were estimated after each potentiostatic hold. The increase in L_a (see Figure IV - 3 b) indicates that amorphous carbon domains and the edges of graphitic crystallites are preferentially oxidized in PEMFC operational potential range. Note however that different constants of proportionality between L_a and I_{D1}/I_G exist in the literature [37, 51, 52], therefore the L_a values should be considered with caution.

Figure IV - 4 shows the PSDs of the electrocatalysts and their respective number-averaged mean particle size ($\overline{d}_N$) and surface-averaged mean particle size ($\overline{d}_S$). The PSDs were built from representative TEM images of the fresh/aged Pt/HSAC electrocatalyst (Figure IV - 5). The realization of PSDs was not possible for $E > 1.00$ V due to severe aggregation of the Pt nanocrystallites (see Figure IV - 5e and f). The fresh Pt/HSAC catalyst has mean particle sizes comprised between 1 and 4 nm, with a $\overline{d}_N = 2.0$ nm and a $\overline{d}_S = 2.3$ nm. Upon ageing, the mean Pt/HSAC particle size is shifted to larger particles sizes, the tailing towards larger particles sizes increases and the fraction of particles with diameter smaller than 2 nm decreases progressively. These features are typical of electrochemical 3D Ostwald ripening, that is preferential dissolution of the smallest Pt nanocrystallites over time (production of Pt^{z+} ions). These ionic species are highly mobile and can re-precipitate within the proton-exchange membrane [21, 53] at the surface of the carbon support or on neighbouring Pt nanoparticles. It is interesting to note that Pt nanoparticles with a size less than 2 nm re-appear for $E \geq 0.7$ V *vs*. RHE. In this potential region, water is dissociated onto Pt: this may prevent the redeposition of ions into other Pt nanoparticles in favour of the nucleation of Pt nanoparticles onto the HSAC support. As shown in **Chapter III**, the redeposition of Pt^{z+} ions produced by electrochemical Ostwald ripening is facilitated during the negative-going potential sweep in cyclic voltammetry experiments. This will eventually translate in the decrease of the number-averaged mean particle size.

Typical features of the migration/agglomeration of the Pt nanoparticles were also observed in the TEM images. In general, this phenomenon gets more pronounced with an increase in electrode potential, suggesting that it is facilitated by the electrochemical corrosion of the HSAC support. The TEM images also allow monitoring the extent of degradation of the HSAC support. For 0.4 V < E_{AST} < 0.6 V *vs.* RHE the HSAC support shows no significant changes, presenting the general turbostratic structure of carbon blacks materials. In the potential range 0.8 V < E_{AST} < 1.2 V *vs.* RHE, larger and better organized carbon crystallites are visible in the borders of the carbon particles, due to the preferential corrosion of the smaller and disorganized graphitic domains (see Figure IV-3). For E_{AST} = 1.4 V *vs.* RHE, collapsed carbon primary particles are observed: this results into a blockage of the initial porosity observed at the fresh state.

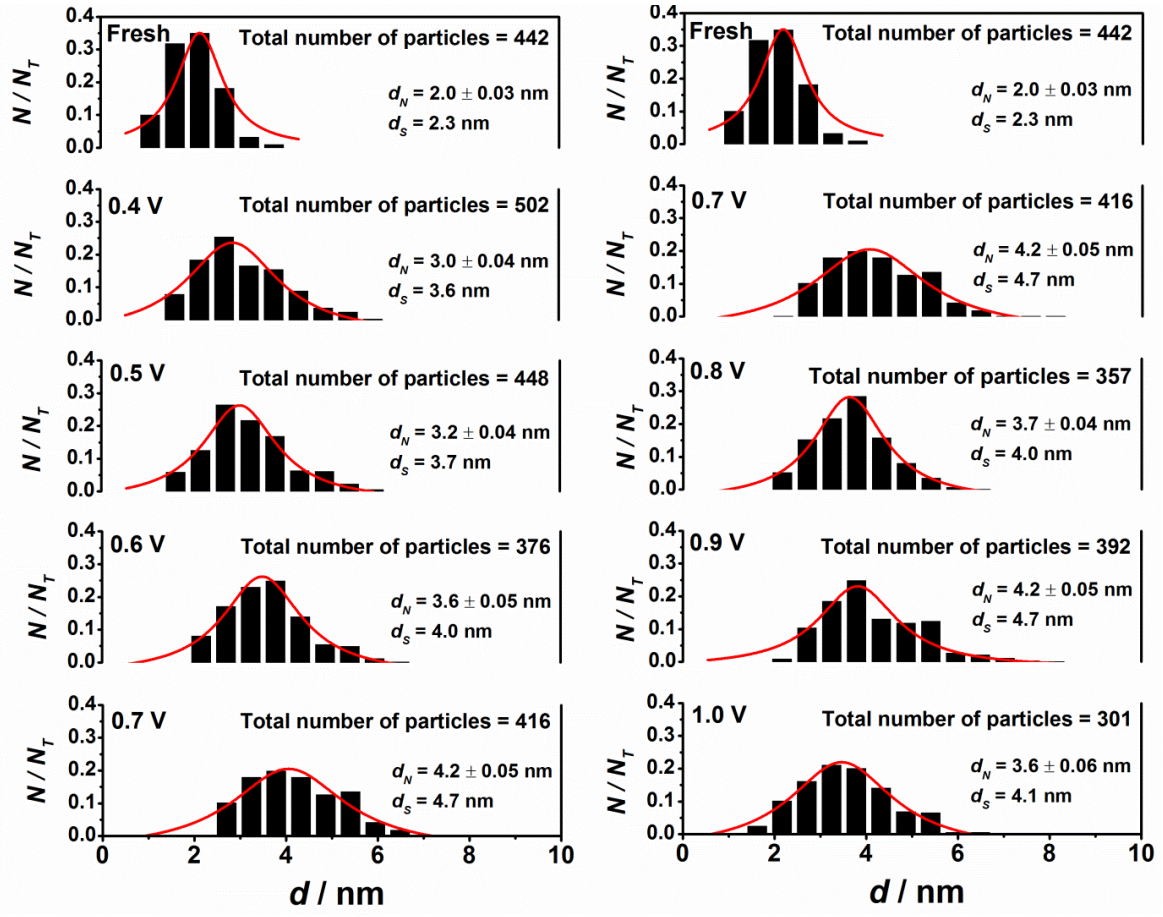

Figure IV - 4. Particle size distribution, total number of particles (NT), number-averaged diameter ($\bar{d}_N$) and surface-average diameter ($\bar{d}_S$) for the fresh/aged Pt/HSAC electrocatalysts after a 96 h-polarization at 0.40 V, 0.60 V, 0.80 V, 1.00 V, 1.20 V or 1.40 V *vs.* RHE.

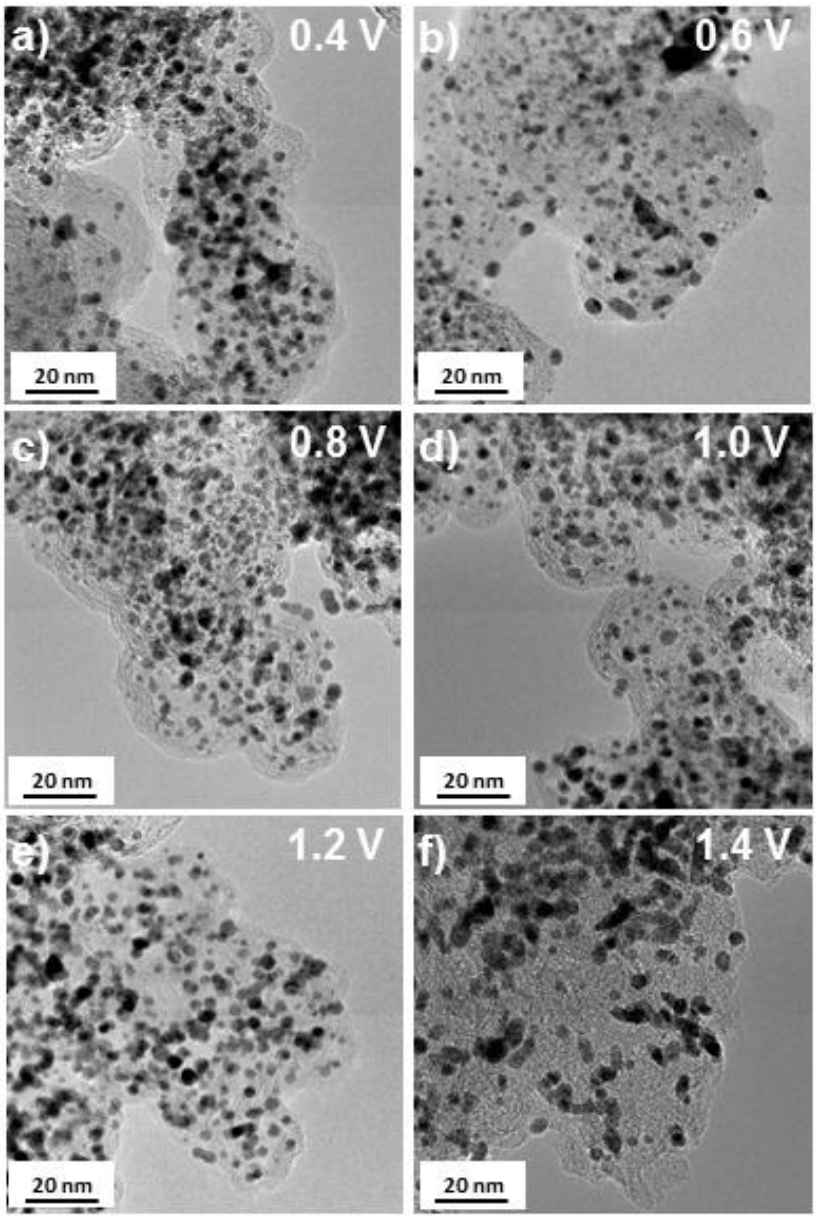

Figure IV - 5. TEM images of the fresh/aged Pt/HSAC electrocatalysts after a 96 h-polarization at a) 0.40 V, b) 0.60 V, c) 0.80 V, d) 1.00 V, e) 1.20 V or e) 1.40 V *vs.* RHE.

4.2.3 Chemical characterization

Figure IV - 6 displays the O1s/C1s atomic ratio measured by XPS before/after the different ASTs, and the carbon surface oxide composition obtained by deconvolution of the C1s peak into different functional groups: C–C (sp^2 and sp^3-hybridized carbon atoms at 284.3 eV), C–O (hydroxyl, epoxy and ethers at 286.0 eV), C=O (carbonyl and/or quinone-like at 287.7 eV), O–C=O (carboxylic acid, lactone, anhydride at 289.4 eV) and C-F_2 and C-OF_2 and/or C-F_3 (Nafion ionomer at 291.3 eV and 293 eV respectively). The raw C1s and O1s spectra for each sample are provided in Figure IV - 7 and Figure IV - 8. Since the ECSA was determined using CO_{ads} stripping coulometry, the O1s/C1s atomic ratio on the fresh sample is

0.33 (see **Chapter III Figure III - 7** and **Table III - 2**). This ratio increased during the AST but the trend is, again, non-monotonous: the coverage with CO_{surf} species steadily increased at E_{AST} = 0.40 V *vs*. RHE but was depreciated for increasing polarization potentials up to 0.80 V *vs*. RHE. As discussed previously, this can be rationalized by considering that the formation of oxygenated species on Pt nanoparticles (water splitting at E > 0.60 V *vs*. RHE) catalyses the oxidation of CO_{surf} groups into CO_2 [7, 8, 54].

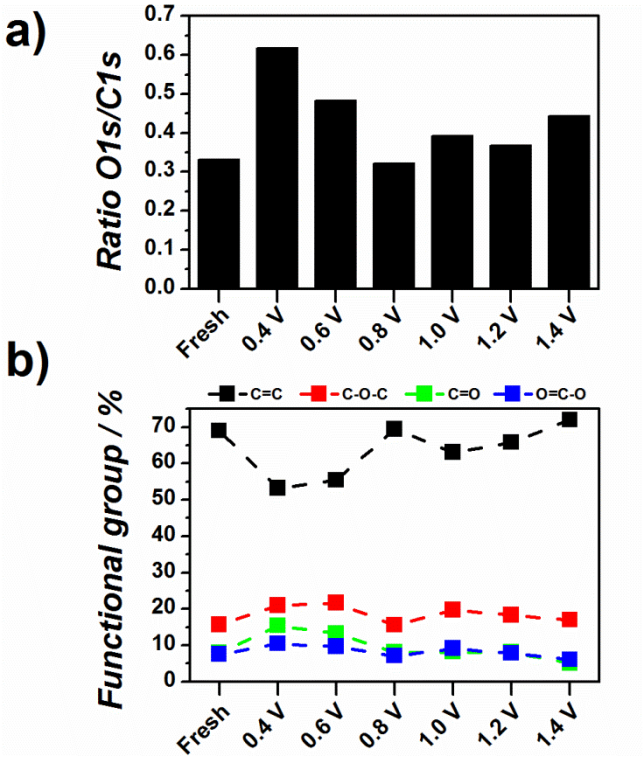

Figure IV - 6. Variation of the a) O1s/C1s atomic ratio and of the b) concentration of the functional groups as function of the polarization potential. Electrolyte: 0.1 M H_2SO_4; T = 330 K.

It is also striking to note that the concentration with CO_{surf} groups monitored by XPS and the structural changes monitored by Raman spectroscopy vary almost in parallel. Indeed, in the potential range 0.60 < E_{AST} < 0.80 V *vs*. RHE, the observed decrease in D1-band intensity in Raman spectra (Figure IV - 3) is nicely accompanied by a decreased oxygen content in XPS (Figure IV - 6). This simply reflects the fact that any structural defect is eager to chemisorb oxygen. Therefore, the preferential consumption of amorphous and defective-graphite crystallites in this potential range translates into a decrease CO_{surf} coverage. Similarly, at E_{AST} > 1.00 V *vs*. RHE, the formation of structural defects on graphitic crystallites parallels the pronounced increase in oxygen content monitored in XPS.

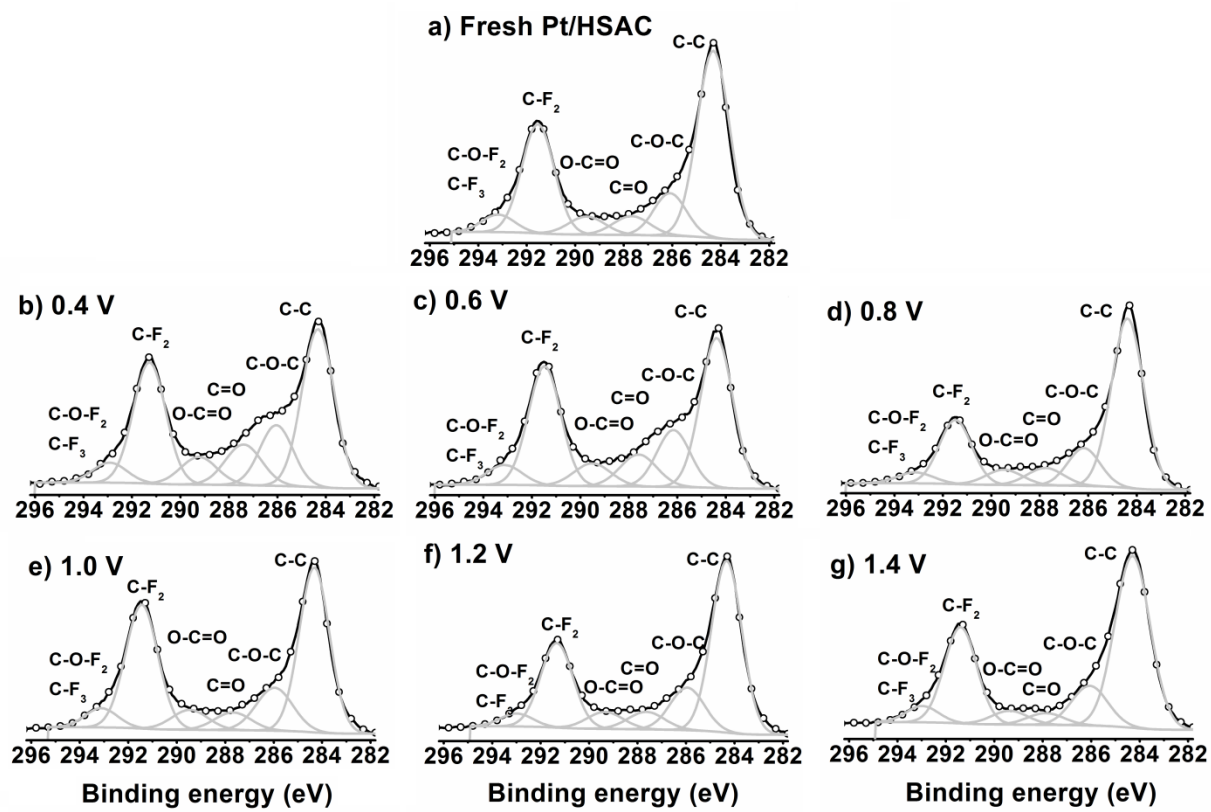

Figure IV - 7. C1s X-ray photoelectron spectra measured on the 40 % wt. Pt/HSAC electrocatalyst in the a) fresh state and after polarization at b) 0.40 V c) 0.60 V d) 0.80 V e) 1.00 V f) 1.20 V and g) 1.40 V *vs*. RHE.

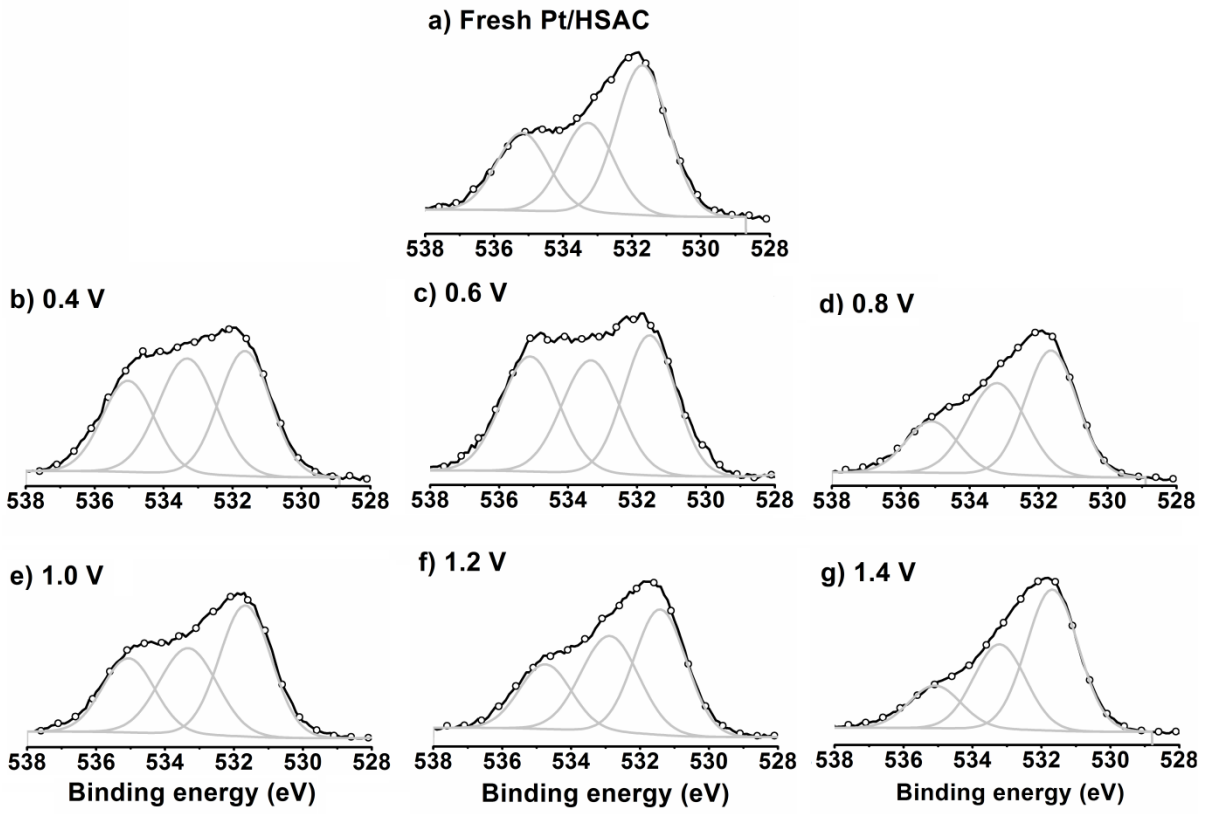

Figure IV - 8. O1s X-ray photoelectron spectra measured on the 40 % wt. Pt/HSAC electrocatalyst in the a) fresh state and after polarization at b) 0.40 V c) 0.60 V d) 0.80 V e) 1.00 V f) 1.20 V and g) 1.40 V *vs*. RHE.

4.2.4 Comparison with MEA operated on site during 12,860h

Finally, the results obtained in model experiments (liquid electrolyte, T = 330 K, 96 h polarization) are compared to those derived from a PEMFC cathode aged in real operating conditions (solid polymer electrolyte, T = 335 K). For that purpose, a stack composed of 2 x 55 MEAs was operated on-site (*i.e.* with oxygen from the ambient air) at j = 0.25 A cm^{-2} and T = 335 K for t = 12,860 h. During the aging, the cell voltage was always comprised between $0.65 < E_{cell} < 0.77$ V (voltage decay rate ~ 3.5 µV h^{-1}), and 250 start/stops events did occur during the operation of the PEMFC stack. The variation of the mean cell voltage (calculated on the 110 cells) at j = 0.25 A cm^{-2} is provided in Figure IV - 9**.** Such long-term PEMFC test places itself among the longest performed worldwide ever [24, 55-57]. The changes in structure (monitored by Raman spectroscopy), in morphology (monitored by scanning and transmission electron microscopy), and in chemistry (monitored by X-ray photoelectron spectroscopy) of the Pt/HSAC cathode electrocatalyst are summarized in Figure IV - 10.

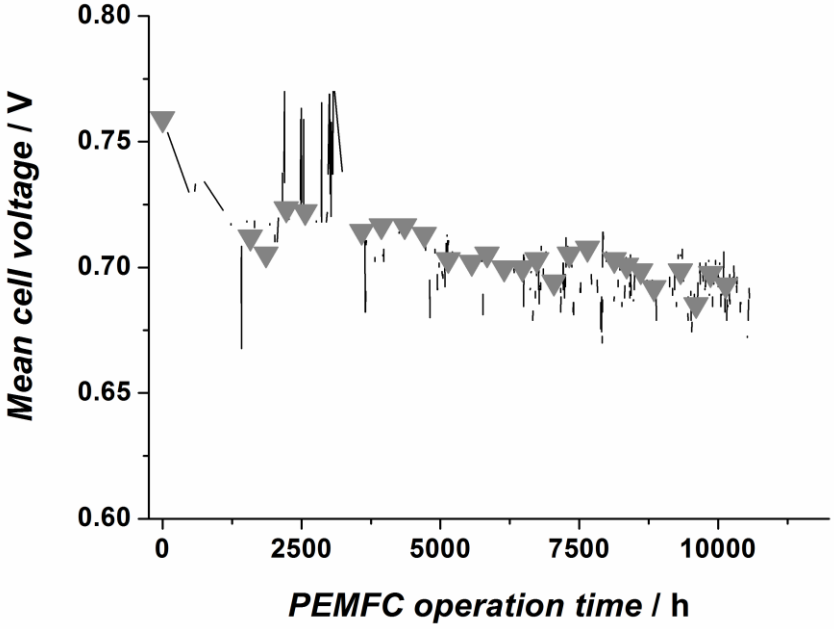

Figure IV - 9. Mean cell voltage (calculated on the 110 cells) during the 12,860 h PEMFC ageing test at j = 0.25 A cm^{-2}.

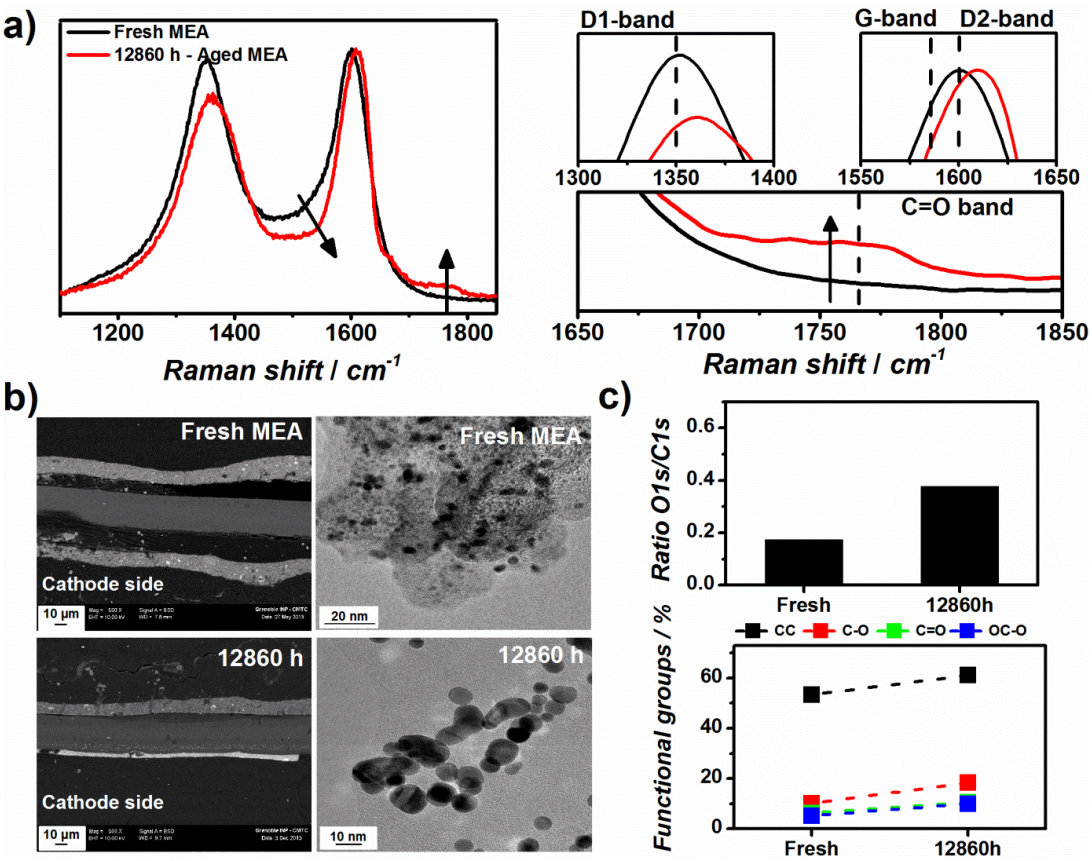

Figure IV - 10. Characterization of MEAs operated under "real-life" PEMFC conditions: a) Raman spectra b) Scanning electron microscopy (SEM) and transmission electron microscopy (TEM) images and c) XPS-derived parameters. PEMFC operating conditions: j = 0.25 A cm^{-2}, 0.65 < E_{cell} < 0.77 V, T = 335 K, t = 12,860 h, 250 start/stop events.

The Raman spectroscopy results (Figure IV - 10a) confirm the preferential degradation of the disordered graphite domains of the HSAC supports, as shown by the decrease of the D1-band intensity and the thinning of the G and D2-bands at $\overline{\upsilon}$ ~ 1610 cm^{-1}. The ordered graphite crystallites were also corroded (emergence of the carbonyl band at $\overline{\upsilon}$ ~ 1760 cm^{-1}). Figure IV - 10b presents SEM and TEM images of the fresh/aged MEAs. The cathode thickness estimated from SEM images decreased from 13.1 µm at the fresh state to 3.8 µm after 12,860 h of operation (- 71 % relative to the fresh cathode), in agreement with previous findings in the field [12, 21, 22, 27, 28, 31, 58, 59]. Furthermore, the TEM images revealed an increased fraction of agglomerated Pt nanoparticles, as well as changes of the structure of the carbon particles. Those changes are in perfect agreement with what was observed on the model PEMFC electrocatalyst during the 96 h-polarization (see Pt particle size distribution, the variation of the mean Pt particle size and TEM images in Figure IV - 4 and Figure IV - 5). Finally, the concentration of CO_{surf} species and the O1s/C1s ratio monitored by X-ray photoelectron spectroscopy are presented in Figure IV - 10c. The larger value of the O1s/C1s ratio indicates that, in average, the surface of the HSAC is more

oxidized after 12,860 h of operation than at beginning of life. As stressed in the introduction, this trend has great importance in terms of water management in the membrane electrode assembly. Indeed, a more oxidized HSAC support is less prone to evacuate water formed during the ORR, and may cause mass-transport losses [16, 24, 27, 56] and even further accelerate the corrosion of the HSAC support/microporous layer [21, 29].

4.2.5 Degradation mechanism of HSAC supports

The combined physical, chemical and electrochemical results presented in this study all point towards structure-sensitive COR kinetics on the HSAC supports used in PEMFC cathodes. They provide first evidence that selective corrosion occurs on the disordered domains and the defective graphite crystallites in the potential range $0.40 < E_{AST} < 1.00$ V *vs.* RHE (Figure IV - 11). Our results also indicate that, during excursion in potential at $E_{AST} > 1.00$ V *vs.* RHE, the ordered graphitic domains are corroded.

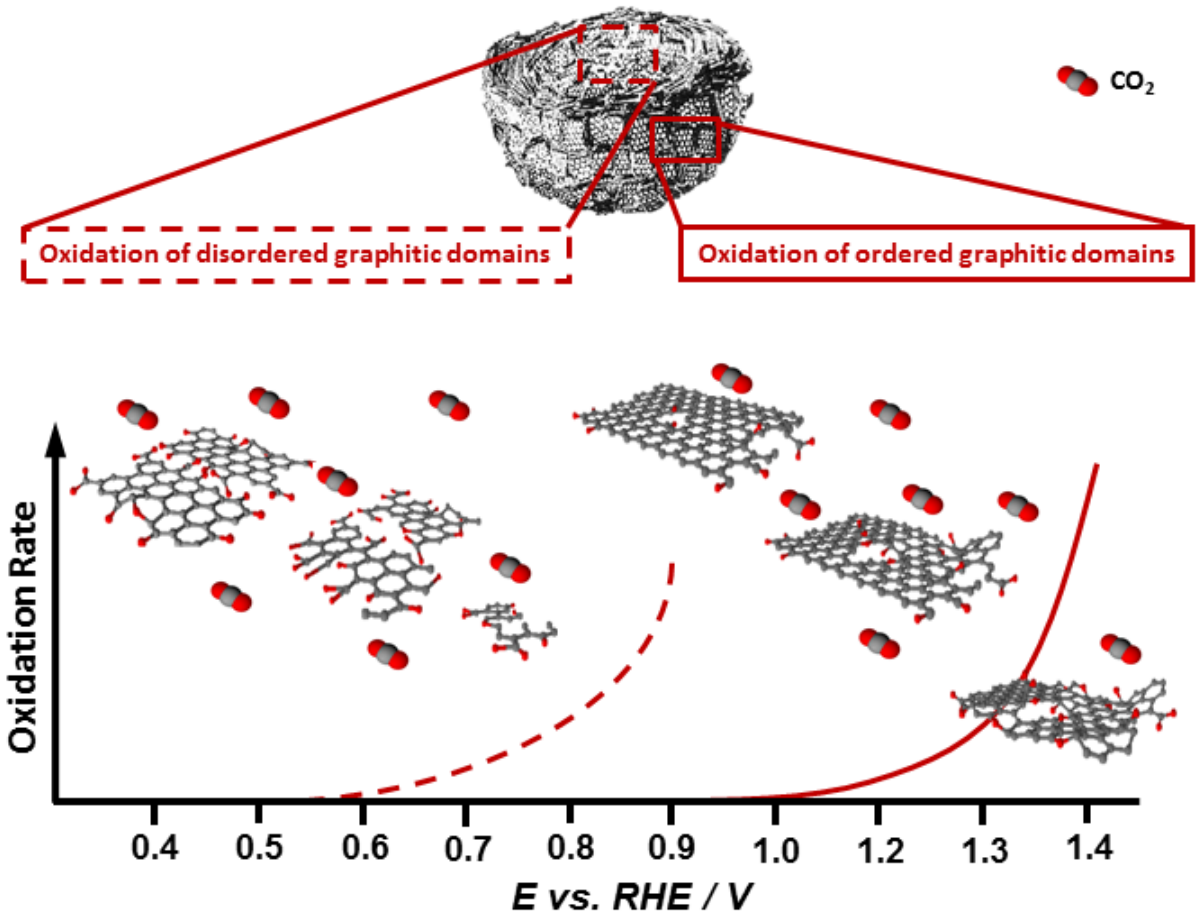

Figure IV - 11. Schematic representation of the structure sensitivity of the COR kinetics on Pt/HSAC electrocatalysts. The scheme representing the primary carbon particle is reproduced from reference [35] with permission of Wiley.

For both disordered and ordered domains of the HSAC, the COR mechanisms is believed to proceed via a similar mechanism, which involves the electrochemical formation of $C_{(s)}^{+}$ surface sites (Eq. IV - 2). Those sites are then rapidly hydrolysed into carbon surface oxides (Eq. IV - 3), before being evolved into CO_2 (Eq. IV - 4) as shown by the potential dependency of the surface oxide concentrations (Figure IV - 6). This step is catalysed by the presence of Pt nanoparticles (Eq. IV – 5 and Eq. IV - 6) [6, 7, 19, 20]:

$$C \rightarrow C^{+}_{(s)} + e^{-} \qquad \text{(Eq. IV - 2)}$$

$$C^{+}_{(s)} + H_2O \rightarrow CO_{surf} + 2\,H^{+} + 2\,e^{-} \qquad \text{(Eq. IV - 3)}$$

$$CO_{surf} + H_2O \rightarrow CO_2 + 2\,H^{+} + 2\,e^{-} \qquad \text{(Eq. IV - 4)}$$

$$CO_{surf} + Pt \rightarrow Pt - CO_{ads} \qquad \text{(Eq. IV - 5)}$$

$$Pt - CO_{ads} + H_2O \rightarrow CO_2 + 2\,H^{+} + 2\,e^{-} \qquad \text{(Eq. IV - 6)}$$

In our former study, the structural changes occurring on a HSAC support during PEMFC operation at constant current (j = 0.6 A cm^{-2}) for 3,422 h suggested a structural dependence of the COR kinetics [28]. The results obtained in model and real PEMFC operating conditions strengthen and validate the proposed scenario on a 4-fold longer basis (12,860 h).

4.3 Conclusion

The degradation mechanisms of HSAC supports used in PEMFCs were investigated during long-term potentiostatic holds in a wide potential range from 0.40 to 1.40 V *vs*. RHE. Our combined electrochemical and physico-chemical findings suggest that the COR kinetics are structure-sensitive, and proceed more rapidly on the disordered domains of the HSAC support (amorphous carbon and defective graphite crystallites). Consequently:

(*i*) at low electrode potential (0.40 < E_{AST} < 1.00 V *vs*. RHE), the amorphous carbon domains and the defective graphite crystallites present in the HSAC support are preferentially corroded. This phenomenon cannot be avoided during real PEMFC operation.

(*ii*) at high electrode potential (E_{AST} > 1.00 V *vs*. RHE) encountered during open circuit potential, start/stop or fuel starvation events, the graphitic domains of the HSAC support are also prone to oxidation. These structural changes can be mitigated during stationary PEMFC operation, so as to delay the stack end-of-life.

Our results suggest that the best possible mitigation strategies to prevent the COR on HSAC supports in real PEMFC operating conditions involves increasing their graphitic content, [14, 49] modifying their chemistry, [23, 60] or blocking the structural defects by halogen atoms or metal oxides so as to prevent their hydrolysis (Eq. IV - 3).

References

[1] K. Kinoshita, Carbon: Electrochemical and Physicochemical Properties, John Wiley & Sons, New York, 1988.
[2] K. Kinoshita, J. Bett, Electrochemical oxidation of carbon black in concentrated phosphoric acid at 135°C, Carbon, 11 (1973) 237-247.
[3] K. Kinoshita, J.A.S. Bett, Potentiodynamic analysis of surface oxides on carbon blacks, Carbon, 11 (1973) 403-411.
[4] K. Kinoshita, J.A.S. Bett, Determination of carbon surface oxides on platinum-catalyzed carbon, Carbon, 12 (1974) 525-533.
[5] K.H. Kangasniemi, D.A. Condit, T.D. Jarvi, Characterization of vulcan electrochemically oxidized under simulated PEM fuel cell conditions, J. Electrochem. Soc., 151 (2004) E125-E132.
[6] L.M. Roen, C.H. Paik, T.D. Jarvi, Electrocatalytic corrosion of carbon support in PEMFC cathodes, Electrochem. Solid-State Lett., 7 (2004) A19-A22.
[7] J. Willsau, J. Heitbaum, The influence of Pt-activation on the corrosion of carbon in gas diffusion electrodes—A DEMS study, J. Electroanal. Chem. Interfacial Electrochem., 161 (1984) 93-101.
[8] F. Maillard, A. Bonnefont, F. Micoud, An EC-FTIR study on the catalytic role of Pt in carbon corrosion, Electrochem. Com., 13 (2011) 1109-1111.
[9] C.A. Reiser, L. Bregoli, T.W. Patterson, J.S. Yi, J.D.L. Yang, M.L. Perry, T.D. Jarvi, A reverse-current decay mechanism for fuel cells, Electrochem. Solid State Lett., 8 (2005) A273-A276.
[10] T.W. Patterson, R.M. Darling, Damage to the cathode catalyst of a PEM fuel cell caused by localized fuel starvation, Electrochem. Solid State Lett., 9 (2006) A183-A185.
[11] J. Dillet, D. Spernjak, A. Lamibrac, G. Maranzana, R. Mukundan, J. Fairweather, S. Didierjean, R.L. Borup, O. Lottin, Impact of flow rates and electrode specifications on degradations during repeated startups and shutdowns in polymer-electrolyte membrane fuel cells, J. Power Sources, 250 (2014) 68-79.
[12] J. Durst, A. Lamibrac, F. Charlot, J. Dillet, L.F. Castanheira, G. Maranzana, L. Dubau, F. Maillard, M. Chatenet, O. Lottin, Degradation heterogeneities induced by repetitive start/stop events in proton exchange membrane fuel cell: Inlet vs. outlet and channel vs. land, Appl. Catal. B, 138-139 (2013) 416-426.
[13] J.P. Meyers, R.M. Darling, Model of carbon corrosion in PEM fuel cells, J. Electrochem. Soc., 153 (2006) A1432-A1442.
[14] K. Artyushkova, S. Pylypenko, M. Dowlapalli, P. Atanassov, Structure-to-property relationships in fuel cell catalyst supports: Correlation of surface chemistry and morphology with oxidation resistance of carbon blacks, J. Power Sources, 214 (2012) 303-313.
[15] F. Maillard, P. Simonov, E.R. Savinova, Carbon materials as support for fuel cells electrocatalysts, in: P. Serp, J.L. Figueiredo (Eds.) Carbon Materials for Catalysis, John Wiley & Sons, Inc., New York, 2009, pp. 429-480.
[16] R. Makharia, S.S. Kocha, P.T. Yu, M.A. Sweikart, W. Gu, F.T. Wagner, H. Gasteiger, Durable PEM fuel cell electrode materials: requirements and benchmarking methodologies, ECS Trans., 1 (2006) 3-18.
[17] O.V. Cherstiouk, A.N. Simonov, N.S. Moseva, S.V. Cherepanova, P.A. Simonov, V.I. Zaikovskii, E.R. Savinova, Microstructure effects on the electrochemical corrosion of carbon materials and carbon-supported Pt catalysts, Electrochim. Acta, 55 (2010) 8453-8460.
[18] S.C. Ball, S.L. Hudson, D. Thompsett, B. Theobald, An investigation into factors affecting the stability of carbons and carbon supported platinum and platinum/cobalt alloy catalysts during 1.2V potentiostatic hold regimes at a range of temperatures, J. Power Sources, 171 (2007) 18-25.
[19] P. Stonehart, Carbon substrates for phosphoric acid fuel cell cathodes, Carbon, 22 (1984) 423-431.
[20] S. Maass, F. Finsterwalder, G. Frank, R. Hartmann, C. Merten, Carbon support oxidation in PEM fuel cell cathodes, J. Power Sources, 176 (2008) 444-451.
[21] E. Guilminot, A. Corcella, F. Charlot, F. Maillard, M. Chatenet, Detection of Pt^{z+} ions and Pt nanoparticles inside the membrane of a used PEMFC, J. Electrochem. Soc., 154 (2007) B96-B105.

[22] Z.Y. Liu, B.K. Brady, R.N. Carter, B. Litteer, M. Budinski, J.K. Hyun, D.A. Muller, Characterization of carbon corrosion-induced structural damage of PEM fuel cell cathode electrodes caused by local fuel starvation, J. Electrochem. Soc., 155 (2008) B979-B984.
[23] P. Urchaga, M. Weissmann, S. Baranton, T. Girardeau, C. Coutanceau, Improvement of the platinum nanopartides-carbon substrate interaction by insertion of a thiophenol molecular bridge, Langmuir, 25 (2009) 6543-6550.
[24] S.J.C. Cleghorn, D.K. Mayfield, D.A. Moore, J.C. Moore, G. Rusch, T.W. Sherman, N.T. Sisofo, U. Beuscher, A polymer electrolyte fuel cell life test: 3 years of continuous operation, J. Power Sources, 158 (2006) 446-454.
[25] N. Giordano, P.L. Antonucci, E. Passalacqua, L. Pino, A.S. Aricò, K. Kinoshita, Relationship between physicochemical properties and electrooxidation behaviour of carbon materials, Electrochim. Acta, 36 (1991) 1931-1935.
[26] U.S.C.f.A.R.L. (USCAR), Fuel cell technical team technology roadmap, http://www.uscar.org/guest/view_team.php?teams_id=17, US DRIVE, 2011.
[27] M.F. Mathias, R. Makharia, H. Gasteiger, J.J. Conley, T.J. Fuller, G.J. Gittleman, S.S. Kocha, D.P. Miller, C.K. Mittelsteadt, T. Xie, S.G. Yan, P.T. Yu, Two fuel cell cars in every garage?, Interface, 14 (2005) 24-35.
[28] L. Dubau, M. Lopez-Haro, L. Castanheira, J. Durst, M. Chatenet, P. Bayle-Guillemaud, L. Guétaz, N. Caqué, E. Rossinot, F. Maillard, Probing the structure, the composition and the ORR activity of Pt3Co/C nanocrystallites during a 3422h PEMFC ageing test, Appl. Catal. B, 142–143 (2013) 801-808.
[29] E. Guilminot, A. Corcella, M. Chatenet, F. Maillard, F. Charlot, G. Berthome, C. Iojoiu, J.Y. Sanchez, E. Rossinot, E. Claude, Membrane and active layer degradation upon PEMFC steady-state operation - I. Platinum dissolution and redistribution within the MEA, J. Electrochem. Soc., 154 (2007) B1106-B1114.
[30] C. Iojoiu, E. Guilminot, F. Maillard, M. Chatenet, J.Y. Sanchez, E. Claude, E. Rossinot, Membrane and active layer degradation following PEMFC steady-state operation - II. Influence of Pt^{z+} on membrane properties, J. Electrochem. Soc., 154 (2007) B1115-B1120.
[31] L. Dubau, F. Maillard, M. Chatenet, L. Guétaz, J. André, E. Rossinot, Durability of Pt_3CoC cathodes in a 16 cell PEMFC stack: macro/microstructural changes and degradation mechanisms, J. Electrochem. Soc., 157 (2010) B1887-B1895.
[32] T. Yoda, H. Uchida, M. Watanabe, Effects of operating potential and temperature on degradation of electrocatalyst layer for PEFCs, Electrochim. Acta, 52 (2007) 5997-6005.
[33] Y.-C. Park, K. Kakinuma, M. Uchida, D.A. Tryk, T. Kamino, H. Uchida, M. Watanabe, Investigation of the corrosion of carbon supports in polymer electrolyte fuel cells using simulated start-up/shutdown cycling, Electrochim. Acta, 91 (2013) 195-207.
[34] Y.-C. Park, K. Kakinuma, M. Uchida, H. Uchida, M. Watanabe, Deleterious effects of interim cyclic voltammetry on Pt/carbon black catalyst degradation during start-up/shutdown cycling evaluation, Electrochim. Acta, 123 (2014) 84-92.
[35] R.D. Heidenreich, W.M. Hess, L.L. Ban, A test object and criteria for high resolution electron microscopy, J. Appl. Crystallogr., 1 (1968) 1-19.
[36] W. Mathis, Graphite and carbon powders for electrochemical applications, J. Power Sources, 156 (2006) 142-150.
[37] D.S. Knight, W.B. White, Characterization of diamond films by Raman spectroscopy, J. Mater. Res., 4 (1989) 385-393.
[38] T. Jawhari, A. Roid, J. Casado, Raman spectroscopic characterization of some commercially available carbon black materials, Carbon, 33 (1995) 1561-1565.
[39] R.J. Nemanich, S.A. Solin, First- and second-order Raman scattering from finite-size crystals of graphite, Physical Review B, 20 (1979) 392-401.
[40] P. Lespade, R. Al-Jishi, M.S. Dresselhaus, Model for Raman scattering from incompletely graphitized carbons, Carbon, 20 (1982) 427-431.
[41] A. Sadezky, H. Muckenhuber, H. Grothe, R. Niessner, U. Pöschl, Raman microspectroscopy of soot and related carbonaceous materials: Spectral analysis and structural information, Carbon, 43 (2005) 1731-1742.
[42] F. Tuinstra, J.L. Koenig, Raman spectrum of graphite, J. Chem. Phys., 53 (1970) 1126-1130.

[43] M. Nakamizo, H. Honda, M. Inagaki, Raman spectra of ground natural graphite, Carbon, 16 (1978) 281-283.
[44] M. Nakamizo, K. Tamai, Raman spectra of the oxidized and polished surfaces of carbon, Carbon, 22 (1984) 197-198.
[45] T. Gruber, T.W. Zerda, M. Gerspacher, Raman studies of heat-treated carbon blacks, Carbon, 32 (1994) 1377-1382.
[46] Z. Zhao, L. Castanheira, L. Dubau, G. Berthomé, A. Crisci, F. Maillard, Carbon corrosion and platinum nanoparticles ripening under open circuit potential conditions, J. Power Sources, 230 (2013) 236-243.
[47] S.K. Sze, N. Siddique, J.J. Sloan, R. Escribano, Raman spectroscopic characterization of carbonaceous aerosols, Atmos. Environ., 35 (2001) 561-568.
[48] Y. Hiramitsu, H. Sato, H. Hosomi, Y. Aoki, T. Harada, Y. Sakiyama, Y. Nakagawa, K. Kobayashi, M. Hori, Influence of humidification on deterioration of gas diffusivity in catalyst layer on polymer electrolyte fuel cell, J. Power Sources, 195 (2010) 435-444.
[49] M. Hara, M. Lee, C.-H. Liu, B.-H. Chen, Y. Yamashita, M. Uchida, H. Uchida, M. Watanabe, Electrochemical and Raman spectroscopic evaluation of Pt/graphitized carbon black catalyst durability for the start/stop operating condition of polymer electrolyte fuel cells, Electrochim. Acta, 70 (2012) 171-181.
[50] M. Bruna, S. Borini, Observation of Raman G -band splitting in top-doped few-layer graphene, Phys. Rev. B: Condens. Matter Mater. Phys., 81 (2010).
[51] M.A. Pimenta, G. Dresselhaus, M.S. Dresselhaus, L.G. Cançado, A. Jorio, R. Saito, Studying disorder in graphite-based systems by Raman spectroscopy, Phys. Chem. Chem. Phys., 9 (2007) 1276-1291.
[52] L.G. Cançado, K. Takai, T. Enoki, M. Endo, Y.A. Kim, H. Mizusaki, A. Jorio, L.N. Coelho, R. Magalhães-Paniago, M.A. Pimenta, General equation for the determination of the crystallite size L_a of nanographite by Raman spectroscopy, Appl. Phys. Lett., 88 (2006) 163106.
[53] K. Yasuda, A. Taniguchi, T. Akita, T. Ioroi, Z. Siroma, Platinum dissolution and deposition in the polymer electrolyte membrane of a PEM fuel cell as studied by potential cycling, Phys. Chem. Chem. Phys., 8 (2006) 746-752.
[54] W. Li, A.M. Lane, Investigation of Pt catalytic effects on carbon support corrosion of the cathode catalyst in PEM fuel cells using DEMS spectra, Electrochem. Com., 11 (2009) 1187-1190.
[55] J. St-Pierre, N.Y. Jia, Successful demonstration of Ballard PEMFCS for space shuttle applications, J. New Mater. Electrochem. Syst., 5 (2002) 263-271.
[56] D. Liu, S. Case, Durability study of proton exchange membrane fuel cells under dynamic testing conditions with cyclic current profile, J. Power Sources, 162 (2006) 521-531.
[57] F.A. de Bruijn, V.A.T. Dam, G.J.M. Janssen, Review: Durability and degradation issues of PEM fuel cell components, Fuel Cells, 8 (2008) 3-22.
[58] K. Gallagher, R. Darling, T. Fuller, Carbon-support corrosion mechanisms and models, in: W. Vielstich, H. Yokokawa, H.A. Gasteiger (Eds.) Handbook of Fuel Cells - Fundamentals, Technology and Applications, John Wilet & Sons, Ltd., New York, 2009, pp. 819-828.
[59] L. Dubau, L. Castanheira, F. Maillard, M. Chatenet, O. Lottin, G. Maranzana, J. Dillet, A. Lamibrac, J.-C. Perrin, E. Moukheiber, A. ElKaddouri, G. De Moor, C. Bas, L. Flandin, N. Caqué, A review of PEM fuel cell durability: materials degradation, local heterogeneities of aging and possible mitigation strategies, Wiley Interdiscip. Rev.: Energy Environ., (2014) DOI: 10.1002/wene.1113.
[60] Y. Shao, J. Sui, G. Yin, Y. Gao, Nitrogen-doped carbon nanostructures and their composites as catalytic materials for proton exchange membrane fuel cell, Appl. Catal. B, 79 (2008) 89-99.

Chapter V.

Carbon corrosion induced by membrane failure: the weak link of PEMFC long-term performance

The results discussed in this chapter have been published in:

Laetitia Dubau, **Luis Castanheira**, Marian Chatenet, Frédéric Maillard, Jérôme Dillet, Gaël Maranzana, Sofyane Abbou, Olivier Lottin, Gilles De Moor, Assma El Kaddouri, Corine Bas, Lionel Flandin, Elisabeth Rossinot, Nicolas Caqué

Carbon corrosion induced by membrane failure: the weak link of PEMFC long-term performance

International Journal of Hydrogen Energy DOI: 10.1016/j.ijhydene.2014.07.099

The contribution of the author of this thesis includes the preparation of TEM, SEM and Raman spectroscopy samples, the treatment and the analysis of SEM and Raman spectroscopy data.

5.1 Introduction

In PEMFC operating systems, a loss of electrical performance is witnessed on the long-term, which originates from the degradation of the materials contained in the membrane electrode assembly (MEA). In particular, the chemical degradation of the proton exchange membrane (PEM) by radical species strongly affects the MEA electrical performance because it induces a thinning that can ultimately evolve into (pin)holes signing the end-of-life on the cell [1, 2]. The morphology of these pinholes was identified as knife-holes along the edges of the land of the bipolar plates due to the weak resistance to crack initiation and propagation of non-reinforced PFSA membranes. The comparison of the essential work of fracture between PFSA SSC (short side chain) and LSC (long side chain) and PTFE/PFSA composite membrane has been made by Moukheiber et *al*.[3]. It was concluded that the PTFE reinforcement strongly increases the fracture resistance and their use might considerably improve the membrane durability. On the catalyst side, four main degradation mechanisms leading to a loss of electrochemically active surface area (ECSA) have been reported: (*i*) dissolution of the Pt nanocrystallites yielding the formation of Pt^{z+} ions and their redeposition onto larger crystallites or (*ii*) their chemical reduction in the ionic conductors (PEM and ionomer of the catalytic layer), leading to electrically disconnected Pt crystallites (*iii*) crystallite migration eventually followed by coalescence and (*iv*) corrosion of the high surface area support (HSAC) [2, 4-7]. Mitigating MEA materials degradation requires identifying the extent and nature of the degradation mechanisms and correlating these with the stack operating conditions (mode of solicitation, load cycle, number of start-stop events) [8]. Recently, it has been pointed out that PEMFC MEAs age heterogeneously at multiple scales. Ferreira and co-workers [7, 9] showed that the region of the cathode located at the interface with the PEM is more degraded than the region located at the interface with the gas diffusion layer, which was later confirmed by others [10, 11]. Dubau *et al*. [12] found that the aging of the cathode material is also heterogeneous along the gas channel as a result of the consumption of H_2 and O_2 gases. In a stack operating in counter flow mode (where the air inlet faces the hydrogen outlet), local current density heterogeneities were found to develop at the cathode essentially due to the depletion in O_2 partial pressure and the increase in water content along the gas channel. As a result, the region of the cathode localized in the air inlet region is much more degraded than the air outlet region [12]. By combining measurements in a segmented PEMFC and electron microscopy, Durst and *al.* [13] recently provided evidences of a third level of heterogeneities linked to the geometry of the flow fields, *i.e.* under a

channel or under a land. During start-up events, oxygen is purged from the anode side. The more difficult removal of oxygen under a land induces transient fuel starvation episodes, and severe carbon corrosion proceeds in the cathode region facing these zones. These studies contributed to a better understanding of the parameters/phenomena affecting the stack performance, and demonstrated that the corrosion of the carbon support is a major contributor to the loss of electrical performance [2].

Herein, the changes of the physical, chemical and electrochemical properties of MEAs operated in a 110-cell stack on-site during *ca*. 13,000 hours (more than 1.5 years) were investigated at the stack, MEA and material scales. Through a fruitful collaboration between three academic laboratories having different specialities (polymer electrolyte membrane and ionomer, carbon-supported metal (electro)catalyst nanoparticles, mass transport and charge transfer) and a stack manufacturer, fundamental and applied findings of prime importance to the development of improved PEMFC materials are highlighted.

5.2 Results and Discussion

5.2.1 110 cell system operating performance

Figure V - 1 displays simplified schematics of Axane EVOPAC system. This system includes two identical 55-cell stacks; the cells were positioned horizontally with the anode side up in the left stack and the cathode side up in the right stack. The stacks were air-cooled, and temperature differences reaching up to 4 °C (measured in the bipolar plate) were observed between individual cells within the same stack.

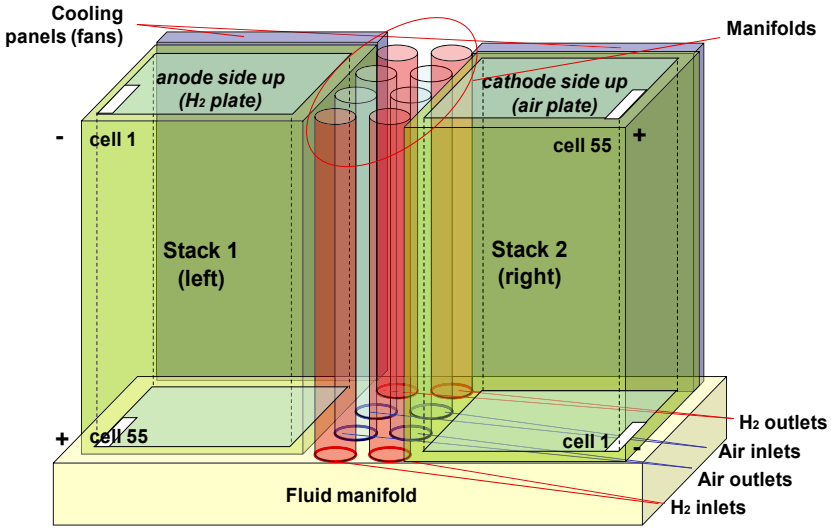

Figure V - 1. Overall view of cell arrangement and system geometry in Axane EVOPAC systems.

The EVOPAC system was operated for more than 1.5 year on the field (12,860 hours of working operation and approximately 250 start/stop procedures) at j = 0.25 A cm^{-2} with humidified ambient air at a stoichiometry of 2.5, pure (dry) H_2 in dead-end supply mode (corresponding to a stoichiometry of *ca.* 1), and at an average stack temperature of 333 to 338 K. The operation was stopped due to recurrent low-level voltage faults. Gas-tightness studies revealed that the right stack presented important membrane leakages. During the aging, the mean cell voltage was always comprised between 0.65 < E_{cell} < 0.77 V (stack voltage decay rate ~ 3.5 µV h^{-1}, see Figure V - 2a), and 250 start/stops events were processed during the operation of the PEMFC stack. Polarization curves recorded at the beginning-of-Life (BoL) and at the end-of-Life (EoL), using a cell-to-cell voltage measurement device, revealed that the performance loss was not homogeneous (Figure V - 2b). Indeed, the electrical performance of the right stack decayed more significantly, with an average cell voltage decay of 4.5 µV h^{-1} cell^{-1} (at j = 0.25 A cm^{-2}). Such large heterogeneity of performance from one

cell to the other may be a consequence of the heterogeneous degradation of their constitutive materials and assembly, as investigated in the following sections.

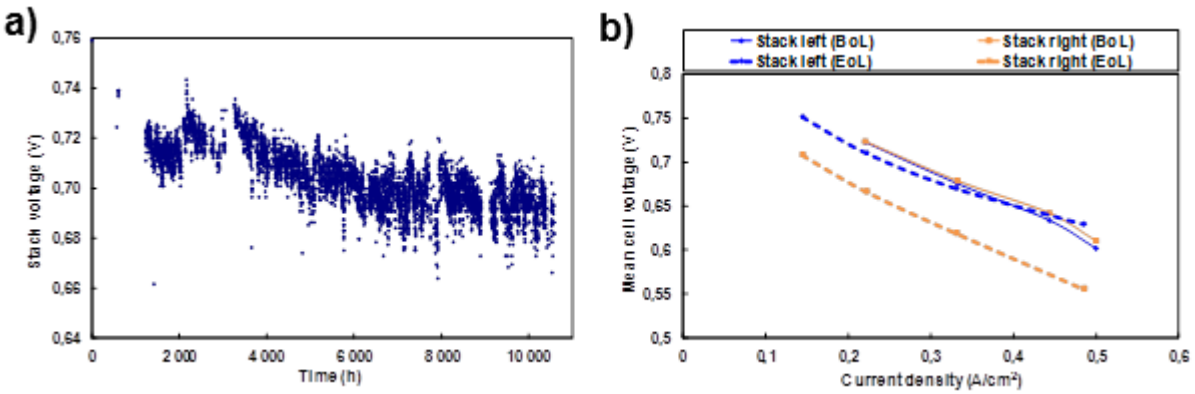

Figure V - 2. a) Mean cell voltage (calculated on the 110 cells) at j = 0.25 A cm-2 during the first 10,500 hours of operation. b) Beginning-of-Life (BoL) and End-of-Life (EoL) polarization plots measured on each stack (expressed in terms of average cell voltage).

Figure V - 3 presents the repartition of the individual cell voltages in the two stacks, measured at a constant current density of j = 0.50 A cm^{-2}. These values were obtained after 12,860 hours of operation, shortly before disassembling the stacks. The cell voltages were comprised between 0.21 and 0.68 V, with an average cell voltage of 0.57 V.

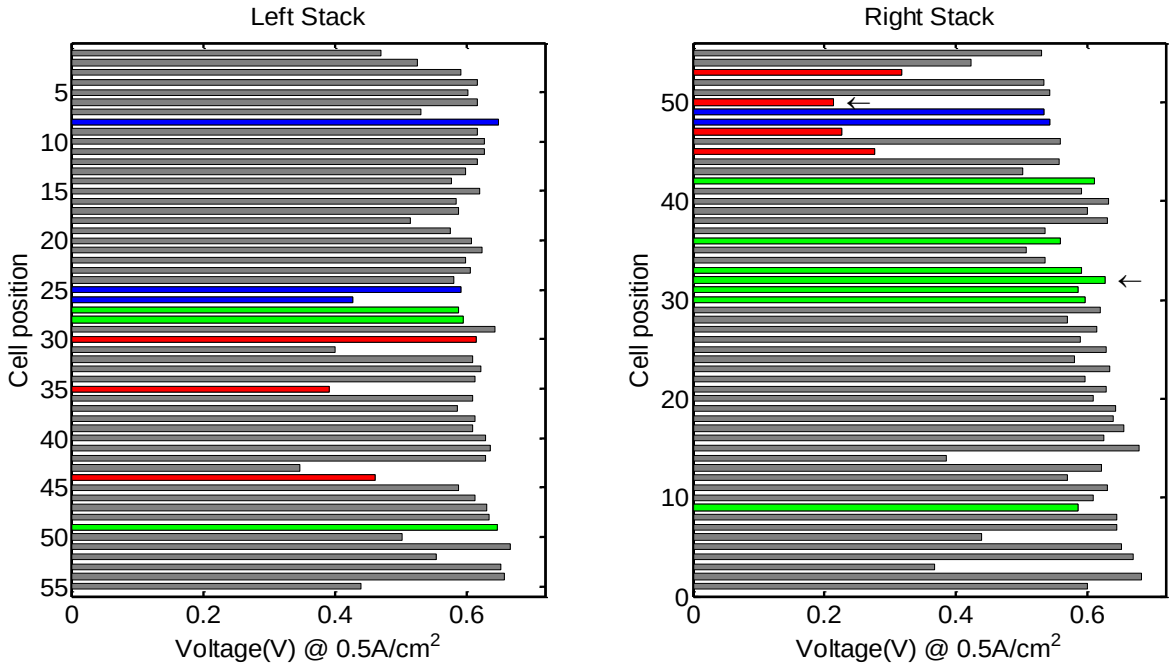

Figure V - 3. End-of-Life (EoL) cell voltage measured at j = 0.50 A cm-2. The MEAs were operated on-site at I = 22 A – T = 335 K – 65 % RH during 12,860 hours in a 110-cell PEMFC stack.

Figure V - 4 confirms that individual cells aged heterogeneously within the PEMFC stack: while some cells perform comparably to the fresh one (see *e.g.* cell #32 in Figure V - 4a), some others strongly degraded, such as the cell #50 (Figure V - 4b), the average voltage of which decayed at a rate of 15 µV h^{-1} at j = 0.25 A cm^{-2} and as much as *ca.* 31 µV h^{-1} at j = 0.50 A cm^{-2}.

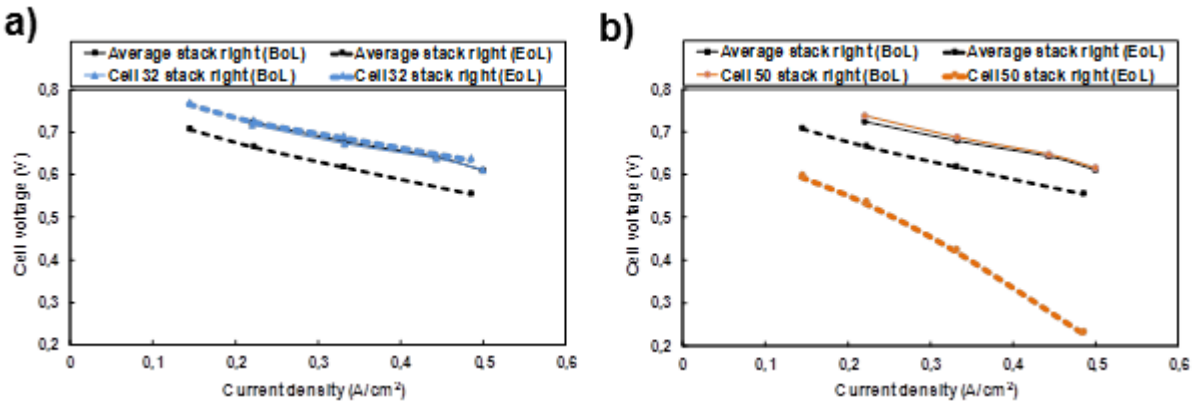

Figure V - 4. Beginning-of-Life (BoL) and End-of-Life (EoL) polarization curves obtained in system on (A) the cell #32 of the right stack and (B) the cell #50 of the right stack. In both cases, the average polarization plots are also given at BoL and EoL.

5.2.2 In situ evidences of performance heterogeneities at the stack and the MEA level

Some MEAs, marked in red, blue, and green inFigure V - 3, were tested using an instrumented cell (Figure V - 5) to gain more insights on the origin of the heterogeneities of performance. A detailed description of the segmented cell is provided in Ref. [14]. The geometry of the flow field plates in this cell is identical to that of the EVOPAC system: this represents a significant improvement over previous models, [13, 15, 16] which were successfully used to investigate internal currents during start-up/shut-down sequences but operated with straight gas channels.

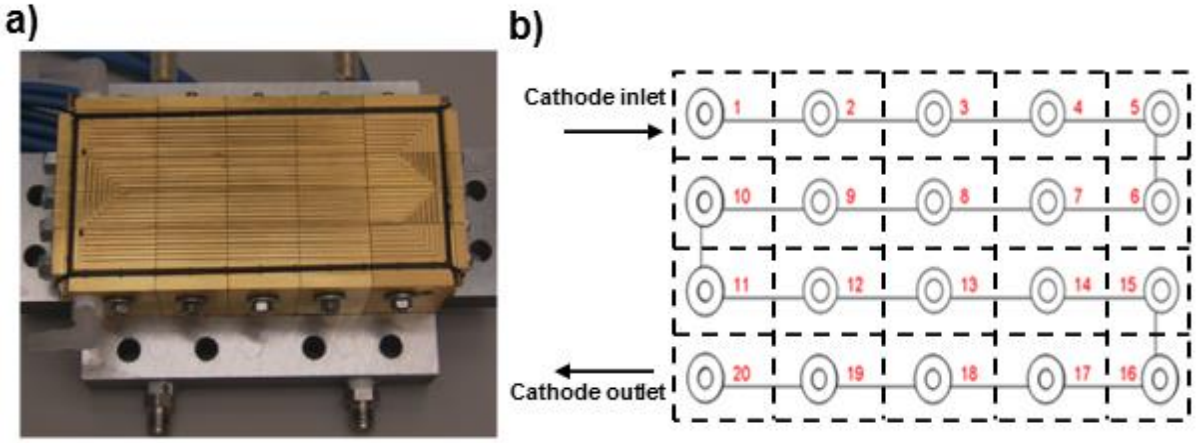

Figure V - 5. Picture of the segmented cell used to unveil heterogeneities of electrical performances: (A) assembled cathode with water–cooled end plate and (B) position of each individual segment along the air flow field.

The electrical tests were performed according to the following protocol:

- The cell was operated in steady state (j =0.50 A cm^{-2} constant current density) during 30 minutes, and then left at open circuit during a few seconds.
- Every two hours, Electrochemical Impedance Spectroscopy (EIS) was performed at j = 0.50 A cm^{-2} and a polarization curve was measured (the current was gradually increased from j = 0.01 to 0.97 A cm^{-2} then decreased again from j =0.97 to 0.01 A cm^{-2} by successive 30 second-steps of 0.008 A cm^{-2}).

The sequence described above was repeated 10 times to ensure re-conditioning of the aged MEA in the segmented cell, and the cell voltage values obtained during the last sequence were reported in Figure V - 6. The air and the hydrogen stoichiometry were 2.5 and 1.2 at 50 % and 100 % RH, respectively. The cell temperature was set to 338 K and kept constant during the whole procedure.

Figure V - 6a displays polarization curves of a fresh/aged MEAs. It is striking to note that the MEA #32, as well as the other MEAs marked in green in Figure V - 3, performs as well as the fresh MEA, in agreement with the measurements performed in the stack (see Figure V - 3 and Figure V - 4). The voltage difference between MEA #32 and the fresh MEA is *ca*. 0.03 V over the whole polarization curve (this corresponds to a decay rate of 2.3 µV h^{-1} loss at j = 0.25 A cm^{-2}). Similar values of the open-circuit potential were obtained for both MEAs and the polarization curves were roughly parallel below j = 0.15 A cm^{-2}: this suggests that the performance losses of the aged one are mainly imputed to a larger ORR activation

overpotential (the HOR is believed to be not limiting [17], even for the aged MEAs) most likely linked to the decrease in Pt loading at the cathode [18, 19]. In particular, this behavior can neither be imputed to any sharp increase of internal resistance nor to larger mass-transport hindrances but originates from a depreciated performance in the air outlet/hydrogen inlet region (segment #20) as seen from Figure V - 6b. Focusing on MEA #50, marked in red inFigure V - 3, which featured more important cell voltage losses after 12,860 hours of operation, shows that its segments 3 to 10, 14 and 15 perform worse than the fresh MEA and MEA #32 (Figure V - 6b). Since the segmented cell was operated in galvanostatic mode, this resulted into much higher local current density in the other segments (this however does not imply that their catalytic performance improved). By comparison with the fresh MEA, the voltage difference is *ca.* 0.47 V at an average current density of j = 0.50 A cm^{-2}, which corresponds to a 34 µV h^{-1} loss, in perfect agreement with the data recorded in the stack (Figure V - 4). Finally, the cells marked in blue in Figure V - 4 featured an intermediate behavior between MEA #32 and MEA #50.

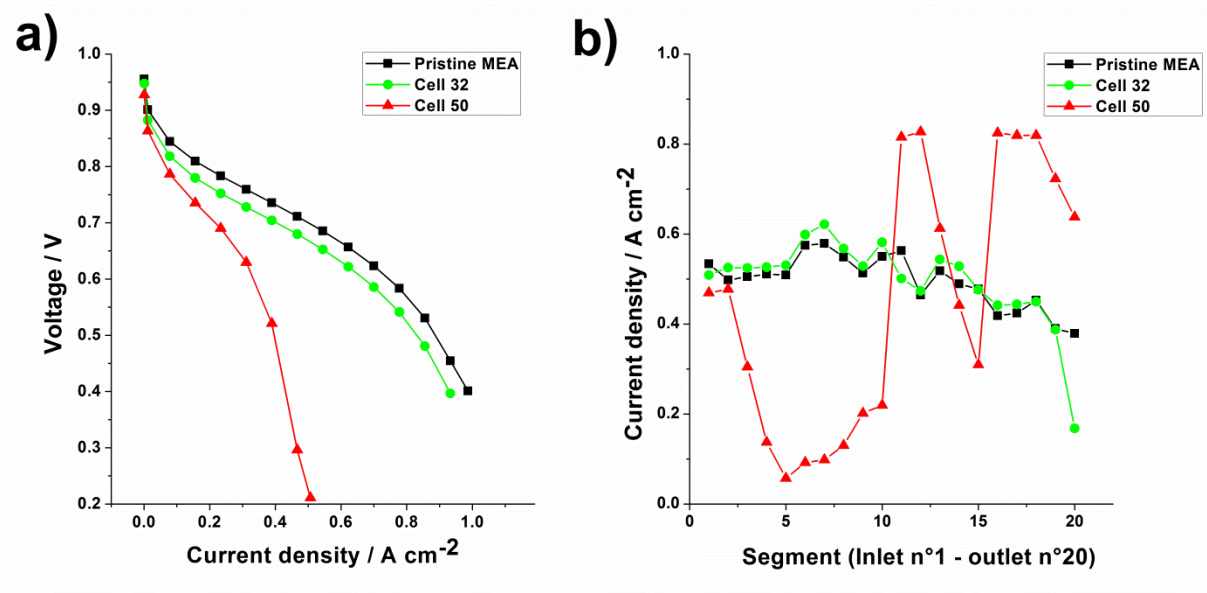

Figure V - 6. a) Beginning-of-Life (BoL) and End-of-Life (EoL) performance of the fresh/aged MEAs (cell #32 and cell #50 of the right stack) measured in the segmented cell. The aged MEAs were operated at I = 22 A – T = 335 K – 65 % RH during 12,860 hours in a 110-cell PEMFC stack. b) The corresponding current density profiles were measured at an average (imposed) value of j = 0.50 A cm-2; the associated cell voltage values were U = 0.7 V with the fresh MEA, U = 0.67 V for MEA #32 and U = 0.23 V for MEA #50 (Figure V - 3).

5.2.3 Linking degradation of electrical performance to membrane failures

Infrared imagery (IR thermography, see Ref. [1] for further details) was used to monitor the extent of degradation of the proton-exchange membrane (PEM) both at the MEA and at the stack level. In this technique, a mixture of nitrogen and hydrogen was fed to the anode side, while air was flowing at the cathode side. Therefore, any hole in the PEM resulted in heat production (combustion of hydrogen), which was detected by the IR camera. Figure V - 7 displays the superimposition of all the pinholes detected within the 55 MEAs of the left (a) and of the right stack (b). For both stacks, the air outlet region of the PEM turned out to be the statistically most degraded area (black dashed-line circle), in agreement with our previous results [1]. 45 % (resp. 80 %) of the MEAs of the left (resp. right) stack contained pinholes in this region, respectively. In addition, few and small pinholes randomly spread through the MEA were detected. These small holes were occasionally found in the fresh MEA as well: they are believed to result from the random perforation of the PEM by the catalytic layer materials. Those holes were neither found to alter much the system performances nor its ability to run for long periods of time. In contrast, four MEAs, among which MEA #50, featured large-size holes (red dashed-line circles in Figure V - 7), which caused significant reduction of the global cell voltage. One of them even led to the shutdown of the system for safety reasons. This type of defect also appeared to be randomly distributed within the PEM.

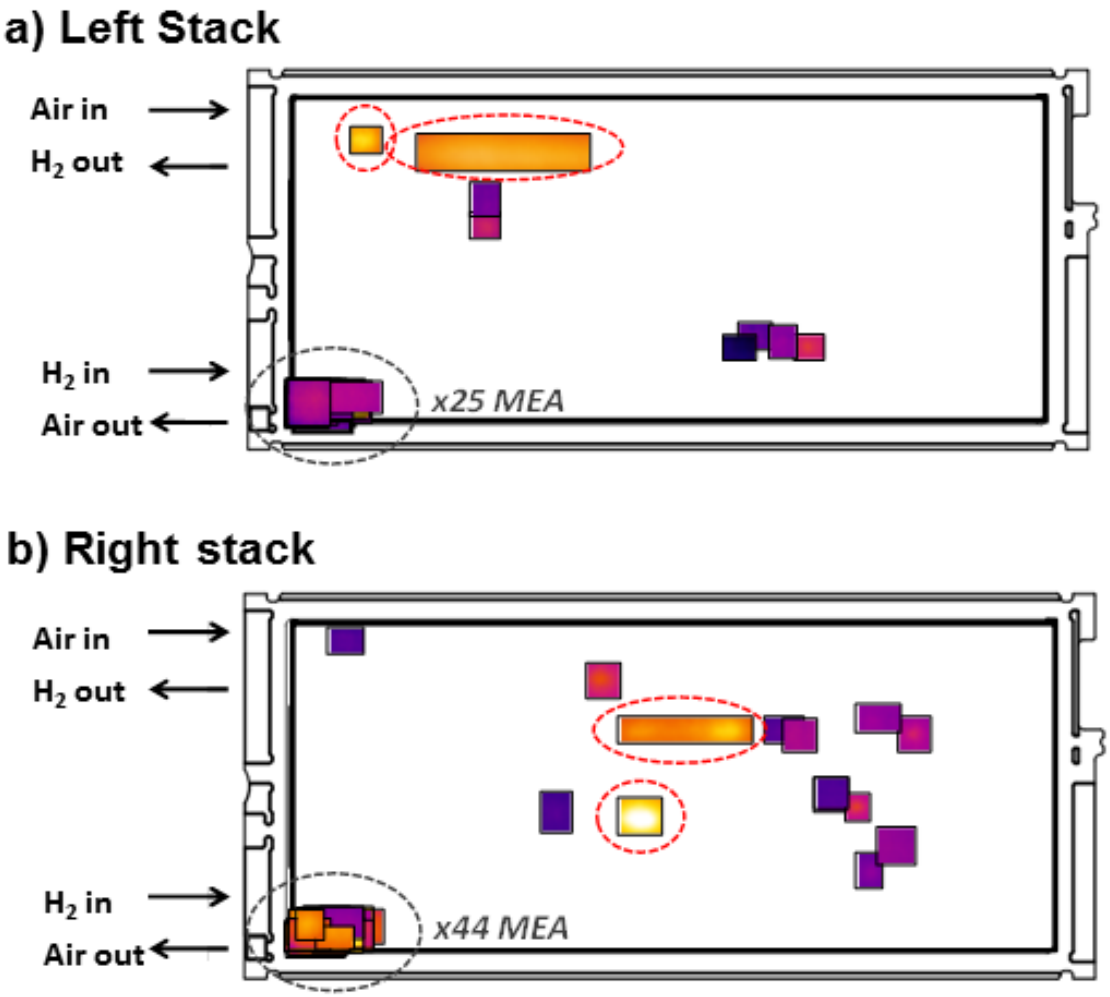

Figure V - 7. Pinholes position superimposed on a single MEA for the (A) left stack and (B) right stack. The MEAs were operated at I = 22 A – T = 335 K – 65 % RH during 12,860 hours in a 110-cell PEMFC stack.

Figure V - 8 schematically represents the position of the cells that contained a hole in the air outlet region (black bars) or a large size hole, the latter being responsible for the fuel cell shut down (red bars). Here again, strong heterogeneities of aging appear at the MEA and at the stack level. Indeed, whereas no significant trace of membrane degradation is witnessed for the upper left stack (cell #1 to cell #30), nearly all the PEMs in the bottom part of the stack are perforated in the air outlet region. Two of the four large size holes were located in the bottom part of the left stack. On the contrary, the right stack had perforated membranes nearly in all cells in the air outlet region, regardless of their position from the bottom to the top; the state of the right stack at this stage overall seems to correspond to an advanced phase concerning membrane degradation, which is not the case for the left stack. The two defects that decreased considerably the cell voltage are located in the upper part of the right stack, but given the small number of such defects, generalizing the rationale for this would be awkward.

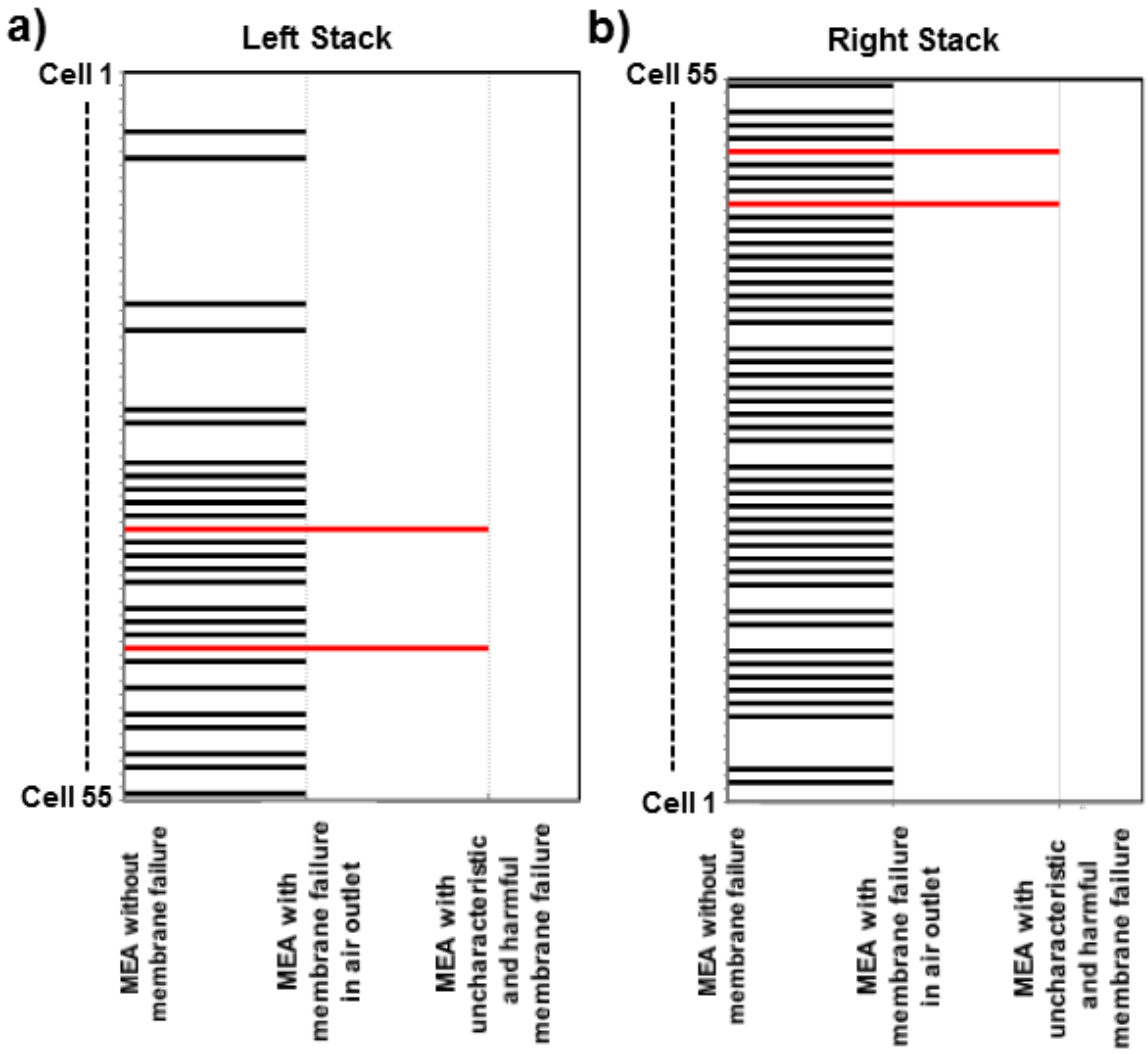

Figure V - 8. Pinhole localization through the a) left and b) right stack. Cells with holes in the air outlet region are shown in black and cells with one of the four pinholes responsible for the fuel cell shut-down are shown in red. The MEAs were operated at I =22 A – T = 335 K – 65 % RH during 12,860 hours in a 110-cell PEMFC stack.

Figure V - 9 shows the infrared image obtained on the fresh and on the aged MEAs (MEA #32 and MEA #50). No sign of pinhole was detected on the fresh MEA, as indicated by the constant temperature measured by IR thermography. The MEA #32, which performed comparably to the fresh MEA in the stack (Figure V - 4) or in the segmented cell (Figure V - 6), featured a pinhole in the air outlet region, in agreement with the region where a local loss of performance was measured in the segmented cell (segment #20, see Figure V - 6). Therefore, the local loss of electrical performance during PEMFC operation likely originates from the formation of a mixed potential in the vicinity of the pinhole, following the increased hydrogen crossover. The MEA #50, which has relatively lower electrical performance (average cell voltage of 0.23 V at 0.50 A cm^{-2}), exhibited one of the large size pinhole that caused the end of operation of the EVOPAC system. From the IR image, the pinhole structure

looked like a membrane failure spread on a straight line of approximately 3 cm. The low resolution of the IR image and the presence of the gas diffusion layer prevented the exact localization of the holes. Therefore, it could not be determined whether the pinholes originated from the channel or from the land region. However, the pinhole region is clearly located in segment #8 of the flow field plate, which is the region where lower local voltages were measured in the segmented cell (segments 2 to 10, see Figure V - 6). These results clearly demonstrate the link between electrical performance degradation and membrane failure. As one will see below, a clear link also exists between the size of the hole, the extent of hydrogen crossover, and the degradation of the cathode catalytic layer.

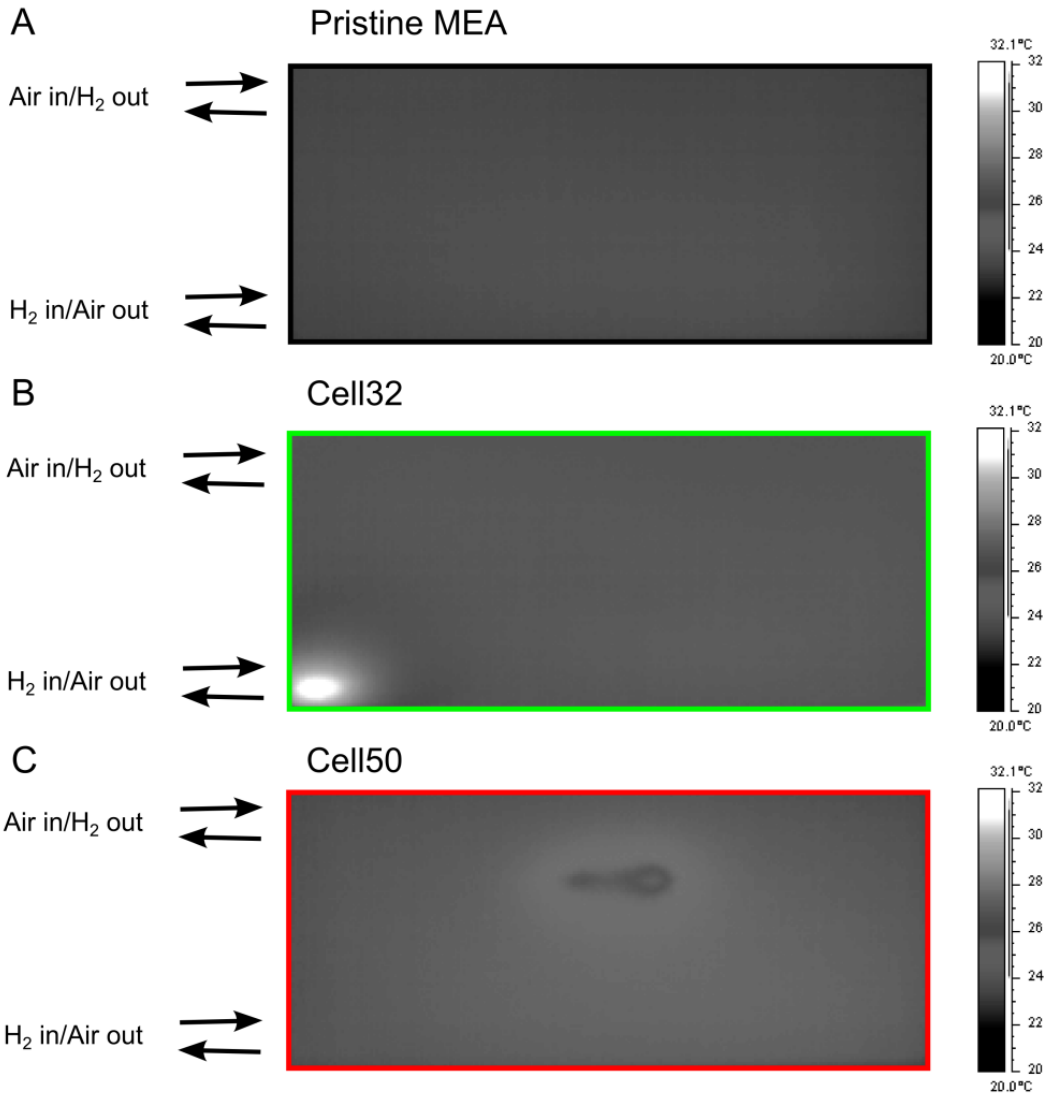

Figure V - 9. Single IR imagery of the (A) fresh and the aged MEAs: (B) cell #32 and (C) cell #50 of the right stack. The MEAs were operated at I = 22 A – T = 335 K – 65 % RH during 12,860 hours in a 110-cell PEMFC stack.

5.2.4 Linking the degradation of the cathode catalytic layer and of the electrical performance to the membrane failures

a. Modification of the thickness of the cathode catalytic layer

Sections 2.2 and 2.3 enabled linking the localization of membrane failure to the local performance measured in the segmented cell. They provided evidence that, in case of large size hole, the local electrical performance can also be detrimental to the MEA global performance. It is now of interest to check whether the formation of membrane pinholes does also modify the morphology of the cathode electrocatalyst and, by extension, to check whether the degradation of the cathode catalytic layer can rationalize (at least to some extent) the decrease of the MEA performance. Figure V - 10 shows representative FEG-SEM images of the MEA in their initial state and after 12,860 h of aging. Here again, the *post mortem* analyses were performed on the same aged MEAs, *i.e.* MEA #32 and MEA #50, which were characterized in the segmented cell (see section 3.2) and by IR thermography (see section 3.3).

The cathode thicknesses of both MEAs measured along the air channel are displayed in Table V - 1: clearly, the cathode thinned heterogeneously. Two particular cases can be distinguished: (i) a low decrease of the cathode thickness from 13.1 µm for the pristine MEA to 10 - 11 µm on MEA #32 (segments #1, 5, 8) and MEA #50 (segment #20) and (ii) a 4-fold larger cathode thinning (*e.g.* down to 3-4 µm) for the other segments. Interestingly, the local electrical performance measured in the segmented cell and the cathode thinning are related parameters: the comparison of Figure V - 6 and Figure V - 10 illustrates that the less-performing segments are those which experienced a drastic cathode thinning. This cathode thinning indicates the corrosion of the HSAC support and the collapsing of its porous structure [20, 21]. Such relation makes sense because, without an adequate porosity network, the access of the gases from the gas-diffusing layers to the catalytic sites, and the removal of the reaction product are both severely hindered, which engenders larger concentration overpotential in the MEA. Interestingly, the segments showing the most pronounced cathode thinning appear brighter in SEM in backscattered electron mode (in this mode of imaging, a brighter contrast means a higher metal loading). This result suggests that the corrosion of the carbon support caused detachment and aggregation of the Pt nanoparticles (in other words, when the HSAC substrate has been corroded into CO_2, the Pt nanoparticles remain, at least partially). However, despite the presence of a substantial amount of Pt, these segments poorly

perform in the segmented cell, probably because Pt is not electronically or ionically (or both) connected and/or not accessible to the reactant. These results firstly highlight that carbon corrosion is a major contributor to the depreciation of the electrical performance of the MEA, and secondly that membrane failure (generation of pinhole) is directly connected to the collapse of the carbon network. They can be rationalized by considering that the creation/presence of membrane pinholes facilitates hydrogen crossover and production of radical species (such as hydroperoxyl ($HOO^{\bullet}$), and hydroxyl ($HO^{\bullet}$) species) in localized regions of the cathode catalytic layer. Those radical species possess a standard potential of 2.80 V *vs*. RHE at T = 25°C, [22, 23] and are extremely aggressive towards the HSAC support, thereby destroying its efficient porosity and further translating into poor electrical performance. Despite its very local origin, the carbon corrosion process can yield complete performance loss of the MEA, provided the pinhole (*i.e.* the H_2 crossover) is large enough. A likely proof for this is the mild decrease of the cathode thicknesses, from 13.1 in 11 micrometres in average (-16 %), in the MEA regions where small size or no pinholes are detected. On the contrary, in regions of the MEA neighbouring a large size pinhole, the cathode thinned by 75 % in average.

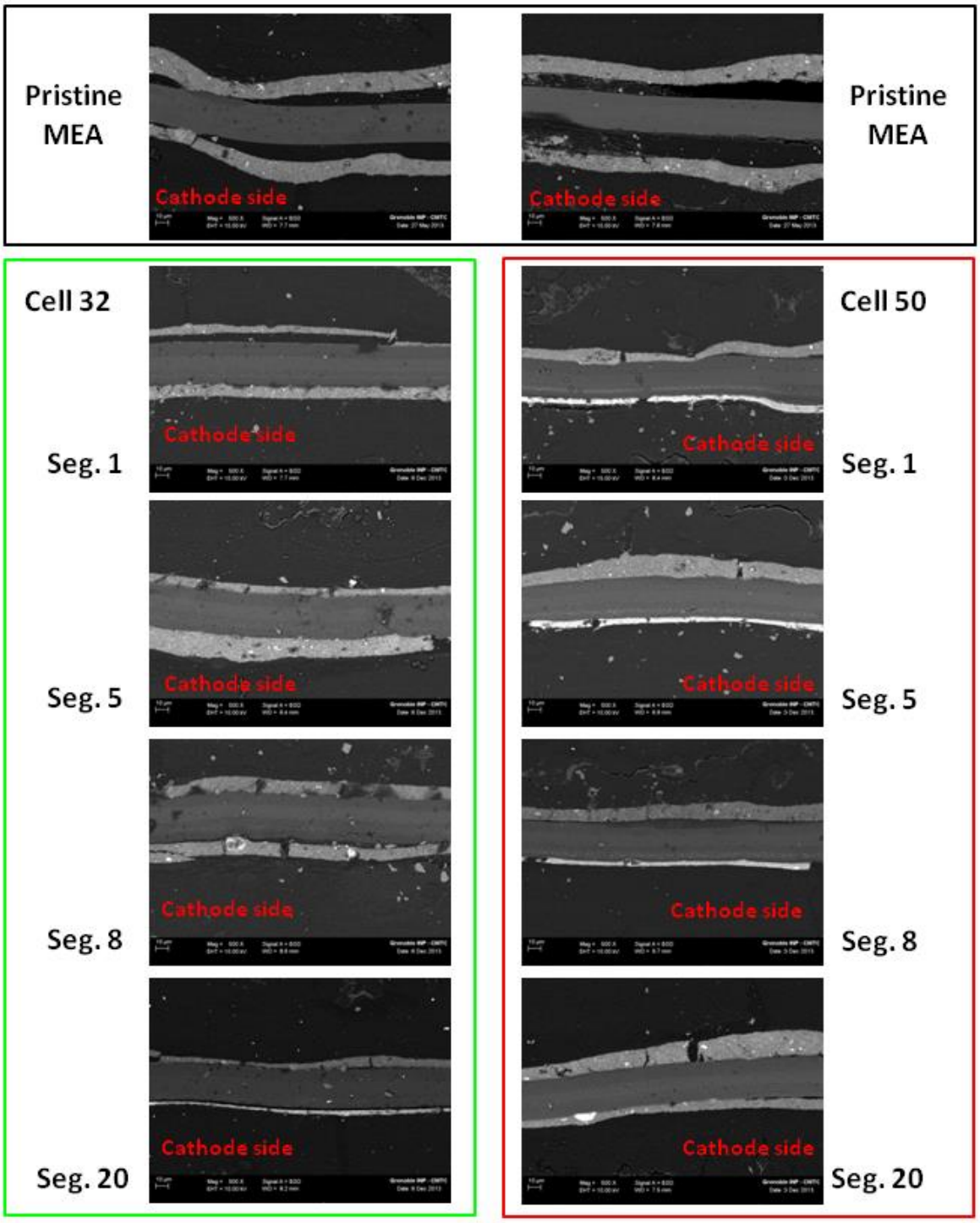

Figure V - 10. FEG-SEM images obtained in back-scattered electrons of the fresh/aged MEAs (cell #32 and cell #50 of the right stack) for different segments. The MEAs were operated at I = 22 A – T = 335 K – 65 % RH during 12,860 hours in a 110-cell PEMFC stack.

Table V - 1. Thicknesses estimated from FEG-SEM images of the fresh/aged MEA cathode catalytic layer operated at I = 22 A – T = 335 K – 65 % RH during 12,860 hours in a 110-cell PEMFC stack.

	Pristine	MEA #32	MEA #50
Segment 1	13.1	10.4	3.8
Segment 5		11.7	3.8
Segment 8		10.8	3.9
Segment 20		3.3	10.7

b. Modification of the cathode catalyst morphology

TEM observations were performed in relevant regions of the MEA to bridge the micrometre-scale morphological changes of the Pt/C nanoparticles observed by SEM to those that occur at the nanometre scale. Figure V - 11 displays representative TEM images of the fresh/aged Pt/C nanoparticles taken in segments #1, 5, 8 and 20 of MEA #32 and MEA #50, *i.e.* those which were previously observed with SEM. It is interesting to note that the pristine Pt/C nanoparticles appear blurred in the TEM, most likely because of the high weight fraction in Nafion® in the fresh MEA. On the contrary, the better contrast of the TEM images on the aged catalyst qualitatively suggests loss in ionomer in the aged cathodes. A major result of the work is the absence of features, which are typical of severe Pt/C degradation mechanisms, such as the large decrease of the density of Pt nanocrystallites, the formation of Pt raft-like structures, or the formation of hollow-core carbon particles [5]. In particular, the cathode of the aged MEA #32 essentially resembles the fresh cathode. However, in agreement with previous findings, the extent of degradation of the Pt/C nanoparticles is largely heterogeneous, and depends on the MEA and cathode region considered. For example, the segments 5 and 8 of MEA #50 show a high degree of agglomeration of the Pt nanoparticles associated with a pronounced extent of Pt dissolution/redeposition (agglomeration of Pt nanoparticles, crystallite growth and necking are obvious in the TEM images). Furthermore, unsupported Pt nanoparticles/aggregates are observed for these two segments. Those morphological changes at the nanometre scale confirm the previous findings by SEM: segments 3 to 10 do correspond to the thinner (that is the more degraded) cathode regions.

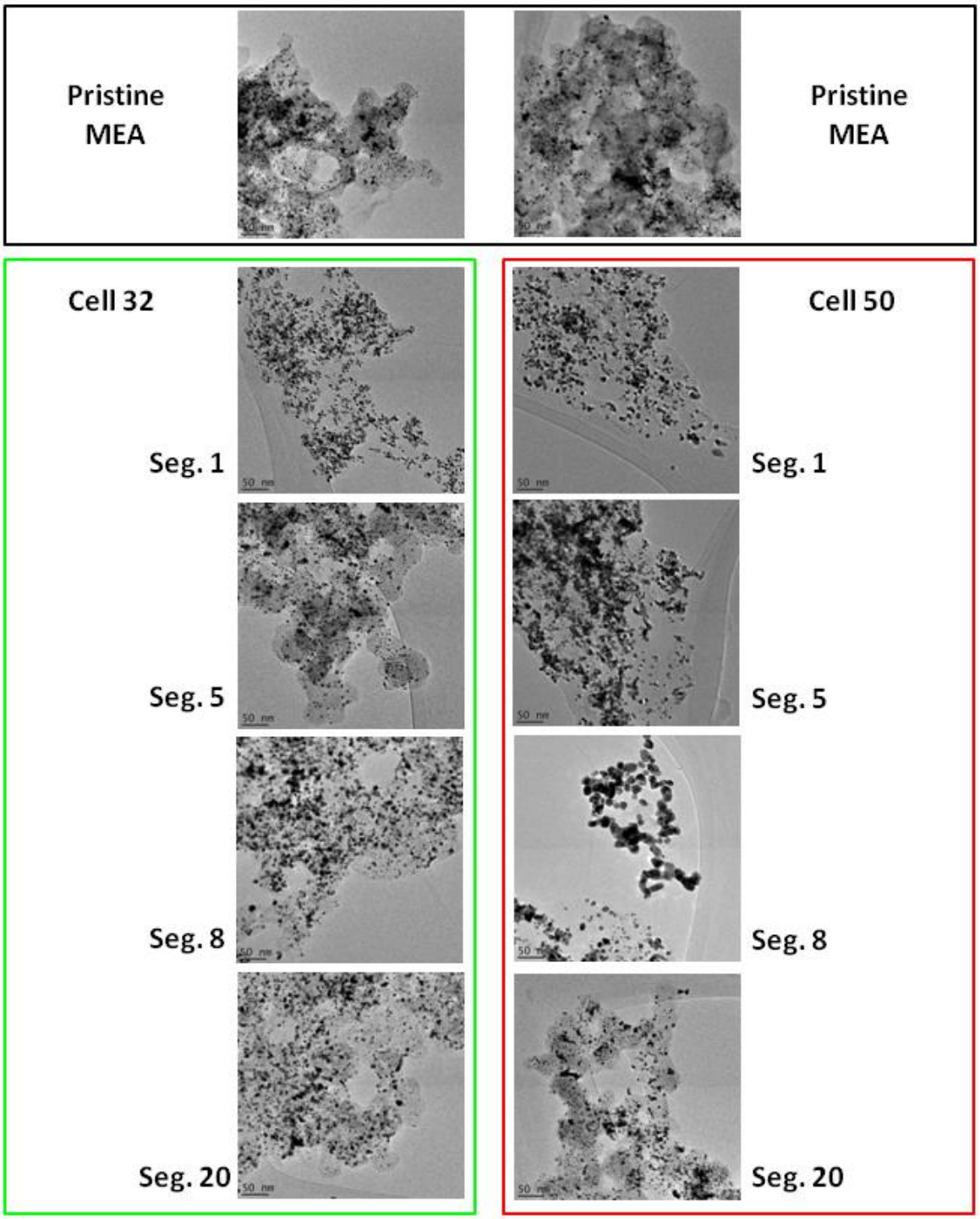

Figure V - 11. Representative TEM images of the fresh/aged cathode catalyst (cell #32 and cell #50 of the right stack) for different segment. The MEAs were operated at I = 22 A – T = 335 K – 65 % RH during 12,860 hours in a 110-cell PEMFC stack.

c. Following carbon structural modifications by Raman spectroscopy

Additional evidences of the heterogeneous corrosion of the HSAC were provided by Raman spectroscopy (Figure V - 12). The characteristic Raman bands observed at 1350 cm^{-1} and 1595 cm^{-1} are related to disordered (D1-band) and ordered (G-band) domains of the carbon support, respectively [24-26]. In agreement with the SEM and TEM observations, the Raman signal observed on the cathode of MEA #32 resembles that obtained on the fresh one. In particular, the D1 and G bands are similar in intensity and shape, except for segment #20, for which the decrease of the D1-band intensity suggests that preferential corrosion of the disordered domains of the HSAC has occurred there. It is important to note that such segment poorly performed in the segmented cell suggesting that, even if graphitic domains remain in a PEMFC cathode, its porous structure might be lost and the whole region would be unable to operate correctly. Identical results were obtained for segments #1, 5 and 8 of MEA #50: in all cases, the decrease of the D1-band intensity resulted into a decrease of the electrical performance. This trend is most pronounced for segment #5, which is the most degraded segment in SEM (Figure V - 10), TEM (Figure V - 11) and Raman measurements (Figure V - 12) and the worst performing in the segmented cell (Figure V - 6). On the contrary, the segment #20, which features minor decrease of the fraction of disordered carbon domains in Raman spectroscopy, possesses excellent electrical performance (since the MEA was operated in galvanostatic mode, the local current density is larger in this segment relative to what was measured on the pristine MEA, because it has to compensate for the poorly performing segments). These results suggest that disordered domains of the HSAC are essential to PEMFC performance. Such result can be understood by considering that disordered carbon is present between the basic structural units of the HSAC support (graphite crystallites); consequently the removal of these domains cause a collapse of the porous structure of the electrode and hence yields poor electrical performance. It is also worthwhile noting that a new Raman band develops in some segments at 1760 cm^{-1} (*cf.* inset in Figure V - 12). This band is ascribed to carbonyl surface functions (C=O), [27-29] and is particularly visible for the most degraded segments: segment #20 of MEA #32 and segments #5 and 8 of MEA #50. Its presence suggests that ordered domains of the HSAC support were also corroded, yielding the emergence of structural defects and the formation of CO-containing surface groups (alcohol, quinone, and carboxylic acid). Summing up, the Raman spectroscopy results are in agreement with the previous findings derived from electron microscopy, membrane analysis and the local performance; they point towards an obvious relationship between the electrical

performance loss, the existence of membrane pinholes and the corrosion of the carbon support of the cathode catalytic layer in the region of the catalytic layer facing the pinholes.

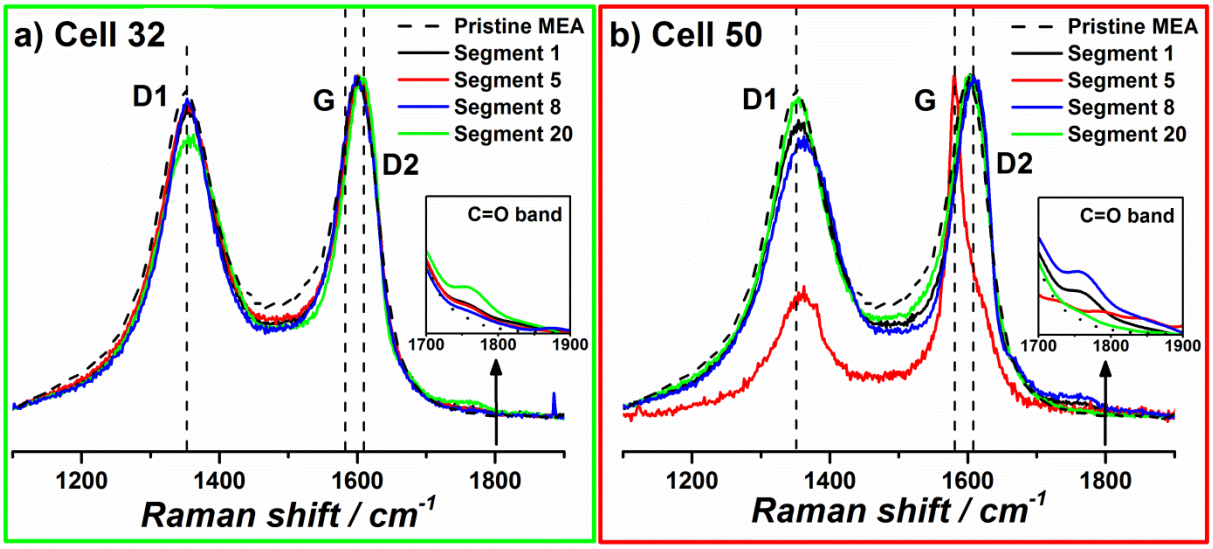

Figure V - 12. Raman spectra of the fresh/aged cathodes (A: cell #32 and B: cell #50 of the right stack) for different segments of the segmented cell. The MEAs were operated at I = 22 A – T = 335 K – 65 % RH during 12,860 hours in a 110-cell PEMFC stack. The inset shows the changes of the intensity of 1760 cm^{-1} band versus the segment number.

5.3 Discussion

The broad set of complementary analyses performed on a 12,860 hours long-term on-site PEMFC aging test has highlighted the main causes of electrical performances loss and enabled understanding the reasons for the end-of-life of the stack. The variation of the cell voltage as a function of aging time gives an average performance loss of -3.5 µV h^{-1} $cell^{-1}$. With this averaged performance loss (which is very small and comparable to that monitored in Ref. [30]), the extrapolated end-of-life at the lower acceptable voltage limit would be estimated to be *ca*. 50,000 hours, which would fulfil the DoE target for stationary PEMFC systems. However, the end-of-life was practically reached *ca*. 4 times faster due to the generation of pinholes in the membrane; this demonstrates that membrane failure is directly at the origin of the end-of-life of the system, as postulated in Ref. [30]. Here, the scenario leading to the PEMFC end-of-life was however understood in deeper details, and it was shown that the pinholes in the membrane do not exert the same influence regarding the degradation of the MEA constitutive materials and of the MEA electrical performance.

On the one hand, the size of the pinholes plays a major role. The small but numerous pinholes forming preferentially in the air outlet/H_2 inlet region only contribute in a small extent to the global loss of electrical performance. Due to their localized position, their impact

on the electrical performance is limited, because these holes are confined on around 5% of the total active surface area of the MEA and downstream the air channel, *i.e*. the region that naturally operates the "worst" in the present cell design (see trace for the pristine MEA in Figure V - 6b, especially regarding segment #20). This means that the rest of the MEA is capable of providing the current required by the load, even for a long period of time. Clearly, such holes do not drive the MEA end-of-life for this relative short period of time (12,860 hours). However, they remain a real source of premature shut-down for longer lifetime and could prevent reaching the 50,000 targeted for stationary PEMFC applications. On the contrary, the end-of-life of the fuel cell was in this case controlled by the failure of the membranes in the "middle region" of 4 MEA over the 110 MEA that composed the two stacks. Around these large holes, located "in the middle" of the air channel, the amount of hydrogen crossover was high enough to destroy the cathode catalytic layer, and affect the local electrical performance of the MEA in the direct vicinity of the hole. Furthermore, Figure V - 6 showed that several segments downstream (for H_2) the segment in which the hole is located also display severely degraded electrical performance and corroded cathode catalytic layer. Indeed, the large size of the hole enabled substantial hydrogen crossover in its vicinity, resulting in fuel starvation in the following segments, and the cathode catalytic layer in this region experienced larger extent of carbon corrosion. For such pinholes, the proportion of MEA surface area that gets rapidly degraded is therefore much larger than for the holes located in the air outlet/H_2 inlet region. As a consequence, this yields severe drop the stack voltage, which becomes lower than the admissible limit and results in the complete shut-down of the system. In addition, the physicochemical analyses performed on selected aged MEAs enabled understanding the causes of the electrical performance losses. The appearance of membrane pinholes favoured the degradation of the high surface area carbon support of the catalytic layer. Such degradation is characterized by the collapse of the porous structure of the catalytic layer, which is essential to provide an efficient access of the reactive gazes and a proper removal of the reaction products. Once its adequate porosity is lost, the catalytic layer behaves improperly, resulting in drastically depreciated electrical performance of the whole MEA.

5.4 Conclusion

In this chapter, a broad set of complementary physicochemical analyses was performed on PEMFC MEAs that operated for 12,860 hours on-site. This strategy enabled highlighting the main causes of electrical performances loss and understanding the reasons for the stack

end-of-life. It was notably demonstrated that the apparition of membrane pinholes favours the local degradation of the high surface area carbon support of the cathode catalytic layer that neighbours the hole. Such degradation is characterized by the collapse of the porous structure of the catalytic layer, which is essential to provide an efficient access of the reactive gazes and a proper removal of the reaction products. Once its adequate porosity is lost, the catalytic layer behaves improperly, resulting in drastically depreciated electrical performance of the whole MEA. This study underlines the need to improve the stability of PEM and develop mitigation strategies to carbon corrosion remain pre-requisites to extend the lifetime of PEMFC MEAs and therefore allow the widespread deployment of the PEMFC technology.

References

[1] G. De Moor, C. Bas, N. Charvin, E. Moukheiber, F. Niepceron, N. Breilly, J. André, E. Rossinot, E. Claude, N.D. Albérola, L. Flandin, Understanding membrane failure in PEMFC: Comparison of diagnostic tools at different observation scales, Fuel Cells, 12 (2012) 356-364.
[2] L. Dubau, L. Castanheira, F. Maillard, M. Chatenet, O. Lottin, G. Maranzana, J. Dillet, A. Lamibrac, J.-C. Perrin, E. Moukheiber, A. ElKaddouri, G. De Moor, C. Bas, L. Flandin, N. Caqué, A review of PEM fuel cell durability: materials degradation, local heterogeneities of aging and possible mitigation strategies, Wiley Interdiscip. Rev.: Energy Environ., 3 (2014) in press, doi.org/10.1002/wene.1113.
[3] E. Moukheiber, C. Bas, L. Flandin, Understanding the formation of pinholes in PFSA membranes with the essential work of fracture (EWF), Int. J. Hydrogen Energy, 39 (2014) 2717-2723.
[4] P.J. Ferreira, Y. Shao-Horn, Formation mechanism of Pt single-crystal nanoparticles in proton exchange membrane fuel cells, Electrochem. Solid State Lett., 10 (2007) B60-B63.
[5] E. Guilminot, A. Corcella, F. Charlot, F. Maillard, M. Chatenet, Detection of Pt^{z+} ions and Pt nanoparticles inside the membrane of a used PEMFC, J. Electrochem. Soc., 154 (2007) B96-B105.
[6] M. Chatenet, E. Guilminot, C. Iojoiu, J.-Y. Sanchez, E. Rossinot, F. Maillard, Pt redistribution within PEMFC MEAs and its consequence on their performances, ECS Trans., 11 (2007) 1203-1214.
[7] Y. Shao-Horn, W. Sheng, S. Chen, P. Ferreira, E. Holby, D. Morgan, Instability of supported platinum nanoparticles in low-temperature fuel cells, Topics Catal., 46 (2007) 285-305.
[8] F.A. de Bruijn, V.A.T. Dam, G.J.M. Janssen, Durability and degradation issues of PEM fuel cell components, Fuel Cells, 8 (2008) 3-22.
[9] P.J. Ferreira, G.J. la O', Y. Shao-Horn, D. Morgan, R. Makharia, S. Kocha, H.A. Gasteiger, Instability of Pt/C electrocatalysts in proton exchange membrane fuel cells - A mechanistic investigation, J. Electrochem. Soc., 152 (2005) A2256-A2271.
[10] L. Dubau, J. Durst, L. Gue az, F. Maillard, M. Chatenet, J. Andre, E. Rossinot, Heterogeneities of aging through-the-plane of a proton-exchange membrane fuel cell cathode, ECS Trans., 41 (2011) 827-836.
[11] L. Dubau, J. Durst, L. Guétaz, F. Maillard, M. Chatenet, J. André, E. Rossinot, Evidences of through-plane heterogeneities of ageing in a proton-exchange membrane fuel cell, ECS Electrochem. Lett., 1 (2012) F13-F15.
[12] L. Dubau, J. Durst, F. Maillard, M. Chatenet, L. Guétaz, J. André, E. Rossinot, Heterogeneities of aging within a PEMFC MEA, Fuel Cells, 12 (2012) 188-198.
[13] J. Durst, A. Lamibrac, F. Charlot, J. Dillet, L.F. Castanheira, G. Maranzana, L. Dubau, F. Maillard, M. Chatenet, O. Lottin, Degradation heterogeneities induced by repetitive start/stop events in proton exchange membrane fuel cell: Inlet *vs*. outlet and channel *vs*. land, Appl. Catal. B, 138-139 (2013) 416-426.
[14] J. Dillet, D. Spernjak, A. Lamibrac, G. Maranzana, R. Mukundan, J. Fairweather, S. Didierjean, R.L. Borup, O. Lottin, Impact of flow rates and electrode specifications on degradations during repeated startups and shutdowns in polymer-electrolyte membrane fuel cells, J. Power Sources, 250 (2014) 68-79.
[15] A. Lamibrac, G. Maranzana, O. Lottin, J. Dillet, J. Mainka, S. Didierjean, A. Thomas, C. Moyne, Experimental characterization of internal currents during the start-up of a proton exchange membrane fuel cell, J. Power Sources, 196 (2011) 9451-9458.
[16] S. Didierjean, A. Lamibrac, T. Geneston, A. Rakotondrainibe, G. Maranzana, E. Rozier, F. Beille, O. Lottin, Internal currents in response to a load change during fuel cell start-up, Int. J. Hydrogen Energy, 37 (2012) 6798-6807.
[17] H.A. Gasteiger, S.S. Kocha, B. Sompalli, F.T. Wagner, Activity benchmarks and requirements for Pt, Pt-alloy, and non-Pt oxygen reduction catalysts for PEMFCs, Appl. Catal. B, 56 (2005) 9-35.
[18] H.A. Gasteiger, J.E. Panels, S.G. Yan, Dependence of PEM fuel cell performance on catalyst loading, J. Power Sources, 127 (2004) 162-171.
[19] E. Billy, F. Maillard, A. Morin, L. Guétaz, F. Emmieux, C. Thurier, P. Doppelt, S. Donet, S. Mailley, Impact of ultra-low Pt loadings on the performance of anode/cathode in a proton exchange membrane fuel cell, J. Power Sources, 195 (2010) 2737–2746.

[20] K. Gallagher, R. Darling, T. Fuller, Carbon-support corrosion mechanisms and models, Handbook of Fuel Cells - Fundamentals, Technology and Applications, 6 (2009).
[21] Z.Y. Liu, B.K. Brady, R.N. Carter, B. Litteer, M. Budinski, J.K. Hyun, D.A. Muller, Characterization of carbon corrosion-induced structural damage of PEM fuel cell cathode electrodes caused by local fuel starvation, J. Electrochem. Soc., 155 (2008) B979-B984.
[22] O. Legrini, E. Oliveros, A.M. Braun, Photochemical processes for water-treatment, Chem. Rev., 93 (1993) 671-698.
[23] O. Antoine, R. Durand, RRDE study of oxygen reduction on Pt nanoparticles inside Nafion: H_2O_2 production in PEMFC cathode conditions, J. Appl. Electrochem., 30 (2000) 839-844.
[24] L. Castanheira, L. Dubau, M. Mermoux, G. Berthomé, N. Caqué, E. Rossinot, M. Chatenet, F. Maillard, Carbon corrosion in proton-exchange membrane fuel cells: From model experiments to real-life operation in membrane electrode assemblies, ACS Catal., (2014) submitted.
[25] D.S. Knight, W.B. White, Characterization of diamond films by Raman spectroscopy, J. Mater. Res., 4 (1989) 385-393.
[26] M.A. Pimenta, G. Dresselhaus, M.S. Dresselhaus, L.G. Cançado, A. Jorio, R. Saito, Studying disorder in graphite-based systems by Raman spectroscopy, Phys. Chem. Chem. Phys., 9 (2007) 1276-1291.
[27] M. Hara, M. Lee, C.-H. Liu, B.-H. Chen, Y. Yamashita, M. Uchida, H. Uchida, M. Watanabe, Electrochemical and Raman spectroscopic evaluation of Pt/graphitized carbon black catalyst durability for the start/stop operating condition of polymer electrolyte fuel cells, Electrochim. Acta, 70 (2012) 171-181.
[28] Y. Hiramitsu, H. Sato, H. Hosomi, Y. Aoki, T. Harada, Y. Sakiyama, Y. Nakagawa, K. Kobayashi, M. Hori, Influence of humidification on deterioration of gas diffusivity in catalyst layer on polymer electrolyte fuel cell, J. Power Sources, 195 (2010) 435-444.
[29] S.K. Sze, N. Siddique, J.J. Sloan, R. Escribano, Raman spectroscopic characterization of carbonaceous aerosols, Atmos. Environ., 35 (2001) 561-568.
[30] S.J.C. Cleghorn, D.K. Mayfield, D.A. Moore, J.C. Moore, G. Rusch, T.W. Sherman, N.T. Sisofo, U. Beuscher, A polymer electrolyte fuel cell life test: 3 years of continuous operation, J. Power Sources, 158 (2006) 446-454.

Chapter VI.

Conclusion and Outlook

6.1 Conclusion

The present thesis has addressed stability issues of high surface area carbon supported Pt nanoparticles used as electrocatalysts in MEAs. The degradation of Pt/HSAC electrocatalysts is most pronounced at the cathode, and is responsible for the decay of the PEMFC performance over time. The long-term physical and chemical changes of Pt/HSAC electrocatalysts were investigated in model and real PEMFC operating conditions with a special emphasis on the HSAC support.

Firstly, the structural and the chemical properties of different HSAC supports were established. The HSAC TKK and the Vulcan TKK supports are the more disordered carbon supports: they feature smaller graphitic crystallites and superior values of S_{BET} in comparison to the RG TKK carbon. This translates by more pronounced intensity of the D1 and the D2-bands in Raman spectra. The porosity of the carbon support influences the dispersion of the Pt nanoparticles: at constant Pt mass fraction, larger values of S_{BET} result in better dispersion and lower degree of agglomeration of the Pt nanoparticles.

The definition of the initial surface chemistry of the carbon supports is essential to understand the changes induced by PEMFC operation. The surface chemistry of the HSAC TKK support-based electrodes was found to depend on the presence of Nafion® ionomer and on the initial electrochemical characterizations performed. Nafion® is used as a binder and as a proton conductor in the catalyst inks. However, it yields the formation of local galvanic cells, which contribute to the oxidation of the carbon supports in the presence of air. A non-monotonic change of both the surface chemistry and the structure of HSAC TKK and Vulcan E-TEK carbon supports was observed during their storage in glass flasks. At short-term, the surface chemistry of the carbon support changes and at long-term, its structure is modified. Furthermore, evidences were provided that electrochemical characterizations modify the surface chemistry of the carbon supports.

The effect of intermediate electrochemical characterizations, of the gas atmosphere and of the upper potential limit used in ASTs was investigated. Firstly, we showed that intermediate electrochemical characterizations used to monitor the variations of the ECSA and the Q/HQ electrical charge during ASTs level off the “real” degradation rate of Pt/HSAC electrocatalysts. This suggests that the number and the type of intermediate characterizations

during an AST has to be properly thought, and its "contribution" on the final degradation result has to be taken into account. Secondly, the ECSA losses of Pt/HSAC, Pt/Vulcan and Pt/RG electrocatalysts, all from TKK, were investigated under the AST protocols of the FCCJ. Distinct ASTs allowed investigating the stability of the Pt nanoparticles (load-cycle protocol – $0.60 < E < 1.00$ V *vs*. RHE) or that of the carbon support (start-up/shutdown protocol – $1.00 < E < 1.50$ V *vs*. RHE). The ECSA losses depend on the investigated electrochemical potential range and on the structure of the carbon support. The most resistant carbon support is the RG TKK, followed by the Vulcan TKK and the less resistant is the HSAC TKK. The gas atmosphere negligibly influences the ECSA losses but affects the surface chemistry of the carbon supports as shown by combined physical and electrochemical results.

In "real-life" operating conditions the PEMFC cathode is exposed to potential values below 1.00 V *vs*. RHE (especially for stationary applications where few start-up/shutdown events occur), that is significantly lower than the ones witnessed during ASTs. To mimic such "real-life" conditions, the COR was investigated in potentiostatic conditions (96 h potentiostatic holds at different electrode potentials ranging from 0.40 to 1.40 V *vs*. RHE) on the Pt/HSAC TKK electrocatalyst. The combined physical, chemical and electrochemical results point towards structure-sensitive COR kinetics. The disordered domains of the HSAC support (amorphous carbon and defective graphite crystallites) are preferentially oxidized at voltages relevant of the PEMFC cathode ($0.40 < E < 1.00$ V). Excursions to high electrode potential ($E > 1.00$ V), witnessed during start-up and shut-down of PEMFC systems, accelerate this phenomenon, and propagate the electrochemical oxidation to the graphitic domains of the HSAC. For both disordered and ordered domains of the HSAC, the COR mechanism is believed to proceed via a similar mechanism (eventual formation of defective sites, which are then oxidized before being evolved in CO_2). Another important finding was the non-monotonic evolution of the Q/HQ oxidation charge with the applied electrochemical potential and the polarization duration. This finding questions the general idea present in the literature that the surface concentration of Q/HQ species progressively increases during ASTs.

Finally, membrane electrode assemblies operated in a 110-cell stack at constant current for 12,860h were used to correlate the findings in model and real PEMFC operating conditions. It was found that individual cells age heterogeneously within the same PEMFC stack, and that the long-term performance of a PEMFC system is related to both PEM and

catalytic layer degradation. The MEAs, which revealed higher electrical performance losses presented large size pinholes in the PEM. These pinholes facilitate the hydrogen crossover, and lead to the local production of radical species that actively participate in the irreversible corrosion of the carbon support in the pinhole region. Such degradation induces significant charge- and mass-transport resistances due to the collapse of the electrode structure, which prevent the access of reactive gas and the removal of the reaction products.

6.2 Outlook

The studies performed in this PhD thesis provided a deeper mechanistic insight of the COR. They revealed (*i*) the structural dependency of the COR kinetics (disordered and/or ordered graphitic domains are oxidized depending on the electrochemical potential experienced), (*ii*) the minor influence of the gas atmosphere towards the COR kinetics, (*iii*) the severe degradation of the carbon support during start-up/shutdown events and (*iv*) the catalytic effect of intermediate characterizations during ASTs .

Promising strategies to overcome the existing issues will depend on the efforts provided by stack developers/engineers and materials scientists. The interplay between these two disciplines will provide “system solutions” combined with “materials solutions”, which will help the industrialization and commercialization of PEMFC systems. In this respect, the following topics are worth investigating:

- Pt loading of the catalytic layers:

  The Pt loading strongly influences the performance of the electrodes. At the anode, the HOR kinetics is very fast, thus allowing small Pt loadings (*ca*. 50 µgPt cm^{-2}) to be used [1]. However, the sluggish ORR kinetics at the cathode requires high Pt loadings. When a PEMFC stack is stopped, both electrodes are filled with air, leading to a decrease of the cell voltages to zero. Upon start-up, hydrogen and air are fed into the anode and cathode gas channels, respectively leading to transitory hydrogen/air boundary in the anode compartments, and the appearance of reverse currents [2]. These reverse currents occur in the passive part of the cell (*i.e*., the part of the anode compartment filled with air), while the active part (*i.e*., the part already filled with hydrogen) operates normally. The potential of the cathode region in the passive part may reach up to 1.50 V *vs*. RHE [3, 4]. As shown by Eom *et al*. [5], the

intensity of the reverse current, and thus the cathode degradation rate, decreases with decreasing the anode Pt loading. This is likely to be due to the smaller ORR current in the passive part of the cell. Therefore, a decrease of the anode Pt loading is interesting from both catalytic activity and stability perspectives.

- As stated above, high cathode Pt loading is required to accelerate the ORR rate [6]. Since a PEMFC cathode should also be thin to minimize mass transport limitations at high current, a high Pt mass fraction is also required. As first shown by Willsau and Heitbaum, [7, 8] the COR kinetics is catalysed by Pt. Different Pt loading change the nanoparticle size, the inter-particle distance and the exposed surface area of the carbon support to the electrolyte [9]. Are these parameters relevant to the COR under PEMFC operation? A systematic evaluation which allows separating the Pt nanoparticle size and the inter-particle distance should bring light to these questions [10, 11].

▪ Start-up/shutdown events:

The most crucial operating conditions that a PEMFC system has to overcome are start-up/shutdown events. These events are extremely aggressive towards the carbon support, [2, 12, 13] and have been extensively studied by using segmented cells [3, 4, 14-16]. The impact of these events can be controlled with “system solutions”:

- The use of an external load during gas purges avoids excursions to high electrode potentials. Similarly, a precise control of the reactant gas pressures is mandatory to avoid the detrimental effect of reverse currents [3].

The “materials solutions” consist in:

- Increasing the graphitic content of the carbon support at the cathode to minimize CO_2 evolution during these events. However, an adequate balance between high graphitic content and adequate porosity has to be found. Such balance has recently been reported by Galeano *et al*. [17]: hollow microporous graphitic spheres were used to support Pt nanoparticles, and catalytic performance was reported in both model and real PEMFC operating conditions. Further long-term tests should be performed to confirm or infirm the potential of this “material solution”,

- Adding a selectively conducting component at the anode, in order to limit the potential transients. Such concept has been presented by the Automotive Fuel Cell Cooperation [18]. A tin oxide (SnO_2) layer was placed between the anode catalyst layer and the GDL. It is conductive under normal operation and resistive under air, which limits the in-plane currents, holds the anodic potential to lower values during start-up transients and prevent degradation of the cathode structure,

- Metal oxides are also of interest at PEMFC cathodes because of their large corrosion resistance in oxidizing conditions. However, a careful analysis of these materials is needed to prove their application in PEMFC systems [19].

To conclude, with the ongoing work of this thesis, still some questions were left unanswered and might contribute as starting points of future projects. These are:

- On both disordered and ordered domains of HSAC, the degradation proceeds on defective-sites. The stabilization of these defects by halogen, nitrogen or metal oxides appears to be a promising “material solution”, and should be tested in a near future.

- The faradaic efficiency of the COR in ordinary PEMFC operating conditions is a still open question. Does the faradaic efficiency vary over time under stationary operation conditions? How is it influenced by abrupt changes of the electrochemical potential? O_2 partial pressure? Relative humidity? Electrochemical experiments coupled to DEMS (regular electrochemical cell) or CO_2 detectors (PEMFC cell) [20, 21] are likely to provide answers to these questions;

- A better understanding of the heterogeneities of ageing developing during COR in a PEMFC cathode is required to elaborate more resistant PEMFC cathodes. Studies from our group have shown three levels of heterogeneity: at the GDL|CL and the CL|PEM interfaces, at the inlet/outlet, and under the channel/under the land [22-27]. Further investigations in PEMFC operating conditions should now focus on the role of gas humidity and O_2 partial pressure, as proposed by Linse *et al.* [28].

- Finally, the development of ASTs specific to HSAC is a hot issue. Can we create the equivalent of the Fenton test used for PEMs to ensure a fast screening of

different HSACs? Are chemical and electrochemical corrosion equivalent? Acid-treatments of Pt/HSAC with nitric acid and hydrogen peroxide are interesting in terms of creating "artificially" CO_{surf} species, and would modify the stability of the Pt nanoparticles and the reactivity of the carbon support.

References

[1] E. Billy, F. Maillard, A. Morin, L. Guétaz, F. Emmieux, C. Thurier, P. Doppelt, S. Donet, S. Mailley, Impact of ultra-low Pt loadings on the performance of anode/cathode in a Proton Exchange Membrane Fuel Cell, J. Power Sources, 195 (2010) 2737.
[2] C.A. Reiser, L. Bregoli, T.W. Patterson, J.S. Yi, J.D. Yang, M.L. Perry, T.D. Jarvi, A reverse-current decay lechanism for fuel cells, Electrochemical and Solid-State Letters, 8 (2005) A273.
[3] A. Lamibrac, G. Maranzana, O. Lottin, J. Dillet, J. Mainka, S. Didierjean, A. Thomas, C. Moyne, Experimental characterization of internal currents during the start-up of a proton exchange membrane fuel cell, Journal of Power Sources, 196 (2011) 9451.
[4] G. Maranzana, O. Lottin, T. Colinart, S. Chupin, S. Didierjean, A multi-instrumented polymer exchange membrane fuel cell: Observation of the in-plane non-homogeneities, Journal of Power Sources, 180 (2008) 748.
[5] K. Eom, G. Kim, E. Cho, J.H. Jang, H.-J. Kim, S.J. Yoo, S.-K. Kim, B.K. Hong, Effects of Pt loading in the anode on the durability of a membrane–electrode assembly for polymer electrolyte membrane fuel cells during startup/shutdown cycling, International Journal of Hydrogen Energy, 37 (2012) 18455.
[6] F. Maillard, S. Pronkin, E.R. Savinova, Influence of size on the electrocatalytic activities of supported metal nanoparticles in fuel cells related reactions, in: W. Vielstich, H.A. Gasteiger, H. Yokokawa (Eds.) Handbook of Fuel Cells, Volume 5, vol. 5, John Wiley & Sons, Inc., New York, 2009, pp. 91.
[7] J. Willsau, J. Heitbaum, The influence of Pt-activation on the corrosion of carbon in gas diffusion electrodes—A dems study, Journal of Electroanalytical Chemistry and Interfacial Electrochemistry, 161 (1984) 93.
[8] L.M. Roen, C.H. Paik, T.D. Jarvi, Electrocatalytic Corrosion of Carbon Support in PEMFC Cathodes, Electrochemical and Solid-State Letters, 7 (2004) A19.
[9] F. Maillard, A. Bonnefont, F. Micoud, An EC-FTIR study on the catalytic role of Pt in carbon corrosion, Electrochemistry Communications, 13 (2011) 1109.
[10] J. Speder, A. Zana, I. Spanos, J.J.K. Kirkensgaard, K. Mortensen, M. Arenz, On the influence of the Pt to carbon ratio on the degradation of high surface area carbon supported PEM fuel cell electrocatalysts, Electrochemistry Communications, 34 (2013) 153.
[11] J. Speder, A. Zana, I. Spanos, J.J.K. Kirkensgaard, K. Mortensen, M. Hanzlik, M. Arenz, Comparative degradation study of carbon supported proton exchange membrane fuel cell electrocatalysts – The influence of the platinum to carbon ratio on the degradation rate, Journal of Power Sources, 261 (2014) 14.
[12] M. Hara, M. Lee, C.-H. Liu, B.-H. Chen, Y. Yamashita, M. Uchida, H. Uchida, M. Watanabe, Electrochemical and Raman spectroscopic evaluation of Pt/graphitized carbon black catalyst durability for the start/stop operating condition of polymer electrolyte fuel cells, Electrochimica Acta, 70 (2012) 171.
[13] Y.-C. Park, K. Kakinuma, M. Uchida, D.A. Tryk, T. Kamino, H. Uchida, M. Watanabe, Investigation of the corrosion of carbon supports in polymer electrolyte fuel cells using simulated start-up/shutdown cycling, Electrochimica Acta, 91 (2013) 195.
[14] G. Maranzana, C. Moyne, J. Dillet, S. Didierjean, O. Lottin, About internal currents during start-up in proton exchange membrane fuel cell, Journal of Power Sources, 195 (2010) 5990.
[15] J. Kim, J. Lee, Y. Tak, Relationship between carbon corrosion and positive electrode potential in a proton-exchange membrane fuel cell during start/stop operation, Journal of Power Sources, 192 (2009) 674.
[16] Z. Siroma, N. Fujiwara, T. Loroi, S. Yamazaki, H. Senoh, K. Yasuda, K. Tanimoto, Transient phenomena in a PEMFC during the start-up of gas feeding observed with a 97-fold segmented cell, Journal of Power Sources, 172 (2007) 155.
[17] C. Galeano, J.C. Meier, V. Peinecke, H. Bongard, I. Katsounaros, A.A. Topalov, A. Lu, K.J.J. Mayrhofer, F. Schüth, Toward Highly Stable Electrocatalysts via Nanoparticle Pore Confinement, Journal of the American Chemical Society, 134 (2012) 20457.
[18] A.F.C. Cooperation, The challenges for PEMFC catalysts in automotive applications, (2013) Accessible at: http://energy.gov/sites/prod/files/2014/03/f11/cwg_may2013_campbell.pdf.

[19] E. Fabbri, A. Rabis, R. Kotz, T.J. Schmidt, Pt nanoparticles supported on Sb-doped SnO2 porous structures: developments and issues, Physical Chemistry Chemical Physics, 16 (2014) 13672.
[20] N. Linse, L. Gubler, G.G. Scherer, A. Wokaun, The effect of platinum on carbon corrosion behavior in polymer electrolyte fuel cells, Electrochimica Acta, 56 (2011) 7541.
[21] N. Linse, G.G. Scherer, A. Wokaun, L. Gubler, Asme, Start/stop induced carbon corrosion in polymer electrolyte fuel cells, 2010.
[22] E. Guilminot, A. Corcella, M. Chatenet, F. Maillard, F. Charlot, G. Berthomé, C. Iojoiu, J.-Y. Sanchez, E. Rossinot, E. Claude, Membrane and Active Layer Degradation upon PEMFC Steady-State Operation: I. Platinum Dissolution and Redistribution within the MEA, Journal of The Electrochemical Society, 154 (2007) B1106.
[23] L. Dubau, J. Durst, L. Guétaz, F. Maillard, M. Chatenet, J. André, E. Rossinot, Heterogeneities of Aging Through-The-Plane of a Proton-Exchange Membrane Fuel Cell Cathode, ECS Transactions, 41 (2011) 827.
[24] L. Dubau, J. Durst, F. Maillard, M. Chatenet, J. André, E. Rossinot, Heterogeneities of Aging within a PEMFC MEA, Fuel Cells, 12 (2012) 188.
[25] L. Dubau, L. Guétaz, J. Durst, F. Maillard, M. Chatenet, J. André, E. Rossinot, Evidences of "Through-Plane" Heterogeneities of Aging in a Proton-Exchange Membrane Fuel Cell, ECS Electrochemistry Letters, 1 (2012) F13.
[26] L. Dubau, M. Lopez-Haro, L. Castanheira, J. Durst, M. Chatenet, P. Bayle-Guillemaud, L. Guétaz, N. Caqué, E. Rossinot, F. Maillard, Probing the structure, the composition and the ORR activity of Pt3Co/C nanocrystallites during a 3422 h PEMFC ageing test, Applied Catalysis B: Environmental, 142–143 (2013) 801.
[27] J. Durst, A. Lamibrac, F. Charlot, J. Dillet, L.F. Castanheira, G. Maranzana, L. Dubau, F. Maillard, M. Chatenet, O. Lottin, Degradation heterogeneities induced by repetitive start/stop events in proton exchange membrane fuel cell: Inlet vs. outlet and channel vs. land, Applied Catalysis B: Environmental, 138–139 (2013) 416.
[28] N. Linse, Start/stop phenomena in polymer electrolyte fuel cells, in, ETH Zurich, 2012.

Résumé

Cette thèse est consacrée à l'étude des mécanismes de dégradation de noirs de carbone de forte surface spécifique (HSAC) utilisés comme supports d'électrocatalyseurs dans une pile à combustible à membrane échangeuse de protons (PEMFC). Nous avons montré que le mécanisme et les cinétiques de la corrosion électrochimique du carbone (COR) sont influencés par la présence d'ionomère Nafion®, la limite supérieure de potentiel électrochimique, la nature et le nombre de caractérisations intermédiaires présentes dans des tests de dégradation accélérés. En utilisant la spectroscopie Raman, il apparaît que la COR est sensible à la structure cristallographique des HSAC et procède plus rapidement sur les domaines désordonnés (carbone amorphe, cristallites de graphite présentant des défauts). Le taux de recouvrement en espèces oxygénées évalué par spectroscopie de photoélectrons X a été comparé à celui trouvé en intégrant l'intensité du pic quinone/hydroquinone (Q/HQ) en voltampérométrie cyclique. Finalement, une comparaison avec des matériaux carbonés ayant fonctionné pendant 12860 heures en PEMFC confirme nos principaux résultats et permet d'élaborer des stratégies pour atténuer les conséquences de la COR.

Mots-clés : pile à combustible à membrane échangeuse de protons (PEMFC), durabilité des matériaux de PEMFC, supports catalytiques, corrosion électrochimique du carbone

Abstract

This thesis investigates the degradation mechanism of high surface area carbon (HSAC) supports used in proton-exchange membrane fuel cell (PEMFC) electrodes. The structural and the chemical properties of different HSAC supports were established. The effect of the Nafion® ionomer used as a proton conductor, the gas atmosphere, the upper potential limit and the intermediate electrochemical characterizations used to monitor the changes of the electrochemical surface area during accelerated stress tests (ASTs) were investigated. The long-term physical and chemical changes of Pt/HSAC electrocatalysts were investigated in simulated PEMFC operating conditions. Using Raman spectroscopy, we showed that the COR is strongly structure-sensitive and proceeds more rapidly on disordered domains of the HSAC (amorphous carbon and defective graphite crystallites) than on graphitic domains. The coverage with carbon surface oxides was investigated with X-ray photoelectron spectroscopy and bridged to the intensity of the quinone/hydroquinone (Q/HQ) peak monitored by cyclic voltammetry. Finally, the analyses realized on membrane electrode assemblies operated for 12,860h disclosed a perfect agreement between model and real PEMFC operating conditions, and confirmed the structural dependency of the COR kinetics.

Keywords: Proton exchange membrane fuel cell (PEMFC), durability of PEMFC materials, catalyst support materials, electrochemical carbon corrosion.